October 2019

STRUCTURAL CONTROL OF OFFSHORE WIND TURBINES USING PASSIVE AND SEMI-ACTIVE CONTROL

Semyung Park

STRUCTURAL CONTROL OF OFFSHORE WIND TURBINES USING PASSIVE AND SEMI-ACTIVE CONTROL

A Dissertation Presented

by

SEMYUNG PARK

Submitted to the Graduate School of the
University of Massachusetts Amherst in partial fulfillment
of the requirements for the degree of

DOCTOR OF PHILOSOPHY

September 2019

Mechanical and Industrial Engineering

STRUCTURAL CONTROL OF OFFSHORE WIND TURBINES USING PASSIVE AND SEMI-ACTIVE CONTROL

A Dissertation Presented

by

SEMYUNG PARK

Approved as to style and content by:

_____
Matthew Lackner, Chair

_____
James Manwell, Member

_____
Sanjay Arwade, Member

_____
Sundar Krishnamurty, Department Head
Mechanical and Industrial Engineering

ACKNOWLEDGMENTS

I would like to thank my academic advisor Professor Matthew Lackner for giving me such a great opportunity to conduct structural control projects. His guidance touched many facets of my PhD life and I have learned a lot under his tutelage. I am also grateful for my committee; Professor James Manwell and Professor Sanjay Arwade for their guidance of my dissertation. Additionally, I would like to thank my coworkers; Arturo Rodriguez, Albert Fisas, and Mohammad Attia who carried out the project together for over two years in GE Renewable Energy. Lastly, I am very thankful to Meghan Glade for her contribution of some of the works in my dissertation, as well as my lab members. Also, I would like to thank to my first roommates, Jeong-hyun and Insung. None of this would have ever been possible without their supports. My wife Jaeyoung always has supported me and has been with me. I cannot tell you how much I appreciate what you have done for me, and I want to say I love you. Lastly, I would like to dedicate my dissertation to my mother and late father.

ABSTRACT

STRUCTURAL CONTROL OF OFFSHORE WIND TURBINES USING PASSIVE AND SEMI-ACTIVE CONTROL

SEPTEMBER 2019

SEMYUNG PARK

B.E.M.E., YEUNGNAM UNIVERSITY

M.S.M.E., YEUNGNAM UNIVERSITY

Ph.D., UNIVERSITY OF MASSACHUSETTS, AMHERST

Directed by: Professor Matthew Lackner

Offshore wind energy has the potential to generate substantial electricity production compared to onshore locations, due to the high-quality wind resource. Offshore wind turbines must endure severe offshore environmental conditions and be cost effective, in order to be sustainable. As a result, load mitigation becomes crucial in successfully enabling deployment of offshore wind turbines. A direct approach to reduce loads in offshore wind turbines is the application of structural control techniques. So far, the application of structural control techniques to offshore wind turbines has shown to be effective in reducing fatigue and extreme loads of turbine structures. However, the majority of previous research regarding the application of structural control to offshore wind turbine noted the needs for the high-fidelity analysis for structural control using a computer aided engineering (CAE) tool, such as FASTv8. In this dissertation, a structural control module coupled with FASTv8 is developed to meet the needs for high-fidelity analysis of structural control techniques for various OWTs. In addition, the developed control module is updated to analyze various structural control devices operating both

passively and semi-actively. The dynamics of an omni-directional pendulum-type tuned mass damper and orthogonal tuned liquid column dampers (TLCDs) are mathematically modeled and incorporated into the structural control module. With the developed control module, several structural control devices are optimized through a variety of techniques (parametric study, exhaustive search and multi-objective optimization). Solving optimization problems not only provides the parameters for each control device that can be applicable to other multi-megawatts offshore wind turbines, but also provides insight into the effects of design variables on the control performance. Site-specific meteorological and oceanographic data that consists of a combination of wind and wave data are processed and compiled in order to establish key design load cases. With the optimal designs of structural control devices, non-linear fully-coupled time marching simulations are conducted by running a series of design load cases in order to investigate the impacts of passive and semi-active structural control on improving fatigue and extreme behaviors of fixed-bottom and floating offshore wind turbines. The simulation results demonstrate the effectiveness of various structural control techniques on reducing fatigue and extreme loadings.

TABLE OF CONTENTS

Page

ACKNOWLEDGEMENTS iv

ABSTRACT v

LIST OF TABLES x

LIST OF FIGURES xiii

LIST OF ABBREVIATIONS xix

CHAPTER

INTRODUCTION 1

1. LITERATURE REVIEW 7

1.1 Offshore Wind Technology 7

1.2 Structural Control in Offshore Wind Turbines 10

1.2.1 Structural Control for Tower Response Control 11

1.2.2 Structural Control for Blade Response Control 14

1.3 Identified Research Topics 14

2. OWT MODELS AND SIMULATIONS TOOLS 17

2.1 Offshore Wind Turbine Models 17

2.2 Simulation Tools 20

2.2.1 FASTv8 20

2.2.2 TurbSim 22

2.2.3 BModes 22

2.2.4 MLife 22

3. MODELING OF STRUCTURAL CONTROL DEVICES IN FASTv8 23

3.1 Modeling of a Tower-TMD 24
3.2 Modeling of a Blade-TMD 29
3.3 Modeling of Nacelle-TLCDs 33
3.4 Structural Control Module TMD in FASTv8 38
4. METOCEAN DATA PROCESSING AND DESIGN LOAD CASES 40
4.1 Metocean Conditions at Southeast of Nantucket 41
4.2 Metocean Conditions at Wave Hub Site 47
5. CONTROL STRATEGIES AND OPTIMIZATION 51
5.1 Parameter Optimization for a Tower-TMD 51
5.2 Parameter Optimization for a Blade-TMD 59
5.3 Parameter Optimization for Nacelle-TLCDs 69
5.3.1 Reduced Order Exhaustive Search Study 69
5.3.2 Multi-Objective Optimization 81
5.3.3 Analysis of MOO Results 86
5.4 Semi-Active Control for a Tower-TMD 90
5.4.1 Modeling of Magnetorheological Damper 90
5.4.2 Ground Hook Control Algorithms 97
6. LOAD ANALYSIS AND SIMULATION RESULTS 102
6.1 Tower Response Control 102
6.1.1 Fatigue Load Analysis for NREL 5-MW OWTs 103
6.1.1.1 Monopile OWTs 105
6.1.1.2 TLP OWTs 110
6.1.2 Extreme Load Analysis for NREL 5-MW OWTs 117

6.1.2.1 Monopile OWTs 119
6.1.2.2 TLP OWTs.....123
6.1.3 Fatigue Load Analysis for GE 6-MW OWTs.....129
6.1.3.1 Monopile OWTs 130
6.1.3.2 TLP OWTs.....132
6.1.4 Extreme Load Analysis for GE 6-MW OWTs 134
6.1.4.1 Monopile OWTs 135
6.1.4.2 TLP OWTs.....138
6.1.4.3 Impacts of Stroke Limitation of a Tower-TMD 141
6.1.4.4 Mooring Line Sensitivity Analysis 145
6.2 Blade Response Control.....148
6.2.1 Fatigue Load Analysis 148
6.2.2 Extreme Load Analysis.....153
6.2.3 Sensitivity Analysis 156
7. CONCLUSIONS.....159
APPENDICES
A. NOMENCLATURE.....165
B. EXPECTED VALUES AND CORRESPONDING PROBABILITIES.....167
C. FREQUENCY RESPONSE OF TOWER MOTION FOR NREL 5-MW and GE 6-MW OWTs.....168
D. EXAMPLE TMD MODULE INPUT FILE.....172
E. COMPARISON OF LINEAR AND MR DAMPER.....173
BIBLIOGRAPHY.....176

LIST OF TABLES

Table Page

2.1: Properties of the NREL 5-MW turbine....18

2.2: Properties of the GE Haliade 6-MW turbine....18

2.3: Properties of the DTU 10-MW turbine....19

2.4: Properties of the monopole substructures....19

2.5: Properties of the TLP substructures....20

4.1: Description of measurement of the metocean data at buoy 44008....41

4.2: Statistics of variables of interest based on 8 years historical data....45

4.3: Extreme values for 1, 50, 100, 200, and 500-year return periods....46

4.4: Summary of design load cases and type of analysis....46

4.5: Summary of extreme wind and wave conditions at the Wave Hub site....49

4.6: Summary of operational wind and wave conditions....49

4.7: Statistics of variables of interest....49

4.8: Summary of design load cases and type of analysis....50

5.1: Simulation conditions for a parametric study....55

5.2: Main input parameters for the tower-TMD....55

5.3: Design formulas for the optimal frequency and damping ratio....58

5.4: Optimal stiffness and damping ratio for the TMD with mass of 20 tons for the different OWTs....59

5.5: Main input parameters for the blade-TMD....65

5.6: Design formulas for the optimal blade-TMD position....66

5.7: Design formulas for the optimal frequency ratio and damping ratio for the blade-TMD....67

5.8: Design variables and their lower and upper bounds for the reduced ES approach....74

5.9: Inequality design constraints and their descriptions 74

5.10: Parameter for NSGA-II with parallel computing 83

5.11: Design variables for MOO problem and their boundaries (NREL TLP OWT) 86

5.12: Design variables for MOO problem and their boundaries (NREL monopile OWT) 86

5.13: Parameters of selected designs 88

5.14: Parameters of the modified Bouc-Wen model 92

5.15: MR damper parameters as a function of input current i 93

5.16: Damping coefficients and equivalent input currents for different OWTs 94

6.1: The number of simulations for each case 105

6.2: Simulation results for the fatigue loads analysis for the fixed-bottom OWT 107

6.3: Simulation results for the fatigue loads analysis for the floating OWT 111

6.4: The number of simulations for each case 118

6.5: Simulation results for the extreme loads analysis for the fixed-bottom OWT 120

6.6: The reduction rate of the averaged ultimate loadings 122

6.7: Simulation results for the extreme loads analysis for the floating OWT 124

6.8: The reduction rate of the averaged ultimate loadings 126

6.9: The number of simulations for each case 130

6.10: Simulation results for the fatigue loads analysis for the fixed-bottom OWT 130

6.11: Simulation results for the fatigue loads analysis for the floating OWT 132

6.12: The number of simulations for each case 135

6.13: Simulation results for the extreme loads analysis for the fixed-bottom OWT (GE 6MW) 136

6.14: Simulation results for the extreme loads analysis for the floating OWT (GE 6MW) 138

6.15: Changes in the frequency of the critical mode versus mooring line stiffness 146

6.16: The optimal location, frequency ratio and damping ratio as a function of μ (NREL) 149

6.17: The optimal location, frequency ratio and damping ratio as a function of μ (DTU) 149

6.18: Simulation results for the fatigue loads analysis for the NREL 5-MW and DTU 10-MW blades 150

6.19: Simulation results for the extreme loads analysis for the NREL and DTU blade 155

A.1: Nomenclature for the tower-TMD and blade-TMD 165

A.2: Nomenclature for the nacelle-TLCD 166

B.1: Expected values of H_s and T_p corresponding the intersection between U and β ….....167

B.2: Probabilities corresponding the intersection between U and β.....167

E.1: Performance comparison of the linear and MR damper.....175

E.2: Dynamic characteristic comparison of the linear and MR damper 175

LIST OF FIGURES

Figures Page

1.1 : Types of floating substructure for offshore wind turbine 9

2.1 : Schematic of FASTv8 modules with structural control module.....21

3.1 : Schematic of the pendulum-type omni-directinal TMD.....24

3.2 : Schematic of the pendulum-type TMD located on top of the tower 24

3.3 : Schematic of the pendulum-type TMD located inside the blade.....29

3.4 : Schematic of the orthogonal TLCDs, (a): Orthogonal TLCDs inside a nacelle, (b): Top-view, (c): Side-view 33

4.1 : Conditional probability density and expected values of H_s and T_P 44

4.2 : Joint probability density as functions of U and β, and expected values of H_s and T_P (a): 3-D view of distribution, (b): 2-D view of distribution, (c): expected value of H_s for each intersection, (d): expected value of T_P for each intersection 44

4.3: Extreme values and the corresponding return periods 45

4.4 : Probability distribution of operational wind speed and corresponding turbulence intensity (a): hub height of 90 m, (b): hub height of 119 m 45

4.5 : Contour plot of 50-year return period wave heights and periods 48

4.6 : Wind speed distribution and wind/wave misalignment probability 49

5.1 : An example of fore-aft and side-to-side mode shapes of a turbine tower 52

5.2 : Optimal tuning ratio as a function of the mass ratio, (a): NREL 5-MW monopile, (b): NREL 5-MW TLP, (c): GE 6-MW monopile, (d): GE 6-MW TLP 55

5.3 : Optimal damping ratio as a function of the mass ratio, (a): NREL 5-MW monopile, (b): NREL 5-MW TLP, (c): GE 6-MW monopile, (d): GE 6-MW TLP 56

5.4 : Contour plot of the standard deviation of the tower top displacement for optimization of γ and ζ, (a): μ = 0.017, (b): μ = 0.033, (c): μ = 0.049, (d): μ = 0.066 58

5.5 : Optimal stiffness and damping ratio for the TMD with mass of 20 tons 59

5.6 : Deflections of the blades as the blades rotate 62

5.7 : Time response of the blade deflection 63

5.8 : Time response and frequency response of edgewise tip displacement for baseline, and the lighter TMD and the heavier TMD cases 63

5.9 : BMode results showing the 1st edgewise natural fruqunecies (Hz).....64

5.10 : Contour plot of the standard deviation of the blade edgewise displacement (m) 68

5.11 : Scatter plots showing optimal γ and ζ, (a) and (b): 3-D view, (c) and (d): 2-D view.....68

5.12 : Feasible region of design variables for NREL TLP OWT, the color bar represents the area ratio. ■: Constraint 1, ■: Constraint 2 ■: Constraint 3, ■: Constraint 4, (a): FA-TLCD (Circular area), (b): SS-TLCD (Circular area), (c): FA-TLCD (Rectangular area), (d): SS-TLCD (Rectangular area) 75

5.13 : Feasible region of design variables for NREL monopile OWT, the color bar represents the area ratio. ■: Constraint 1, ■: Constraint 2 ■: Constraint 3, ■: Constraint 4, (a): FA-TLCD (Circular area), (b): SS-TLCD (Circular area), (c): FA-TLCD (Rectangular area), (d): SS-TLCD (Rectangular area) 76

5.14 : The percentage of the feasible area as a function of the mass ratio, κ 79

5.15 : Surface response plot as functions of *L* and *B* for the NREL 5-MW TLP, (a): Standard deviations of tower top displacement (Fore-aft), (b): Area ratios (FA-TLCD), (c) Standard deviations of tower top displacement (Side-to-side), (d), Area ratios (SS-TLCD)…. 80

5.16 : Surface response plot as functions of *L* and *B* for the NREL 5-MW monopile, (a): Standard deviations of tower top displacement (Fore-aft), (b): Area ratios (FA-TLCD), (c) Standard deviations of tower top displacement (Side-to-side), (d), Area ratios (SS-TLCD)…. 80

5.17 : Procedure of NSGA-II with parallel computing.....83

5.18 : Multi-objective optimization result for the NREL TLP OWT, (a): optimal Pareto front, (b): total length L, (c): horizontal length B, (d): mass ratio μ.....89

5.19 : Multi-objective optimization result for the NREL monopile OWT, (a): optimal Pareto front, (b): total length L, (c): horizontal length B, (d): mass ratio μ.....89

5.20 : Frequency ratio and head loss coefficient of the TLCDs as a function of the mass ratio (NREL TLP OWT) 90

5.21 : SDOF-TMD model (a) TMD using linear damper; (b) TMD using MR damper 94

5.22 : Comparison of force capacity between the linear damper and MR damper.....96

5.23 : Damping forces versus time, damper displacement and velocity for the different OWTs….....96

5.24 : Ground hook control strategy 100

5.25 : Power spectral density of the tower top motion for each control scheme 101

6.1 : Standard deviation of tower top displacement as a function of wind/wave misalignment 106

6.2 : Time response of the tower top motion as a function of β, (a): tower top displacement in the fore-aft direction, (b): tower top displacement in the side-to-side direction 108

6.3 : TMD excursion in all directions for the fixed-bottom OWT, (a) mean wind speed of 6 m/s, (b) mean win speed of 10 m/s, (c) mean wind speed of 14 m/s, (d) mean win speed of 18 m/s.....109

6.4 : Surface plot of the liquid displacement for the NREL monopile OWT, (a): FB-TLCD for case 3, (b): SS-TLCD for case 3, (c): FA-TLCD for case 1, (d): SS-TLCD for case 1.....110

6.5 : Frequency response of the tower motion for the fixed-bottom and the floating OWTs.. 112

6.6 : Time series, (a): tower top displacement (fore-aft) (b): TMD displacement (fore-aft)…… 113

6.7 : Time series, (a): tower top displacement (StS) (b): TMD displacement (StS).....114

6.8 : Frequency response of the tower base moment in the fore-aft direction.....114

6.9 : Probability of the stop spring operation during the entire simulations.....115

6.10 : TMD excursion in all directions for the floating OWT, (a) mean wind speed of 6 m/s, (b) mean win speed of 10 m/s, (c) mean wind speed of 14 m/s, (d) mean win speed of 18 m/s....116

6.11 : Surface plot of the liquid displacement for the NREL TLP OWT, (a): FA-TLCD for case 3, (b): SS-TLCD for case 3, (c): FA-TLCD for case 1, (d): SS-TLCD for case 1 117

6.12 : Ultimate loadings as functions of the yaw errors and β, (a): tower base moment (fore-aft), (b): tower base moment (StS), (c): nacelle acceleration (fore-aft), (d): nacelle acceleration (StS), (e): tower top displacement (fore-aft), (f): tower top displacement (StS)....120

6.13 : Time response of the tower base moment in the fore-aft and side-to-side direction....121

6.14 : Frequency response of the tower base moment in the fore-aft and side-to-side....121

6.15 : Ultimate loadings as functions of the yaw errors and β, (a): tower base moment (fore-aft), (b): tower base moment (StS), (c): nacelle acceleration (fore-aft), (d): nacelle acceleration (StS), (e): tower top displacement (fore-aft), (f): tower top displacement (StS)....123

6.16 : Frequency response of the tower motion for the fixed-bottom and the floating OWTs..... 125

6.17 : Probability of the stop spring operation during the entire simulations....125

6.18 : Time response of the tower base moment in the fore-aft and side-to-side direction....127

6.19 : Minimum mooring line tension for line #1 to #4, (a) β of -30 deg, (b): β of 0 deg, (c): β of 30 deg, (d): zoomed-in view of (b) focusing on line #3 for the baseline and TLCD cases 128

6.20 : Time response plot of the platform pitch motion and the minimum line tension....129

6.21 : Frequency response plots (upper) and time response plots (lower) of the fixed-bottom OWT under DLC 1.2....131

6.22 : Frequency response of the tower-top motion (upper) and time response (lower) of the tower base moments for the floating OWT (depth of 55 m) under DLC 1.2....133

6.23 : Frequency response of the tower-top motion (upper) and time response (lower) of the tower base moments for the floating OWT (depth of 100 m) under DLC 1.2 134

6.24 : Comparison of force capacity between the linear and MR damper under DLC 6.1……. 137

6.25 : Frequency response of the tower top motion (upper) and time response (lower) of the tower base moment for the floating OWT under DLC 6.1 140

6.26 : Time response for the tower base moment (upper) and the tendon tension (lower)… 140

6.27 : Non-linear spring force curves according to the stroke limitations 141

6.28 : Effect of tuning frequency on a structural response 142

6.29 : Effect of TMD stroke on reducing maximum loads 143

6.30 : Time response of the tower base moment to show the negative effect of the stop-spring 144

6.31 : Frequency response of the tower base moment to show the negative effect of the stop-spring 144

6.32 : Frequency response of the tower base moment according to the mooring line stiffness 146

6.33 : Reduction in maximum tower base moment and nacelle acceleration, as a function of mooring line stiffness 147

6.34 : Reduction in 90^{th} percentile TMD stroke according to the mooring line stiffness…. 147

6.35 : Reduction rates of DELs according to different design cases for the NREL blade……. 151

6.36 : Reduction rates of DELs according to different design cases for the DTU blade…… 151

6.37 : Ratio of the peak to peak TMD stroke to the chord length where the TMD is mounted 152

6.38 : Ultimate loadings as functions of the yaw errors and β for the NREL blade, (a): blade root moment (fore-aft), (b): blade root moment (StS) 154

6.39 : Ultimate loadings as functions of the yaw errors and β for the DTU blade, (a): blade root moment (fore-aft), (b): blade root moment (StS) 154

6.40 : Time response of the blade motion in the edge-wise direction (DTU 10-MW) 155

6.41 : Sensitivity analysis result as a function of (a): position ratio, (b): mass ratio, (c): frequency ratio, (d): damping ratio 156

C.1 : Frequency response of TTDspFA for floating OWTs (NREL TLP and GE TLP), Mean wind speed of (a): 4 m/s, (b): 8 m/s, (c): 12 m/s, (d): 16 m/s, (e): 20 m/s, (f): 24 m/s……. 168

C.2 : Frequency response of TTDspSS for floating OWTs (NREL TLP and GE TLP), Mean wind speed of (a): 4 m/s, (b): 8 m/s, (c): 12 m/s, (d): 16 m/s, (e): 20 m/s, (f): 24 m/s…… 169

C.3 : Frequency response of TTDspFA for fixed-bottom OWTs (NREL Monopile and GE Monopile), Mean wind speed of (a): 4 m/s, (b): 8 m/s, (c): 12 m/s, (d): 16 m/s, (e): 20 m/s, (f): 24 m/s 170

C.4 : Frequency response of TTDspSS for fixed-bottom OWTs (NREL monopile and GE monopile), Mean wind speed of (a): 4 m/s, (b): 8 m/s, (c): 12 m/s, (d): 16 m/s, (e): 20 m/s, (f): 24 m/s 171

D.1 : TMD module input file 172

E.1 : Power spectral density of the fore-aft tower base moments for the baseline and IVB-GH approach using the linear and MR damper 173

E.2 : Time response plot of the tower base moment for the baseline and IVB-GH approach using the linear and MR damper 173

E.3 : Input damping coefficient and current following the IVB-GH algorithms, and damping forces 174

E.4 : Comparison of the damper forces between the linear and MR damper in the low and high velocity region 174

LIST OF ABBREVIATIONS

AMD	=	active mass damper
ASL	=	above sea level
CAE	=	computer-aided engineering
CPC	=	collective pitch control
DB-GH	=	displacement based ground hook
DEL	=	damage equivalent load
DLC	=	design load case
DLL	=	dynamic link library
DNV	=	Der Norske Veritas
DOWEC	=	Dutch Offshore Wind Energy Converter
EA	=	evolutionary algorithm
ESS	=	extreme sea state
ETI	=	Energy Technology Institute
ETM	=	extreme turbulence model
EVA	=	extreme value analysis
EWM	=	extreme wind model
FAST	=	Fatigue, Aerodynamics, Structures, and Turbulence
FLS	=	fatigue limit state
GA	=	genetic algorithm
GE	=	General Electric
HMD	=	hybrid mass damper
IEC	=	International Electrotechnical Commission
IPC	=	individual pitch control
IVB-GH	=	inverse velocity based ground hook
JONSWAP	=	Joint North Sea Wave Project
LIDAR	=	Light Detection and Ranging
LQG	=	Linear-quadratic Gaussian
LQR	=	Linear-quadratic Regulator
MAP	=	Mooring Analysis Program

MOO	=	multi-objective optimization
MR	=	magnetorheological
NacAccFA	=	nacelle acceleration in the fore-aft direction
NacAccSS	=	nacelle acceleration in the side-to-side direction
NDBC	=	National Data Buoy Center
NREL	=	National Renewable Energy Laboratory
NSGA-II	=	non-dominated sorting genetic algorithm II
NSS	=	normal sea state
NTM	=	normal turbulence model
OC3	=	Offshore Code Comparison Collaboration
OWT	=	offshore wind turbine
PID	=	proportional-integral-derivative
PMD	=	pendulum mass damper
RootFx	=	blade root force in the x-direction
RootFy	=	blade root force in the y-direction
RootMx	=	blade root moment in the x-direction
RootMy	=	blade root moment in the y-direction
SCGA	=	simplex coding genetic algorithm
SDOF	=	single degree of freedom
STFT	=	short-time Fourier transform
TLCD	=	tuned liquid column damper
TLP	=	tension leg platform
TMD	=	tuned mass damper

INTRODUCTION

Offshore wind turbine (OWT) systems have the potential for substantial electricity production due to the high quality wind resource, compared to onshore locations [1-3]. While OWTs can be deployed in locations with high quality wind resources, the operational environment of OWTs is harsher than onshore turbines because of the combined effects of aerodynamic loading from the wind as well as the hydrodynamic loading from sea waves and currents. These high speed winds and severe waves cause fatigue and extreme loads on the structure, which may lead to failures of OWTs and necessitate large, heavy structures to withstand the loads. In order for OWTs to be viable, they must be able to withstand the harsh offshore environment while still being cost effective. Thus, load mitigation is extremely important in order to enable successful deployment of fixed-bottom and floating OWTs.

In this context, a wide range of load mitigation approaches have been investigated. One class of methods utilizes the pitch of the blades as a control actuator, such as blade pitch control with feedback [4-9], or feedforward control (preview control) using LIDAR (light detection and ranging) [10-13]. Collective Pitch Control (CPC) can adjust the pitch of all rotor blades to the same angle simultaneously, so it allows the control of the turbine speed and thrust in order to limit power in above rated wind speeds. This approach has been successful in OWTs by using gain-scheduled proportional-integral-derivative (PID) control based on the speed differences between the rated (constant) and the filtered generator speed [4]. CPC can be used to damp out tower vibrations through feedback control of the tower fore-aft acceleration [6]. However,

CPC is incapable of coping with the unsteady and asymmetric aerodynamic loads caused by inhomogeneous wind fields such as wind shear, turbulence, and yaw misalignment, etc. [7].

Another approach for load mitigation is Individual Pitch Control (IPC), in which the pitch of each blade is adjusted individually, in order to reduce the fatigue loads on the rotor blades, hub, and other components. The control algorithms of IPC may use the multi-blade coordinate transformation [8, 10], or optimal state feedback control, using Linear Quadratic Regulator (LQR) and Linear Quadratic Gaussian (LQG) methods [9-11]. Also, further load reductions to the IPC strategy can be achieved by adding a feedforward term in parallel with feedback control [12]. In addition, IPC can compensate for asymmetric aerodynamic loads by regulating the pitch angle of each blade independently with preview pitch control based on feedforward control using LIDAR [13-15].

"Smart rotors," in which aerodynamic load control devices are distributed along the blade span, are a novel approach for blade load mitigation. These devices could be controllable trailing edge flaps, micro-tabs, synthetic jets, plasma actuators, etc. In all cases, the devices are capable of modifying the local sectional lift coefficient on the blade. In smart rotor approaches, the blade loads are sensed through accelerometers or strain gauges, and the actuators are commanded using a control algorithm to adjust the lift and reduce the variation in the local lift. While simulation results have indicated significant promise for smart rotors, they have not been implemented commercially to date [16].

The common rationale behind the aforementioned strategies above is to control the aerodynamic characteristics of the rotor in order to add aerodynamic damping to the turbine blades, tower, and platform. Although the approaches have been shown to be very effective in improving the dynamic response of structures, they suffer from potential drawbacks that prompt further examination into additional load mitigation approaches [17, 18]. Methods that rely on modifying the aerodynamic characteristics of the rotor will increase the usage of the blade pitch actuator, and are incapable of operating during shutdowns. The methods also primarily impact the blade loads; however, tower vibrations caused by wave loading have been shown to cause failures in many non-structural components, such as transformers, yaw drives, etc, and they can also lead to lower reliabilities and significant unscheduled maintenance of OWTs. In addition, the strategies add little aerodynamic damping to the lightly damped tower side-to-side motion. Thus, additional control approaches to reduce loads on OWT structures may be appealing.

A more direct approach for load control is to apply structural control techniques to OWTs. Structural control has been investigated for over two decades in civil engineering, and has shown to be effective in protecting and improving dynamic responses of structures such as skyscrapers and bridges from dynamic loadings caused by earthquakes, wind, and waves [19-21]. Structural control techniques have been investigated for its application in OWTs in recent years in order to cope with harsher conditions in the offshore environments [22-28]. Unlike the strategies mentioned above that increase aerodynamic damping of structures, structural control is a more direct way to add additional damping to structures. In general, the structural damping ratio of a

typical multi-megawatt turbine tower ranges from 0.5 to 2%, which is much lower than the aerodynamic damping from the rotor (~ 5%). Such numbers demonstrate the potential of using structural control techniques that have the capability of adding the additional damping for structures of wind turbines.

The main objective of this dissertation is to apply various structural control techniques to OWTs and to evaluate the potential and the control performance through a rigorous loads analysis using aero-hydro-servo-elastic code FASTv8 [29]. The dissertation develops structural control simulation software coupled with FASTv8, and optimizes both passive and semi-active structural control devices using tuned mass damper (TMDs), pendulum mass dampers (PMDs) and tuned liquid column dampers (TLCDs). The control effects of such devices on reducing fatigue and extreme loads are investigated by running a series of design load cases (DLCs) in accordance with IEC 61400-3 [30]. The primary contributions of this thesis are:

1. This research is the first to develop structural control simulation software coupled with FASTv8. It is able to simulate the dynamic behavior of several structural control devices such as tuned mass dampers (TMDs), pendulum mass dampers (PMDs) and tuned liquid column dampers (TLCDs). As the dynamic response of structural control devices are coupled with the turbine dynamics through the mesh-mapping utility of FASTv8, it allows for non-linear fully-coupled aero-hydro-servo-elastic simulations while analyzing the impact of structural control devices.
2. This research is the first to establish the optimal design formulas for important design variables of structural control devices. The proposed optimal design

formulas can overcome a limitation inherent in utilizing a limited degree of freedom model of a main structure and a control system. In addition, they provide an effective approach for designing structural control devices applied to offshore wind turbines.

3. This research is the first to perform a multi-objective optimization using NSGA-II for orthogonal nacelle-TLCDs. The most influential factors are identified that strongly affect the two objectives that are in conflict. In addition, we derive a Pareto optimal front that provides insights for a decision maker considering the trade-off between the two objective functions.
4. This research is the first to comprehensively analyze the impacts of optimized structural control devices, operating either passively or semi-actively, on reducing fatigue and extreme loads for fixed-bottom and floating offshore wind turbines by utilizing the high-fidelity wind turbine design code, FASTv8 with the developed structural control module. For more rigorous load analysis, the key design load cases recommended by the IEC standard were further modified based on the results of the site-specific metocean data processing.

The structure of the dissertation is organized as follows. Chapter 1 provides a general overview of OWTs and a review of the literature on the subject of structural control techniques for OWTs. A review of previous studies on structural control for OWTs shows the potential of structural control and presents problems to be addressed in this dissertation. In Chapter 2, OWT models and simulation tools used in this dissertation are reviewed. Chapter 3 describes modeling of various structural control devices. The dynamics of each control device are modeled and coded in accordance with the

FASTv8's framework. In Chapter 4, site-specific meteorological oceanographic (metocean) data is processed to create design load cases (DLCs) for load analysis. Chapter 5 presents structural control strategies and solves the optimization problems of passive structural control devices. In addition, various semi-active control strategies are investigated and magnetorheological (MR) dampers are modeled to realize semi-active control algorithms. With the optimal parameters and control strategies determined in Chapter 5, Chapter 6 investigates the impact of the optimized structural control devices on reducing the fatigue and extreme loads for OWTs by running a series of DLCs which are derived in Chapter 4. Finally, Chapter 7 summarizes the work and provides concluding remarks and future work.

CHAPTER 1

LITERATURE REVIEW

This chapter introduces the background of offshore wind technologies and identifies the intrinsic issues of OWTs. Also, the chapter reviews previous research on the application of structural control to OWTs, in order to overcome such issues. Finally, this chapter identifies research topics taking into account the technical limits and problems of previous work to date.

1.1 Offshore Wind Technology

Recent offshore wind turbine types can be classified into two categories: fixed-bottom OWTs, which are a relatively mature commercial technology, and floating OWTs. Fixed-bottom OWTs are only commercially viable in shallow water depth that are typically less than 60 m but are no longer feasible in deeper water sites [1]. Deep water sites tend to be farther from shore, with fewer visual impacts and qualitative wind resources. For deployment of OWTs in deeper water sites, floating substructures have been considered as an economically feasible way, and a number of projects have begun to commercialize floating technologies in recent years [31].

There are different types of fixed bottom substructures depending on the ocean floor conditions and water depth. A monopile and a gravity base substructure are suitable to be deployed in shallow water depths (less than 30 m). In transition water depths between 30 and 60 m, a tripod and a jacket substructure are usually utilized. Among those support structures, the monopile has a relatively simple fabrication process and are

more quickly installed offshore, which generally enables a cost-effective solution in comparison to complicated fixed-bottom structures such as a jacket or a tri-pod. Thus, the monopile support structure will be mainly utilized in this dissertation as the representative fixed bottom OWTs. The current trend in offshore wind development is toward larger turbines installed in deeper water. This results in a lower natural frequency of the system that is closer to the wave excitation frequencies, which may shorten the reliability of the system [32]. While the fore-aft motion has substantial aerodynamic damping during power production from the rotor, the side-to-side motion is poorly damped especially when the wind and waves are misaligned. Therefore, reducing the side-to-side motion is expected to play a critical role in designing a monopile-OWT.

While floating substructures are reasonable in comparison with fixed-bottom OWTs in deeper waters, they tend to retain more complicated dynamics and have to safely endure harsher environmental conditions caused by the combined effects of aerodynamic and hydrodynamic loadings [33]. There are currently different types of floating substructures for OWTs that have been developed for use in deeper water sites. These include a spar buoy, a semi-submersible, and a tension leg platform (TLP), as shown in Figure 1.1. These types of floating substructures have distinct characteristics. The spar buoy uses a large ballast mass to achieve static stability, and it is tethered by catenary mooring lines. The spar buoy is easily influenced by yaw motion [34]. The semi-submersible consists of a main column and some number of offset cylindrical columns. The main column is attached to the tower structure, and pontoons and cross members are used to connect the offset columns to the main column. These substructures float like ships, but remain in place through mooring lines and anchors, which are

attached to the sea floor [35, 36, 37]. A TLP is a vertically moored floating structure, which can achieve stability through the use of taut mooring lines on each leg to provide a restoring force. It may also contain a central spar that contains a buoyancy system and ballast weight to help offset any motion of the turbine. The TLP tends to be much stiffer than other floating substructures, with smaller amplitude motions [38]. The combined loadings induce a pitch and a roll motion of the platform, which significantly affect dynamic responses of a turbine tower due to strong moments of inertia exerted by the pitch and roll mode [39]. In addition, the TLP is very sensitive to severe wave conditions, which can cause a significant structural response and may lead to failure of the system [40]. Among various floating substructures, TLP substructures will be used in this dissertation as the representative floating OWTs. Based on the observations, advanced control systems using structural control techniques are required for OWTs to be more reliable. Previous researches surrounding the application of structural control techniques to OWTs will be reviewed in the next section.

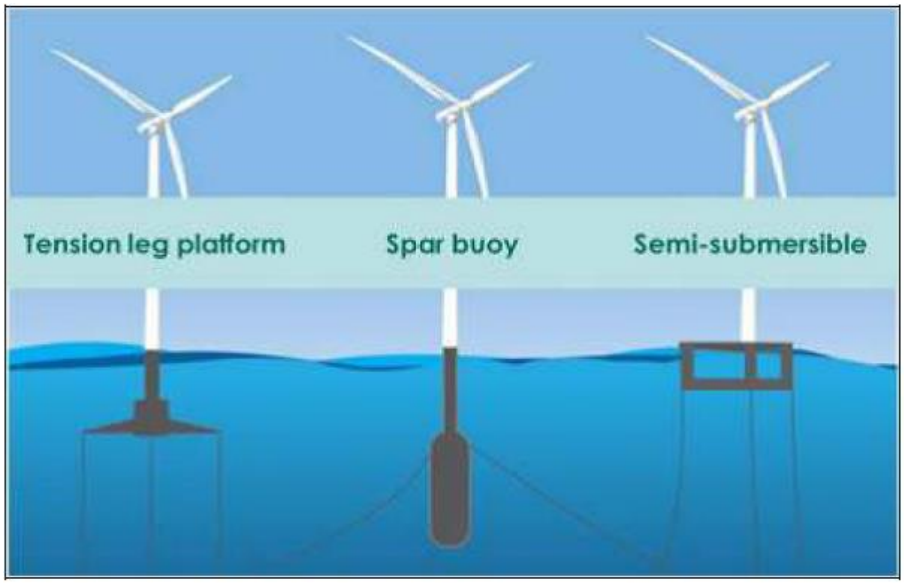

Figure 1.1: Types of floating substructures for offshore wind turbine [37]

1.2 Structural Control in Offshore Wind Turbines

Structural control approaches in the field of civil engineering have been applied to improve dynamic responses of wind turbine structures [22-28]. Mainly, there are three control ways for structural control devices that operate passively, actively and semi-actively. The mechanical parameters of the passive structural control system, such as the spring stiffness and the damping coefficient, are constant during operation. The passive system generally operates in a manner that absorbs a vibrational energy of a critical mode of a main structure by tuning it to a critical mode of a main structure. This approach is commonly used due to its simple mechanism, robustness, and no need for external power consumption [41, 42]. However, the effective frequency band of a passive control system is relatively narrow. In addition, the constant mechanical parameters of a passive system may result in performance deterioration due to the inability of addressing detuning issues. A structural control device controlled actively is more sophisticated approach and it makes use of a variety of actuators to generate the control forces on a main structure [25, 26, 27]. The active control system potentially has superior control performance compared to a passive system, but it requires high power consumption to produce control forces. It is also vulnerable to possible power failures, which may occur under abnormal events, such as loss of electricity and failure of power supplies. Semi-active control system, which has the capability of adjusting the mechanical properties of the control system in real-time with a low power consumption, is an attractive compromise to cope with the drawbacks of the passive and active control systems [43, 44].

1.2.1 Structural Control for Tower Response Control

A variety of passive structural control techniques are being applied to wind turbine systems, especially offshore, in order to improve dynamic responses of an OWT's tower. In recent years, a considerable amount of studies on the application of passive TMDs, TLCDs and pendulum-type mass dampers, and more on OWTs have been conducted [22-28]. Earlier studies focused on fixed bottom OWTs. The control effect of a passive TLCD to improve the dynamic response of a fixed-bottom OWT has been investigated by Colwell et al. [28]. Chen et al. [45] conducted a physical experiment for a TLCD attached to a nacelle of a fixed-bottom OWT. A 1/13-scaled model for a wind turbine system equipped with a TLCD is tested via shaking table tests, which can produce equivalent accelerations of wind/wave excitations. They proved experimental results through a numerical analysis using a simplified single degree of freedom model of the OWT. Moreover, Sun et al. [46] proposed analytical formulations of a bi-directional pendulum type TMD and have shown the effectiveness on reducing the fore-aft and side-to-side motion of a fixed-bottom OWT tower. Li et al. [47] verified the effect of a ball vibration absorber installed inside the nacelle through experimental study. Guimarães et al. [48] investigated an inverted pendulum-type TMDs for reducing the vibration of the fixed-bottom OWT tower. For floating OWTs, Si et al. [49] modeled a passive TMD installed in the spar by considering the platform's three critical modes such as surge, heave, and pitch. Also, they optimized the passive TMDs and investigated the impact of the control system thorough high-fidelity non-linear simulations. Coudurier et al. [50] investigated the impact of a passive and semi-active TLCD on reducing a pitch motion of OWT by incorporating the equations of motion for the TLCD into the floating

substructure's dynamics which includes a pitch, surge and heave motions. As they considered only three motions of the substructure instead of a full-system of OWT that includes the interaction of coupled dynamics between a turbine tower and a rotor system, they noted the needs for the high-fidelity analysis using FAST or other equivalent wind engineering CAE tools. Later, O'Donnell et al. [51] carried out experiments for a scaled floating OWT equipped with multi tuned liquid dampers (MTLCDs) and showed the potential of MTLCDs reducing motions of the floating OWTs. Whilst optimal passive control systems are shown to be very effective on reducing the tower vibrations, they are incapable of coping with off-tuning issues. Since the offshore wind turbines with complicated system dynamics excited by a number of combined loadings are vulnerable to changes in the dynamic natures and the dominant frequency, more advanced control approaches need to be investigated in order to resolve the intrinsic weakness of the passive control system. In addition, the majority of previous research regarding the application of structural control systems to OWTs has been limited to utilizing reduced order models by considering some of critical modes of the turbine and the control system, rather than using high-fidelity wind turbine design code. So, it might not take all of the complicated non-linear dynamics of OWTs. This is likely to result in a further loss in the case of a floating substructure that requires more complex dynamics. So, there's a need for a high-fidelity computer aided engineering (CAE) tool for structural control.

In order to complement such issues regarding the detuning issues of the passive control system and the usage of the simplified models, Lackner et al. [22] developed a new structural control tool in 2011, named FAST-SC. The tool is coupled with FASTv7 and it enabled non-linear fully-coupled aero-hydro-servo-elastic simulations while

analyzing the impact of a passive and an active TMD for floating OWTs. They not only thoroughly examined an optimal passive TMD for floating OWTs but also proposed a hybrid mass damper (HMD) by utilizing the developed tool. In the research of Lackner et al [27], the HMD system is able to reduce the tower fatigue loads by up to about 20 ~ 30 % compared to the baseline system by consuming 2 ~ 8 % (100 ~ 400 kW) of the rated turbine power (5 MW) to operate the actuator. It is shown that the HMD system is very effective in reducing loads on the tower with a large damper stroke. This larger damper stroke and high power consumption of the active control system for floating OWTs may not be suitable for practical use. Later on, Stewart and Lackner [25] enhanced the previous work by introducing a pure active mass damper (AMD) which can resolve the weakness of the HMD system such as the large stroke.

Semi-active control approaches have been widely studied in the field of civil engineering by a number of researchers. However, the application of semi-active control to wind turbines is a relatively new field. Limited studies on semi-active controls have been carried out in the field of wind energy. In 2002, Kirkegaard et al. [52] investigated the semi-active control device using a magnetorheological (MR) damper through experimental and numerical methods. The authors have shown the effects of the MR damper on improving the lateral motion of the turbine. Later on, Karimi et al. [53] proposed a feed-back control technique to change the damping characteristics of the TLCD in real-time by adjusting the valve of the TLCD. Furthermore, Dinh et al. [54] introduced a short time fourier transform (STFT) algorithm for a semi-active TMD. The algorithm commands to change the stiffness of the TMD by tracking the real-time frequencies through STFT algorithm. The authors proved that the semi-active control can

cope with the changes in the dynamic nature of the turbine structures, which makes the TMD free from detuning issues.

1.2.2 Structural Control for Blade Response Control

In the current trend toward using larger rotors to capture more wind energy for modern multi-megawatt wind turbines, the diameter of turbine blades increases and they become more flexible compared to the shorter blades, making them relatively vulnerable to external loads. For this reason, it is also highly desirable to apply structural control concepts to the blades themselves, rather than confining them to towers. However, most of the studies regarding structural control in the field of wind energy focused on reducing loads on wind turbine towers. Limited number of studies on structural control for blade vibrations has been conducted. Arrigan et al. [44] proposed a semi-active TMD to reduce the flapwise vibrations of turbine blades. The tuning frequency of the semi-active TMD can be adjusted in real-time by tracking the dominant frequencies of the system through the STFT. Later on, Zhang et al. [55, 56] proposed roller dampers and tuned liquid dampers to mitigate the edgewise vibrations in rotating blades. They are shown to be effective in decreasing the edgewise vibrations where the aerodynamic damping effect is relatively low, leading to more severe vibrations and increased fatigue loads.

1.3 Identified Research Topics

As discussed in the previous section, there has been extensive research on the application of the advanced structural control systems to OWT, and the effectiveness of structural control for reducing dynamic responses of OWTs have been validated as well.

Nonetheless, the majority of previous research, excluding the ones based on the cutting edge high-fidelity wind engineering code, has not considered the comprehensive dynamics of OWTs with complex system modes. Instead, most of them employ only a few critical dynamic modes of the entire system of OWTs while analyzing and optimizing the structural control devices. Such methods may raise several questions about the validity and reliability of the analysis, as the system may not capture the specificities of the coupled nonlinear dynamics of wind turbines.

As mentioned in the previous section, the work done by Lackner et al. [22] has offered a new way of analyzing structural control techniques for OWTs, that complements the limitations of previous researches. The developed tool (FAST-SC) is coupled to the existing high-fidelity wind engineering tool, FASTv7, so it can provide more reliable and accurate simulation results for structural control. However, TMDs are only applicable with the tool among other structural control devices, and the tool has no function to implement semi-active control approaches as well. In order to employ other structural control devices, further development on the tool is crucial and necessary. As a result, this dissertation aims to develop and upgrade the structural control tool to incorporate various kinds of control devices operating both passively and semi-actively as well. Motivated by these observations, the major tasks of this dissertation follows:

- The dissertation develops structural control modules coupled with FASTv8 in order to meet the needs for the high-fidelity analysis of structural control techniques for OWTS. Now, the module is capable of simulating the dynamic behaviors of translational TMDs, pendulum-type TMDs, and TLCDs. In addition, the TMD can be controlled in a passive and semi-active way. The module enables the analysis of a

wide range of structural control devices and implementations. The module can be applied to fixed-bottom and floating OWTs.

- The dissertation optimizes design variables of structural control devices applied to each respective OWT models in an attempt to improve fatigue and extreme behaviors. Parametric studies and a multi-objective optimization strategy are performed to optimize the control systems. Through this, we also identify the effects of each design variables and their influences on control performance, as well as present the optimal design formulas which can be applicable to multi-megawatts OWTs.
- The dissertation proposes various semi-active control strategies and models a MR damper in FASTv8 to physically implement passive and semi-active TMDs. High-fidelity modeling is required to properly capture non-linear dynamic characteristic of the MR damper. Also, the parameters of the MR damper are identified with 4^{th} order polynomials as a function of input current. In addition, we present the frequency response characteristics of three different semi-active ground hook controls.
- Site-specific meteorological oceanographic data at Southeast of Nantucket and Wave Hub site are post-processed to create design load cases for fatigue and extreme load analysis. We calculate key statistics of variables for wind and waves that specifies the site-specific external conditions by processing raw data measured over the years.
- The dissertation conducts fully-coupled time domain simulations using FASTv8 with the developed structural control modules, in order to investigate the impact of a number of structural control techniques on reducing fatigue and extreme loads of particular. Through a rigorous load analysis and investigation, we demonstrate the potential of application of structural control to OWTs and their technical values.

CHAPTER 2

OWT MODELS AND SIMULATION TOOLS

This chapter reviews various computer aided engineering (CAE) tools for wind energy developed at the National Renewable Energy Laboratory (NREL). The tools are utilized for the analysis of structural control techniques for various OWT models. In addition, this chapter describes the various OWT and support structure models used in this study in order to investigate the impact of structural control approaches.

2.1 Offshore Wind Turbine Models

The wind turbine models used in this study are multi-megawatts turbines with rotor diameters of over 120 meters. One of representative multi-megawatts turbines used in this dissertation is the NREL 5-MW wind turbine model, which has been widely used as a simulation model. In addition to the NREL 5-MW turbine model, the GE Haliade 6-MW wind turbine [57] with a rotor diameter of 150 m is utilized as a baseline OWT model. These turbines are mounted on two types of substructures: fixed-bottom substructures or floating substructures. The monopile support structure is utilized as the fixed-bottom substructure, and the TLP is utilized for floating systems. The monopile substructure developed in the Offshore Code Comparison Collaboration (OC3) [58] project, and the MIT/NREL TLP [59] are adopted to support the NREL 5-MW wind turbine. Separate monopile substructure and TLP to support the GE Haliade 6-MW turbine are also used. The TLP model for the GE Haliade 6-MW turbine is Glosten's PelaStar TLP [57]. It is designed for the Wave Hub test site off the coast of Cornwall, UK, in a FEED study sponsored by the Energy Technology Institute (ETI) of

Loughborough, UK. It is also designed in accordance with DNV specifications [60]. These fixed bottom and floating OWTs (NREL 5-MW and GE Haliade 6-MW) are mainly used to examine the effects on the tower response using a tower-TMD and nacelle-TLCDs in this dissertation. In order to investigate the impact of a blade-TMD, the DTU 10-MW reference turbine model [61] with a rotor diameter of 178.4 m and the NREL 5-MW baseline turbine model are utilized as test models and they are assumed as onshore turbines. The properties and structural parameters of the turbine models and support structures are summarized in Table 2.1 to 2.5. For the NREL/OC3 monopile support structures, the portion of the monopile embedded into the soil has a constant diameter of 6 m and extends to 32 m. Likewise, the subsoil part of the GE monopile is simply an extension (~ 32 m with diameter of 8 m) of the monopile above the mudline. The apparent fixity (AF) length model is applied to each monopile substructure [53].

Rated Power	5 MW
Rotor orientation, number of blades	Upwind, 3 blades
Cut-in, rated, cut-out wind speed	3 m/s, 11.4 m/s, 25m/s
Cut-in, rated rotor speed	6.9 rpm, 12.1 rpm
Rotor Diameter	126 m
Hub Height	90 m
Nacelle dimension (length, width, height)	14.2 m, 2.3 m, 3.5 m
Tower mass	347,460 kg
Rotor nacelle assembly mass	350,000 kg
RNA control	Variable speed, Collective pitch control

Table 2.1: Properties of the NREL 5-MW turbine

Rated Power	6 MW
Rotor orientation, number of blades	Upwind, 3 blades
Cut-in, rated, cut-out wind speed	3 m/s, 10.4 m/s, 25m/s
Cut-in, rated rotor speed	4 rpm, 11.5 rpm
Rotor Diameter	150 m
Hub Height	100 m
Generator Type	Direct drive
RNA control	Variable speed, Independent pitch control

Table 2.2: Properties of the GE Haliade 6-MW turbine

Rated Power	10 MW
Rotor orientation, number of blades	Upwind, 3 blades
Cut-in, rated, cut-out wind speed	4 m/s, 11.4 m/s, 25m/s
Cut-in, rated rotor speed	6 rpm, 9.6 rpm
Rotor Diameter	178.3 m
Hub Height	119 m
Nacelle dimension (length, width, height)	14.2 m, 2.3 m, 3.5 m
Tower mass	628,442 kg
Rotor mass	227,962 kg
Nacelle mass	446,036 kg
RNA control	Variable speed, Collective pitch control

Table 2.3: Properties of the DTU 10-MW turbine

NREL/OC3 Monopile	Length of monopile	30 m (Above mudline)
	Total mass	587,098 kg
	Diameter at monopile base (mudline)	6 m
	Thickness at monopile base (mudline)	0.027 m
	Diameter at monopile top	3.87 m
	Thickness at monopile top	0.019 m
	Tower base height	10 m above the MSL
	Young's modulus	210×10^9 Pa
	Shear modulus	80.8×10^9 Pa
	Effective mass density	8,500 kg/m^3
GE/Monopile	Length of monopile	53 m (Above mudline)
	Total mass	834,746 kg
	Diameter at monopile base (mudline)	8 m
	Thickness at monopile base (mudline)	0.085 m
	Diameter at monopile top	6 m
	Thickness at monopile top	0.065 m
	Tower base height	15.64 m above the MSL
	Young's modulus	210×10^9 Pa
	Shear modulus	80.8×10^9 Pa
	Effective mass density	8,500 kg/m^3

Table 2.4: Properties of the monopole substructures

NREL/TLP	Number of mooring lines	8 (4 pairs)
	Draft	47.89 m
	Displaced volume	12,179 m^3
	Mass including ballast	8,600,410 kg
	CM location below SWL	40.61 m
	Mooring line diameter	0.127 m
	Mooring line stiffness	1.5e^9 N
	Unstretched line length	151.7 m
Glosten Pelastar TLP	Number of mooring lines	5
	Draft	25.6 m
	Displaced volume	4,706 m^3
	Platform mass	1,276,433 kg
	CM location below SWL	14.38 m
	Mooring line diameter	0.159 m
	Mooring line stiffness	1.58e^9 N
	Unstretched line length	81.8 m

Table 2.5: Properties of the TLP substructures

2.2 Simulation Tools

This dissertation utilizes various computer-aided engineering (CAE) tools developed at the National Renewable Energy Laboratory (NREL). BModes and Turbsim are used as preprocessors and FASTv8 with the developed structural control module is used as the main simulator. MLife is used to process wind turbine simulation data calculated by FASTv8. The tools have been validated against experiments, and provide a high degree of confidence. The descriptions of the tools used in this dissertation are outlined in the following section.

2.2.1 FASTv8

The main simulator used in this dissertation is the FAST (Fatigue, Aerodynamics, Structures, and Turbulence) code, which is a fully-coupled aero-hydro-servo-elastic code

for wind turbines. The current version of FAST (FASTv8) modularizes each different physical domain, with simulation modules such as AeroDyn, ElastoDyn, HydroDyn and ServoDyn, etc. as seen in Figure 2.1. AeroDyn is a module to calculate aerodynamic loading on the turbine rotor based on blade-element momentum (BEM) theory. Structural dynamics including structural models of the rotor, drivetrain, nacelle, tower and support structure are modeled in the ElastoDyn module. The hydrodynamic loading, from irregular waves and current for OWTs, are calculated using the HydroDyn module based on a combined potential flow and Morison's equation formulation. The mooring lines are modeled using a quasi-static formulation in MAP (Mooring Analysis Program). The main control system of the turbines implements torque and a pitch control through the ServoDyn module. In the structural control module (sub-module of ServoDyn), additional degrees of freedom for control devices are established to influence the structural behavior.

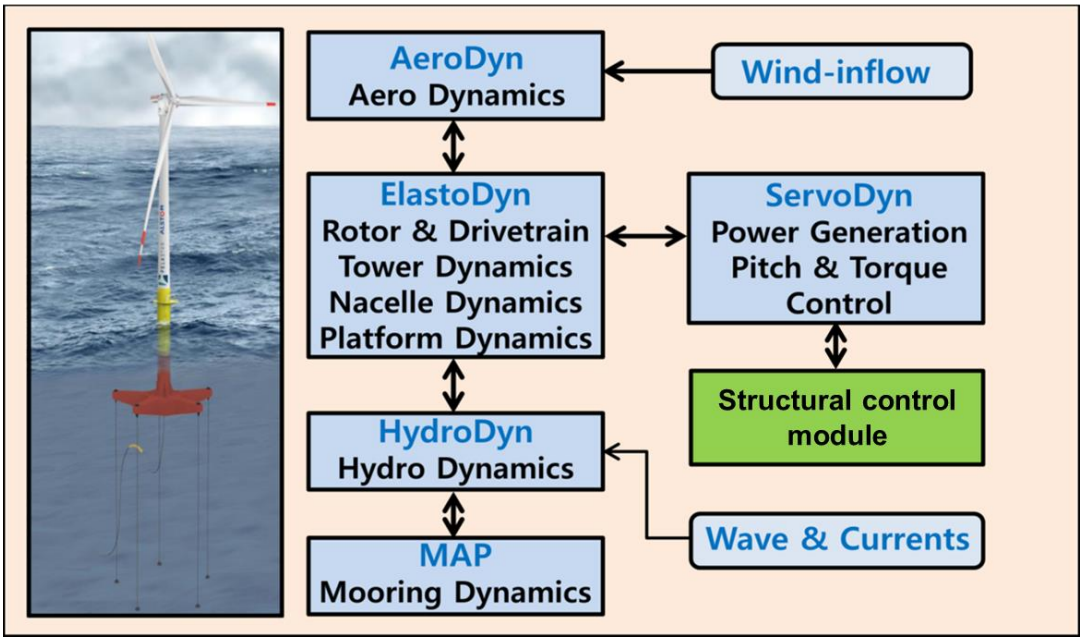

Figure 2.1: Schematic of FASTv8 modules with structural control module

2.2.2 TurbSim

TurbSim is a preprocessor to generate stochastic turbulent wind, which uses a statistical model to simulate the time series of three-component wind speed vectors [62]. In this dissertation, TurbSim is used to create a full-field turbulent wind in time series based on site-specific metocean conditions. The wind data file is generated to meet the requirements of the specific design load cases, which follows the IEC 61400-3 standards [30].

2.2.3 BModes

BModes is a finite-element code that computes coupled modes for both the rotating blades or non-rotating tower [63]. In this dissertation, BModes is utilized to calculate the 1^{st} edgewise natural frequency of certain blades with the blade-TMD installed. The change of the 1^{st} edgewise natural frequency of the blade according to the mass and the location of the blade-TMD is evaluated. This demonstrates the feasibility of the blade-TMD and also provides meaningful information in the selection of the tuning frequency of the blade-TMD.

2.2.4 MLife

MLife is a post-processor and a MATLAB-based tool to estimate the fatigue behavior of wind turbines [64]. In this dissertation, MLife is utilized to post-process the results from the simulations in order to evaluate the impact of structural control techniques on reducing the lifetime fatigue loads of the OWTs used.

CHAPTER 3

MODELING OF STRUCTURAL CONTROL DEVICES IN FASTv8

Previously, a structural control module in FASTv8 was developed by La Cava and Lackner [65]. The module simulates the dynamic behaviors of a tuned mass damper (TMD) mounted inside a nacelle. The module was limited to considering two independent single degree of freedom TMDs operating only passively. In this dissertation, the control module has been updated to add a variety of functions and control devices, i.e. omni-directional pendulum-type mass dampers, tuned liquid column dampers, and semi-active control algorithms. In this chapter, the modeling of the dynamics of a tower-TMD, a blade-TMD, and nacelle-TLCDs are discussed. Non-linear models based on analytical dynamic formulas are established for each control device. The mathematical models are coded in accordance with FASTv8's framework and are incorporated into the structural control module in FASTv8. Note that the words like tower, blade and nacelle written before the device name (TMD or TLCD) in this dissertation refer to the structure in which the device is installed. Nomenclature used to model the control devices are provided in Appendix A: Nomenclature. The content regarding the tower-TMD has been published in *Wind Energy* [66]. The content regarding the nacelle-TLCDs are results of collaboration with an undergraduate student, Meghan Glade, and are now prepared for publication [67].

3.1 Modeling of a Tower-TMD

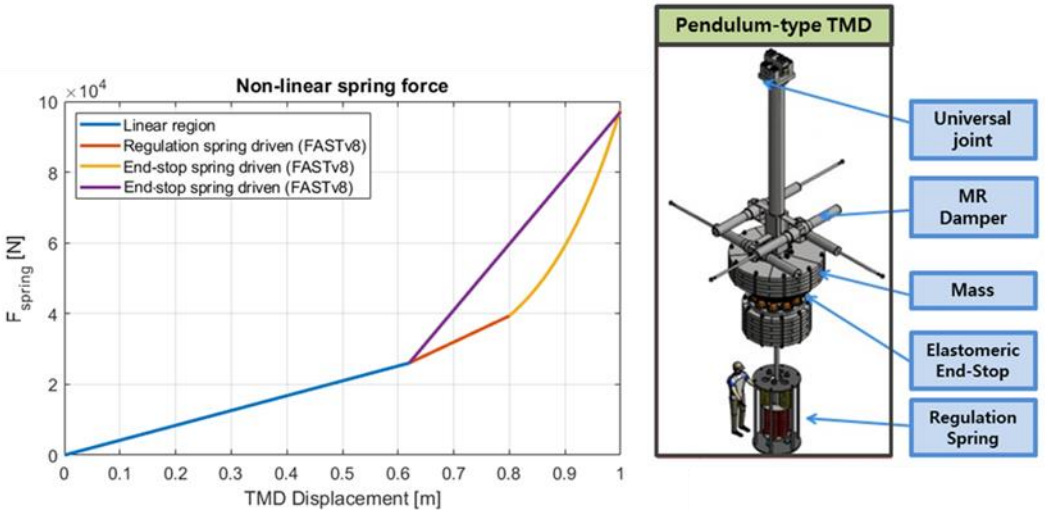

Figure 3.1: Schematic of the pendulum-type omni-directional TMD [66]

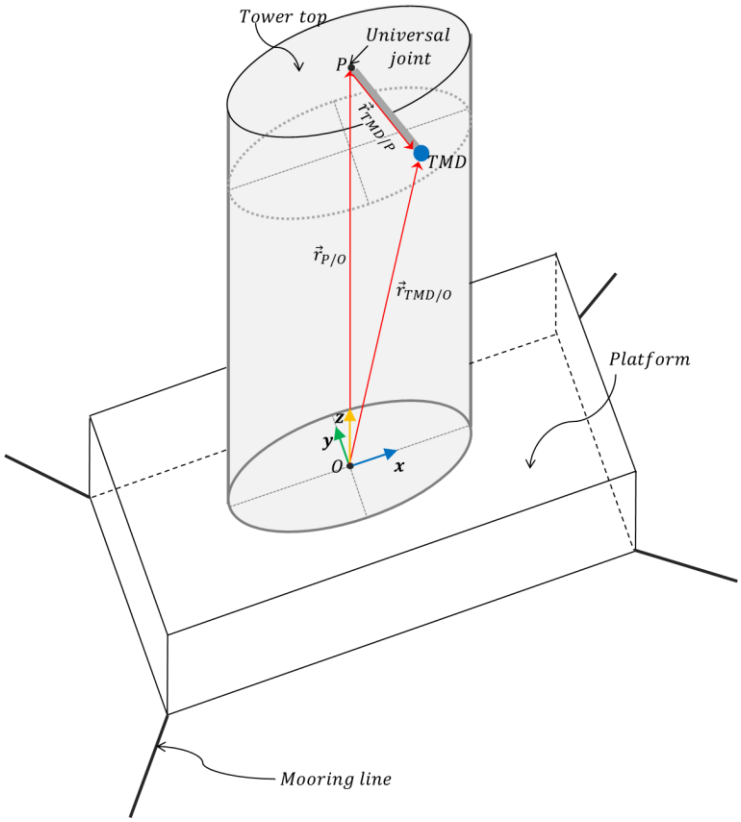

Figure 3.2: Schematic of the pendulum-type TMD located on top of the tower

The analytical formulas of a tower-TMD designed by ESM GmBH are established in this section [66]. The tower-TMD is mounted inside a turbine tower (usually on top of a tower) and a single pendulum-type TMD that can oscillate omni-directionally, i.e. in two dimensions (fore-aft and side-to-side). The ability to oscillate omni-directionally allows the TMDs to absorb the energy of the tower fore-aft and side-to-side motion simultaneously with a single mass. It consists of a universal joint, magnetorheological dampers, a mass, an elastomeric end-stop spring, and a regulation spring system as shown in Figure 3.1. Figure 3.2 shows a schematic of a turbine tower with the pendulum-type tower-TMD at the tower top.

The position of the moving mass "TMD" from the global fixed point "*O*" (at the tower base) in the orientation *G* can be expressed in the form of the position vector as follows:

$$\vec{r}_{TMD/O_G} = \vec{r}_{P/O_G} + \vec{r}_{TMD/P_G} = {}^{TMD}_{O_G}[x\ y\ z]^T \tag{3.1}$$

where point *O* represents the origin point of the global inertial reference frame and point *P* is the origin point of the non-inertial reference frame fixed to the tower top where the TMD is at rest. *G* is the axis orientation of the global reference frame. The point TMD is the origin point of the moving mass of the TMD. The velocity and acceleration vector of the moving mass in the orientation of the tower top reference frame *T* can be derived by differentiating Eq. (3.1):

$$\dot{\vec{r}}_{TMD/P_T} = \dot{\vec{r}}_{TMD/O_T} - \dot{\vec{r}}_{P/O_T} - \vec{\omega}_{T/O_T} \times \vec{r}_{TMD/P_T} \tag{3.2}$$

$$\ddot{\vec{r}}_{TMD/P_T} = \ddot{\vec{r}}_{TMD/O_T} - \ddot{\vec{r}}_{P/O_T} - \vec{\omega}_{T/O_T} \times (\vec{\omega}_{T/O_T} \times \vec{r}_{TMD/P_T}) - \vec{\alpha}_{T/O_T} \times \vec{r}_{TMD/P_T} - 2\vec{\omega}_{T/O_T} \times \dot{\vec{r}}_{TMD/P_T} \tag{3.3}$$

where $\vec{\alpha}_{T/O_T} \times \vec{r}_{TMD/P_T}$, $2\vec{\omega}_{T/O_T} \times \dot{\vec{r}}_{TMD/P_T}$, $\vec{\omega}_{T/O_T} \times (\vec{\omega}_{T/O_T} \times \vec{r}_{TMD/P_T})$ are associated with non-inertial terms such as the angular, Coriolis, and the centrifugal acceleration. The acceleration in the inertial frame $\ddot{\vec{r}}_{TMD/O_T}$ can be replaced with a force balance, per Newton's second law:

$$\ddot{\vec{r}}_{TMD/O_T} = \frac{1}{m}{}^{TMD}_{O_T}\left[\Sigma F_x \; \Sigma F_y \; \Sigma F_z\right]^T = \frac{1}{m}\vec{F}_{TMD/O_T} \tag{3.4}$$

$$\frac{1}{m}\vec{F}_{TMD/O_T} = \begin{bmatrix} -c_x\dot{x}_{TMD/P_T} - k_x x_{TMD/P_T} + m\alpha_{Gx/O_T} + F_{x,stop-spring} \\ -c_y\dot{y}_{TMD/P_T} - k_y y_{TMD/P_T} + m\alpha_{Gy/O_T} + F_{y,stop-spring} \\ F_{z,TMD/O_T} + m\alpha_{Gz/O_T} \end{bmatrix} \tag{3.5}$$

where $F_{x,stop-spring}$ and $F_{y,stop-spring}$ are non-linear stop-spring forces for restricting the TMD motion. In general, the larger the stroke of the TMD, the more vibrational energy of the main structure can be absorbed. However, the trade-off between the load reduction and the acceptable TMD stroke must be considered, since the space where the TMD operates is limited for real applications. This TMD design has a feature that causes nonlinear position constraints, which are achieved by applying a nonlinear spring force curve defined in the TMD input file, restricting the TMD motion at certain positions. For small displacements (within the stroke limits), the TMD oscillates at the tuning frequency in a linear stiffness region (blue line in Figure 3.1), and then the nonlinear force curve (red and orange lines in Figure 3.1) is applied when the TMD excursion exceeds some defined limit. This can be realized by a trilinear stiffness representation, composed of the regulation spring and the elastomeric stop springs as shown in Figure 3.1.

The TMD is only fixed to the frame *T* in the z direction because the TMD is free to move in the x and y directions (omni-directional). So, the vector $\vec{r}_{TMD/P_T}$ can be decomposed as follows:

$$\vec{r}_{TMD/P_T} = \begin{bmatrix} x_{TMD/P_T} & y_{TMD/P_T} & 0 \end{bmatrix}^T \tag{3.6}$$

The other components, such as the angular, centrifugal and Coriolis accelerations are:

$$\vec{\omega}_{T/O_T} \times \left(\vec{\omega}_{T/O_T} \times \vec{r}_{TMD/P_T}\right) = \begin{bmatrix} -x_{TMD/P_T}\left(\dot{\phi}_{P_T}^2 + \dot{\psi}_{P_T}^2\right) + y_{TMD/P_T}\left(\dot{\theta}_{P_T}\dot{\phi}_{P_T}\right) \\ -y_{TMD/P_T}\left(\dot{\theta}_{P_T}^2 + \dot{\psi}_{P_T}^2\right) + x_{TMD/P_T}\left(\dot{\theta}_{P_T}\dot{\phi}_{P_T}\right) \\ x_{TMD/P_T}\left(\dot{\theta}_{P_T}\dot{\psi}_{P_T}\right) + y_{TMD/P_T}\left(\dot{\phi}_{P_T}\dot{\psi}_{P_T}\right) \end{bmatrix} \tag{3.7}$$

$$2\vec{\omega}_{T/O_T} \times \dot{\vec{r}}_{TMD/P_T} = \begin{bmatrix} -2\dot{\psi}_{P_T}\dot{y}_{TMD/P_T} \\ 2\dot{\psi}_{P_T}\dot{x}_{TMD/P_T} \\ -2\dot{\phi}_{P_T}\dot{x}_{TMD/P_T} - 2\dot{\theta}_{P_T}\dot{y}_{TMD/P_T} \end{bmatrix} \tag{3.8}$$

$$\vec{\alpha}_{T/O_T} \times \vec{r}_{TMD/P_T} = \begin{bmatrix} -\ddot{\psi}_{P_T} y_{TMD/P_T} \\ \ddot{\psi}_{P_T} x_{TMD/P_T} \\ -\ddot{\phi}_{P_T} x_{TMD/P_T} + \ddot{\theta}_{P_T} y_{TMD/P_T} \end{bmatrix} \tag{3.9}$$

Combining and simplifying Eqs. (3.3) – (3.9) yields the governing equations, describing the movement of the TMD in the *x* and *y* directions:

$$\ddot{x}_{TMD/P_T} = \left(\dot{\phi}_{P_T}^2 + \dot{\psi}_{P_T}^2 - \frac{k_x}{m}\right) x_{TMD/P_T} - \left(\frac{c_x}{m}\right)\dot{x}_{TMD/P_T} - \ddot{x}_{P/O_T} + \alpha_{Gx/O_T} - \left(\dot{\theta}_{P_T}\dot{\phi}_{P_T} - \ddot{\psi}_{P_T}\right) y_{TMD/P_T} + 2\dot{\psi}_{P_T}\dot{y}_{TMD/P_T} \tag{3.10}$$

$$\ddot{y}_{TMD/P_T} = \left(\dot{\theta}_{P_T}^2 + \dot{\psi}_{P_T}^2 - \frac{k_y}{m}\right) y_{TMD/P_T} - \left(\frac{c_y}{m}\right)\dot{y}_{TMD/P_T} - \ddot{y}_{P/O_T} + \alpha_{Gy/O_T} - \left(\dot{\theta}_{P_T}\dot{\phi}_{P_T} + \ddot{\psi}_{P_T}\right) x_{TMD/P_T} - 2\dot{\psi}_{P_T}\dot{x}_{TMD/P_T} \tag{3.11}$$

The reaction forces in the *z* direction by the TMD can be solved by noting $\ddot{z}_{TMD/P_T} = 0$:

$$F_{Z_{TMD/O_T}} = -m\left(\alpha_{Gz/O_T} - \ddot{z}_{P/O_T} + \left(\ddot{\phi}_{P_T} - \dot{\theta}_{P_T}\dot{\psi}_{P_T}\right) x_{TMD/P_T} - \left(\ddot{\theta}_{P_T} - \dot{\phi}_{P_T}\dot{\psi}_{P_T}\right) y_{TMD/P_T} + 2\dot{\phi}_{P_T}\dot{x}_{TMD/P_T} - 2\dot{\theta}_{P_T}\dot{y}_{TMD/P_T}\right) \tag{3.12}$$

The first-order state space form for the relationship between the TMD motions and the tower top motions can be expressed by modifying Eqs. (3.10) to (3.12):

$$\dot{\vec{R}}_{TMD/P_T} = \mathrm{A}(\vec{U})\vec{R}_{TMD/P_T} + B(\vec{U}) \tag{3.13}$$

$$\vec{R}_{TMD/P_T} = \begin{bmatrix} x_{TMD/P_T} \\ \dot{x}_{TMD/P_T} \\ y_{TMD/P_T} \\ \dot{y}_{TMD/P_T} \end{bmatrix} \tag{3.14}$$

$$\mathrm{A}(\vec{U}) = \begin{bmatrix} 0 & 1 & 0 & 0 \\ \dot{\phi}_{P_T}^2 + \dot{\psi}_{P_T}^2 - \frac{k_x}{m} & -\left(\frac{c_x}{m}\right) & -\left(\dot{\theta}_{P_T}\dot{\phi}_{P_T} - \ddot{\psi}_{P_T}\right) & 2\dot{\psi}_{P_T} \\ 0 & 0 & 0 & 1 \\ -\left(\dot{\theta}_{P_T}\dot{\phi}_{P_T} + \ddot{\psi}_{P_T}\right) & -2\dot{\psi}_{P_T} & \dot{\phi}_{P_T}^2 + \dot{\psi}_{P_T}^2 - \frac{k_y}{m} & -\left(\frac{c_y}{m}\right) \end{bmatrix} \tag{3.15}$$

$$\mathrm{B}(\vec{U}) = \begin{bmatrix} 0 \\ -\ddot{x}_{P/O_T} + \alpha_{Gx/O_T} + \frac{1}{m}\left(F_{x,stop-spring}\right) \\ 0 \\ -\ddot{y}_{P/O_T} + \alpha_{Gy/O_T} + \frac{1}{m}\left(F_{y,stop-spring}\right) \end{bmatrix} \tag{3.16}$$

where $\vec{R}_{TMD/P_T}$ is a vector for the TMD position and velocity in the *x* and *y* directions. $A(\vec{U})$ is a 4 by 4 state matrix as a function of input $\vec{U}$. $B(\vec{U})$ is an input vector in the state space representation. The tower top translational acceleration ($\ddot{\vec{r}}_{P/O_T}$) and angular velocity ($\vec{\omega}_{T/O_T}$) and acceleration ($\vec{\alpha}_{T/O_T}$) are inputs ($\vec{U}$) for Eq. (3.13), and they are calculated in ElastoDyn in FASTv8. As the control module is coupled with FASTv8, the tower top motions can be inputted to Eq. (3.13).

The output vectors $\vec{F}_{P_G}$and $\vec{M}_{P_G}$ which are reaction forces and moments by the TMD acting on the tower local node where the TMD is attached (usually tower top) can be expressed as:

$$\vec{F}_{P_G} = R_{T/G}^{T}\begin{bmatrix} k_x x_{TMD/P_T} + c_x \dot{x}_{TMD/P_T} - F_{x,stop-spring} \\ k_y y_{TMD/P_T} + c_y \dot{y}_{TMD/P_T} - F_{y,stop-spring} \\ -F_{z_{TMD/O_T}} \end{bmatrix} \tag{3.17}$$

$$\vec{M}_{P_G} = R_{T/G}^{T}\begin{bmatrix} -F_{z_{TMD/O_T}} y_{TMD/P_T} \\ F_{z_{TMD/O_T}} x_{TMD/P_T} \\ 0 \end{bmatrix} \tag{3.18}$$

Eqs. (3.13), (3.17) and (3.18) are incorporated into the control module in FASTv8, and a fourth order Runge-Kutta numerical method is utilized to solve them within the module. As the dynamics of the structural control devices are fully coupled to the wind turbine dynamics, the turbine motions (at the tower top) are inputted to drive the control devices, and the reaction forces and moments from the control devices affect the turbine responses. The motions between the turbine tower and the TMD interact with each other every time step during a fully-coupled time domain simulation. The TMD module is publicly released and can be downloaded on the NWTC site [68].

3.2 Modeling of a Blade-TMD

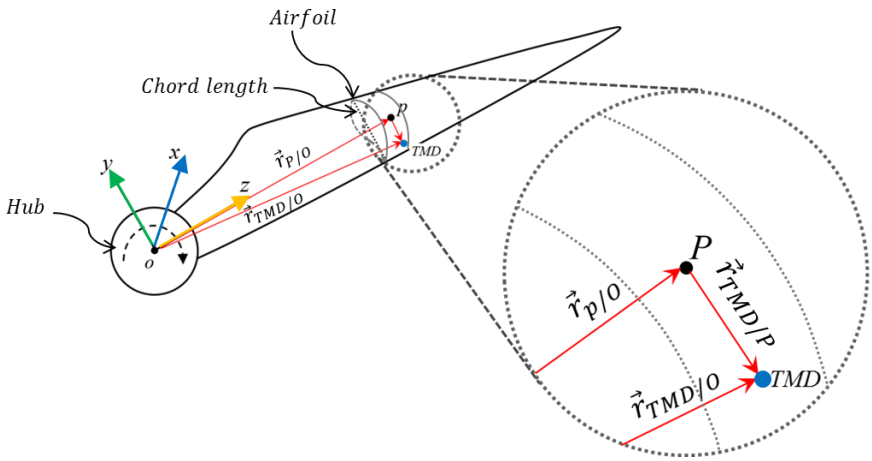

Figure 3.3: Schematic of the pendulum-type TMD located inside the blade

The analytical formulation of a blade-TMD is established in this section. Unlike the tower-TMD, the blade-TMD oscillates only in the edgewise direction. The main objective of the blade-TMD is to mitigate the edgewise vibration, as the vibration in this direction is lightly damped due to the lack of the aerodynamic damping from the rotor. Moreover, due to the intrinsic shape of the blades, the application of the TMD to reduce the flap-wise vibration is still questionable, as there is insufficient room for the TMD to vibrate in the flap-wise direction. On the other hand, the space in the edgewise direction inside the hollow blade is on the scale of the chord length as seen in Figure 3.3. The configuration of the blade-TMD is the same as the tower-TMD. The analytical formulation for the blade-TMD is similar to that for the tower-TMD except for a few differences, in that the motion of the blade-TMD in the flap-wise direction (x-direction as seen in Figure 3.3) is limited and the global fixed point is on the center of the hub. As the blade-TMD is fixed to frame *B* (orientation of blade reference frame) in the *x* (flap-wise) and *z* direction, the position vector for the blade-TMD in the non-inertial reference frame is modified as:

$$\vec{r}_{TMD/P_B} = \begin{bmatrix} 0 & y_{TMD/P_B} & 0 \end{bmatrix}^T \tag{3.19}$$

The change of the position vector affects the angular, centrifugal and Coriolis acceleration so that:

$$\vec{\omega}_{B/O_B} \times \left(\vec{\omega}_{B/O_B} \times \vec{r}_{TMD/P_B}\right) = \begin{bmatrix} y_{TMD/P_B}\left(\dot{\theta}_{P_B}\dot{\phi}_{P_B}\right) \\ -y_{TMD/P_B}\left(\dot{\theta}_{P_B}^2 + \dot{\psi}_{P_B}^2\right) \\ y_{TMD/P_B}\left(\dot{\phi}_{P_B}\dot{\psi}_{P_B}\right) \end{bmatrix} \tag{3.20}$$

$$2\vec{\omega}_{B/O_B} \times \dot{\vec{r}}_{TMD/P_B} = \begin{bmatrix} -2\dot{\psi}_{P_B}\dot{y}_{TMD/P_B} \\ 0 \\ 2\dot{\theta}_{P_B}\dot{y}_{TMD/P_B} \end{bmatrix} \tag{3.21}$$

$$\vec{\alpha}_{B/O_B} \times \vec{r}_{TMD/P_B} = \begin{bmatrix} -\ddot{\psi}_{P_B} y_{TMD/P_B} \\ 0 \\ \ddot{\theta}_{P_B} y_{TMD/P_B} \end{bmatrix} \tag{3.22}$$

The reaction forces in the *x* and *z* direction by the TMD can be solved by noting $\ddot{x}_{TMD/P_B} = \ddot{z}_{TMD/P_B} = 0$:

$$F_{x_{TMD/O_B}} = -m\left(\alpha_{Gx/O_B} - \ddot{x}_{P/O_B} + \left(\ddot{\psi}_{P_B} - \dot{\theta}_{P_B}\dot{\phi}_{P_B}\right)y_{TMD/P_B} - 2\dot{\psi}_{P_B}\dot{y}_{TMD/P_B}\right) \tag{3.23}$$

$$F_{Z_{TMD/O_B}} = -m\left(\alpha_{Gz/O_B} - \ddot{z}_{P/O_B} + \left(\ddot{\theta}_{P_B} + \dot{\phi}_{P_B}\dot{\psi}_{P_B}\right)y_{TMD/P_B} + 2\dot{\theta}_{P_B}\dot{y}_{TMD/P_B}\right) \tag{3.24}$$

The state matrix $A(\vec{U})$ for the blade-TMD is a 2 by 2 matrix and the input vector $B(\vec{U})$ is a 2-dimensional vector (y_{TMD/P_B} and $\dot{y}_{TMD/P_B}$). The state matrix $A(\vec{U})$ and the input vector $B(\vec{U})$ can be expressed as:

$$\mathrm{A}(\vec{U}) = \begin{bmatrix} 1 & 0 \\ \left(\dot{\theta}_{P_B}^2 + \dot{\psi}_{P_B}^2 - \frac{k_y}{m}\right) & -\frac{c_y}{m} \end{bmatrix} \tag{3.25}$$

$$\mathrm{B}(\vec{U}) = \begin{bmatrix} 0 \\ -\ddot{y}_{P/O_B} + \alpha_{Gy/O_B} + \frac{1}{m}\left(F_{y,stop-spring}\right) \end{bmatrix} \tag{3.26}$$

The output vectors $\vec{F}_{P_G}$and $\vec{M}_{P_G}$, which are reaction forces and moments by the blade-TMD acting on the tower top, can be expressed as:

$$\vec{F}_{P_G} = R_{B/G}^{T} \begin{bmatrix} -F_{x_{TMD/O_B}} \\ k_y y_{TMD/P_B} + c_y \dot{y}_{TMD/P_B} - F_{y,stop-spring} \\ -F_{z_{TMD/O_B}} \end{bmatrix} \tag{3.27}$$

$$\vec{M}_{P_G} = R_{B/G}^{T} \begin{bmatrix} -F_{z_{TMD/O_B}} y_{TMD/P_B} \\ 0 \\ F_{x_{TMD/O_B}} y_{TMD/P_B} \end{bmatrix} \tag{3.28}$$

Similar to the tower-TMD, Eqs. (3.25) – (3.28) are incorporated into the control module in FASTv8 and are solved by a Runge Kutta numerical method. The blade motions are inputted to drive the blade-TMD, and the reaction forces and moments from the blade-TMD affect the blade responses. The motions between the turbine blade and the TMD interact with each other every time step during a fully-coupled time domain simulation. Various mechanical parameters specifying the blade-TMD such as the position, mass, stiffness, and damping coefficient, etc. can be defined in the input file, as shown in Appendix D: Example TMD module Input File. The equations of motion for the blade-TMD has similarities with that for the tower-TMD except for a few differences: the motion of the blade-TMD in the flapwise direction is limited; the global fixed point is on the center of the hub; and the centrifugal acceleration of the rotating blade is a main driver to operate the blade-TMD while the translational acceleration of the tower governs the motion of the tower-TMD. The code for the blade-TMD is the same as the tower-TMD except that the reference point changes from the tower base to the center of the hub. The mesh-mapping utility to couple the blade motions with the TMD motions will be updated and released publicly in the future.

3.3 Modeling of Nacelle-TLCDs

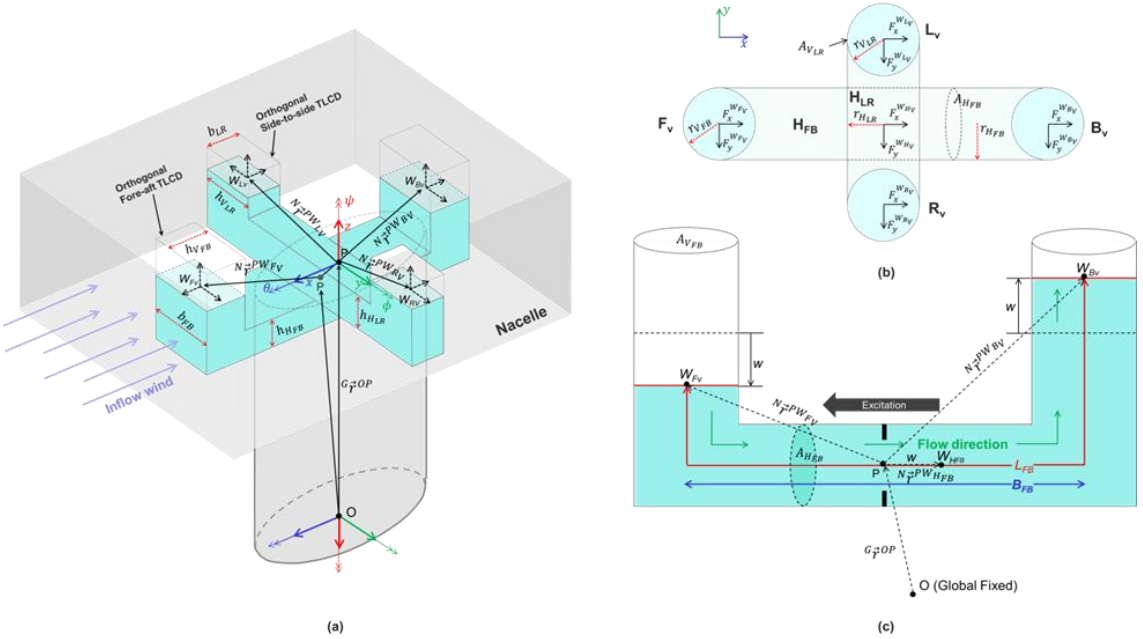

Figure 3.4: Schematic of the orthogonal TLCDs, (a): Orthogonal TLCDs inside a nacelle, (b): Top-view, (c): Side-view

Another structural control module has been developed that employs orthogonal TLCDs to improve the fore-aft and side-to-side dynamic response of the turbine tower. A TLCD used in this dissertation is a "U-shaped" tank of water, composed of two vertical sections connected by a horizontal section, and an orifice through which the flow may pass. The liquid inside the TLCDs sloshes under excitation by the main structure, and produces a resultant force on the main structure in order to suppress tower vibrations. Figure 3.4 (a) shows the schematic of a nacelle equipped with orthogonal TLCDs. The individual TLCDs are placed orthogonally to each other in order to dampen both the fore-aft and side-to-side directions. One is aligned in the fore-aft direction of the turbine, and is referred to as FA-TLCD (FA meaning Fore-aft); and the other one is aligned

orthogonally to FA-TLCD and controls side-to-side vibration, referred to as SS-TLCD (SS standing for Site-to-side). There are two vertical columns and one horizontal column in each TLCD configuration. For convenience, the front vertical column is noted as "F_V ", the back vertical column as "B_V", and the horizontal column as "$\mathrm{H_{FA}}$". Likewise, the left vertical column is noted as "L_V", the right vertical column as "R_V", and the horizontal column as "H_{SS}" as seen in Figure 3.4 (b). The cross-sectional area for each column can be modeled as either a rectangle or a circle, as seen in Figure 3.4 (a) and (b). The two vertical columns and a horizontal column are filled with a volume of liquid, i.e. water or a water/glycol mixture, where the fluid is assumed to be incompressible. In the FA-TLCD, the two vertical columns with cross-sectional area $A_{V,FA}$ are connected by the horizontal column with cross-sectional area $A_{H,FA}$. The term "non-uniform area" means that a different cross-sectional area may be chosen for both $A_{V,FA}$ and $A_{H,FA}$. The geometric shape of the TLCD is thus defined by four parameters; L_{FA}, B_{FA}, $A_{V,FA}$, $A_{H,FA,}$ as seen in Figure 1 (c). These not only represent the geometric shape, but also influence important dynamic characteristics of the TLCD, i.e. the tuning frequency and total mass of the system. The rationale behind these four parameters applies in the same way to the SS-TLCD by introducing different subscripts, i.e. L_{SS}, B_{SS}, $A_{V,SS}$, $A_{H,SS}$. In Figure 3.4 (a) and (c), the position of the moving center of mass in the vertical columns, as well as the stationary center of mass of the horizontal column from the global fixed point "*O*" to point W_i ($i = F_V, B_V, H_{FA}$) for the FA-TLCD, can be expressed in the form of the position vector as follows:

$$ {}^{G}\vec{r}^{OW_i} = {}^{G}\vec{r}^{OP} + {}^{N}\vec{r}^{PW_i} = {}^{OW_i}_{G}[x\ y\ z]^T \tag{3.29} $$

where W_i represent the points of the center of mass of each of the columns. The subscript G on the left side of the bracket indicates the axis orientation of the global reference frame, and the superscript O_{W_i} indicates the position vector of the center of the liquid mass with respect to the origin point of the global reference frame O. The velocity and acceleration vector of the fluid particle in the global reference frame can be derived by differentiating Eq. (3.29):

$$ {}^{G}\dot{\vec{r}}^{OW_i} = {}^{G}\dot{\vec{r}}^{OP} + {}^{N}\dot{\vec{r}}^{PW_i} + {}^{G}\vec{\omega}^{N} \times {}^{N}\vec{r}^{PW_i} \tag{3.30} $$

$$ {}^{G}\ddot{\vec{r}}^{OW_i} = {}^{G}\ddot{\vec{r}}^{OP} + {}^{N}\ddot{\vec{r}}^{PW_i} + 2\,{}^{G}\vec{\omega}^{N} \times {}^{N}\dot{\vec{r}}^{PW_i} + {}^{G}\vec{\alpha}^{N} \times {}^{N}\vec{r}^{PW_i} + {}^{G}\vec{\omega}^{N} \times \left({}^{G}\vec{\omega}^{N} \times {}^{N}\vec{r}^{PW_i}\right) \tag{3.31} $$

where ${}^{G}\vec{\alpha}^{N} \times {}^{N}\vec{r}^{PW_i}$, ${}^{G}\vec{\alpha}^{N} \times {}^{N}\vec{r}^{PW_i}$ and ${}^{G}\vec{\omega}^{N} \times \left({}^{G}\vec{\omega}^{N} \times {}^{N}\vec{r}^{PW_i}\right)$ are associated with non-inertial terms such as the angular, Coriolis, and the centrifugal acceleration. The acceleration in the inertial reference frame ${}^{G}\vec{r}^{OW_i}$ can be replaced with a force balance, per Newton's second law. For the vertical columns (F_V and B_V), the acceleration vector in terms of force components can be expressed as follows:

$$ {}^{G}\ddot{\vec{r}}^{OW_i} = \frac{1}{m_i}\,{}^{OW_i}_{G}\left[\Sigma F_x \;\Sigma F_y \;\Sigma F_z\right]^T = \frac{1}{m_i}\,{}^{OW_i}_{G}\left[F_x{}^{W_i} + m_i\,{}^{N}g_x \quad F_y{}^{W_i} + m_i\,{}^{N}g_y \quad m_i\,{}^{N}g_z\right]^T \tag{3.32} $$

The position vectors in the vertical columns (F_V and B_V) can be expressed as:

$$ {}^{N}\vec{r}^{PW_{F_V}} = {}^{PW_{F_V}}_{N}[x \;\; y \;\; z]^T = {}^{PW_{F_V}}_{N}[B_{FA}/2 \quad 0 \quad (L_{FA} - B_{FA})/2 + w]^T \tag{3.33} $$

$$ {}^{N}\vec{r}^{PW_{B_V}} = {}^{PW_{B_V}}_{N}[x \;\; y \;\; z]^T = {}^{PW_{B_V}}_{N}[-B_{FA}/2 \quad 0 \quad (L_{FA} - B_{FA})/2 - w]^T \tag{3.34} $$

To derive the acceleration vector in the horizontal column (H_{FA}), the continuity equation (Eq. (3.35)) with incompressible fluid is applied, and the acceleration vector in terms of force components is as follows:

$$ {}^{N}\dot{w}^{W_{H_{FA}}} = \frac{A_{v_{FA}}}{A_{H_{FA}}} {}^{N}\dot{w}^{W_{F_v}} = \alpha_{FA} {}^{N}\dot{w}^{W_{F_v}} \tag{3.35} $$

$$ {}^{G}\ddot{\vec{r}}^{OW_i} = {}^{1}/_{m_{H_{FA}}} {}^{OW_{H_{FA}}}_{G}\left[m_{H_{FA}} {}^{N}g_x - {}^{1}/_{2}\,\rho A_{H_{FA}}\xi\alpha_{FA}^2|\dot{w}|\dot{w} \quad F_y^{W_{H_{FA}}} + m_{H_{FA}} {}^{N}g_y \quad F_z^{W_{H_{FA}}} + m_{H_{FA}} {}^{N}g_z\right]^T \tag{3.36} $$

The position vector for fluid particle in the horizontal column in the nacelle reference frame N can be expressed as:

$$ {}^{N}\vec{r}^{PW_{H_{FA}}} = {}^{PW_{H_{FA}}}_{N}[x \;\; y \;\; z]^T = {}^{PW_{H_{FA}}}_{N}[\alpha_{FA}w \quad 0 \quad 0]^T \tag{3.37} $$

Substituting Eqs. (3.34) - (3.37) into Eq. (3.31) and computing all cross-products yields three distinct expressions regarding the acceleration of the fluid particle (w) for the two vertical columns and one horizontal column of the FA-TLCD:

$$ Front\ column\ (F_v): \ddot{w}_{F_V} = -\,{}^{G}\ddot{z}^{P} + \ddot{\phi}\frac{B_{FA}}{2} - \dot{\theta}^2\dot{\psi}\frac{B_{FA}}{2} + \dot{\theta}^2\left(\frac{L_{FA}-B_{FA}}{2}+w\right) + \dot{\phi}^2\left(\frac{L_{FA}-B_{FA}}{2}+w\right) + {}^{N}g_z \tag{3.38} $$

$$ Back\ column\ (B_v): \ddot{w}_{B_V} = {}^{G}\ddot{z}^{P} + \ddot{\phi}\frac{B_{FA}}{2} - \dot{\theta}^2\dot{\psi}\frac{B_{FA}}{2} - \dot{\theta}^2\left(\frac{L_{FA}-B_{FA}}{2}-w\right) - \dot{\phi}^2\left(\frac{L_{FA}-B_{FA}}{2}-w\right) - {}^{N}g_z \tag{3.39} $$

$$ Horizontal\ column\ (H_{FB}): \ddot{w}_{H_{FB}} = -\,{}^{G}\ddot{x}^{P} + {}^{N}g_x - \frac{1}{m_{H_{FA}}}\left(\frac{1}{2}\rho A_{H_{FA}}\xi\alpha_{FA}^2|\dot{w}_{F_V}|\dot{w}_{F_V}\right) \tag{3.40} $$

The acceleration of the total liquid mass (m_{tot}) can be described accordingly:

$$ m_{tot}\ddot{w} = m_{F_V}\ddot{w}_{F_V} + m_{B_V}\ddot{w}_{B_V} + m_{H_{FA}}\ddot{w}_{H_{FA}} \tag{3.41} $$

Combining and simplifying Eqs. (3.38) - (3.41) yields the governing equation, describing the movement of the liquid through the FA-TLCD:

$$ \ddot{w} = \frac{\rho A_{V_{FA}} B_{FA}\left(\frac{L_{FA}-B_{FA}}{2}\right)\left(\ddot{\phi} - \dot{\theta}\dot{\psi} - \frac{2}{L_{FA}-B_{FA}}\left({}^{G}\ddot{x}^{P} + g_x\right)\right) + 2\rho A_{V_{FA}}(L_{FA}-B_{FA})\left(\dot{\theta}^2 + \dot{\phi}^2 + \frac{g_z + {}^{G}\ddot{z}^{P}}{L_{FA}-B_{FA}}\right)w - \frac{1}{2}\rho A_{V_{FA}}\xi\alpha_{FA}^2|\dot{w}|\dot{w}}{\rho A_{V_{FA}}(L_{FA}-B_{FA}+\alpha_{FA}B_{FA})} \tag{3.42} $$

The equation for the SS-TLCD can be derived by applying the same process from Eqs. (3.32) to (3.41):

$$\ddot{w} = \frac{\rho A_{V_{SS}} B_{SS} \left(\frac{L_{SS} - B_{SS}}{2}\right)\left(\ddot{\theta} - \dot{\phi}\dot{\psi} - \frac{2}{L_{SS} - B_{SS}}\left({}^{G}\ddot{x}^{P} + g_y\right)\right) + 2\rho A_{V_{SS}}(L_{SS} - B_{SS})\left(\dot{\theta}^2 + \dot{\phi}^2 + \frac{g_z + {}^{G}\ddot{z}^{P}}{L_{SS} - B_{SS}}\right)w - \frac{1}{2}\rho A_{V_{SS}}\xi\alpha_{SS}^2|\dot{w}|\dot{w}}{\rho A_{V_{SS}}(L_{SS} - B_{SS} + \alpha_{SS}B_{SS})} \tag{3.43}$$

The output force vector ($\vec{F}$) and moment vector ($\vec{M}$) produced by the TLCDs acting on the nacelle is:

$$\vec{F} = \begin{bmatrix} -F_x^{W_{F_V}} - F_x^{W_{B_V}} - \rho A_{V_{FA}} B_{FA}\ddot{w}_{FA} - F_x^{W_{L_V}} - F_x^{W_{R_V}} - F_x^{W_{H_{SS}}} \\ -F_y^{W_{F_V}} - F_y^{W_{B_V}} - \rho A_{V_{SS}} B_{FA}\ddot{w}_{SS} - F_y^{W_{H_{FA}}} - F_y^{W_{L_V}} - F_y^{W_{R_V}} \\ -F_z^{W_{H_{FA}}} - F_z^{W_{H_{SS}}} \end{bmatrix} \tag{3.44}$$

$$\vec{M} = \begin{bmatrix} F_y^{W_{F_V}}\left(\frac{L_{FA} - B_{FA}}{2} + w_{FA}\right) + F_y^{W_{B_V}}\left(\frac{L_{FA} - B_{FA}}{2} - w\right) - F_y^{W_{L_V}}\left(\frac{L_{SS} - B_{SS}}{2} + w_{SS}\right) - F_y^{W_{R_V}}\left(\frac{L_{SS} - B_{SS}}{2} - w_{SS}\right) \\ F_x^{W_{F_V}}\left(\frac{L_{FA} - B_{FA}}{2} + w_{FA}\right) + F_x^{W_{B_V}}\left(\frac{L_{FA} - B_{FA}}{2} - w\right) - F_x^{W_{L_V}}\left(\frac{L_{SS} - B_{SS}}{2} + w_{SS}\right) - F_x^{W_{R_V}}\left(\frac{L_{SS} - B_{SS}}{2} - w_{SS}\right) \\ F_y^{W_{F_V}}\left(\frac{B_{FA}}{2}\right) - F_y^{W_{B_V}}\left(\frac{B_{FA}}{2}\right) F_x^{W_{L_V}}\left(\frac{B_{FA}}{2}\right) - F_x^{W_{R_V}}\left(\frac{B_{FA}}{2}\right) \end{bmatrix} \tag{3.45}$$

Eqs. (3.42) to (3.45) are incorporated into the control module in FASTv8, and a fourth order Runge-Kutta numerical method is utilized to solve them within the module. The motions between the nacelle and the TLCD interact with each other every time step. Important assumptions and an overview of the TLCD code implementation are as follows:

- The two TLCDs (FA-TLCD and SS-TLCD) are assumed to be mounted inside the nacelle, and they are orthogonal to each other.
- Non-inertial terms and rotational effects are considered.
- The FA-TLCD and SS-TLCDs are independent, so they can be implemented separately or simultaneously by turning the mode on or off in the input file.
- The geometric parameters (L, B, A, and α) and the head-loss coefficient (ξ) can be defined by the user in the input file of the module.

The code for the nacelle TLCDs will be publicly released in the future [68].

3.4 Structural Control Module TMD in FASTv8

As mentioned earlier, we have updated a structural control module, TMD in FASTv8, in order to include more functions to implement various control devices and control techniques. Once the theoretical equations of motion of the tower-TMD, blade-TMD, and nacelle-TLCDs are developed, they are incorporated into the TMD module and implemented in the FASTv8. A brief overview of the features and implementation details of the module is as follows:

- The module TMD has been updated with the ability to model an omni-directional TMD as an alternative to the two independent TMDs previously available. In addition, it has been updated to include an option to model orthogonal TLCDs.
- The control device such as the tower-TMD, blade-TMD and nacelle-TLCDs can be used to achieve a certain control objective. For example, the tower-TMD can be mounted anywhere inside a tower by defining the reference position of the TMD in the direction of *x*, *y* and *z*. For the tower-TMD, the motion of the tower at the local node of the tower where the TMD is mounted drive the TMD, and the output vectors of forces and moments from the TMD are applied to the local node of the tower. Such input-output coupling relationships between the tower motion (input) and the TMD motion (output) can be realized by a mesh-mapping utility of FASTv8 [29].
- The user can define the physical and geometric parameters for each structural control device and control approaches in the input file. It also contains a new option to use several semi-active damping control algorithms and has a magnetorheological

damper model to realize semi-active damping control algorithms.

- The module contains a new option to use spring forces from a user-defined table in the input file (Use_F_TBL on line 48). An example input file is provided at the end of the document, in Appendix D: Example TMD module Input File. The nonlinear stop-spring forces ($F_{x,stop-spring}$ and $F_{y,stop-spring}$) can be applied by a user-defined spring force table. The previous version (FAST-SC) has also an option to restrict the TMD stroke by modeling a much stiffer spring that comes into contact with the TMD mass near a defined position. This can be regarded as a combination of only two linear spring forces (blue line and purple line in Figure 3.1), which makes the system highly nonlinear and discontinuous due to the lack of the regulation spring.

CHAPTER 4

METOCEAN DATA PROCESSING AND DESIGN LOAD CASES

As the interest in offshore wind technology increases, the demand to characterize site-specific environmental conditions also increases. Offshore structures deployed in the ocean are subjected to a site-specific offshore environment. It is important to know the effect of the environmental conditions on the offshore structures for the successful deployment of OWTs. Also, in order to more precisely estimate the effect of structural control techniques applied to OWTs installed in a specific offshore site, a proper statistical interpretation of the site-specific environmental conditions is required.

In order to create Design Load Cases (DLCs) for predicting dynamic responses of OWTs and to evaluate the impact of structural control techniques on reducing loads of OWTs, site-specific meteorological oceanographic (metocean) data that consists of a combination of wind (speed and direction) and wave (height, period and direction) data has been processed and compiled. In this dissertation, through various techniques, the site-specific wind and wave characteristics are defined, and also estimates are made of the probabilities that particular wind and wave conditions occur and to predict extreme wind and wave conditions. Such conditions are mainly utilized to evaluate fatigue and extreme behavior of OWTs by running several key DLCs, such as DLC 1.2, 1.3, 6.1 and 6.2. Turbulent wind data files can then be created by TurbSim, and irregular waves using the JONSWAP spectrum can be generated using FASTv8's built-in wave generator. This wind and wave data, which corresponds to the specific DLCs, are created in accordance with the International Electrotechnical Commission (IEC) offshore design standards [30].

4.1 Metocean Conditions at Southeast of Nantucket

The primary source to analyze the metocean data is from buoy 44008 (Southeast of Nantucket) of the National Data Buoy Center (NDBC) [69]. Over 30 years of historical data are available on the NDBC's website, but data for wave directions are not recorded prior to 2007. Consequently, data produced after 2007 (by 2016) have been adopted for the post-processing. DLC 1.2 needs a joint probability distribution of wind speeds (U), significant wave heights (H_s), peak spectral periods (T_P) and wind/wave misalignment (β). In addition, data recorded in 2013 and 2014 are excluded due to the lack of sufficient data. The description of measurements is summarized in Table 4.1, and a more detailed description of measurements can be found on the NDBC website.

Parameter	Description	Report time	Unit
Wind speed	8-min average	Hourly	m/s
Wind direction	8-min average, clockwise	Hourly	deg
Significant wave height	20-min average of the highest one-third	Hourly	m
Peak spectral period	Dominant wave period	Hourly	sec
Wave direction	Clockwise	Hourly	deg

Table 4.1: Description of measurement of the metocean data at buoy 44008

In this dissertation, post-processing the raw data is performed in order to specify the site-specific external conditions that are applicable to key DLCs for fatigue and ultimate analysis of OWTs equipped with structural control devices. The main conditions and outputs of the post-processing are:

- A wind shear exponent of 0.14 is used for the power law in order to extrapolate the wind speed from the anemometer (5 m ASL) to the hub-height of 90 m (NREL 5-

MW turbine) and 119 m (DTU 10-MW turbine). According to IEC 61400-3, an exponent of 0.14 is normally recommended for offshore locations. The data for turbulence intensity (TI) and standard deviation of the wind speed are not available on the NDBC's website. It is assumed that the TI follows the IEC category B [30].

- For the 8 years of historical data, key statistics of variables of interest, such as U, H_S, T_P and β are calculated. These are used as external conditions to conduct a parametric study of the tower-TMD and the blade-TMD as well as a preliminary design of the nacelle-TLCDs. The overall statistics of the variables based on eight years of historical metocean data are summarized in Table 4.2.

- A conditional probability distribution near the rated wind speed is created as a function of β. To do this, the data for β are sorted for wind speeds between 11 m/s to 13 m/s in order to create a conditional probability distribution. Also, H_S and T_P corresponding to each bin of β (bin width of 45 degrees, 9 total bins from -180 to 180 degrees) are determined as seen in Figure 4.1. This conditional probability distribution is used to calculate damage equivalent loads (DELs) for a multi-objective optimization problem of the nacelle-TLCDs. Further details are discussed in Section 5.3.2.

- A joint probability distribution is created as a function of U and β, as seen in Figure 4.2 (a) and (b). The wind speed at the hub height of 90 m is binned with a width of 2 m/s from the cut-in wind speed (3 m/s) to the cut-out wind speed (25 m/s). The data for β is binned with a width of 15 degrees from -180 to 180 degrees. The expected values of H_S and T_P corresponding to each set of conditions are determined and can be seen in Figure 4.2 (c) and (d). The expected values and corresponding probabilities are listed in Appendix B: Expected Values and Corresponding Probabilities (Table B.1 and B.2). The joint probability distribution and the expected values of H_S and T_P are used to create a comprehensive DLC 1.2 for fatigue analysis in order to investigate the impact of the optimized tower-TMD and nacelle-TLCDs for the NREL/OC3 monopile OWT and NREL/MIT TLP OWT.

- Extreme value analysis [71] (EVA) is performed to estimate the extreme return period wind and wave. The extrapolated annual maxima (U, H_S and T_P) are sorted from the metocean data ranging from 1982 to 2016, and are modelled by a Gumbel distribution, which is a generalized extreme value distribution with a shape parameter of zero [71]. Figure 4.3 shows the annual maxima and the extreme values for different return periods. Table 4.3 shows extreme wind speed, significant wave height, and peak spectral period for 1, 50, 100, 200 and 500-year return periods. The outputs of the EVA are then used to create conditions for DLC 6.2 in accordance with IEC 61400-3 for extreme loading analysis in order to evaluate the control effect of the optimized tower-TMD and nacelle-TLCDs for the NREL/OC3 monopile-OWT and NREL/MIT TLP-OWT.

- For the blade-TMD, probability distributions of operational wind speeds (4 m/s to 24 m/s) at each hub-height of 90 m and 119 m are created as shown in Figure 4.4. The wave conditions are not considered in this analysis. The probability distributions are used to post-process DLC 1.2 simulation results. The lifetime damage equivalent loads (DELs) are evaluated to determine the fatigue behaviors of the blades with the TMD. The turbulence intensity in accordance with the IEC category B for DLC 1.2 and 1.3 are also included in Figure 4.4.

Table 4.4 summarizes DLCs and the types of analysis applied to each OWT and structural control device. Wind and wave models associated with each DLC are also specified. The acronyms NTM, ETM, and EWM stand for the normal turbulence model, extreme turbulence model and extreme wind model (50-year recurrence), respectively. The acronyms NSS and ESS are related to waves and they stand for the normal sea state and the extreme sea state, respectively. For the fatigue limit state (FLS) analysis, DLC 1.2 is mainly adopted, and DLC 1.3 and 6.2 are mainly utilized for the ultimate limit state (ULS) analysis.

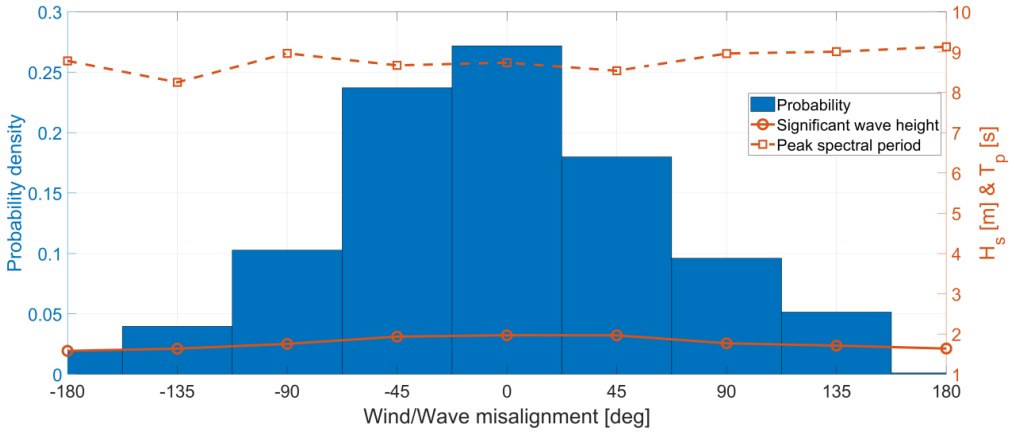

Figure 4.1: Conditional probability density and expected values of H_s and T_P

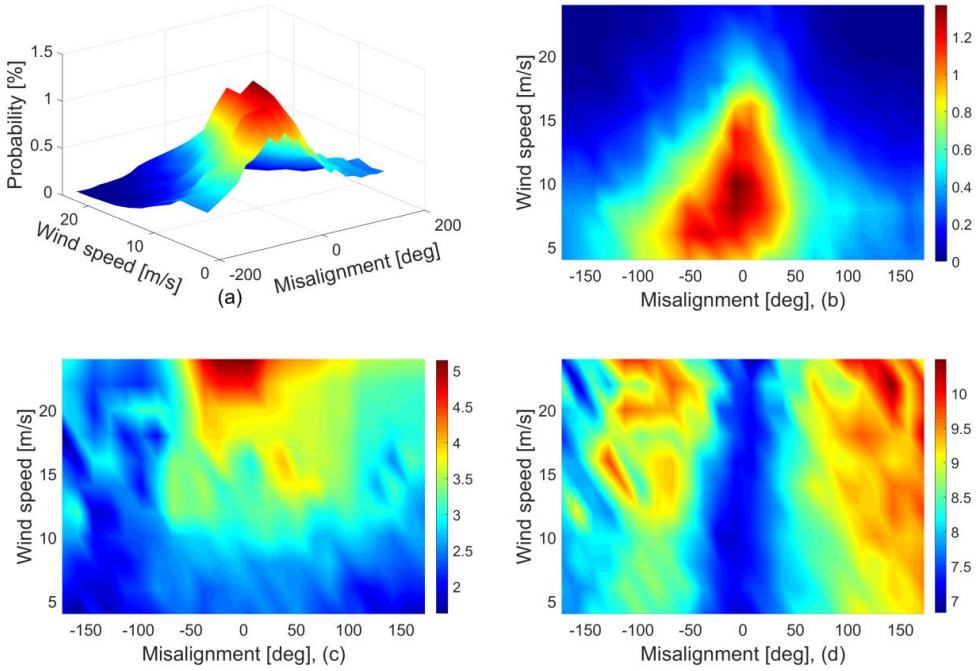

Figure 4.2: Joint probability density as functions of U and β, and expected values of H_s and T_P (a): 3-D view of distribution, (b): 2-D view of distribution, (c): expected value of H_s for each intersection, (d): expected value of T_P for each intersection

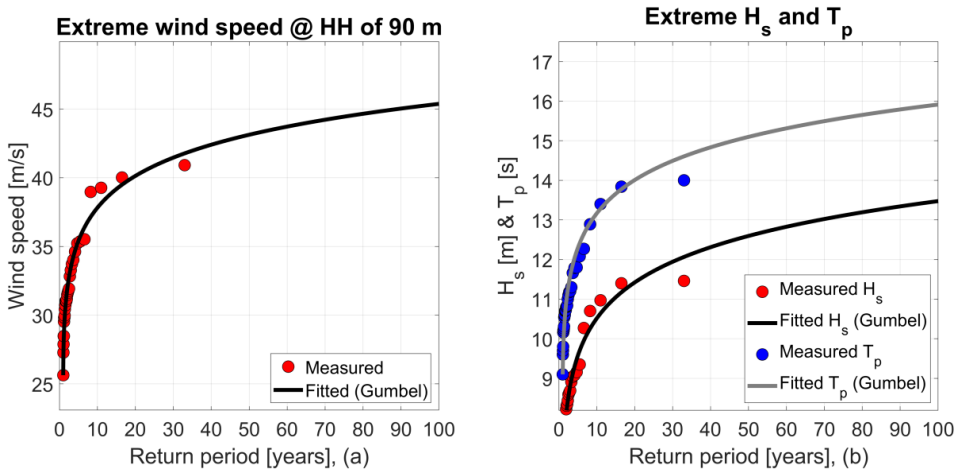

Figure 4.3: Extreme values and the corresponding return periods

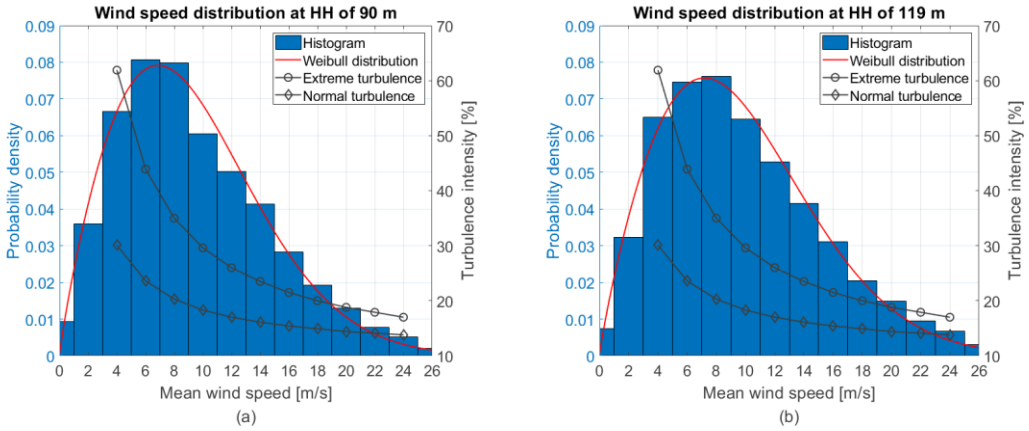

Figure 4.4: Probability distribution of operational wind speed and corresponding turbulence intensity (a): hub height of 90 m, (b): hub height of 119 m

Parameter	Value
Mean wind speed, U	9.4 m/s
Significant wave height, H_s	1.7 m
Peak wave spectral period, T_P	8.2 s
Mean wind/wave misalignment, β	15.3 deg
Turbulence intensity, TI	18.8 % (IEC Turbulence category B)

Table 4.2: Statistics of variables of interest based on 8 years historical data

Return period	Wind speeds	Significant wave heights	Peak spectral periods
1 year	25.6 m/s	5.93 m	9.1 s
50 years	43.1 m/s	12.6 m	15.1 s
100 years	45.4 m/s	13.5 m	15.9 s
200 years	47.6 m/s	14.4 m	16.7 s
500 years	50.6 m/s	15.5 m	17.8 s

Table 4.3: Extreme values for 1, 50, 100, 200 and 500-year return periods

Control device	Turbine model	Design load case	Anlaysis	Wind/ wave model	Reference Figure / Table
Tower-TMD	NREL/OC3 monopile	Mean of U, H_s, T_P, β	Parametric	NTM/NSS	N/A / 4.2
		DLC 1.2 (Joint probability of U, β)	FLS	NTM/NSS	4.2 / A.1 & 2
		DLC 6.2 ($U = U_{50}$, $H_s = H_{s50}$, $T_p = T_{p50}$)	ULS	EWM/ESS	4.3 / 4.3
	MREL/MIT TLP	Mean U, H_s, T_P, β	Parametric	NTM/NSS	N/A / 4.2
		DLC 1.2 (Joint probability of U, β)	FLS	NTM/NSS	4.2 / A.1 & 2
		DLC 6.2 ($U = U_{50}$, $H_s = H_{s50}$, $T_p = T_{p50}$)	ULS	EWM/ESS	4.3 / 4.3
Nacelle-TLCDs	NREL/OC3 monopile	Mean U, H_s, T_P, β	ES	NTM/NSS	N/A / 4.2
		Conditional probability of U, β	MOO	NTM/NSS	4.1 / N/A
		DLC 1.2 (Joint probability of U, β)	FLS	NTM/NSS	4.2 / A.1 & 2
		DLC 6.2 ($U = U_{50}$, $H_s = H_{s50}$, $T_p = T_{p50}$)	ULS	EWM/ESS	4.3 / 4.3
	MREL/MIT TLP	Mean U, H_s, T_P, β	ES	NTM/NSS	N/A / 4.2
		Conditional probability of U, β	MOO	NTM/NSS	4.1 / N/A
		DLC 1.2 (Joint probability of U, β)	FLS	NTM/NSS	4.2 / A.1 & 2
		DLC 6.2 ($U = U_{50}$, $H_s = H_{s50}$, $T_p = T_{p50}$)	ULS	EWM/ESS	4.3 / 4.3
Blade-TMD	NREL 5-MW blade	Mean of U	Parametric	NTM	N/A / 4.2
		DLC 1.2 (Probability of operational wind)	FLS	NTM	4.4 / N/A
		DLC 1.3	ULS	ETM	4.4 / N/A
	DTU 10-MW blade	Mean of U	Parametric	NTM	N/A / 4.2
		DLC 1.2 (Probability of operational wind)	FLS	NTM	4.4 / N/A
		DLC 1.3	ULS	ETM	4.4 / N/A

Table 4.4: Summary of design load cases and type of analysis

4.2 Metocean Conditions at Wave Hub Site

The metocean conditions of the Wave Hub site are measured and estimated through a hind cast approach conducted by HR Wallingford hydraulics laboratory in UK [72]. The Wave Hub site is permitted as a test site for wave energy devices and has relatively severe wave conditions. In this dissertation, the metocean conditions at this site are mainly utilized to conduct ULS analysis (extreme load analysis) for evaluating the control effect of the tower-TMD on reducing extreme loads of the GE Haliade 6-MW supported by a monopile-OWT and Glosten's PelaStar TLP-OWT. The extreme wind conditions are taken from statistical analyses of 30 years and 10 year hind cast wind data sets. The extreme wave conditions are estimated from wave hind cast data based on wave propagation models. The post-processing of the wave data returns a 50-year return period H_S and T_P. The post-processed wave data is further modified by Glosten to provide conservative 50-year return period extreme wave conditions. Figure 4.5 shows a contour plot of H_S and T_P provided by Glosten. The extreme 50-year return wind speed of 38.1 m/s at the hub height is used in the ULS analysis. In addition, two significant wave heights, 9.94 m (T_P of 14.04 s) and 10.26 m (T_P of 14.69 s), are used to represent severe wave conditions at the Wave Hub site. Table 4.5 shows the ULS conditions for the GE Haliade 6-MW PelaSatr TLP-OWT. The conditions listed in Table 4.5 for ULS analysis are used to create a set of conditions for DLC 6.1 according to the IEC 61400-3. To derive FLS conditions, a probability distribution for operational wind speed and a probability distribution for wind/wave misalignment are created, as shown in Figure 4.6. The wind speed at the hub height of 100 m is binned with a width of 2 m/s from the cut-in wind speed (3 m/s) to the cut-out wind speed (25 m/s). The data for wind/wave

misalignment is binned with a width of 30 degrees from 0 to 90 degrees. The expected values of H_S and T_P associated with each wind bin are determined and shown in Table 4.6. The turbulence intensity follows the IEC category B. The probability regarding wind/wave misalignments and the expected values of H_S and T_P are used to create a set of DLC 1.2 conditions for investigating the impact of the tower-TMD on reducing fatigue loads of GE Haliade 6-MW OWTs. Table 4.7 shows some important statistics of variables of interest, such as U, H_S, T_P and β are also estimated, which are used for a parametric study of the tower-TMD for GE Haliade 6-MW OWTs. Table 4.8 summarizes DLCs and the types of analysis.

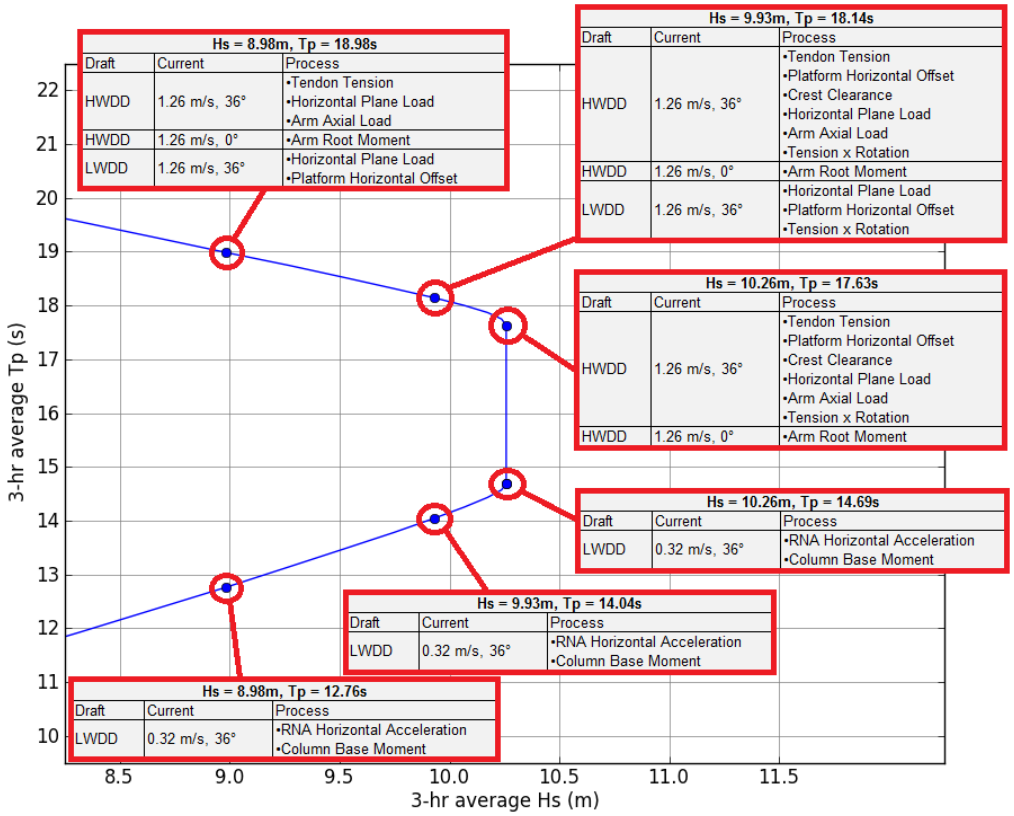

Figure 4.5: Contour plot of 50-year return period wave heights and periods [72]

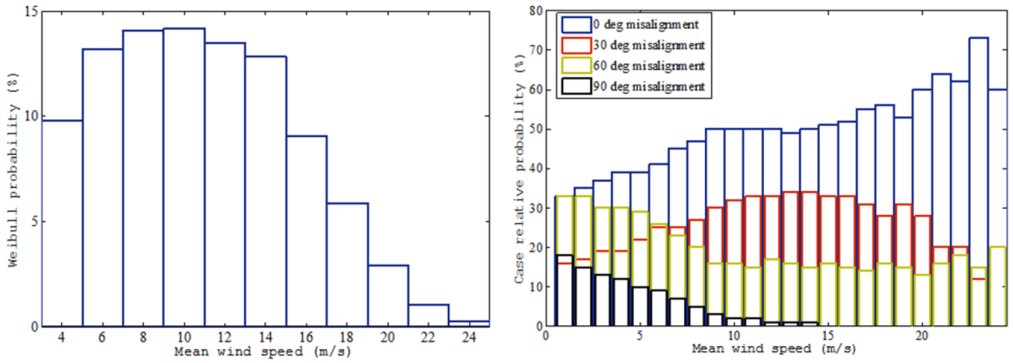

Figure 4.6: Wind speed distribution and wind/wave misalignment probability [72]

Wind speed (m/s)	TI (%)	Current (m/s)	H_s (m)	T_P (s)
38.1	11.0	0.354	10.26	14.69
38.1	11.0	0.354	9.94	14.04

Table 4.5: Summary of extreme wind and wave conditions at the Wave Hub site

Wind speed (m/s)	Turbulence intensity (%)	Significant wave heights (m)	Peak spectral periods (s)
4	30.1	0.37	3.79
6	23.6	0.48	4.01
8	20.3	0.61	4.26
10	18.3	0.76	4.54
12	17.0	0.93	4.84
14	16.1	1.12	5.12
16	15.4	1.32	5.49
18	14.9	1.55	5.84
20	14.4	1.80	6.19
22	14.1	2.06	6.54
24	13.8	2.34	6.89

Table 4.6: Summary of operational wind and wave conditions

Parameter	Value
Mean wind speed, U	9.1 m/s
Significant wave height, H_s	0.65 m
Peak wave spectral period, T_P	4.37 s
Mean wind/wave misalignment, β	10.7 deg
Turbulence intensity, TI	19.8 %

Table 4.7: Statistics of variables of interest

Control device	Turbine model	Design load case	Anlaysis	Wind/ wave model	Reference Figure / Table
Tower-TMD	GE Haliade/ monopile	Mean of U, H_s, T_P, β	Parametric study	NTM/NSS	N/A / 5.6
		DLC 1.2 (Joint probability of U, β)	FLS	NTM/NSS	5.6 / N/A
		DLC 6.1 ($U = U_{50}$, $H_s = H_{s50}$, $T_p = T_{p50}$)	ULS	EWM/ESS	5.5 / 5.5
	GE Haliade/ TLP	Mean U, H_s, T_P, β	Parametric study	NTM/NSS	N/A / 5.6
		DLC 1.2 (Joint probability of U, β)	FLS	NTM/NSS	5.6 / N/A
		DLC 6.1 ($U = U_{50}$, $H_s = H_{s50}$, $T_p = T_{p50}$)	ULS	EWM/ESS	5.5 / 5.5

Table 4.8: Summary of design load cases and type of analysis

CHAPTER 5

CONTROL STRATEGIES AND OPTIMIZATION

It is important to establish control strategies to investigate the impact of structural control approaches on reducing fatigue and extreme load reductions of OWTs. This chapter describes passive and semi-active control techniques for the tower-TMD, the blade-TMD and the nacelle-TLCDs. Different optimization approaches for each control device are utilized. Several semi-active control algorithms for the tower-TMD used in this dissertation are presented and the optimal combination is determined based on their distinct frequency characteristics. Some of the results regarding the tower-TMDs for GE's OWTs have been published in *Wind Energy* [66].

5.1 Parameter Optimization for a Tower-TMD

A parametric study is conducted to determine the optimal parameters of the passive pendulum-type omni-directional TMD situated on the top of a tower (see Figure 3.1). The OWT models used in this analysis are the NREL 5 MW baseline wind turbine supported by OC3 monopile and MIT-NREL TLP, and the GE Haliade 6 MW wind turbine with the monopile and the Pelastar TLP support structures. The main parameters to be optimized are the mass ratio, tuning frequency ratio, and damping ratio of the tower-TMD. Typically, the vibrational energy of a turbine tower increases as it goes toward the end of the tower, and is mostly distributed near the tower top as the magnitude of the critical tower mode is the largest as shown in Figure 5.1. Although the space for driving the tower-TMD gradually decreases, it is still desirable for the tower-TMD to be installed where the magnitude of the critical mode is the largest. The control

effect is further increased as the mass of the TMD increases. Though the heavier TMD is better in terms of control performance, there are limitations in using the heavier mass of the TMDs for real application. In structural control engineering, the mass ratio μ is defined as the ratio of the TMD mass to the first modal mass of the main structure.

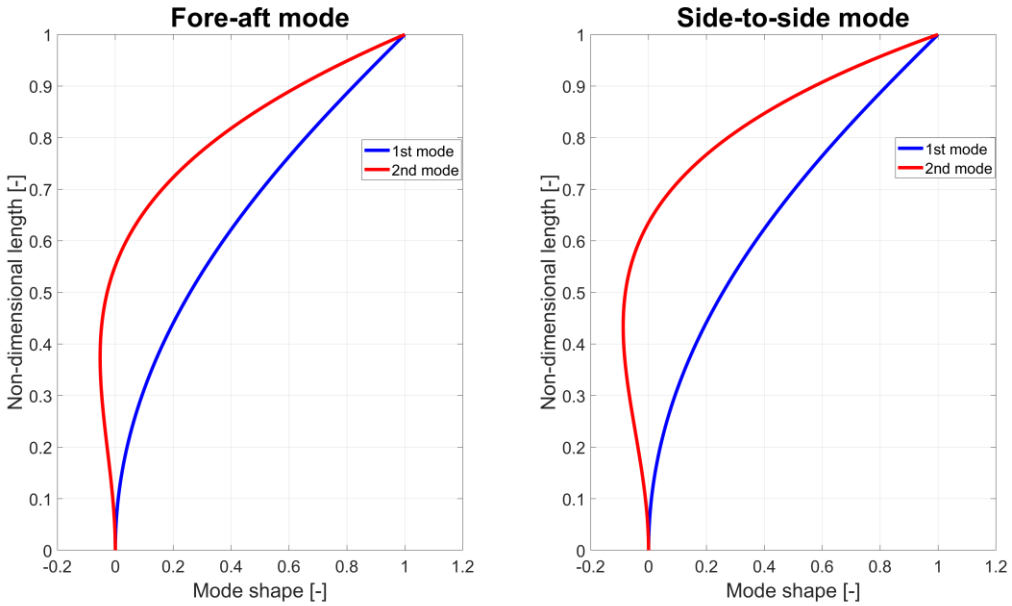

Figure 5.1: An example of fore-aft and side-to-side mode shapes of a turbine tower

Previous research conducted by Adam and Furtmüller pointed out that a range of mass ratios of 2 - 8% are considered to be effective and the practically applicable range for structural control [73]. In addition, He et al. [74] concluded that the suppression rates of the vibration response for OWTs vary according to the TMD mass. In this dissertation, the TMD mass has been chosen within the range of 0.7 – 8.2 % of the 1st tower modal mass. In general, the optimal tuning frequency and the damping coefficient depend on the mass ratio, so it is critical to identify the optimal parameters for the tuning frequency

and the damping ratio as a function of the mass ratio. The first modal mass of the tower can be directly calculated from the equation below:

$$m_{1st} = \int_0^L \rho(z) E^2(z) dz \tag{5.1}$$

where m_{1st} is the first modal mass of the tower, $\rho(z)$ is mass density per unit length, and $E(z)$ denotes the normalized mode shape of the tower fore-aft direction. The values of $\rho(z)$ and $E(z)$ can be determined from the FASTv8 input files. Once the mass ratio μ is determined, the optimal frequency ratio γ and damping ratio ζ can be specified through a parametric study. In a previous paper, Lackner and Rotea determined the optimal parameters of a passive tuned mass damper (TMD) for a floating OWT, the ITI barge [27]. The control performance of the passive TMD was shown to be superior when tuned to the most critical mode (platform pitch motion). This is because the tower's dynamic response might be highly affected by modes other than the tower mode itself for floating OWTs. This means that the control device does not necessarily need to be tuned to the 1st tower mode even if the target of the control device is to improve the dynamic response of the tower. In this context, it is essential to identify the critical mode that causes the largest loads on the tower for each different turbine configurations before conducting a parametric study. The critical mode is identified by checking the frequency responses of the system, and then a parametric study is conducted in order to find out the optimal parameters of the passive TMD near the critical mode of the system. The frequency responses of the tower top motions for fixed-bottom and floating OWTs are provided in Appendix C: Frequency response of tower top motion for NREL 5-MW OWTs and GE 6-MW OWTs. It can be seen from the frequency response results that the

pitch and roll mode is the critical mode of the TLP-OWTs, and the tower 1st eigenmode is the critical mode that affects the largest loads on the tower of the monopile-OWTs. The frequency of the critical mode (control target frequency) for each OWT is listed in Table 5.2.

As discussed in Section 4.1, the basic statistics of variables of interest for wind and wave conditions (U, H_s, T_P and β) were derived based on eight years of historical metocean data at the south east of Nantucket site. The overall statistics of variables used for the simulation conditions are summarized in Table 5.1. With these, TurbSim is used to generate a full-field wind in accordance with IEC 61400-3. In addition, the derived statistics of the wave conditions are set in the HydroDyn input file to create a JONSWAP wave spectrum. The wind turbine is assumed to operate normally for power production. The collective pitch control and the variable speed torque control are implemented using the Bladed-style DLL controller developed at NREL [4]. The standard deviation of the tower top displacement is used to quantify control performance and is considered as the cost function to be minimized, which strongly correlates with fatigue loads of the turbine tower. In order to evaluate the control performance of the tower-TMDs within the feasible range of design variables, non-linear fully-coupled aero-hydro-servo-elastic simulations were performed in FASTv8. All possible combinations of the three design variables of the mass ratio, tuning frequency, and damping ratio are utilized as input parameters for the tower-TMD. This allows both the control performance exerted by each combination as well as the influence of the change of the mass ratio on the other two parameters to be examined. The values for the main input parameters for the tower-TMD are summarized in Table 5.2.

Parameter	Value
Mean wind speed	9.4 m/s
Significant wave height	1.7 m
Peak wave spectral period	8.2 s
Mean wind/wave misalignment	15.3 deg
Turbulence intensity	18.8 % (IEC Turbulence category B)
Turbine situation	Power production
Simulation length	10 minutes

Table 5.1: Simulation conditions for a parametric study

Test turbine	NREL 5-MW Monopile	NREL 5-MW TLP	GE 6-MW Monopile	GE 6-MW TLP
Rotational speed	12.1 rpm	12.1 rpm	11.5 rpm	11.5 rpm
TMD location	77.6 m	87.6 m	82.9 m	105.2 m
Tower 1st modal mass	487,805 kg	612,820 kg	521,770 kg	640,540 kg
TMD mass ratio	0.0082 ~ 0.082	0.0078 ~ 0.078	0.0077 ~ 0.077	0.0074 ~ 0.074
Target frequency (F-A / StS)	0.269 / 0.261 Hz	0.221 / 0.223 Hz	0.246 / 0.243 Hz	0.237 /0.230 Hz
Tuning frequency ratio	0.9 ~ 1.1	0.9 ~ 1.1	0.9 ~ 1.1	0.9 ~ 1.1
Damping ratio	0.01 ~ 0.16	0.01 ~ 0.16	0.01 ~ 0.16	0.01 ~ 0.16

Table 5.2: Main input parameters for the tower-TMD

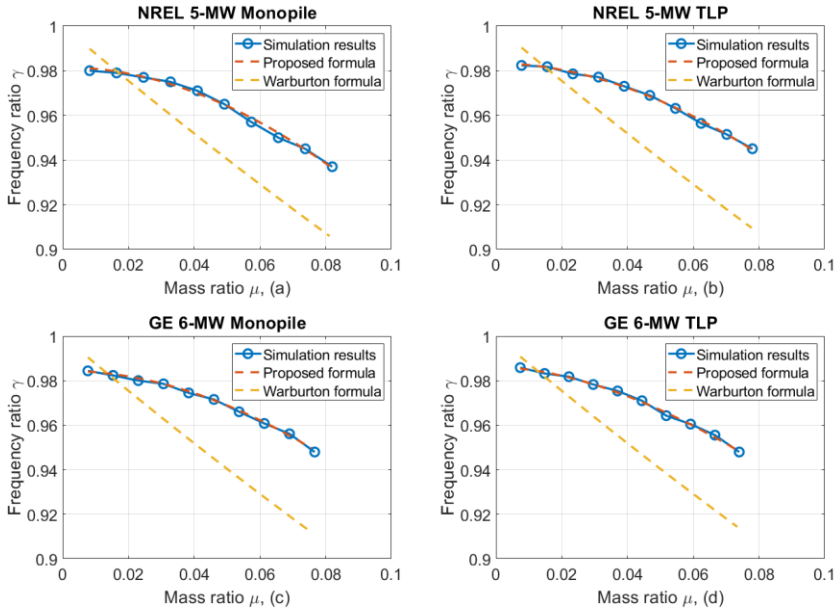

Figure 5.2: Optimal tuning ratio as a function of the mass ratio, (a): NREL 5-MW monopile, (b): NREL 5-MW TLP, (c): GE 6-MW monopile, (d): GE 6-MW TLP

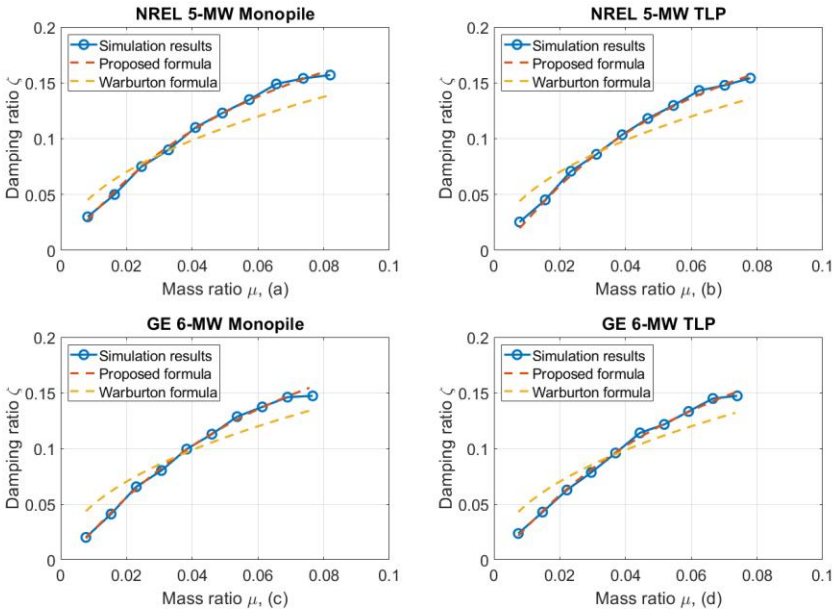

Figure 5.3: Optimal damping ratio as a function of the mass ratio, (a): NREL 5-MW monopile, (b): NREL 5-MW TLP, (c): GE 6-MW monopile, (d): GE 6-MW TLP

The optimal frequency ratio and damping ratio as a function of the mass ratio are obtained through a parametric study and they are shown in Figure 5.2 and 5.3. The points (blue circle) indicate the optimal values for the frequency ratio and the damping ratio corresponding to the mass ratios, which can minimize the standard deviation of the tower top displacement (cost function). It can be seen from Figure 5.2 and 5.3 that the change in the mass ratio requires different optimum values for the tuning ratio and damping ratio. An increase in the mass ratio leads to a decrease in the optimal tuning ratio. In contrast, the optimal damping ratio increases with the larger mass of the TMD. Such phenomena can also be seen in contour plots as shown in Figure 5.4. It can be seen from the contour plots that the de-tuning of the frequency and the damping ratio becomes less sensitive as the mass ratio increases, because the increase in the mass ratio broadens the interval of each contour line. The resulting optimal values are used in a non-linear curve-fitting

scheme in order to derive design formulas of the optimal frequency and damping ratios of the tower-TMD for a given mass ratio μ. In 1982, Warburton et al. [75] established the optimal design formulas for these two parameters. As shown in Figure 5.2 and 5.3, Warburton's formulas cannot precisely predict the optimums for fully-coupled complicated physical systems, like offshore wind turbines as they utilized a single degree of freedom model for the main structure and the control system. New design formulas are needed that can be applied to offshore wind turbines. In order to establish the optimal design formulas, Warburton's formulas are adopted as basic forms and they are further modified in this dissertation. The basic forms are as follows:

$$\gamma_{opt} = \frac{a_f}{b_f + x^{c_f}} \tag{5.2}$$

$$\zeta_{opt} = \left(\frac{a_z \mu}{b_z + c_z \mu}\right)^{d_z} \tag{5.3}$$

Eqs. (5.2) and (5.3) are modified forms of Warburton's formulas to fit the non-linear curves in Figure 5.2 and 5.3. The coefficients a_f, b_f, c_f, a_z, b_z, c_z and d_z are determined through a non-linear curve fitting method as given in Table 5.3. The optimal design formulas using the identified coefficients are plotted in Figure 5.2 and 5.3.

The tower-TMD is originally designed to have a mass of 20 tons by ESM GmBH. With the TMD mass of 20 tons, the mass ratio varies depending on the types of OWTs. So, the design formulas are used to find the stiffness and damping coefficient of the TMD with mass of 20 tons in this dissertation. The surface response plot to represent the optimal stiffness and damping ratio for each OWT are shown in Figure 5.5, and the

optimal values are listed in Table 5.4. In Chapter 6, the optimal parameters corresponding to the mass of 20 tons are used to investigate the impact of the TMD on reducing extreme and fatigue loads of OWTs.

Model	Optimal frequency ratio γ_{opt}	Optimal damping ratio ζ_{opt}
NREL 5-MW Monopile	$\frac{0.1381}{0.1407+\mu^{1.997}}$	$\left(\frac{0.421\mu}{0.0648+1.194\mu}\right)^{1.176}$
NREL 5-MW TLP	$\frac{0.1767}{0.1797+\mu^{1.925}}$	$\left(\frac{0.577\mu}{0.0478+1.319\mu}\right)^{1.535}$
GE 6-MW Monopile	$\frac{0.1583}{0.1608+\mu^{1.989}}$	$\left(\frac{0.474\mu}{0.0516+1.105\mu}\right)^{1.407}$
GE 6-MW TLP	$\frac{0.2479}{0.2514+\mu^{1.768}}$	$\left(\frac{0.389\mu}{0.0640+1.029\mu}\right)^{1.194}$

Table 5.3: Design formulas for the optimal frequency and damping ratio

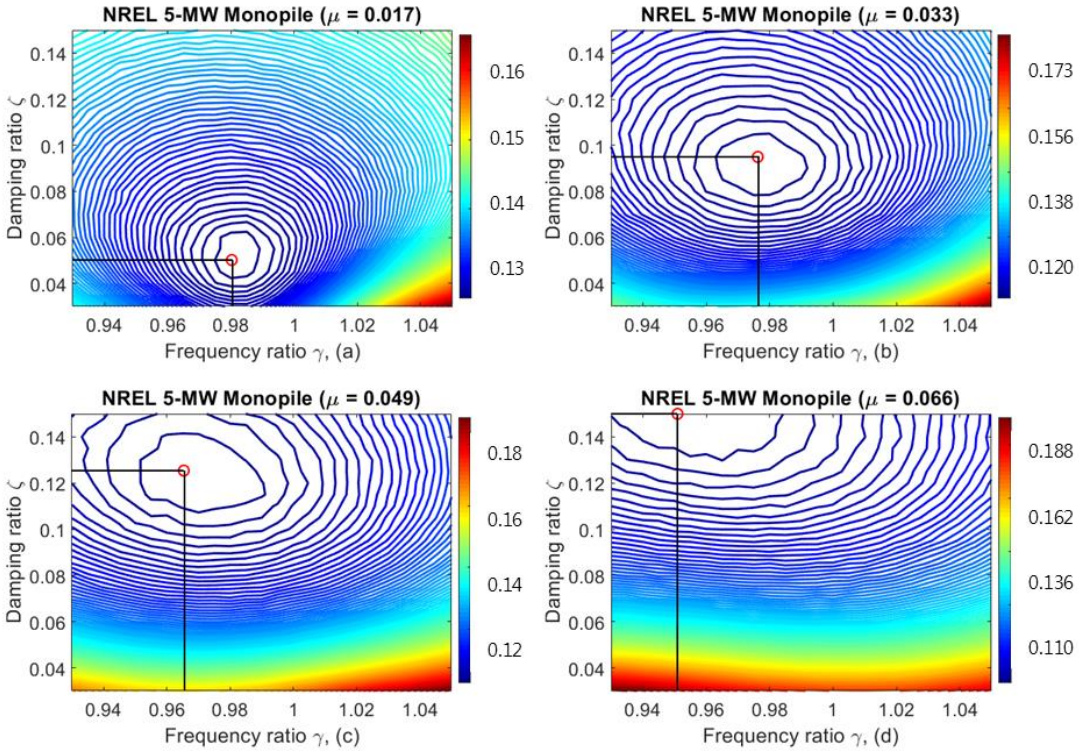

Figure 5.4 Contour plot of the standard deviation of the tower top displacement for optimization of γ and ζ, (a): μ = 0.017, (b): μ = 0.033, (c): μ = 0.049, (d): μ = 0.066

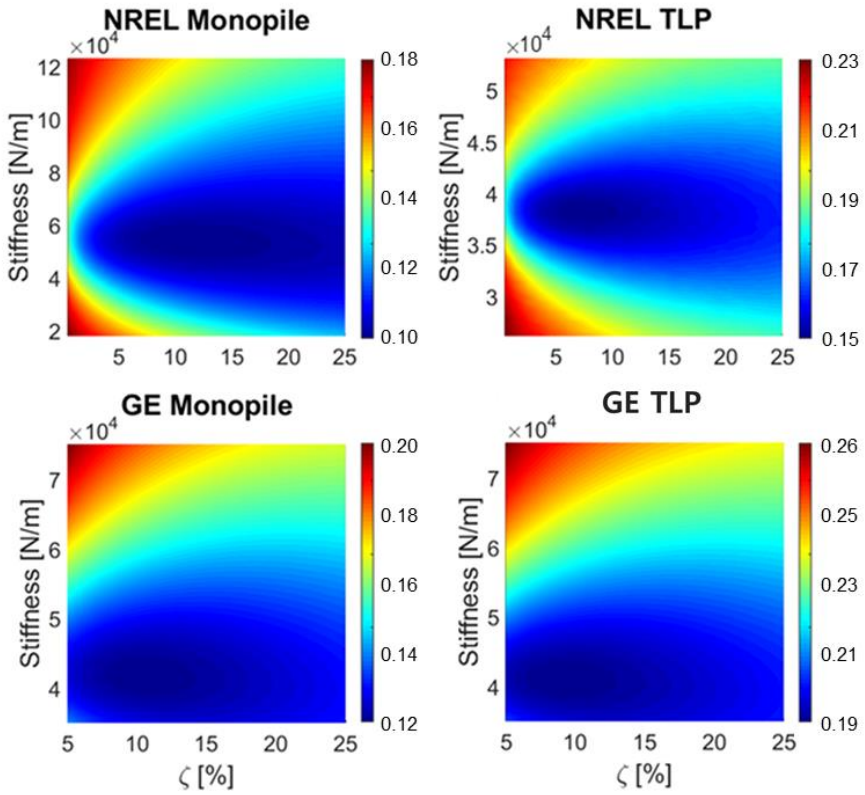

Figure 5.5: Optimal stiffness and damping ratio for the TMD with mass of 20 tons

OWT model	TMD mass	k_{tmd} (Fore-aft)	k_{tmd} (StS)	ζ
NREL Monopile	20,000 kg	53,730 N/m	50,590 N/m	10.9 %
NREL TLP	20,000 kg	36,720 N/m	37,390 N/m	8.9 %
GE Monopile	20,000 kg	45,440 N/m	44,340 N/m	9.9 %
GE TLP (100 m)	20,000 kg	42,800 N/m	42,230 N/m	10.0 %

Table 5.4: Optimal stiffness and damping ratio for the TMD with mass of 20 tons for the different OWTs

5.2 Parameter Optimization for a Blade-TMD

For OWTs, it is highly desirable to control the dynamic responses of the tower or support structure in order to withstand harsher environmental conditions than their land based counterparts. In this regard, numerous research regarding structural control

approaches for OWTs have focused on reducing dynamic loads on wind turbine towers and support structure. In the current trend toward the use of larger rotors for modern multi-megawatt wind turbines, it is also of interest to apply structural control techniques to the blades themselves, rather than confining them to towers or support structures. As the diameter of the blades increases, they become more flexible, making them relatively vulnerable to external loads [55]. In general, the vibrational energy of the blades in the flap-wise direction is damped out by aerodynamic damping caused by the rotor during normal operation [56]. In contrast, the blade vibrations in the edgewise direction are lightly damped due to the lack of aerodynamic damping from the rotor. The insignificant aerodynamic damping acting on the edgewise direction causes larger dynamic responses and shortens the reliability of the blade. For this reason, reducing the edgewise vibration can be a solution to increase the fatigue life and stability of the blade. In this dissertation, the objective of the blade-TMD is to mitigate the edgewise fatigue and ultimate loadings in rotating wind turbine blades.

In general, it is most desirable in terms of the control performance that the blade-TMDs are placed toward the blade tip where the vibrational energy is the largest. Also, the motion of the blade-TMD is mostly dominated by the centrifugal acceleration of the blade, which is proportional to the distance from the center of the rotation. Thus, it is expected that the blade-TMD has a better control performance by mounting it close to the blade tip. However, the added mass of the blade-TMD located near the tip may counteract the control effects of the blade-TMD, and can lead to additional deflections by the weight of the blade-TMD. The correlation between the deflection due to the effect of gravity and the blade rotation can be seen in Figure 5.6. The blade is deflected in the

edgewise direction (or in-plane direction) as it rotates. In Figure 5.6 (a), the first blade (number 1) does not experience the deflection by the effect of gravity in the edgewise direction, as the azimuth angle is zero. As the blade starts to rotate, the deflection by the effect of gravity occurs as shown in Figure 5.6 (b). In reality, deflection in the edgewise direction occurs inevitably even if the azimuth angle is zero, since the blade is usually twisted. Figure 5.7 shows an example of the time response of the edgewise tip deflection when the blade rotates at 12.1 rpm (0.2 Hz). It can be seen that the frequency of the deflection corresponds to the rotational speed of the blade. Figure 5.8 shows an example of the control effects of the blade-TMD and additional deflections of the blade caused by the blade-TMD. While the control target frequency-component (1st edgewise natural frequency of 1.09 Hz) can be relieved by both lighter (μ=0.05), and heavier TMDs (μ=0.25), the heavier TMD results in larger deflection related to the rotational frequency-component (0.2 Hz =12.1 rpm).

In addition, the added mass by the blade-TMD affects the 1st edgewise natural frequency. BModes is utilized to calculate the 1st edgewise natural frequency of the blade equipped with the blade-TMD. In order to evaluate the impacts of the mass and the location of the blade-TMD on the natural frequency, iterative simulations using BModes are performed by changing the mass distribution (lighter to heavier) at each blade element (blade bottom to tip) to compensate for the blade-TMD mass located in the blade along the z-direction. Figure 5.9 shows the results of the BModes simulations, which illustrates the 1st natural frequency as functions of the TMD mass and the locations. The x-axis represents the mass ratio of the TMD mass to the 1st modal mass of the blade and the y-axis represents the TMD position along the blade length. The information about the

first modal mass and the maximum blade length is shown in Table 5.4. The color bar indicates the 1st edgewise natural frequency. The 1st natural frequency of the NREL-5MW blade and DTU 10-MW blade without a TMD are 1.09 Hz and 0.97 Hz, respectively. It can be seen from Figure 5.9 that the natural frequency drops considerably as the TMD is closer to the tip of the blade. This phenomenon becomes worse with larger mass. In beam theory, it is well known that the mass ratio of the attached tip mass to the whole mass of the beam is a significant factor affecting the natural frequencies of the system [76]. The effect of added mass by the TMD on the natural frequency is negligible when the mass ratio μ is less than 0.08 and the TMD is positioned approximately 2/3 of the total blade length. Conversely, when the mass ratio is larger than 0.08 and the TMD is positioned beyond 2/3 of the total blade length, the potential of the blade-TMD is no longer meaningful, since it results in a significant decrease in the 1st natural frequency of the blade. The 1st natural frequency determined by BModes analysis is used to tune the blade-TMD for a parametric study to determine the optimal position of the blade-TMD.

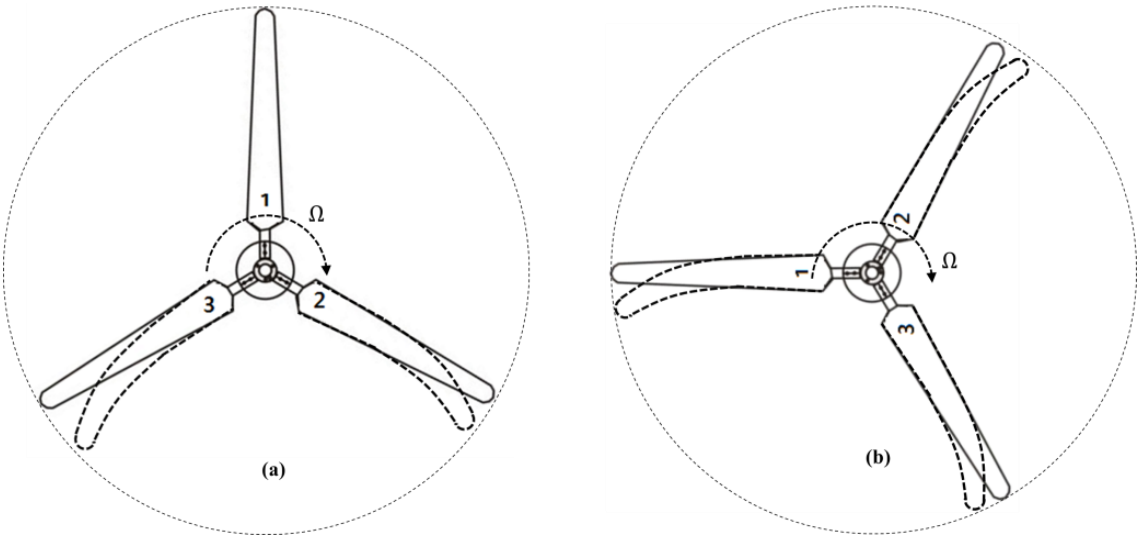

Figure 5.6: Deflections of the blades as the blades rotate

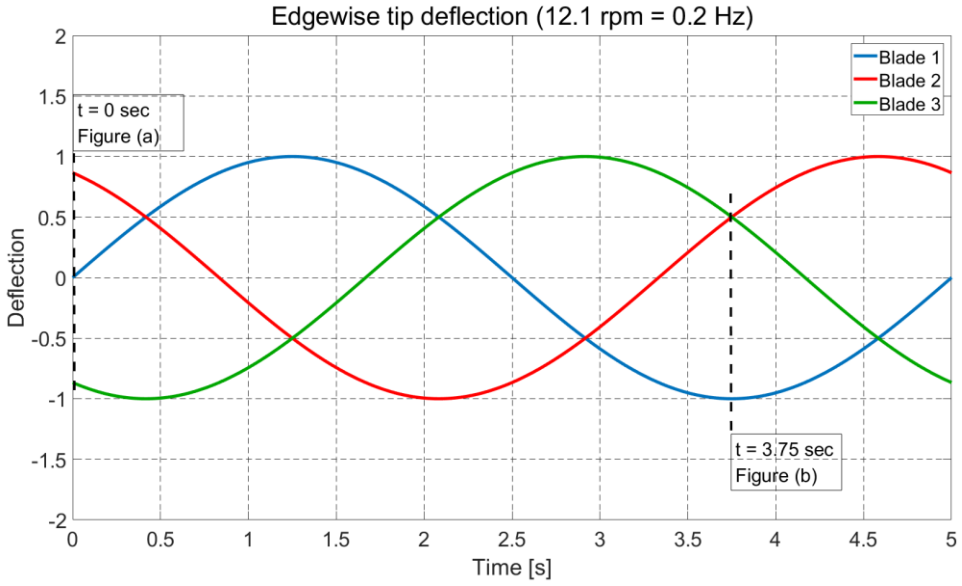

Figure 5.7: Time response of the blade deflection

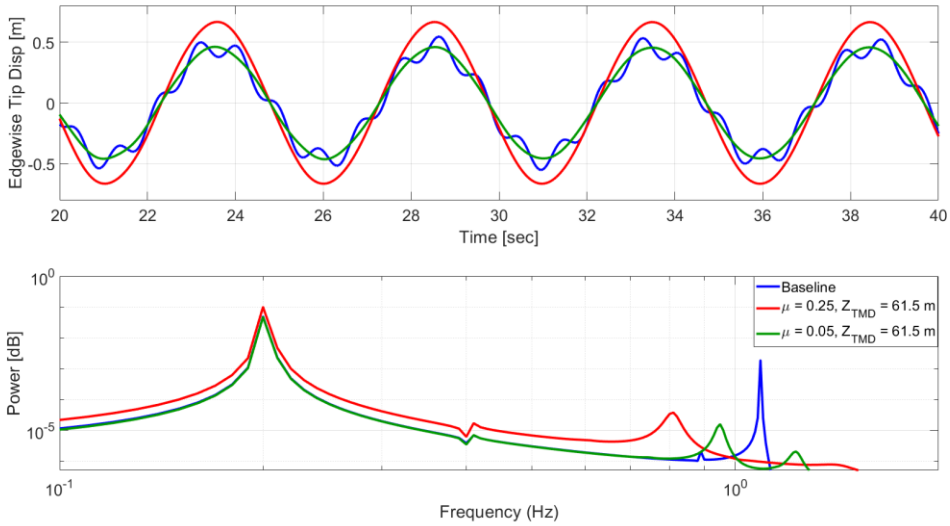

Figure 5.8: Time response and frequency response of edgewise tip displacement for baseline, and the lighter TMD and the heavier TMD cases

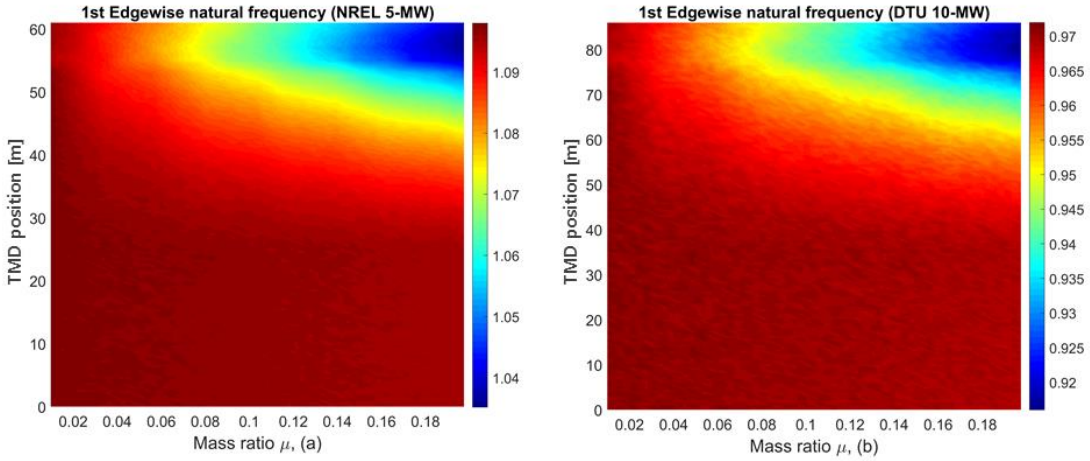

Figure 5.9: BMode results showing the 1st edgewise natural frequencies (Hz)

In addition, the available space inside the blade can also be a factor to determine the position of the TMD, since the space for the blade-TMD operation dramatically decreases towards the blade tip. While it is important to mount the blade-TMD as close to the blade tip as possible in order to achieve better control performance, it is more noteworthy to avoid such negative effects and reserve enough space by locating the TMD at a lower position. For this reason, the blade-TMD mass and the positon along the blade length are critical parameters that should be determined first. The optimization scheme mainly consists of the following two steps:

1) Conduct a parametric study for the mass and the location of the blade-TMD. For this parametric study, the TMD mass and the location are variable within the ranges. The tuning frequency is fixed to a certain value that corresponds to the value of intersection between the mass ratio and the TMD location obtained from BModes analysis as shown in Figure 5.9. The damping coefficient of the TMD is adjusted to maintain the damping ratio of 8 %.

2) Once the optimal TMD location as a function of the mass ratio is determined, then a second parametric study to determine the optimal tuning frequency and damping ratio of the blade TMD is performed. In contrast to the first parametric study, this time, the simulation is performed by varying the tuning frequency and damping ratio within a certain range while keeping the fixed mass and location of the TMD obtained from the first parametric study.

The first parametric study routine considers every possible combination of the mass and the location of the blade TMD for each the NREL-5MW and the DTU 10-MW blade. To find the optimal mass ratio and location, successive simulations with a range of the evenly spaced TMD mass and location are conducted using FASTv8 the structural control module. The main simulation conditions are the same as those performed in the tower parametric study. The turbines operate normally, and the same blade pitch and torque controls are applied. The cost function to be minimized is the standard deviation of the blade edgewise vibration. The values for the main input parameters are summarized in Table 5.5. The blade rotates at the rated speed of each turbine model. Like the tower-TMD, the mass ratio μ is defined as the ratio of the TMD mass to the first modal mass of the blade. The mass ratios μ evaluated in this analysis range from 0.01 to 0.2, and the TMD is positioned from the root to the tip.

Test blade	NREL 5-MW Blade	DTU 10-MW Blade
Rotation speed	12.1 rpm	9.6 rpm
Initial perturbation at the blade tip	0.5 m	0.5 m
Blade length	61.5 m	86.4 m
Blade 1st modal mass	1300 kg	1950 kg
TMD mass	μ = 0.01 ~ 0.2	μ = 0.01 ~ 0.2
TMD location (z-direction)	0 ~ 61 m	0 ~ 86 m

Table 5.5: Main input parameters for the blade-TMD

Figure 5.10 shows the contour plot obtained by the first parametric study. The color bar indicates the standard deviation of the blade edgewise vibration. As expected, the control performance deteriorates as the TMD approaches the blade tip with larger mass. Also, it can be seen that the optimal position of the blade TMD becomes lower as the TMD mass increases. The black circle represents the location of the minimum standard deviation according to the TMD mass ratio. The points show the optimal position of the blade-TMD corresponding to the mass ratio, and are nonlinearly distributed. The curves formed by the points are used to derive optimal design formulas for the TMD location by conducting a nonlinear curve fitting method. The formulas are expressed as 4^{th} order polynomials as shown in Table 5.6.

Model	Design formula (4^{th} order polynomial)
NREL 5-MW Blade	$51300\mu^4 - 31240\mu^3 + 7324\mu^2 - 847\mu + 73$
DTU 10-MW Blade	$72400\mu^4 - 42800\mu^3 + 9705\mu^2 - 1106\mu + 103$

Table 5.6: Design formulas for the optimal blade-TMD position

Once the optimal positions for the given range of the mass ratios are determined, the remaining parameters such as the tuning frequency ratio and the damping ratio of the blade-TMD are further optimized. As mentioned earlier, the TMD tuning frequency and the damping coefficient were set to constant values in the first parametric study to determine the optimal position of the TMD. In fact, these constant values are not exact optimal values, so the second parametric study is performed. Through the second parametric study, the optimum tuning frequency and damping coefficient are obtained at each intersection on the curve from the design formula for the TMD location. Figure 5.11 (a) and (b) show the 3-dimensional scatter plots that represent the optimal frequency ratio

(γ) and the optimal damping ratio (ζ) as functions of the mass ratios and the locations. Figure 5.11 (c) and (d) show the 2-dimensional view (x-z plane). It is clear from Figure 5.11 (c) that the frequency ratio decreases as the mass ratio increases. In contrast, an increase in the mass ratio leads to a larger damping ratio. Such phenomena have been demonstrated and validated in previous structural control research [75]. Like the tower-TMD, Warburton's formulas are adopted as basic forms and are further modified to establish design formulas for the optimal frequency and the damping ratio:

$$f_{opt} = \frac{\sqrt{1+\alpha\mu}}{1+\beta\mu} \tag{5.4}$$

$$\zeta_{opt} = \left(\frac{\kappa\mu}{\phi+\chi\mu}\right)^{\lambda} \tag{5.5}$$

Eqs. (5.4) and (5.5) are modified forms of Warburton's formulas to fit the curves in Figure 5.11 (c) and (d). The coefficients α, β, κ, ϕ, χ and λ are determined through a non-linear curve fitting scheme as given in Table 5.7. The design formulas regarding the optimal TMD location, frequency ratio and damping ratio are utilized in order to evaluate the impact of the optimal blade-TMD on reducing fatigue and extreme loads of OWTs in Chapter 6.

Model	Optimal frequency ratio γ_{opt}	Optimal damping ratio ζ_{opt}
NREL 5-MW Blade	$\frac{\sqrt{1-1.176\mu}}{1+0.04315\mu}$	$\left(\frac{3.216\mu}{8.648+7.966\mu}\right)^{0.5147}$
DTU 10-MW Blade	$\frac{\sqrt{1-1.210\mu}}{1+0.2242\mu}$	$\left(\frac{2.561\mu}{6.309+8.254\mu}\right)^{0.5588}$

Table 5.7: Design formulas for the optimal frequency ratio and damping ratio for the blade-TMD

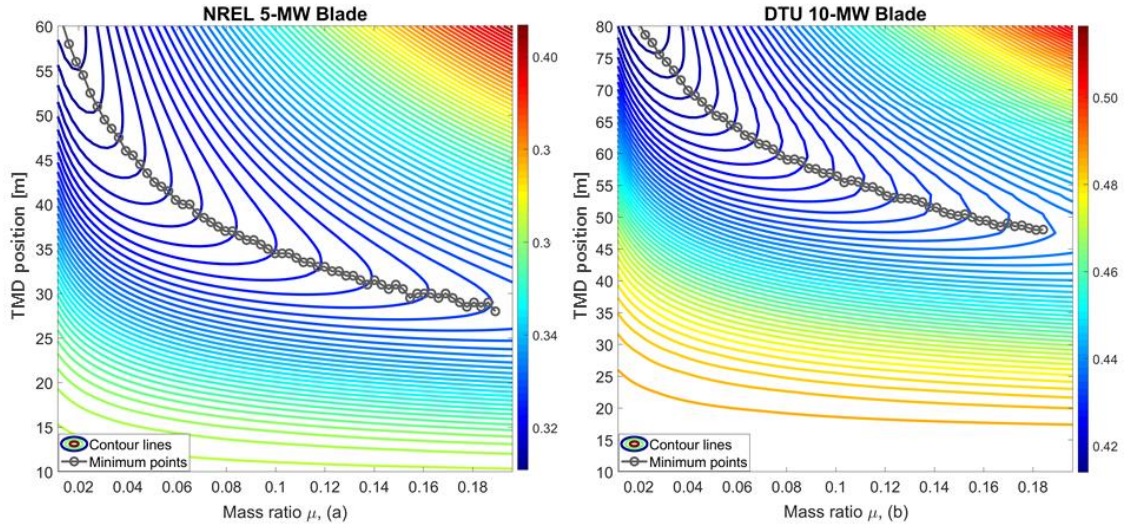

Figure 5.10: Contour plot of the standard deviation of the blade edgewise displacement (m)

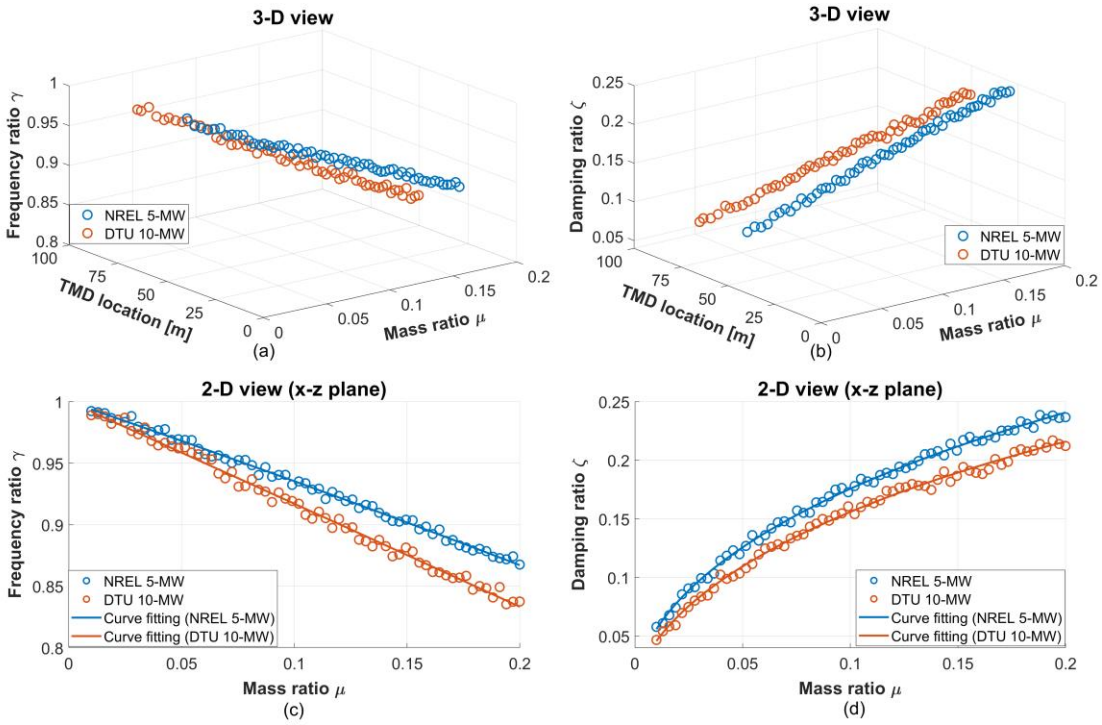

Figure 5.11: Scatter plots showing optimal γ and ζ, (a) and (b): 3-D view, (c) and (d): 2-D view

5.3 Parameter Optimization for Nacelle-TLCDs

For parameter optimization of the nacelle-TLCDs, two optimization schemes are performed sequentially. First, a preliminary design using a reduced order exhaustive search method is performed to identify the appropriate ranges of design variables for a multi-objective optimization problem (MOO). Once the boundaries of variables are derived by the preliminary design, a MOO process is conducted in order to optimize the orthogonal nacelle-TLCDs.

5.3.1 Reduced Order Exhaustive Search Study

A reliable way of determining the optimal parameters with certainty is to test all possible cases of the design variables. An exhaustive search (ES) approach can be used to evaluate all possible combinations of the design variables for the TLCD. However, this method requires at least tens of thousands of calls from a simulator to test all combinations of each design variable within the specified bounds and geometric design constraints. The number of simulations to conduct a general ES approach for the TLCD outweighs that of the TMD because the number of design variables to be optimized is much larger. As FASTv8 is used as a main simulator in the parameter optimization, it might be infeasible to evaluate every combination of the design variables (possibly more than tens of simulations), since FASTv8 is computationally expensive. In this context, the number of design variables needs to be reasonably limited.

In this section, the ES method with a reduced order of design variables is conducted for the preliminary design of the TLCDs, in order to evaluate the overall impacts of key design variables and to provide insights needed to select the appropriate

ranges of each design variable, which is applicable to other optimization approaches. The insights derived from the preliminary design are used to solve a full-scale multi objective optimization (MOO) problem based on a genetic algorithm detailed in Section 5.3.2. Setting a proper range for the design variables allows for appropriate diversity of this population, which is a critical factor in making the genetic algorithm more efficient.

The main procedure of the reduced ES approach is: (i) to determine which design variable has the greatest influence on control performance, and set it to a certain value; (ii) to eliminate the design variables that violate the design constraints; (iii) to run simulations with feasible combinations of the design variables determined in procedure (ii); (iv) finally to exclude the combinations that violate the liquid stroke constraint that cannot be considered in the selection of possible combinations of design variables in procedure (ii) as the liquid stroke is unknown before simulation.

As with most structural control devices, tuning the device to the critical mode of the main structure is the most important in terms of control performance. Thus, the tuning frequency (f_{TLCD}) is fixed to a constant value corresponding to the optimal tuning frequency from the optimal design formulas as shown in Table 5.3. Like the tower-TMD, the orthogonal TLCDs are assumed to be tuned to the pitch and roll mode for the NREL 5-MW TLP OWT. This is because the bending response of the tower is highly affected by the pitch and roll mode as also discussed in Section 5.1. The frequencies of the pitch and roll mode of the turbine model are 0.221 and 0.223 Hz, respectively, as shown in Table 5.2. With the design formulas, the optimal tuning frequencies for the FA-TLCD and the SS-TLCD can be calculated as 0.216 and 0.218 Hz, respectively, with a mass ratio of κ as 0.0165 for each TLCD (meaning, the total mass ratio is 3.3% or

approximately 20 tons). For the NREL 5-MW monopile OWT, the tower critical mode frequencies are 0.269 (Fore-aft) and 0.261 Hz (Side-to-side). So, the optimal tuning frequencies for the FA-TLCD and the SS-TLCD can be calculated as 0.262 and 0.254 Hz by applying the design formulas. These optimal tuning frequencies are used for the reduced ES approach, and are fixed. Setting the tuning frequencies to a constant value significantly reduces the number of combinations of design variables. From Eqs. (3.42) and (3.43), the tuning frequency f_{TLCD} can be expressed as:

$$f_{TLCD} = \sqrt{\frac{2\rho A\dot{\theta}^2(L-B) + 2\rho A\dot{\phi}^2(L-B) + 2\rho A\left(g_z + {}^{G}\ddot{z}^{P}\right)}{\rho A(L-B+\alpha B)}}\frac{1}{2\pi} \cong \sqrt{\frac{2g_z}{L_{ee}}}\frac{1}{2\pi} \tag{5.5}$$

where $L_{ee}(= L - B + \alpha B)$ is the total length of an equivalent uniform liquid column with a constant cross-sectional area A, meaning that it has the same kinetic energy as a TLCD with variable cross-sectional areas in the vertical and the horizontal columns. The two rotational terms ($2\rho A\dot{\theta}^2(L-B)$ and $2\rho A\dot{\phi}^2(L-B)$) and the translational acceleration term in the direction of z ($2\rho A\,{}^{G}\ddot{z}^{P}$) are very small, and can thus be neglected. Therefore, f_{TLCD} can be expressed as a function of the gravitational acceleration and the equivalent length L_{ee}. Once the optimal tuning frequencies are determined, then the equivalent length L_{ee} can also be determined. The equivalent lengths L_{ee} for the FA-TLCD and the SS-TLCD are 10.7 m and 10.5 m respectively for the NREL TLP OWT. For the NREL monopile OWT, the equivalent lengths are 7.3 m (FA-TLCD) and 7.7 m (SS-TLCD). With L_{ee} determined, the area ratio α can be identified as the function of L and B as seen in the equation below:

$$\alpha = \frac{L_{ee} - L + B}{B} > 0 \tag{5.6}$$

The area ratio α cannot be negative physically. The equivalent length L_{em} gives the same total mass as the TLCD with the variable cross-sectional areas of the vertical and the horizontal column. Like the area ratio parameter, the equivalent length L_{em} also depends on L and B.

$$L_{em} = \frac{B}{\alpha} + (L - B) \tag{5.7}$$

The vertical cross-sectional area A_V is calculated as:

$$A_V = \frac{m_{tot}}{\rho L_{em}} \tag{5.8}$$

According to Eqs. (5.6) - (5.8), the only independent variables are L and B. The remaining variables (α, L_{em}, A_V) depend on L and B. These independent variables should be bounded due to the limited space available inside the nacelle. Also, they should be constrained to avoid geometric conflicts. Even if the combinations of the design variables are within the lower and upper bounds, some of them often present geometrically impossible dimensions. The feasible space for the TLCDs is assumed to be the maximum size of the nacelle. These dimensioning requirements are estimated based on the nacelle side and front area data from a 6-MW DOWEC turbine [77]. The dimensions from the 6-MW DOWEC turbine can be a good basis for making the assumption as the NREL offshore 5-MW turbine is developed by mainly utilizing the data from the DOWEC study. In practice, the fact that the nacelle holds electrical and mechanical equipment including the main shaft, gearbox and generator, etc., complicates use of the space for the TLCDs.

Rather than considering the design of the TLCD in the presence of such equipment, this dissertation focuses on investigating the impact of the orthogonal TLCDs in terms of the load reductions as well as the effects of the design variables on dynamic responses of the turbine system. As such, this dissertation does not consider the layout of the equipment and the TLCDs, though this could be a topic for future work.

The head loss coefficients can also be regarded as design variables and their optimum value can be derived through simulations. However, considering all these combinations in addition to the other two variables (L and B) substantially increases the number of simulations. Consequently, the head loss coefficients are assumed to be an arbitrary value in this preliminary design process. The terms ($1/2\rho A_V \xi \alpha^2 |\dot{w}| \dot{w}$), representing the damping of the TLCDs in Eqs. (3.42) and (3.43) are non-linear in terms of water velocity ($\dot{w}$). Because of the non-linearity, it is difficult to directly determine the head loss coefficient ξ. In order to determine the optimal head loss coefficient, a statistical linearization method has been proposed by Yalla et al. [78]. They derived an expression for the optimal head loss coefficient of a TLCD subject to white noise input by introducing a direct search method. The expression is utilized for the preliminary design process, and the values used for the preliminary design are 3.5 and 2.5 for the FA-TLCD and the SS-TLCD, respectively. Assuming the head loss coefficient as a constant value not only significantly reduces the amount of simulation, but also focuses on the effect of the other two design variables (L and B) on control performance.

Table 5.8 lists the design variables for each TLCD and their minimum and maximum values. The lower and upper bounds are applied to both the monopile and TLP OWTs. Table 5.9 shows the design constraints for the FA-TLCD and SS-TLCD with a

circular cross-sectional area and a rectangular cross-sectional area. The constraint functions vary depending on the shape of the cross-sectional area.

Variables	Description (units)	Min	Max
L_{FB}	Total length of liquid for FA-TLCD (m)	1.0	21.0
B_{FB}	Horizontal length of liquid for FA-TLCD (m)	1.0	14.0
L_{LR}	Total length of liquid for SS-TLCD (m)	1.0	9.3
B_{LR}	Horizontal length of liquid for SS-TLCD (m)	1.0	2.3

Table 5.8: Design variables and their lower and upper bounds for the reduced ES approach

		Constraints (i=FA, SS)	Description
Circle	1	$B_i - L_i < 0$	The total length is longer than the horizontal length
	2	$(L_i - B_i)/2 < 3.5$	The height of vertical column is less than the nacelle height
	3	$r_{H_i} < (L_i - B_i)/2$	The radius of horizontal column is less than the height of liquid
	4	$r_{V_i} < B_i/2$	The radius of vertical column is less than the half of horizontal length
	5	$\max(\lvert w_i \rvert) < (L_i - B_i)/2$	Maximum liquid displacement is less than the height of liquid
Rectangle	1	$B_i - L_i < 0$	The total length is longer than the horizontal length
	2	$(L_i - B_i)/2 < 3.5$	The height of vertical column is less than the nacelle height
	3	$A_{H_i}/2b_i < (L_i - B_i)/2$	The half of height of the horizontal column is less than the height of liquid
	4	$A_{V_i}/2b_i < B_i/2$	The half of height of the vertical column is less than the half of horizontal length
	5	$\max(\lvert w_i \rvert) < (L_i - B_i)/2$	Maximum liquid displacement is less than the height of liquid

Table 5.9: Inequality design constraints and their descriptions

Figure 5.12 shows the range of the design variables L and B, which satisfy the four design constraints for the orthogonal TLCDs with a circular cross-section and a rectangular cross-section for the NREL 5-MW TLP OWT. The color bar indicates the area ratio corresponding to the intersection between L and B. It can be seen from the

figure that the feasible region is restricted by the four constraints. The fourth constraint regarding the relationship between the horizontal length and the radius of the vertical column of the SS-TLCD especially limits the feasibility of the design variables. Since the available width of the nacelle (2.5 m) is much smaller than the longitudinal length of the nacelle, the radius of the vertical column ($r_{V_{SS}}$) must be strongly restricted, which results in a narrow feasible area for the design variables. However, the rectangular configuration has a much wider feasible area, made possibly by adjusting the width (b_{SS} = 7 m, in this dissertation) of the cross-section of the vertical column.

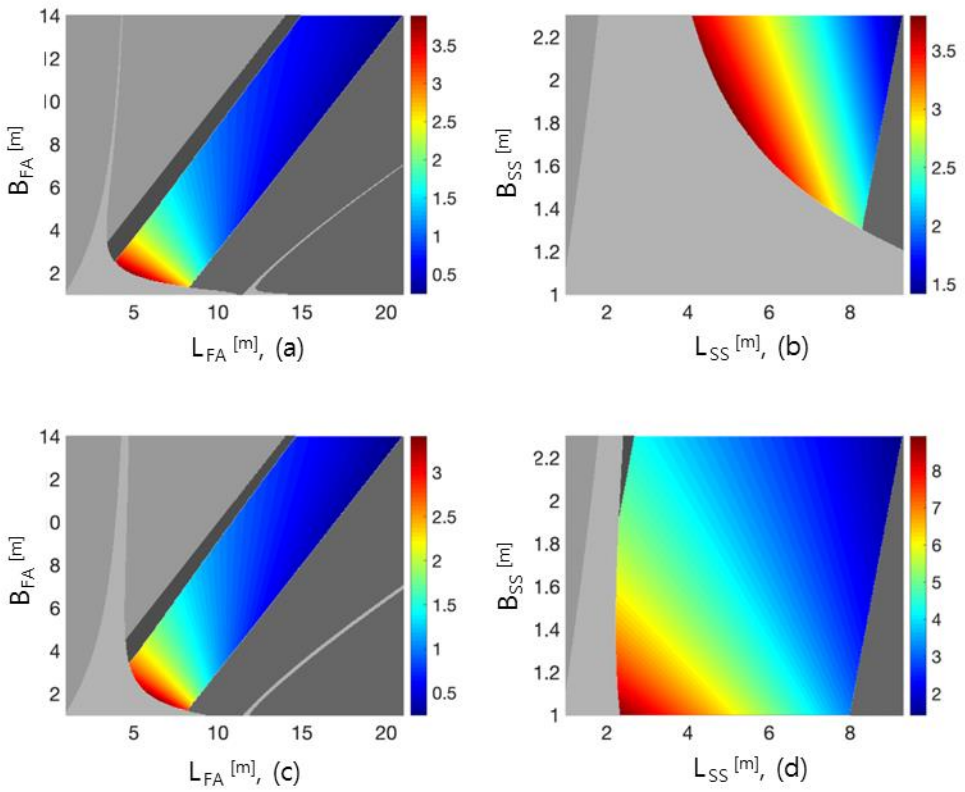

Figure 5.12: Feasible region of design variables for NREL TLP OWT, the color bar represents the area ratio. ■: Constraint 1, ■: Constraint 2 ■: Constraint 3, ■: Constraint 4, (a): FA-TLCD (Circular area), (b): SS-TLCD (Circular area), (c): FA-TLCD (Rectangular area), (d): SS-TLCD (Rectangular area)

For the monopile, the effects of the fourth constraint are not significant in comparison with the TLP OWT, due to higher tuning frequency resulting in shorter effective length L_{ee} as shown in Figure 5.13. A decrease in the effective length leads to a smaller α (See Eq. 5.6), which leads to a decrease in the cross-sectional area of the vertical column (as $A_V = \alpha A_H$). So, the effect of the types of the cross-sectional area on the feasibility of the design variables is relieved with the higher tuning frequency.

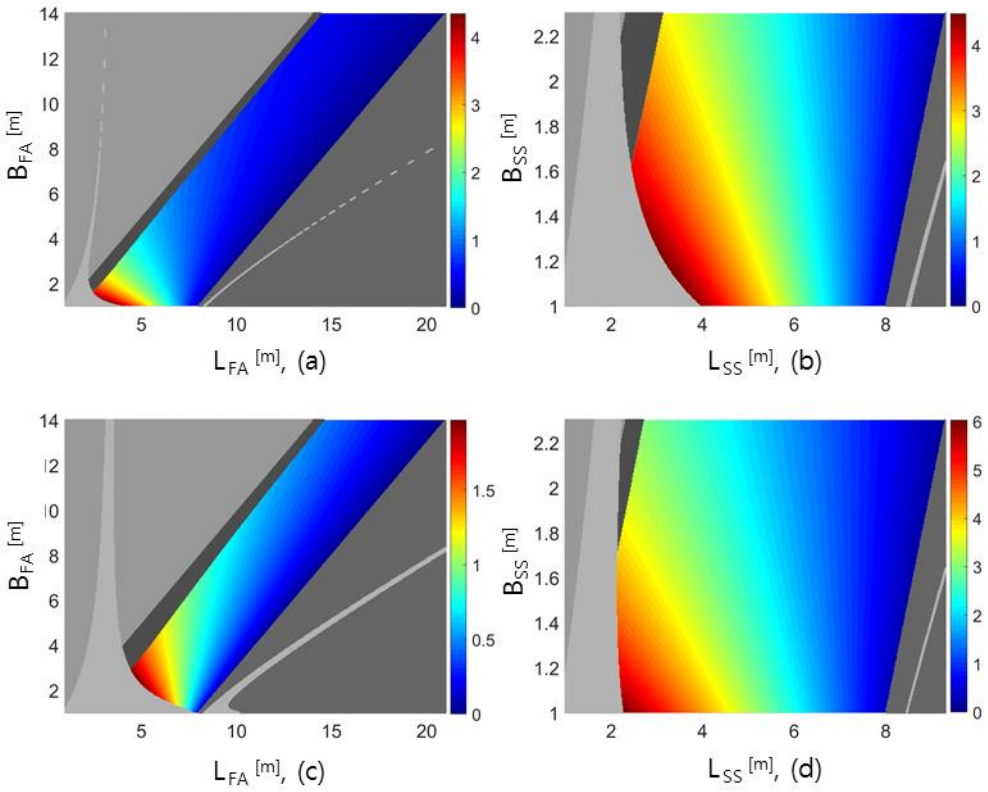

Figure 5.13: Feasible region of design variables for NREL monopile OWT, the color bar represents the area ratio. ■: Constraint 1, ■: Constraint 2 ■: Constraint 3, ■: Constraint 4, (a): FA-TLCD (Circular area), (b): SS-TLCD (Circular area), (c): FA-TLCD (Rectangular area), (d): SS-TLCD (Rectangular area)

Figure 5.14 shows the ratio of the feasible area to the total region according to the mass ratio κ for the NREL TLP OWT. For the SS-TLCD with a circular cross-section, the feasible area ratio converges to zero beyond the mass ratio of 0.05. This means that there are no longer feasible values for design variables L and B that allow the TLCD to be tuned to the tuning frequency of 0.218 Hz, while there are still around 50% possible combinations for the SS-TLCD with the rectangular cross-sectional area.

In order to investigate the control performance of the orthogonal TLCDs within the feasible range of design variables, non-linear fully-coupled aero-hydro-servo-elastic simulations are performed in FASTv8. All possible combinations of the two design variables L and B are utilized as input parameters for the TLCD. Once again, the remaining parameters are determined once L and B are set and the head loss coefficients are constant. This allows both the control performance exerted by each combination as well as the influence of the change of the parameters on the control performance to be examined. Again, the main simulation conditions are the same as those performed in the tower parametric study as shown in Table 5.1. The standard deviation of the tower top displacements in the fore-aft and side-to-side direction are used to evaluate the control performance and is considered as the cost function to be minimized as well. Figure 5.15 shows the surface response (2-D view) of the standard deviations of the tower top displacement of the NREL TLP OWT and the area ratios as a function of every possible combination of L and B. The last constraint in terms of the liquid stroke in Table 5.9 is applied post-simulation in order to exclude the combinations that violate the stroke constraint. The color bars in Figure 5.15 (a) and (c) indicate the standard deviation of the tower top displacement (Fore-aft and Side-to-side), and the color bars in (b) and (d)

indicate the corresponding area ratios. The control performance for the SS-TLCD with the circular cross-section is contained in the region bounded by the gray dotted line. For the FA-TLCD, the TLCDs with both the circular and the rectangular cross section have almost the same feasible region, so there is no indicator to distinguish between the two, unlike the SS-TLCD. For the monopile OWT, the surface response of the standard deviations of the tower top displacement and the area ratios corresponding to the intersection between L and B are shown in Figure 5.16. The boundaries of L and B for a multi-objective optimization problem are selected near a combination of L and B that provides the minimum cost function (standard deviation). Then, the range of the area ratio corresponding to the boundary of L and B is derived.

Based on the results of the reduced ES approach as seen in Figure 7, several important facts can be observed: (i) For the SS-TLCD applied to the floating OWT, the feasible combinations of the SS-TLCD with the circular cross sectional area are strongly limited by the constraint functions, especially the fourth constraint. Therefore, the combinations that provide optimal design variables (in the black dotted box) are infeasible. The SS-TLCD with the rectangular cross-section is able to cope with the geometric constraints better with the longitudinal length of 7 m (b_{SS}) of the cross-section (resulting in the shorter length ($h_{V_{SS}}$)). For the SS-TLCD applied to the fixed-bottom OWT, the feasible combinations of the SS-TLCD with the circular cross-section are almost the same as the SS-TLCD with the rectangular cross-section. This is mainly due to the higher tuning frequency of the fixed-bottom OWT as discussed earlier. (ii) The longer the length ratio of horizontal length (B) to total length (L), the better the control performance even though all the intersections of the design variables have the same

tuning frequency. (iii) The TLCDs with large or small values for the area ratio have the lowest control performance. In addition, for the floating OWT, it can be deduced that the TLCDs with the area ratio larger than 1 have superior control performance. It is obvious that there is an optimum area ratio (see the black dotted box) in the range of 1 to 2 for the FA-TLCD and in the range of 3.8 to 5.5 for the SS-TLCD. Both ranges are moderate and are over 1. (iv) The FA-TLCD with uniform the cross-section ($\alpha = 1$) inevitably increases the size of the device to be tuned to the critical mode, while the TLCD with non-uniform area can be much smaller while keeping the tuning frequency by adjusting α. So, using non-uniform cross-sections for the liquid columns is advantageous not only in terms of control performance, but also in sizing of the TLCD: (v) Based on observations (ii) and (iii), the ranges of the design variables (L and B) can be further narrowed as seen in the black dotted box in Figure 5.15 and 5.16. One of the objectives of the preliminary design is to narrow the boundaries to where there may be a global minimum, which serves as a good guide for the MOO problem using an evolutionary algorithm, which may be solved more efficiently and accurately. The area occupied by the black dotted box is set as the boundary of the design variables for the MOO problem.

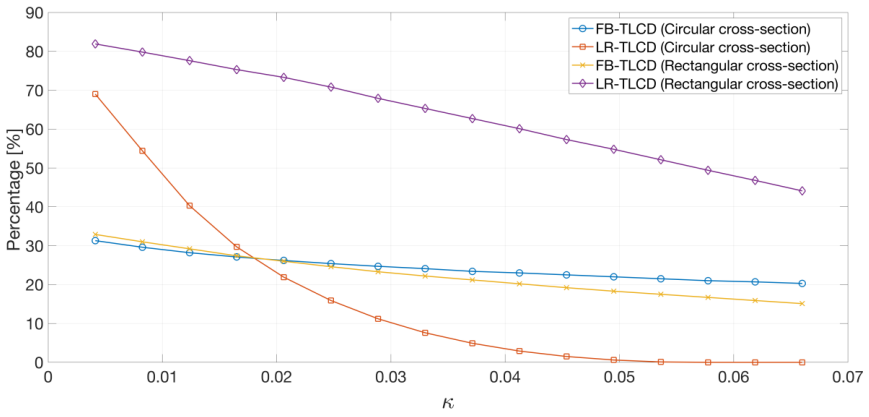

Figure 5.14: The percentage of the feasible area as a function of the mass ratio, κ

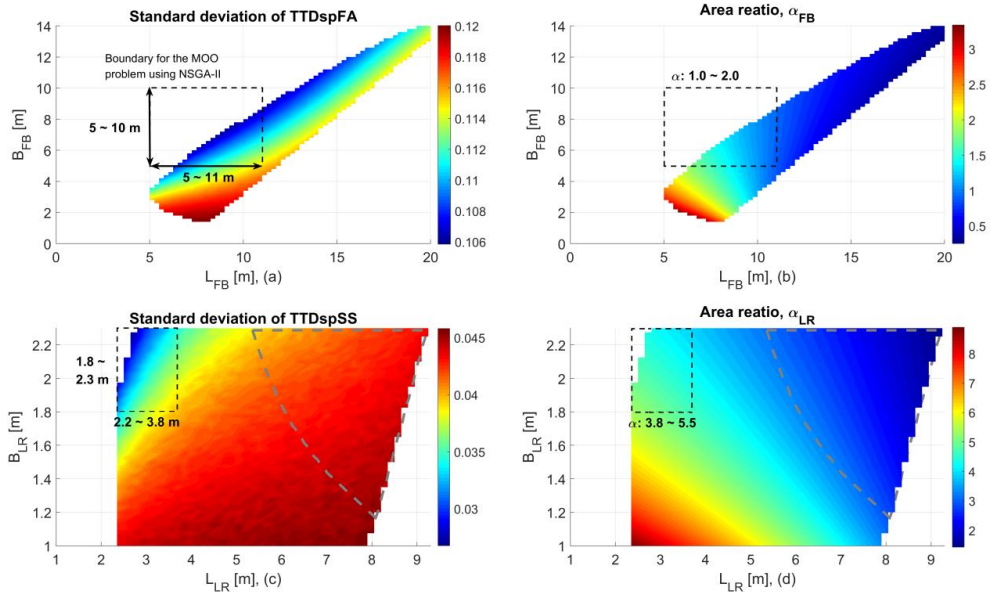

Figure 5.15: Surface response plot as functions of *L* and *B* for the NREL 5-MW TLP (a): Standard deviations of tower top displacement (Fore-aft), (b): Area ratios (FA-TLCD), (c) Standard deviations of tower top displacement (Side-to-side), (d), Area ratios (SS-TLCD)

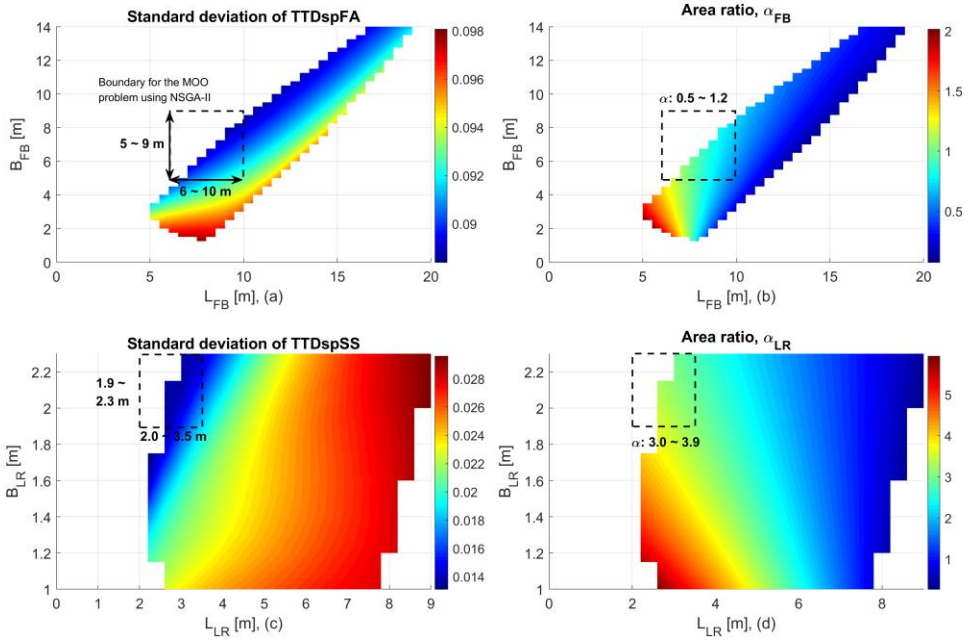

Figure 5.16: Surface response plot as functions of *L* and *B* for the NREL 5-MW monopile (a): Standard deviations of tower top displacement (Fore-aft), (b): Area ratios (FA-TLCD), (c) Standard deviations of tower top displacement (Side-to-side), (d), Area ratios (SS-TLCD)

5.3.2 Multi-Objective Optimization

The aim of the optimization of the orthogonal TLCD is to identify the optimal design variables that minimize the dynamic responses of the wind turbine tower. MOO problems with more than one objective function are capable of finding a set of Pareto-optimal solutions among conflicting objectives rather than accepting a single optimal solution.

The general purpose of the MOO process in this dissertation is to derive a Pareto-optimal front which provides insight for a decision maker considering a trade-off between the two objective functions. Evolutionary algorithms (EA) have been widely adopted for solving numerous MOO problems in a broad spectrum of applications [79, 80, 81], due to its practical advantages over traditional optimization techniques [82]:

- As EAs are global direct searching algorithms, they can be applied to a variety of pr oblems including ones in which the objective function is discontinuous, non-differen tiable and/or highly non-linear.

- Also, the process of evolutionary calculation may be done in parallel at the best indi vidual selection stage. This feature allows the utilization of parallel computing in or der to speed up the processing time by taking advantage of multi-core processing.

The genetic algorithm (GA) is a class of EA, and has been most frequently utilized in MOO problems. With the potential to hybridize with local search methods, GAs have been upgraded in terms of computational efficiency in the last few years [83, 84, 85]. Hedar et al. [83] proposed a simplex coding genetic algorithm (SCGA), which is

achieved by combining a genetic algorithm with a simplex-based local search technique using the Nelder-Mead method. The strength of the local search method in improving initial populations and their children is able to accelerate the GA process. Srinivas et al. [84] proposed a non-dominated sorting genetic algorithm (NSGA), which is mainly characterized by the ability to sort sub-populations into hierarchies based on a Pareto dominance. A fast elitist non-dominated sorting genetic algorithm (NSGA-II), which is an improved version of the classical NSGA, has been proposed by Deb et al in 2002 [85]. They addressed the major issues of NSGA, i.e. high computational complexity of non-dominated sorting and lack of elitism. Three unique features that enable the NSGA-II to be a faster and more efficient algorithm are: (i) the utilization of an elite conserving approach (elitism) with a unique selection operator in order to preserve the excellence of previous generations; (ii) the application of a fast non-dominated sorting approach that significantly reduces computational effort; (iii) the application of a crowding distance operator to maintain population diversity instead of using a sharing parameter.

In this study, NSGA-II is adopted to optimize the parameters of the orthogonal TLCDs. In addition, a parallel computing approach is implemented allowing for faster simulation, since the fully-coupled time marching simulation using FASTv8 is computationally time consuming. The optimization procedure is illustrated in Figure 5.17 and consists of the following steps: 1) Initialize the population randomly in the pre-defined range; 2) Distribute the calls (running FASTv8) to 12 workers and evaluate the objective functions; 3) A non-dominant sorting method ranks the individuals in the population; 4) Create an offspring population using a crowded tournament selection and typical GA operators (crossover and mutation) and evaluate the objective functions: 5)

Replace individuals with the best ones through elitist sorting method for the next generation. The process repeats steps 3 to 5 until the stopping criteria are met, and outputs a non-dominant Pareto front at the end. Important parameters used for running the MOO problem are listed in Table 5.10. The NSGA-II program used in this study is coded by Lin in MATLAB, and is published on MATLAB Central's File Exchange [86]. The program has been further modified in this research so that the program and FASTv8 are coupled and all data exchanges are automatic, and also to take advantage of the parallel computing procedure in the coupled program (NSGA-II with FASTv8). The MATLAB spmd statement is used to assign tasks for each processor.

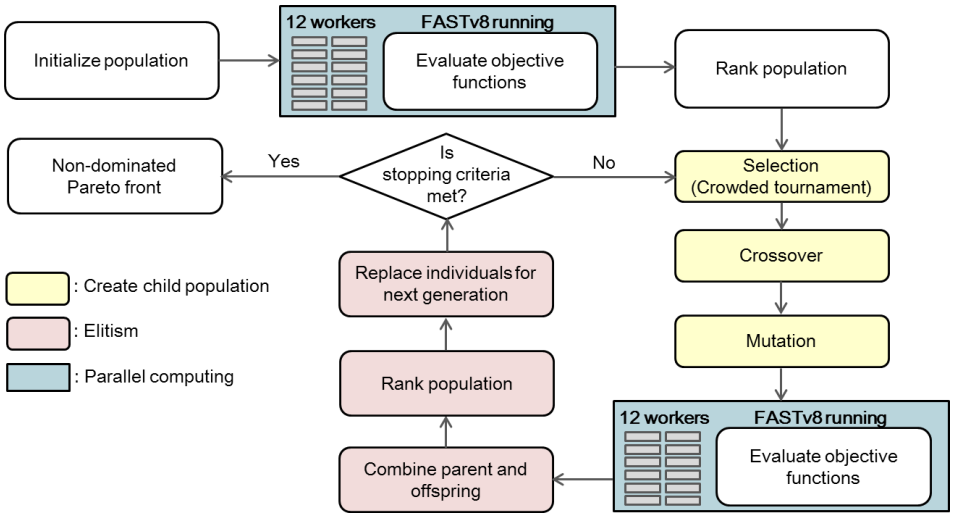

Figure 5.17: Procedure of NSGA-II with parallel computing

Parameter	Value
Maximum generation	150
Population size	50
Crossover operator	Intermediate, ratio = 1.2
Mutation operator	Gaussian, scale = 0.1, shrink = 0.5
Number of workers (parallel computing)	12
Simulator	FASTv8 with structural control module

Table 5.10: Parameter for NSGA-II with parallel computing

In this dissertation, the tower base moment damage equivalent loads (DELs) for both the fore-aft and side-to-side direction are considered as objective functions for the orthogonal TLCD optimization problem.

$$Find\ \vec{\boldsymbol{x}} = [x_1, \dots x_k]\ that\ minimizes \begin{cases} f_1(\vec{\boldsymbol{x}}) \\ f_2(\vec{\boldsymbol{x}}) \end{cases} with\ \vec{\boldsymbol{x}}_{min} \leq \vec{\boldsymbol{x}} \leq \vec{\boldsymbol{x}}_{max} \tag{5.9}$$

where $f_1(\vec{x})$ and $f_2(\vec{x})$ are objective functions, and $\vec{x}$ is an *k*-dimensional vector for design variables with a minimum and a maximum bound. In addition to the lower and upper bounds, the design variables are also restricted by linear and non-linear inequality constraints in this problem:

$$g_i(\vec{\boldsymbol{x}}) \geq 0 \tag{5.10}$$

As discussed in Section 4.1, the simulation conditions are defined in Figure 4.1. The objective functions (tower base moments DELs) are calculated for a turbulent wind field with a rated wind speed of 11.4 m/s. The metocean data corresponding to the bin for the wind speed of 11 to 13 m/s is broken up into 9 bins (bin width of 45 degrees). The expected values of the significant wave heights and the peak spectral periods for each bin of wind/wave misalignment are utilized to create a JONSWAP wave spectrum. A total of 9 simulations for one chromosome are conducted, and then the tower base moments calculated by 9 simulations are weighted by the probabilities for each wind/wave misalignment bin in order to calculate DELs.

The presence of two objective functions yields a set of Pareto-optimal solutions. The solutions that make a set of Pareto-optimal solutions can be retained or even discarded based on the non-dominated sorting concept of the algorithm. The end result of

the continuous sorting process is a global Pareto-optimal front, which is a global non-dominated solution.

There are 9 design variables to be optimized: the total lengths (L_{FA} and L_{SS}), the horizontal lengths (B_{FA} and B_{SS}), the area ratios (α_{FA} and α_{SS}), the head loss coefficients (ξ_{FA} and ξ_{SS}), and the mass ratio (μ) of the SS-TLCD to the FA-TLCD. Table 5.11 and 5.12 list the design variables of each TLCD, and their minimum and maximum values. The dimensions for the variables are bounded as pre-determined values from the preliminary design. The values of the randomly initialized design variables (L, B, and α) will naturally evolve to be tuned near the critical mode of the wind turbine over a number of generations. Additionally, the remaining design variable (ξ) will be adjusted to minimize the objective functions. The last important parameter (A_V), which is not a design variable, can be determined as a function of the other design variables:

$$A_V = \frac{m_{tot}}{\rho\big(B/\alpha + (L-B)\big)} = \frac{m_{tot}}{\rho L_{em}} \tag{5.11}$$

where m_{tot} can be either $m_{FA-TLCD}$ or $m_{SS-TLCD}$. The change of the mass ratio within the specific boundary determines the mass of each TLCD by following the relations:

$$m_{FA-TLCD} + m_{SS-TLCD} = M_{tot} \tag{5.12}$$

$$\mu = \frac{m_{FA-TLCD}}{M_{tot}}, \qquad m_{FA-TLCD} = M_{tot}\mu, \qquad m_{SS-TLCD} = M_{tot}(1-\mu) \tag{5.13}$$

For the constraint function, only the constraint regarding the liquid stroke (constraint 5 in Table 5.9) is applied, as the other constraints have been fulfilled by setting the boundaries that never violate such constraints.

Variables	Description (units)	Min	Max
L_{FA}	Total length of liquid for the FA-TLCD (m)	5.0	11.0
B_{FA}	Horizontal length of liquid for the FA-TLCD (m)	5.0	10.0
α_{FA}	Area ratio of vertical area to horizontal area for the FA-TLCD (-)	1.0	2.0
ξ_{FA}	Coefficient of head loss for the FA-TLCD (-)	0.1	100.0
L_{SS}	Total length of liquid for the SS-TLCD (m)	2.2	3.8
B_{SS}	Horizontal length of liquid for the SS-TLCD (m)	1.8	2.2
α_{SS}	Area ratio of vertical area to horizontal area for the SS-TLCD (-)	3.8	5.5
ξ_{SS}	Coefficient of head loss for the SS-TLCD (-)	0.1	100.0
μ	Mass ratio of the SS-TLCD to the FA-RLCD (-)	0.1	0.9

Table 5.11: Design variables for MOO problem and their boundaries (NREL TLP OWT)

Variables	Description (units)	Min	Max
L_{FA}	Total length of liquid for the FA-TLCD (m)	6.0	10.0
B_{FA}	Horizontal length of liquid for the FA-TLCD (m)	5.0	9.0
α_{FA}	Area ratio of vertical area to horizontal area for the FA-TLCD (-)	0.5	1.2
ξ_{FA}	Coefficient of head loss for the FA-TLCD (-)	0.1	100.0
L_{SS}	Total length of liquid for the SS-TLCD (m)	2.0	3.5
B_{SS}	Horizontal length of liquid for the SS-TLCD (m)	1.9	2.3
α_{SS}	Area ratio of vertical area to horizontal area for the SS-TLCD (-)	3.0	3.9
ξ_{SS}	Coefficient of head loss for the SS-TLCD (-)	0.1	100.0
μ	Mass ratio of the SS-TLCD to the FA-RLCD (-)	0.1	0.9

Table 5.12: Design variables for MOO problem and their boundaries (NREL monopile OWT)

5.3.3 Analysis of MOO Results

It is meaningless to focus on improving one of two objectives that are in conflict in MOO problems. So, a trade-off between two objectives is inevitable in most MOO problems. The trade-off plays a critical role in the formation of Pareto optimal fronts. In

this section, two objectives calculated by FASTv8 are presented and a Pareto optimal front is derived. When there is a trade-off between two objectives, it is also important to determine the main factors that cause a trade-off.

When it comes to the influence of the design variables on the control performance (or objective functions), the design variables, L, B, α, and ξ for one of the orthogonal TLCDs, have little effect on the other TLCD's performance. For example, changes of these variables for the FA-TLCD have little impact on the control performance of the SS-TLCD, although the FA-TLCD generates inertial forces in the y-direction, i.e. ${F_y}^{W_{Fv}} - {F_y}^{W_{Bv}}$. In contrast, the design variable μ has a significant impact on the control performance of both TLCDs. In general, the mass of a structural control device has a significant influence on the control performance. It has been confirmed that a larger mass has the better control performance within the practical range [87, 88]. Therefore, it can be a major factor influencing conflicting objective functions, i.e. while one objective function decreases, the other one increases according to the mass ratio. It is clear from Figure 5.18 (a) and Figure 5.19 (a) that the Pareto curve mainly depends on the mass ratio rather than on the other design variables, given the fact that final individuals for the mass ratio have a fairly broad distribution while the other variables converge to a certain value (to be tuned to the critical mode). An increase in the mass ratio μ decreases in objective 1, whereas objective 2 decreases as μ decreases as $m_{SS-TLCD} = M_{tot}(1-\mu)$.

There are two more meaningful observations to be made: (i) A randomly distributed population at the first generation eventually evolves to form the Pareto optimal front over a number of generations. It can be seen from the result that the design variables L, B and α converge to certain ranges so that the TLCDs can be tuned to a

certain range of the critical mode (platform pitch and roll mode) for the best performance. It is proven that the tower vibrations are mainly governed by the platform pitch and roll mode, given the fact that the TLCDs are eventually tuned to such modes through the evolutionary process: (ii) The optimal tuning frequency increases as the mass of the TLCD increases as seen in Figure 5.20 (a). In addition, increasing the mass ratio shows a tendency to increase the head loss coefficient as seen in Figure 5.20 (b). This strongly agrees with the theoretical formulation used in the preliminary design, as the head loss coefficient is proportional to the mass ratio. Through the Pareto optimal front, one can make a decision depending on given conditions or specific needs. Among variable designs on the Pareto optimal front, three designs are selected and are displayed as green solid circles in Figure 9 (a). Table 5.13 shows the properties of the TLCD parameters for the three selected designs. In Chapter 6, the designs will be utilized to investigate the impact of the orthogonal TLCDs in terms of fatigue and extreme loads reduction.

NREL TLP	μ	L_{FA}	B_{FA}	$A_{V_{FA}}$	α_{FA}	ξ_{FA}	f_{opt}^{FA}	L_{SS}	B_{SS}	$A_{V_{SS}}$	α_{ss}	ξ_{ss}	f_{opt}^{SS}
Case 1	0.41	6.91	5.98	1.77	1.61	1.5	0.981	3.29	2.39	7.65	3.72	1.6	0.975
Case 2	0.60	6.83	5.89	2.67	1.66	1.9	0.974	3.23	2.31	5.23	3.79	1.1	0.981
Case 3	0.74	6.80	5.97	3.38	1.68	2.3	0.968	3.16	2.29	3.53	3.81	0.8	0.985
NREL monopile	μ	L_{FA}	B_{FA}	$A_{V_{FA}}$	α_{FA}	ξ_{FA}	f_{opt}^{FA}	L_{SS}	B_{SS}	$A_{V_{SS}}$	α_{ss}	ξ_{ss}	f_{opt}^{SS}
Case 1	0.55	7.94	6.57	1.28	0.91	1.1	0.967	3.37	1.97	4.47	3.21	1.1	0.972
Case 2	0.75	7.93	6.57	1.76	0.92	1.3	0.960	3.39	1.98	2.47	3.24	0.9	0.966
Case 3	0.87	7.93	6.59	2.05	0.93	1.6	0.956	3.40	2.01	1.29	3.25	0.8	0.959

Table 5.13: Parameters of selected designs

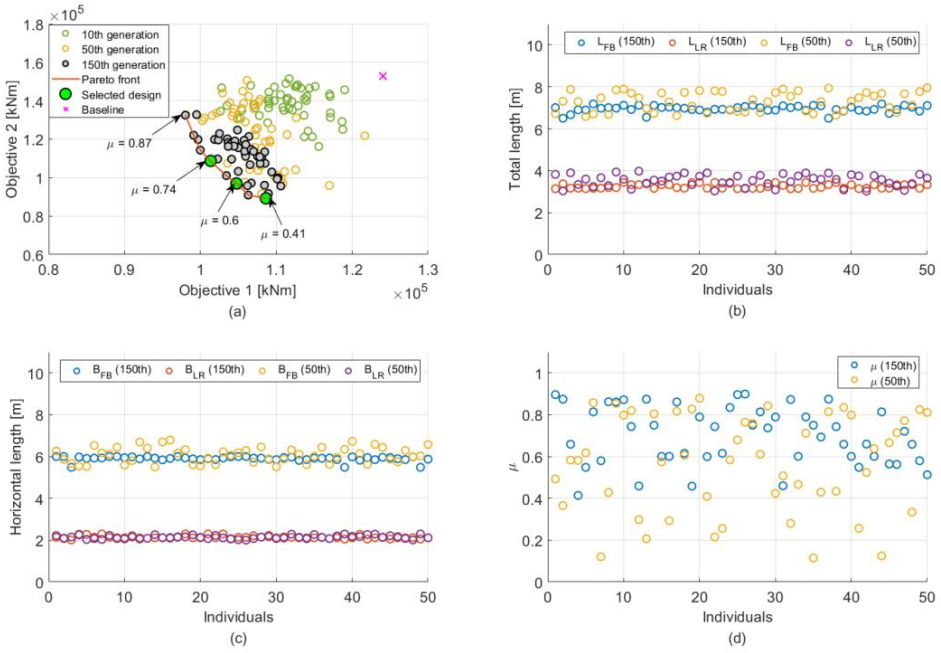

Figure 5.18: Multi-objective optimization result for the NREL TLP OWT, (a): optimal Pareto front, (b): total length L, (c): horizontal length B, (d): mass ratio μ

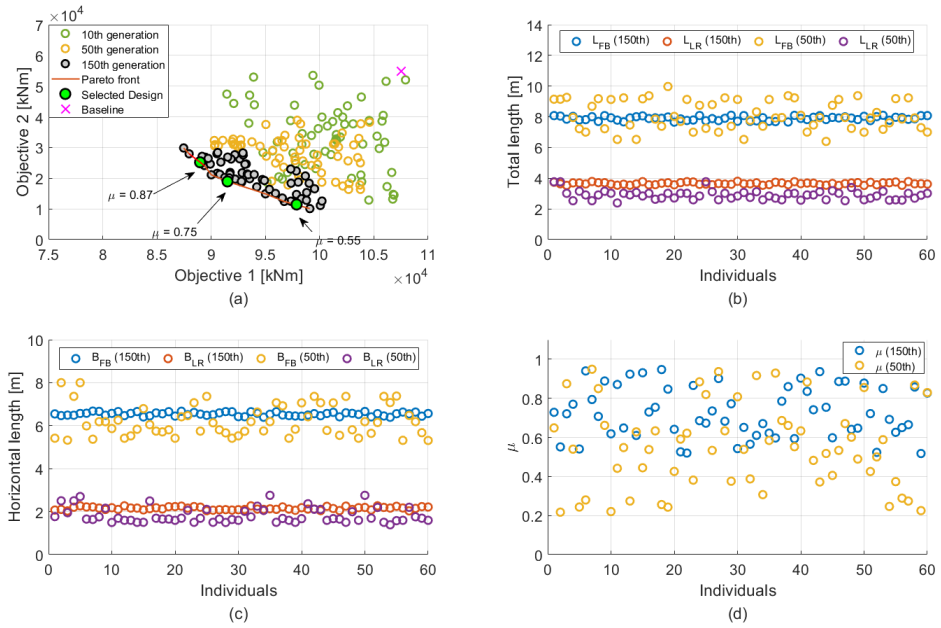

Figure 5.19: Multi-objective optimization result for the NREL monopile OWT, (a): optimal Pareto front, (b): total length L, (c): horizontal length B, (d): mass ratio μ

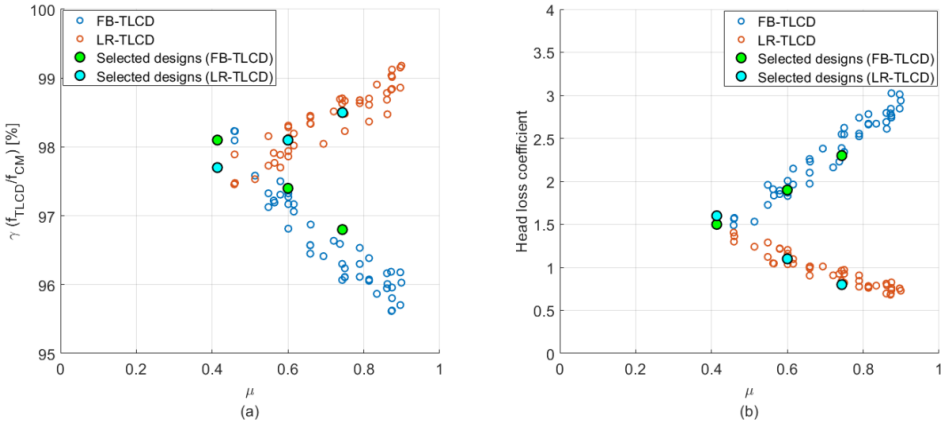

Figure 5.20: Frequency ratio and head loss coefficient of the TLCDs as a function of the mass ratio (NREL TLP OWT)

5.4 Semi-Active Control for a Tower TMD

A semi-active TMD is an attractive compromise to overcome drawbacks of a passive TMD and an active TMD, because it has the potential to change the stiffness and/or damping characteristics of a TMD during an operation. In this dissertation, the main semi-active control strategy is to control damping characteristics through ground hook (GH) control policies. In order to realize the damping control, magnetorheological (MR) dampers are utilized as a damping component of the TMD. This section disccuses the modeling of magnetorheological dampers and introduces three different ground hook control algorithms and their inherent dynamic characteristics. The contents of this chapter have been published in *Wind Energy* [66].

5.4.1 Modeling of Magnetorheological Damper

In S-A structural controls, damping coefficients of a semi-active TMD can be changed dynamically to improve control performance relative to a passive system. In this

dissertation, an "on-off" state damping control approach is used, in which the damping can take on either a large (on-state) or small (off-state) value in real time. More details of the on-off damping control based on the ground hook control algorithm are presented in Section 5.4.2. Ideally, a controllable linear damper could be used for simulations, in which the damping constant C can be controlled and the damping force at any instant is proportional to a relative velocity between a TMD and a main structure, as shown in Eq. (5.14).

$$f_{damping,linear} = Cv \tag{5.14}$$

In practice, however, no such device exists that has both a controllable damping constant and a linear behavior. Instead, a magnetorheological (MR) damper can be used. The MR damper is a device filled with magnetorheological particles that can transform the fluid state by rearranging the particles through exposure to a magnetic field with low power consumption. This controllable fluid state enables the damping force to be controlled [89]. Thus, it may be utilized to implement S-A control in practice. The main purpose of analyzing the ideal linear damper is to quantify the damping forces (for the on-off state) required for specific offshore wind turbines used in this dissertation. The required damping forces are determined based on the parametric study results (Section 4.1) and by considering practical limitations of the MR damper. With the damping force capacity, the parameters of the MR damper can be specified so that the MR damper device has an equivalent force capacity of the ideal linear damper.

The phenomenological MR damper model (Figure 5.21 (b)) represents the non-linear dynamic behavior of the MR damper. This phenomenological model was modified

by Spencer et al. [90], based on the Bouc-Wen model to address the nonlinear hysteretic characteristic of an MR damper, such as a roll-off phenomenon. The equations of motion of this model can be expressed as follows:

$$c_1\dot{y} = \alpha z + k_0(x_r - y) + c_0(\dot{x}_r - \dot{y}) \tag{5.15}$$

$$\dot{z} = -\gamma|(\dot{x}_r - \dot{y})| \cdot |z|^{n-1} \cdot z - \beta(\dot{x}_r - \dot{y}) \cdot |z|^n + A(\dot{x}_r - \dot{y}) \tag{5.16}$$

$$F_{MRD} = c_1\dot{y} + k_1(x_r - x_0) \tag{5.17}$$

Table 5.14 shows the parameters of the modified Bouc-Wen model and descriptions. These parameters define the capacity of the MR damper, and affect the non-linearity and the hysteretic characteristic of the MR damper.

Parameters	Description
x_r	Relative damper displacement ($X - x_{tmd}$)
y	Damper internal pseudodisplacement
z	Damper hysteretic displacement
k_1	Accumulator stiffness
c_0	Damping constant
c_1	Damping constant for roll-off effect
k_0	Damper Stiffness
a	Evolutionary coefficient
β	Shaping parameter for hysteresis curve
γ	Shaping parameter for hysteresis curve
n	Shaping parameter for hysteresis curve
A	Shaping parameter for hysteresis curve

Table 5.14: Parameters of the modified Bouc-Wen model

To calculate the damping force (F_{MRD}), the TMD motion (x_r) is used as an input for the simultaneous first order differential equations (Eqs. (5.15) to (5.17)). A fourth order Runge-Kutta numerical method is utilized to solve them in the structural control module. There are ten parameters (x_0, k_0, k_1, c_0, c_1, α, n, β, A, γ) to be identified in order to characterize the dynamic behavior of the MR damper. Previous research conducted by Kwok et al. [91] has shown that these MR damper parameters can be identified by the

Particle Swarm Optimization (PSO) method. Furthermore, Jiang and Christenson [92] identified the Bouc-Wen model's parameters for a 200 *kN* MR damper (manufactured by the Load Corporation) as 4th order polynomials as a function of the input current through a curve fitting approach. Based on the Bouc-Wen model parameters derived by Jiang and Christenson [92], the 4th order polynomials are further modified in this dissertation so that the MR damper has an equivalent maximum force capacity as the ideal linear damper and the desired stroke of $\pm$ 0.8 m. The five parameters, including k_0, k_1, c_0, c_1 and α that affect the maximum force capacity and the damper stroke are modified in order to fit the force capacity and the stroke. The other five parameters, including $x_{0,}$ n, β, A and γ were retained to preserve the hysteretic characteristic. The identified polynomials are expressed as a function of the input current (i), and the corresponding values according to the on/off state are given in Table 5.15. The last two columns in Table 5.15 present an example showing the values of each parameter when a specific current is applied (on-state: 2.5 A, off-state: 0 A).

Polynomials	Unit	on-state (i =2.5)	off-state (i =0)
$x_0 = -0.00002i^4 + 0.00042i^3 - 0.00303i^2 + 0.0001i + 0.16546$	m	0.15	0.17
$k_0 = -0.17750i^4 + 5.62900i^3 - 58.386i^2 + 212.8725i + 5.00000$	N/m	253.3	5.0
$k_1 = -0.00600i^4 + 0.02000i^3 - 4.6232i^2 - 37.8995i + 151.974$	N/m	75.4	152.0
$c_0 = -2.1115i^4 + 71..4415i^3 - 853.662i^2 + 3683.724i + 5721.69$	Ns/m	10816.9	5721.7
$c_1 = 406.5i^4 - 31431.3i^3 + 149354.6i^2 - 628354.4i + 1461147.9$	Ns/m	629745.2	1461147.9
$\alpha = -2.7855 + 98.206i^3 - 1202.969i^2 + 5924.812i + 380.089$	N/m	9099.2	380.1
$\beta = 0.003050i^4 - 0.06645i^3 + 0.11760i^2 + 4.40618i + 10.0259$	m^2	20.9	10.0
$\gamma = 0.103060i^4 - 3.11188i^3 + 29.16298i^2 - 78.4398i + 1016.2$	m^2	957.8	1016.2
$n = -0.00171i^4 + 0.05751i^3 - 0.65493i^2 + 2.84594i + 2.18467$	-	6.0	2.2
$A = -0.14775i^4 + 4.43947i^3 - 41.6389i^2 + 116.949i + 551.210$	-	646.9	551.2

Table 5.15: MR damper parameters as a function of input current i

A single degree of freedom (SDOF) structural model with an attached TMD, subjected to a sinusoidal excitation, is considered in order to compare the force capacity between the linear damper, and the MR damper using the identified parameters. The magnitude and the frequency of the sinusoidal excitation are chosen so that the TMD oscillates within the maximum displacement range ($\pm$ 0.8m) and the desired frequency. Figure 5.21 (a) and (b) show the diagram of the SDOF-TMD system using the linear damper (a), and the MR damper (b). Table 5.16 shows the two damping constants for the linear damper, and the corresponding input current for the MR damper that can produce an equivalent force of the linear damper.

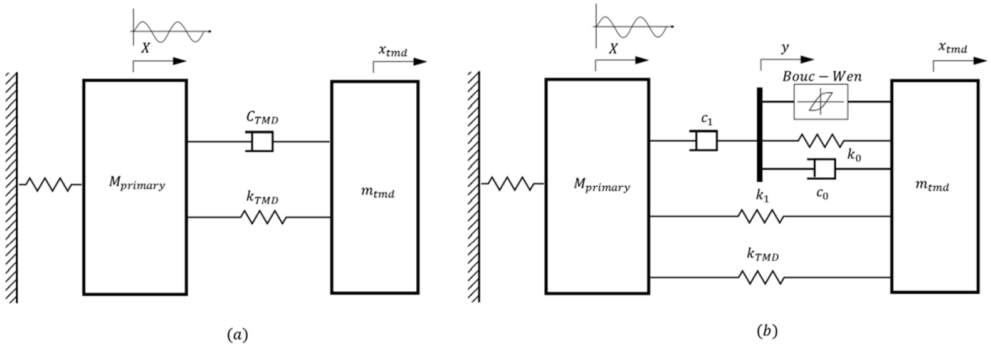

Figure 5.21: SDOF-TMD model (a) linear damper; (b) MR damper

OWT models	Damper Type	Off-state	On-state
NREL monopile	Linear damper	5720 Ns/m (ζ_{min} = 10 %)	19670 Ns/m (ζ_{max} = 30 %)
	MR damper	0 Ampere	4.0 Ampere
NREL TLP	Linear damper	5720 Ns/m (ζ_{min} = 10 %)	14470 Ns/m (ζ_{max} = 27 %)
	MR damper	0 Ampere	1.4 Ampere
GE monopile	Linear damper	5720 Ns/m (ζ_{min} = 10 %)	17900 Ns/m (ζ_{max} = 30 %)
	MR damper	0 Ampere	2.5 Ampere
GE TLP	Linear damper	5720 Ns/m (ζ_{min} = 10 %)	14921 Ns/m (ζ_{max} = 26 %)
	MR damper	0 Ampere	1.5 Ampere

Table 5.16: Damping coefficients and equivalent input currents for different OWTs

In the first case, the MR damper force using an input current of 0 Ampere can match the force-displacement, force-velocity behavior and the maximum force capacity ($\approx 7\ kN$) of the linear damper. This force capacity (using 0 Ampere) of the MR damper is used for the passive control (damping ratio of ζ =10%), and the off-state damping force for the S-A control. In the second case, the on-state MR damper has an equivalent maximum force capacity to the linear damper with the damping ratio of three times larger than the optimal damping ratio. Kang et al. [93] evaluated the impact of the on-off S-A control by applying two different on-state damping ratios. The transmissibility of the S-A TMD with a larger on-state damping ratio showed significant decreases in two peaks (outside the resonance region) while maintaining a comparable performance to the S-A TMD using a lower on-state damping ratio in the resonance region. However, there are practical limitations to the value of the on-state damping [93, 94]. As such, the on-state damping force (ζ=30%) is limited to three times the optimal damping force in this dissertation. Although the force-velocity behaviors between the two dampers are slightly different due to the inherent nonlinear hysteretic characteristic of the MR damper in the lower velocity region (as shown in Figure 5.22), the maximum force capacity of the MR damper using the identified parameters has shown satisfactory agreement with that of the linear damper. Thus, applying 0 and 4.0 Ampere for the off and on states, respectively, allows the MR damper to achieve the desired damping ratio (10% and 30%) of the TMD for passive and S-A control for the different OWTs. Figure 5.23 shows the damping forces of the MR damper for the different OWTs. The identified input currents to produce a minimum and a maximum damping force are utilized to implement several semi-active ground hook control algorithms for a load analysis of OWTs in Chapter 6.

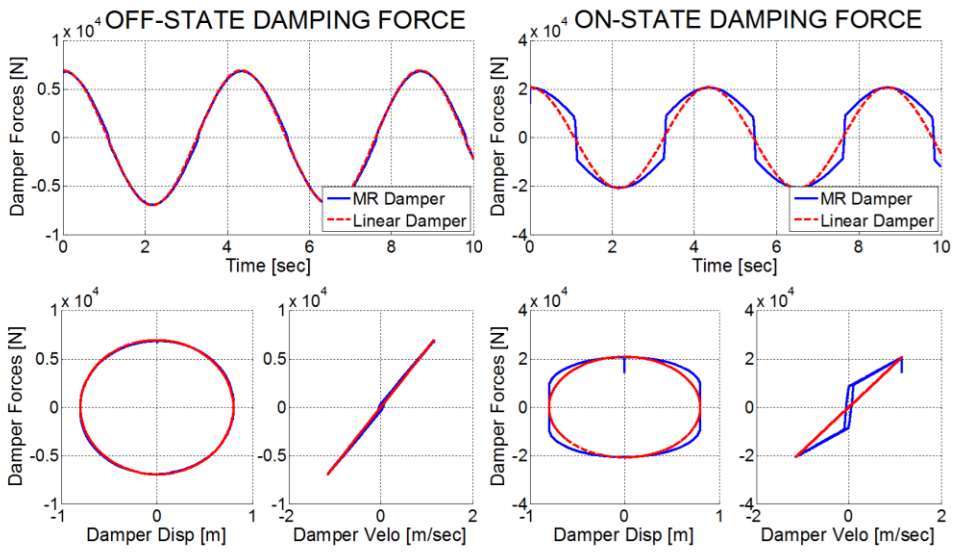

Figure 5.22: Comparison of force capacity between the linear damper and MR damper

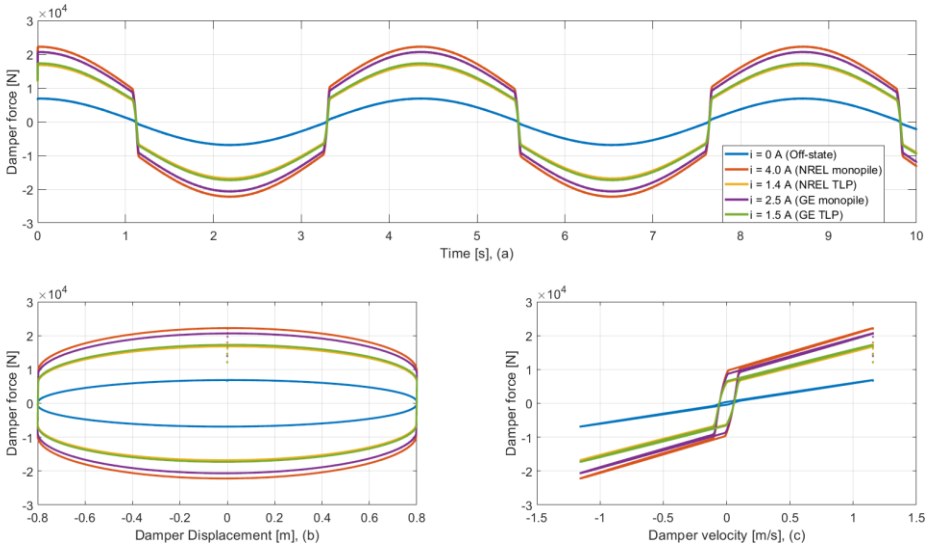

Figure 5.23: Damping forces versus time, damper displacement and velocity for the different OWTs

5.4.2 Ground Hook Control Algorithms

A variety of control algorithms based on a ground hook (GH) strategy for a semi-active TMD are explored in this dissertation. The majority of research in this area has utilized reduced order state space models with limited degree of freedoms for a wind turbine and control systems, such as the translational shear mode, TMD motion, two lowest tower modes, and platform pitch mode (for OWT application) [95, 96]. Lin et al. [97] and Ji et al. [98] utilized S-A TMDs using an optimal clipped control law based on the active control forces that are derived from the basis of optimal Linear Quadratic Regulator (LQR) control algorithms. They have shown that the S-A TMD can have comparable performance to active control even at lower power consumption. Kim and Kang have proposed an optimal fuzzy control law using a multi-objective generic algorithm, and compared the performance with a ground hook (GH) control algorithm [99]. As demonstrated, they have established a set of Pareto optimal solutions according to a trade-off between the TMD stroke and the dynamic response. This scheme, although using a reduced order model, requires a large computational time to determine the optimal solutions of the fuzzy controller, but it has the advantage of satisfying both the desired performance requirements and the TMD stroke constraints. Without considering TMD stroke constraints, however, the results demonstrated that the GH control can be the most promising approach compared to the optimal fuzzy control solutions.

GH control, which is a kind of sub-optimal control, has the advantage that it can be easily implemented based on feedback from the structure; therefore, it has been widely used for real-time structural control without the need to determine the state space model of the system. This research focuses on GH control, instead of optimal control, as

it provides superior performance in terms of reducing the dynamic response, and considers the tradeoff between the TMD stroke and the dynamic response. The rationale is that the TMD stroke can be properly regulated by the combination of the regulation spring and the elastomeric stop-spring as shown in Figure 3.1.

The command input current of the MR damper can be switched between a minimum and a maximum level, which are determined by following control policies based on the absolute motion of the primary structure and the relative velocity or displacement between the TMD and the tower motion. The formulation of the displacement based ground-hook (DB-GH) control policy is as follows.

$$x_{TTD}\dot{x}_{TMD} \leq 0 \quad Then \quad F_{MRD} = F_{MRD}(i_{on}) \; (ON\ state\ damping\ force) \tag{5.18}$$

$$x_{TTD}\dot{x}_{TMD} > 0 \quad Then \quad F_{MRD} = F_{MRD}\left(i_{off}\right) \; (OFF\ state\ damping\ force) \tag{5.19}$$

x_{TTD} is the tower top displacement, and $\dot{x}_{TMD}$ is the relative velocity between the TMD and the tower top. In civil engineering, the translational displacements of wind-induced high-rise buildings can be derived by laser displacement sensors and accelerometers. Park et al. [100] presented an approach using Global Positioning System (GPS) to monitor the horizontal and torsional displacements of the structure. The results from GPS based monitoring showed that the measurements are very consistent with actual displacements measured by laser displacement sensors. Thus, the tower top displacement can also be measured by installing high-precision GPS on the tower top where the TMD systems operate for real applications. The velocity based ground-hook (VB-GH), and the inverse velocity based ground-hook (IVB-GH) control policies depend on the absolute velocity of the tower. The VB-GH policy is formulated as follows:

$$\dot{x}_{TTD}\dot{x}_{TMD} \leq 0 \quad Then \quad F_{MRD} = F_{MRD}(i_{on})\ (ON\ state\ damping\ force) \tag{5.20}$$

$$\dot{x}_{TTD}\dot{x}_{TMD} > 0 \quad Then\ F_{MRD} = F_{MRD}(i_{off})\ (OFF\ state\ damping\ force) \tag{5.21}$$

The IVB-GH control can be achieved with the opposite logic of the VB-GH control, so the opposite command input current would be generated as shown in Figure 7. The tower motion (green line in Figure 5.24) can be represented by two states: moving toward its equilibrium (M.T.E in Figure 5.24), or moving away from its equilibrium (M.A.E in Figure 5.24). The damper can be in one of two possible states, compression ($\dot{x}_{TMD} > 0$) or tension ($\dot{x}_{TMD} < 0$). Referring to Figure 5.24, the IVB-GH logic leads to on-state damping forces when the tower is in the "M.A.E" state. When the tower is moving away from equilibrium (M.A.E), and the damper is in the compression state, the maximum input current (on-state) is required to stabilize the tower. After that, when the tower is moving back toward the equilibrium (M.T.E), the minimum damping force (off-state) is applied, because the damper is still in the state of compression, which generates a destabilizing force on the tower. Unlike the IVB-GH logic, the VB-GH logic leads to on-state damping forces when the tower is in the "M.T.E" state. When the tower is moving back toward the equilibrium (M.T.E) and the damper is in the tension state, the maximum damping force (on-state) stabilizes the tower, while the off-state damping is applied when the tower is moving away from its equilibrium (M.A.E). Taken together, the main differences between the two methods are: 1) The IVB-GH inhibits the "M.A.E" motion by applying the maximum opposite force generated by the MR damper. 2) The VB-GH facilitates the "M.T.E" motion by using the maximum force in the same direction of the tower motion. Such differences cause distinct frequency responses.

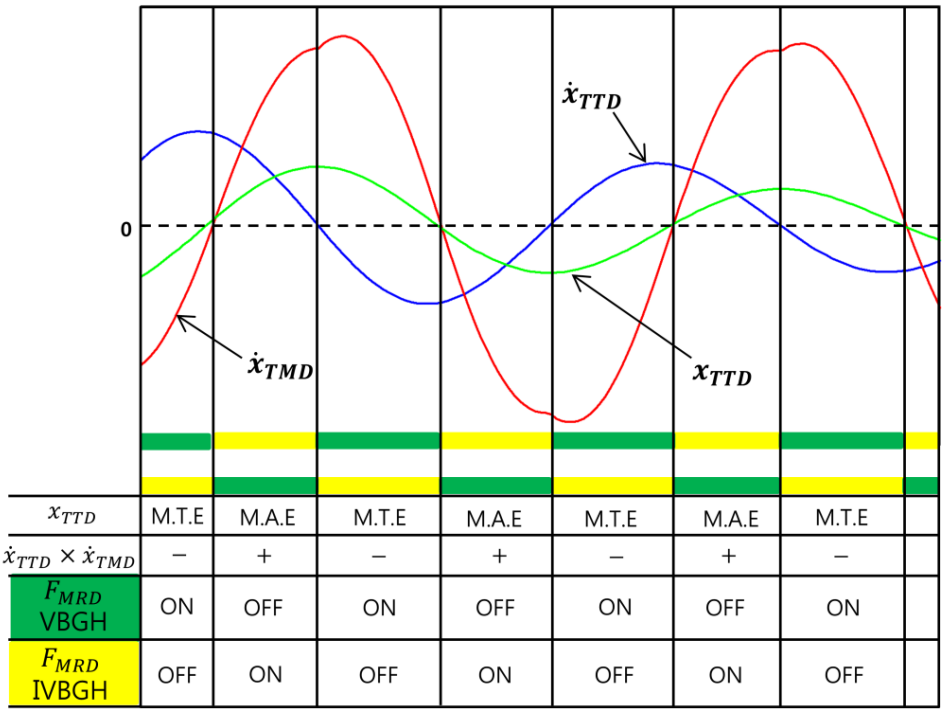

x_{TTD}	M.T.E	M.A.E	M.T.E	M.A.E	M.T.E	M.A.E	M.T.E	
$\dot{x}_{TTD} \times \dot{x}_{TMD}$	−	+	−	+	−	+	−	
F_{MRD} VBGH	ON	OFF	ON	OFF	ON	OFF	ON	
F_{MRD} IVBGH	OFF	ON	OFF	ON	OFF	ON	OFF	

Figure 5.24: Ground hook control strategy

A preliminary investigation on the impact of the passive tower-TMD and the S-A tower-TMD, which follow the GH control algorithms, is conducted by simulating an initial perturbation analysis in FASTv8. The turbine models used to investigate the effects of the S-A tower-TMD are GE Haliade 6-MW PelaStar TLP. For the S-A tower-TMD, the stiffness and mass of the tower-TMD are identical to the passive tower-TMD determined in Section 4.1, and the input current to operate the MR damper is listed in Table 5.16. Figure 5.25 indicates the frequency response of the tower top motion for the baseline with no tower-TMD, passive, and S-A tower-TMDs. The range of effectiveness for each method varies depending on the frequency. The VB-GH control policy has the largest impact compared to the other approaches in the higher frequency region (0.24 ~ 0.28 Hz). In contrast to the VB-GH approach, the power density of the tower top motion can be reduced significantly through the IVB-GH approach in the low frequency region

(0.2 ~ 0.24 Hz) [101]. Because the dominant loading caused by waves is mostly distributed in the low frequency range, the IVB-GH control algorithm is expected to be the most promising method compared to other GH approaches when wave loading is the major contributor to the tower response, such as an extreme sea state.

In the case of the DB-GH (yellow line in Figure 5.25), the power in the frequency range of 0.18-0.28 Hz gradually decreases without any evident peaks. This characteristic is likely to make the DB-GH approach more effective during normal operation where the wave input with the lower frequency component is relatively weak. Because the various TMDs are tuned for the 1st tower eigenmode or the critical mode of the entire system, implementation of a high-pass filter to filter out wave excitation at low frequencies is a possibility. While this study did not implement any filtering of the control input signals, it is a topic for future work.

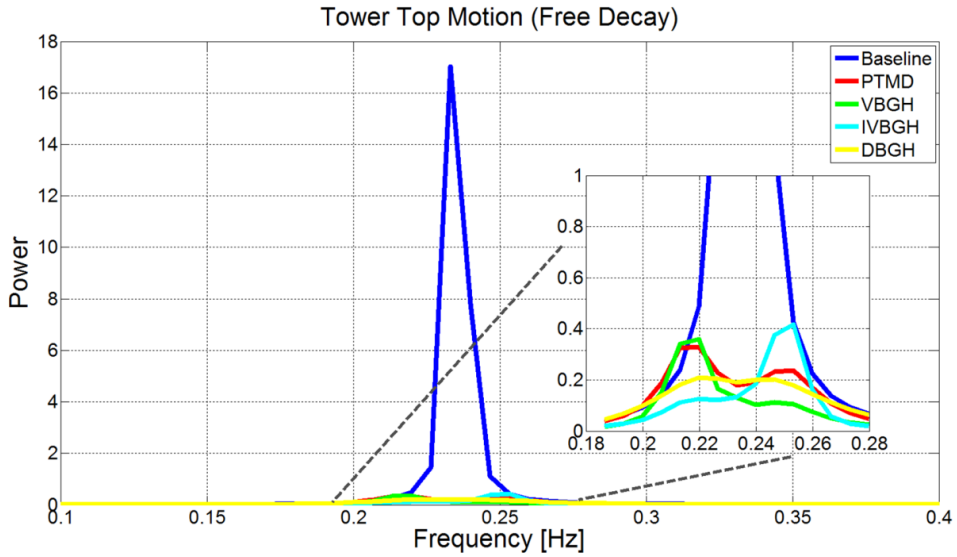

Figure 5.25: Power spectral density of the tower top motion for each control scheme

CHAPTER 6

LOAD ANALYSIS AND SIMULATION RESULTS

This chapter describes the impacts of various structural control techniques on reducing fatigue and extreme loads of OWTs. Rigorous loads analysis is performed using FASTv8 with a structural control module by running a series of DLCs. For fatigue analysis, a number of simulations with DLC 1.2 are conducted in the case of turbines with and without the structural control devices. Fatigue behavior can in most cases be a design driver of wind turbines. DLC 1.2 is one of the key DLCs which can evaluate lifetime fatigue loads of wind turbines under normal operation. DLC 6.2 (parked rotor) is utilized to determine extreme loads of the turbines. The combination of extreme wind and waves in DLC 6.2 induces significant structural responses that may cause failure of the system. The other DLCs including abnormal events such as fault of grid, failure of control system and emergency stop have not been considered in this dissertation. Further details are provided in the following section. The contents of this chapter regarding the tower-TMD for GE Haliade 6-MW OWTs have been published in Wind Energy [66]. The results for the nacelle-TLCDs is now prepared for publication [67]

6.1 Tower Response Control

This section presents the simulation results regarding the impacts of the passive tower-TMD and nacelle-TLCDs as well as the S-A tower-TMD in terms of load reductions under extreme and normal operation conditions. The tower-TMD is mounted on top of the tower to improve the system responses of the turbine tower. The tower-

TMDs operate both passively and semi-actively, and the optimal parameters for the passive control determined in Chapter 5 are utilized. Note that only the DB-GH and IVB-GH approaches are emphasized for the fatigue and extreme analysis, respectively. The other approaches were found to be less effective, which was expected based on the preliminary investigation discussed in Chapter 5. The nacelle-TLCDs are mounted inside the nacelle and operate passively. The three optimal designs of the nacelle-TLCDs determined in Chapter 5 are utilized for this analysis. The control performance of each control device is compared with the baseline system. It should also be noted that in all cases the inclusion of the TMDs and TLCDs has negligible impacts on the behavior of the baseline variable speed and the collective pitch control system.

6.1.1 Fatigue Load Analysis for NREL 5-MW OWTs

A fatigue load analysis is performed in order to quantify the improvements of wind turbine structural reliability by employing the tower-TMDs (passive and semi-active ways) and the nacelle-TLCDs (passive only). The turbine models used in this analysis are the NREL 5-MW monopile OWT and TLP OWT. The conditions of the original DLC 1.2 recommend by IEC 61400-3 are further modified to consider the full range of wind/wave misalignments (β). Taking into account the full range of misalignments allows for more rigorous fatigue load analysis, as the frequency of occurrence of substantial wind/wave misalignments (more than 90 degrees) is not negligible, especially below rated wind speed (See Figure 4.2). For horizontal axis wind turbines (HAWTs), the aerodynamic damping from the rotating rotor affects the tower fore-aft motion and provides substantial damping effects on the tower fore-aft motion

during power production. While the fore-aft motion has substantial aerodynamic damping, the side-to-side motion is poorly damped. The lack of aerodynamic damping in the side-to-side direction may result in larger loads in this direction, which are exacerbated when wind and waves are misaligned. Thus, reducing the side-to-side motion is expected to play a critical role in reducing fatigue loads. The main purpose of using the expanded DLC 1.2 is to examine the overall effects of β on fatigue loads. The simulation conditions determined in Chapter 4 are utilized to create a set of conditions for the expanded DLC 1.2, and are listed in Table B.1 in Appendix B. With the tower top forces and the tower base moments calculated by FASTv8, the lifetime damage equivalent loads (DELs) expected over the lifetime (25 years) of the turbine are estimated based on a rain flow counting algorithm with Whöler exponents (m = 2, 3 and 4) for welded steel plates [102]. The relationship between cycles to failure and load range can be expressed as [64]:

$$N = \left(\frac{L^{ult} - |L^{MF}|}{0.5L^{RF}}\right)^{m} \tag{6.1}$$

where $N(\cdot)$ is the number of cycles to failure, L^{ult} is the ultimate load of the component, L^{MF} is the fixed load-mean L^{RF} is the cycle's load range, and m is Whöler exponent.

The joint probability distribution (See Figure 4.2 and Table B.2) is applied to adjust weights for the loads according to the frequency of occurrence. The total number of simulations for all cases is listed in Table 6.1. The simulation length is 10 minutes. The performance indicators are the lifetime damage equivalent moments and forces at the tower base and top in the fore-aft (TwrBsMyt and TwrTopFxt) and the side-to-side directions (TwrBsMxt and TwrTopFyt). These indicators are compared to the baseline

with no structural control devices to present the reduction rates of the damage equivalent loads.

OWTs	Case	Number of simulatons
NREL/TLP	Baseline	11 wind bins × 24 wind/wave misalignments × 3 random seeds =792
	Passive Tower-TMD	792
	S-A Tower-TMD	792
	Nacelle-TLCD case 1	792
	Nacelle-TLCD case 2	792
	Nacelle-TLCD case 3	792
NREL/Monopile	Baseline	11 wind bins × 24 wind/wave misalignments × 3 random seeds =792
	Passive Tower-TMD	792
	S-A Tower-TMD	792
	Nacelle-TLCD case 1	792
	Nacelle-TLCD case 2	792
	Nacelle-TLCD case 3	792

Table 6.1: The number of simulations for each case

6.1.1.1 Monopile OWTs

Table 6.2 shows the results of the fatigue load analysis for the fixed-bottom OWT. Although structural control can effectively reduce the tower fore-aft and side-to-side motion, the control effect on the fore-aft direction is lower than on the side-to-side direction. Since there is a considerable aerodynamic damping acting on the fore-aft motion, the load reduction effect by structural control is inevitably reduced. In contrast, the lack of aerodynamic damping in the side-to-side direction offers a significant potential to reduce side-to-side motion. Since the conditions of DLC 1.2 include the wind/wave misalignments, the turbine motion in the side-to-side direction would significantly increase when wind and waves are misaligned, even if the turbine is exactly aligned with the inflow wind direction. Figure 6.1 shows the normalized standard deviation of the tower top motions for the baseline case according to β.

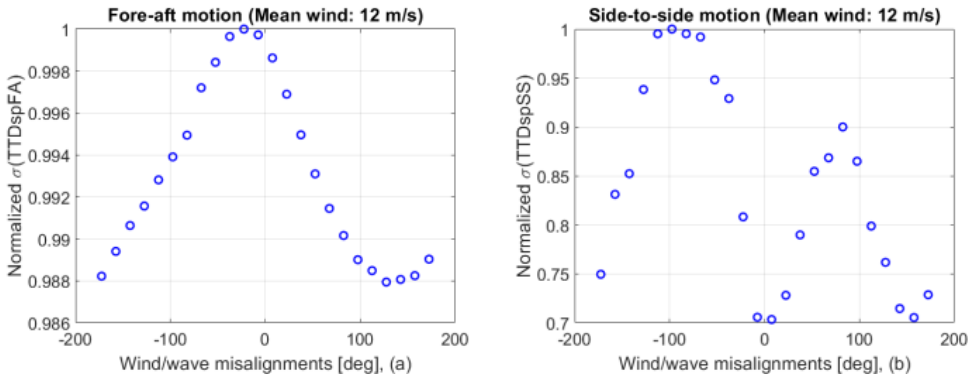

Figure 6.1: Standard deviation of tower top displacement as a function of wind/wave misalignment

It is clear from Figure 6.1 that the tower fore-aft motion reaches a maximum when the wind and wave are aligned, because the hydrodynamic loading caused by waves coincide with the fore-aft direction, which further increases the excitation in the fore-aft direction. However, the difference between the maximum and the minimum value is very small (less than 1.2%). In other words, the effect of β on the tower fore-aft motion is negligible. This is because, as explained above, the excitation by waves in the fore-aft direction can be sufficiently damped out by the substantial aerodynamic damping acting on the fore-aft tower motion. In contrast, the side-to-side motion is maximized when β is 90 degrees because the hydrodynamic loadings are aligned with the tower side-to-side direction. In addition, the difference between the maximum and the minimum value is significant (about 30%). The change in system response according to the external conditions can also be seen from the time response plot as shown in Figure 6.2. Again, the effect of β on the fore-aft direction is negligible, but the effect on the side-to-side direction is significant.

Case	Evaluation index	m = 2	m = 3	m = 4
Passive Tower-TMD	Lifetime DELs TwrBsMyt	19.9 %	15.7 %	14.0 %
	Lifetime DELs TwrBsMxt	77.2 %	76.1 %	75.0 %
	Lifetime DELs TwrTopFxt	18.6 %	14.8 %	13.2 %
	Lifetime DELs TwrTopFyt	72.6 %	73.5 %	72.9 %
S-A Tower-TMD (DB-GH)	Lifetime DELs TwrBsMyt	23.1 %	18.5 %	16.5 %
	Lifetime DELs TwrBsMxt	80.3 %	79.3 %	78.4 %
	Lifetime DELs TwrTopFxt	22.1 %	17.6 %	15.6 %
	Lifetime DELs TwrTopFyt	75.9 %	76.9 %	76.4 %
Nacelle TLCDs Case 1 (μ=0.55)	Lifetime DELs TwrBsMyt	12.1 %	10.5 %	10.0 %
	Lifetime DELs TwrBsMxt	53.6 %	50.4 %	47.8 %
	Lifetime DELs TwrTopFxt	11.8 %	9.9 %	9.2 %
	Lifetime DELs TwrTopFyt	52.2 %	50.1 %	47.1 %
Nacelle TLCDs Case 2 (μ=0.75)	Lifetime DELs TwrBsMyt	13.5 %	11.6 %	10.9 %
	Lifetime DELs TwrBsMxt	48.6 %	45.9 %	43.3 %
	Lifetime DELs TwrTopFxt	13.0 %	10.9 %	9.9 %
	Lifetime DELs TwrTopFyt	47.7 %	45.3 %	42.1 %
Nacelle TLCDs Case 3 (μ=0.87)	Lifetime DELs TwrBsMyt	14.7 %	12.5 %	11.7 %
	Lifetime DELs TwrBsMxt	43.3 %	41.0 %	40.1 %
	Lifetime DELs TwrTopFxt	14.3 %	11.8 %	10.9 %
	Lifetime DELs TwrTopFyt	42.9 %	40.1 %	38.6 %

Table 6.2: Simulation results for the fatigue loads analysis for the fixed-bottom OWT

In addition to the potential of load reduction in the side-to-side direction due to insufficient aerodynamic damping, this result also clearly demonstrates that the potential to reduce the side-to-side motion using structural control is much greater than that for the

fore-aft motion. This has been confirmed by the fatigue load analysis that shows the significant ability of structural control to improve the side-to-side loads of the OWTs. It is also interesting to see that the trade-off between the control performance for each direction (fore-aft and side-to-side) clearly depends on the mass ratio μ between the FA-TLCD and the SS-TLCD. The fact that the mass ratio is the most important parameter to form the Pareto front curve is confirmed again through this analysis. Even though the total mass of TMD and TLCD is the same 20000 kg, the total mass of TLCD is shared by FA-TLCD and SS-TLCD. For example, the FA-TLCD controlling the tower fore-aft motion has a mass of 11,000 kg, which is approximately half of the TMD mass. That is, a reduction in performance is inevitable due to a low mass ratio. Figure 6.3 shows the TMD excursions for the fixed-bottom OWT. It can be seen that the TMD vibrates within the stroke limits in most cases.

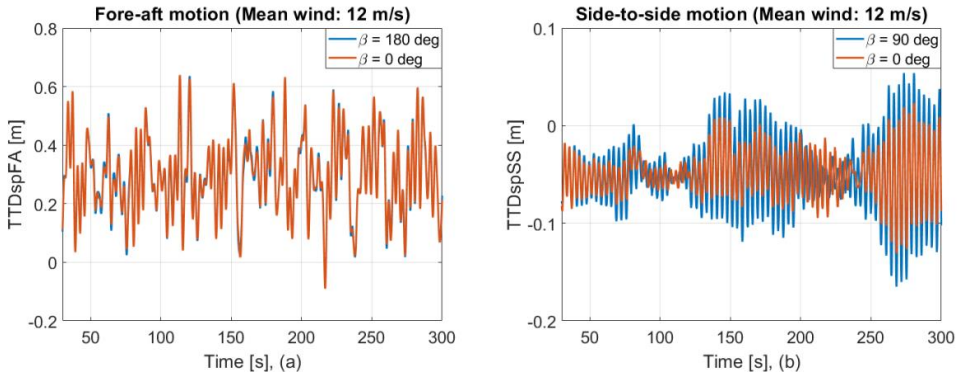

Figure 6.2: Time response of the tower top motion as a function of β, (a): tower top displacement in the fore-aft direction, (b): tower top displacement in the side-to-side direction

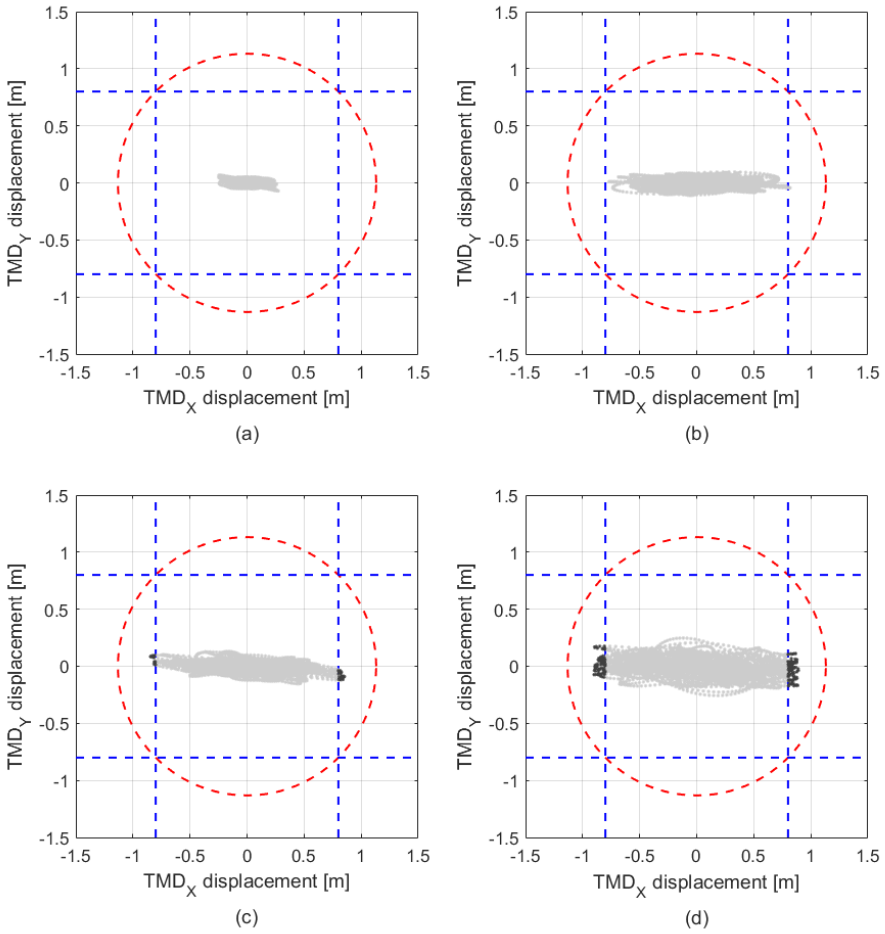

Figure 6.3: TMD excursion in all directions for the fixed-bottom OWT, (a) mean wind speed of 6 m/s, (b) mean win speed of 10 m/s, (c) mean wind speed of 14 m/s, (d) mean win speed of 18 m/s

Figure 6.4 shows the surface plot (2-D view) of the liquid strokes as functions of U and β. The color bar indicates the ratio of the maximum liquid stroke to the height of the vertical column ($(L-B)/2$). The liquid strokes are smaller than the height of the vertical column in all regions, and range from 0.18 to 0.55. For the FA-TLCD, the magnitude of the peak motion of liquid increases with the increased wind speed

regardless of the wind/wave misalignment. For the SS-TLCD, the liquid motion reaches the maximum with the highest wind speed and when the wind and waves are misaligned by 90 degrees.

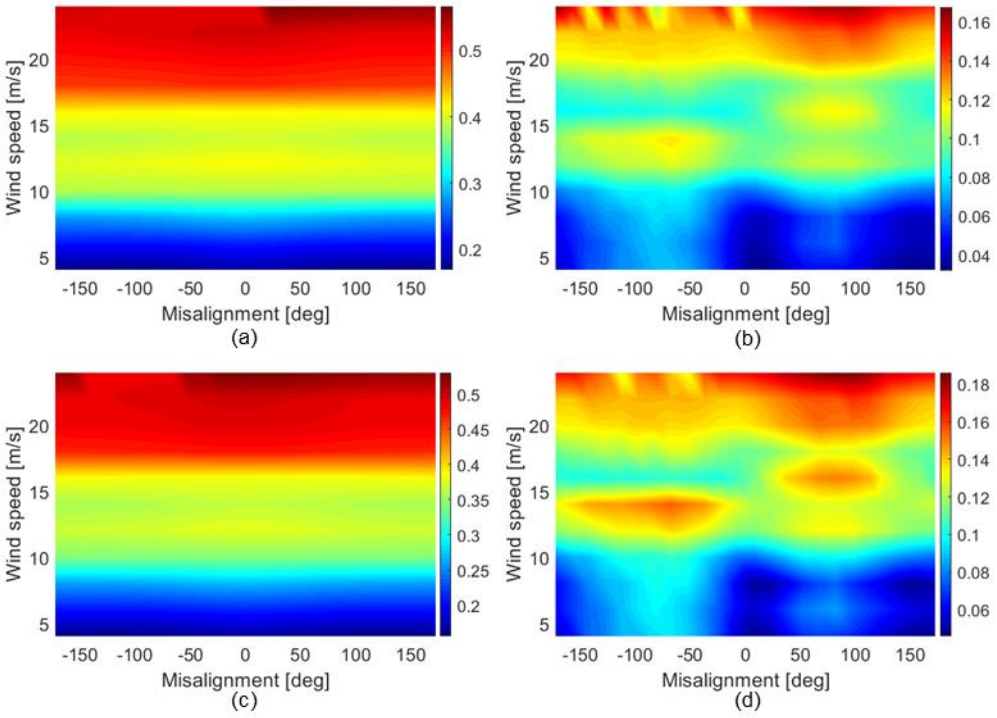

Figure 6.4: Surface plot of the liquid displacement for the NREL monopile OWT, (a): FA-TLCD for case 3, (b): SS-TLCD for case 3, (c): FA-TLCD for case 1, (d): SS-TLCD for case 1

6.1.1.2 TLP OWTs

Table 6.3 shows the simulation results of the fatigue load analysis for the floating OWT.

Case	Evaluation index	m = 2	m = 3	m = 4
Passive Tower-TMD	Lifetime DELs TwrBsMyt	4.2 %	2.0 %	0.8 %
	Lifetime DELs TwrBsMxt	35.6 %	32.1 %	30.1 %
	Lifetime DELs TwrTopFxt	6.9 %	4.9 %	3.7 %
	Lifetime DELs TwrTopFyt	38.5 %	35.5 %	33.6 %
S-A Tower-TMD (DB-GH)	Lifetime DELs TwrBsMyt	6.9 %	4.4 %	3.0 %
	Lifetime DELs TwrBsMxt	37.5 %	34.1 %	31.9 %
	Lifetime DELs TwrTopFxt	8.5 %	6.3 %	4.8 %
	Lifetime DELs TwrTopFyt	39.2 %	36.5 %	34.5 %
Nacelle TLCDs Case 1 (μ=0.41)	Lifetime DELs TwrBsMyt	12.2 %	11.0 %	10.3 %
	Lifetime DELs TwrBsMxt	32.1 %	30.3 %	29.0 %
	Lifetime DELs TwrTopFxt	11.1 %	9.7 %	8.7 %
	Lifetime DELs TwrTopFyt	31.9 %	30.3 %	29.1 %
Nacelle TLCDs Case 2 (μ=0.60)	Lifetime DELs TwrBsMyt	13.1 %	12.3 %	11.3 %
	Lifetime DELs TwrBsMxt	22.6 %	22.0 %	21.6 %
	Lifetime DELs TwrTopFxt	12.7 %	10.9 %	9.9 %
	Lifetime DELs TwrTopFyt	22.7 %	22.3 %	22.1 %
Nacelle TLCDs Case 3 (μ=0.74)	Lifetime DELs TwrBsMyt	13.8 %	13.2 %	12.7 %
	Lifetime DELs TwrBsMxt	17.6 %	16.6 %	15.3 %
	Lifetime DELs TwrTopFxt	13.5 %	12.1 %	10.7 %
	Lifetime DELs TwrTopFyt	18.7 %	18.4 %	17.9 %

Table 6.3: Simulation results for the fatigue loads analysis for the floating OWT

Again, the numbers in Table 6.3 represent the reduction rates of the lifetime DELs compared to the baseline system. The results differ distinctly from the simulation results of the fatigue load analysis for the fixed-bottom OWT. The control effect of

reducing the lifetime DELs of the floating OWT are still present. However, the overall control performances of each device are significantly reduced. In particular, the tower-TMDs are much less effective in reducing the DELs in the fore-aft direction in comparison with the fixed-bottom OWT. This can be explained as follows: the floating substructure pitches and rolls more severely by the waves than the fixed-bottom OWT which is firmly embedded in the sea-bed. Unlike the case where there is a distinct peak near the tower critical mode in the frequency response for the fixed-bottom OWT, the frequency response for the floating OWT not only shows a peak near the tower critical mode, but also shows a large energy distribution in the lower frequency region due to the waves, as shown in Figure 6.5.

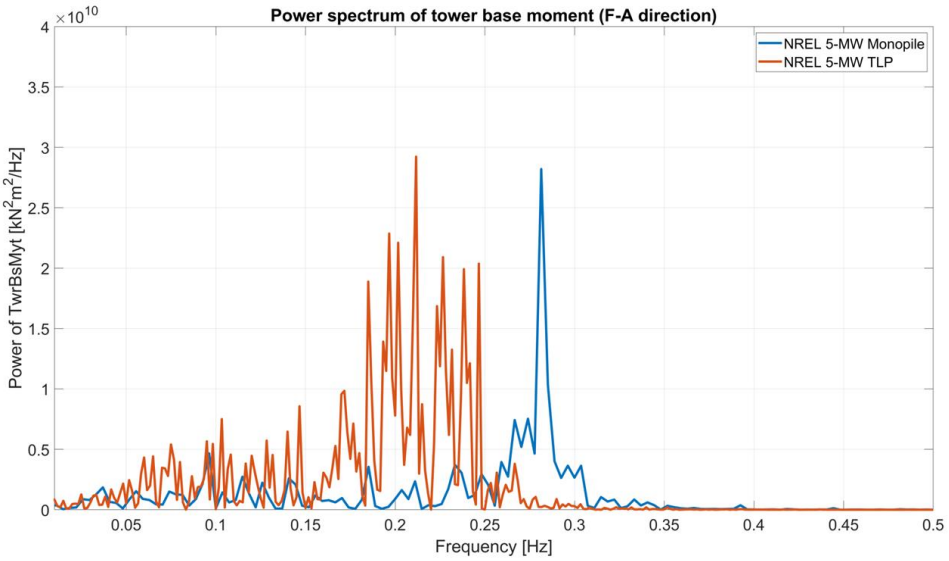

Figure 6.5: Frequency response of the tower motion for the fixed-bottom and the floating OWTs

This means that the tower response is combined with the critical mode and the lower frequency components with the strong intensity. This not only causes issue of de-

tuning the TMD, but also significantly increases the TMD stroke, which results in more stop-spring actions (See Figure 3.1). This physical system can be realized by using a non-linear spring force curve from a user-input table in the input file (See Appendix D). As a result, a strong spring force caused by the stop-spring affects the TMD tuning frequency and also is transferred to the tower system, which deteriorates the control performance of the TMD, as shown in Figure 6.6 and 6.7. The black dotted lines indicate the position where the stop-spring starts to operate. From the time response plots, one can see that the action of the stop-spring is able to maintain the TMD stroke, but it has a negative effect on the tower response in both the fore-aft and the side-to-side directions. This negative effect can also be seen in the frequency response plot as shown in Figure 6.8. The operation of the stop-spring drastically increases the tuning frequency of the TMD, which causes a larger amplitude of the first peak in the frequency response.

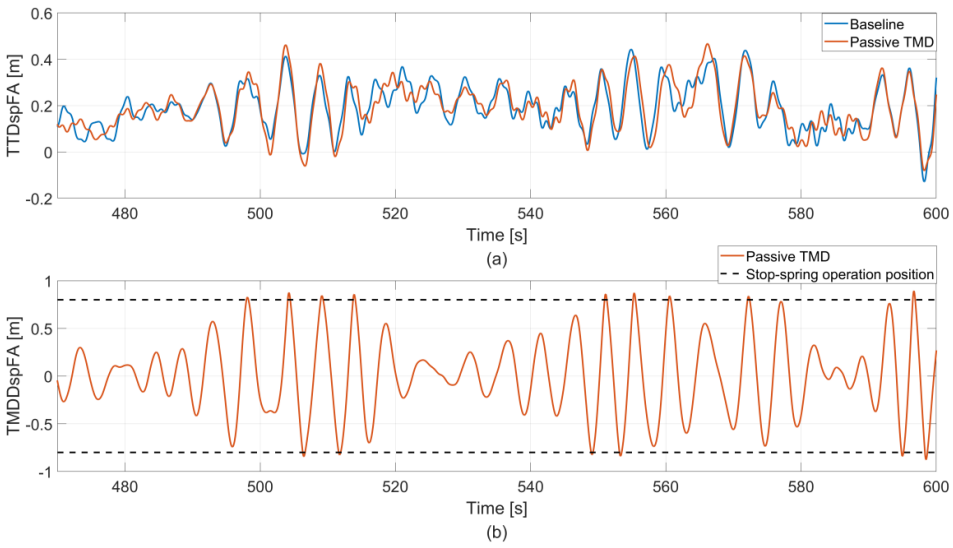

Figure 6.6: Time series, (a): tower top displacement (fore-aft) (b): TMD displacement (fore-aft)

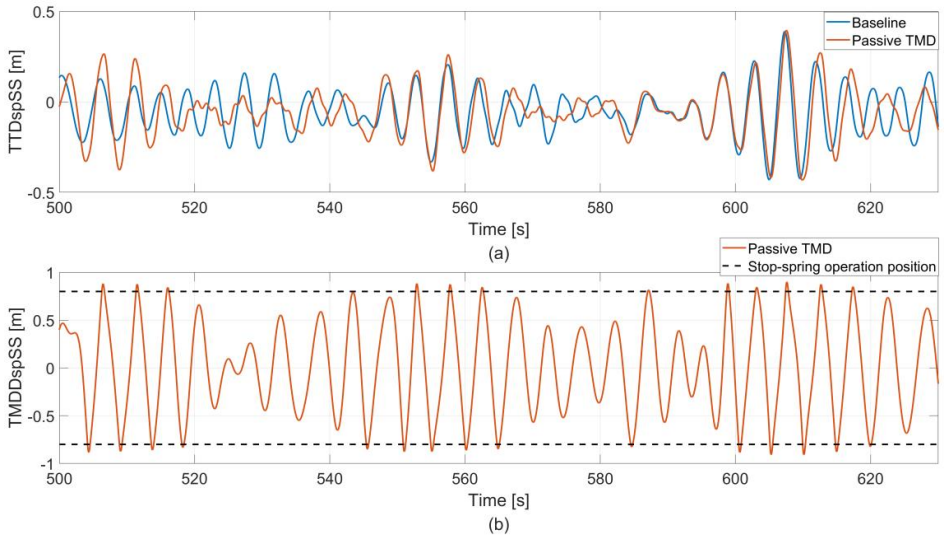

Figure 6.7: Time series, (a): tower top displacement (StS) (b): TMD displacement (StS)

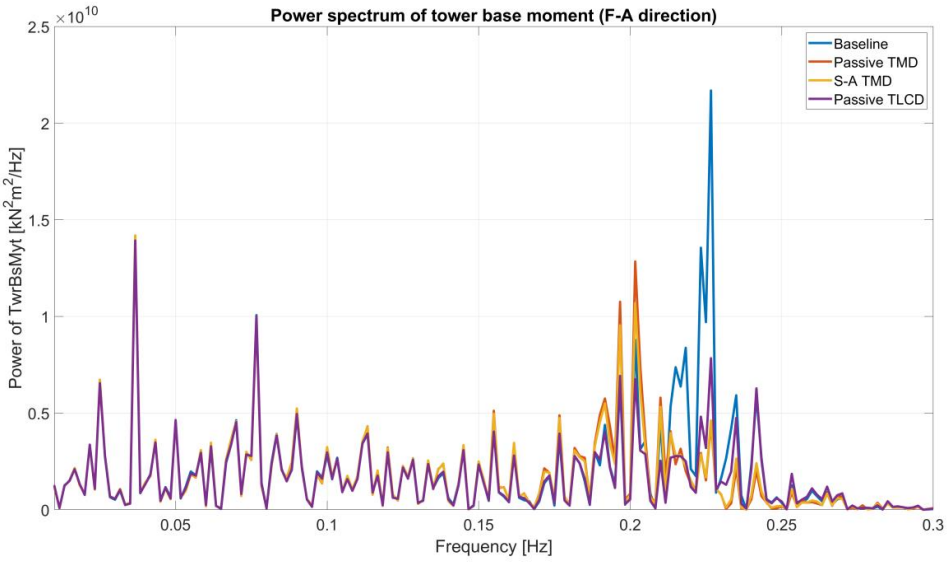

Figure 6.8: Frequency response of the tower base moment in the fore-aft direction

In general, the increase in the tuning frequency response results in a sharp increase in the height of the first peak among the two peaks of the system equipped with

the TMD in the frequency response. Figure 6.9 shows the probability that the stop-spring acts during the entire duration and Figure 6.10 shows the TMD excursions for the floating OWT. It can be seen that more stop-spring action is required to maintain the stroke limit of the TMD for the floating OWT in comparison with the fixed-bottom OWT.

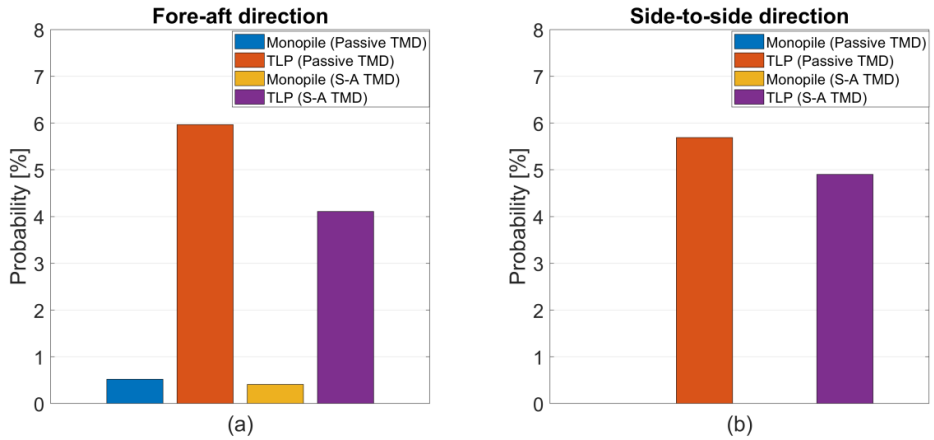

Figure 6.9: Probability of the stop spring operation during the entire simulations

The TLCDs still face the de-tuning issue due to the wave excitation with the low frequency components, but unlike the TMD, there is no need for an additional element, like the stop-spring of the TMD, to limit the stroke of the liquid that causes a negative effect. Also, the stroke of the liquid inside the column of the TLCD never exceeds the stroke limits, as shown in Figure 6.10. The surface plot shows the liquid strokes of the TLCDs as functions of the mean wind speed and the wind/wave misalignment. The color bar indicates the ratio of the maximum liquid stroke to the height of the vertical column. For the FA-TLCD, the liquid oscillates more when wind and waves are aligned, and it is amplified as the wind speed increases. The opposite trends for the SS-TLCD can be seen. The overall liquid strokes are smaller than the height of the vertical column in all regions,

and range from 0.1 to 0.6. As the constraint function regarding the liquid stroke is considered during the optimization process, the liquid stroke does not exceed the stroke limits. Consequently, well-designed TLCDs that deal with both the control performance and the stroke during the optimization process are more promising than the optimal TMD for the floating OWT.

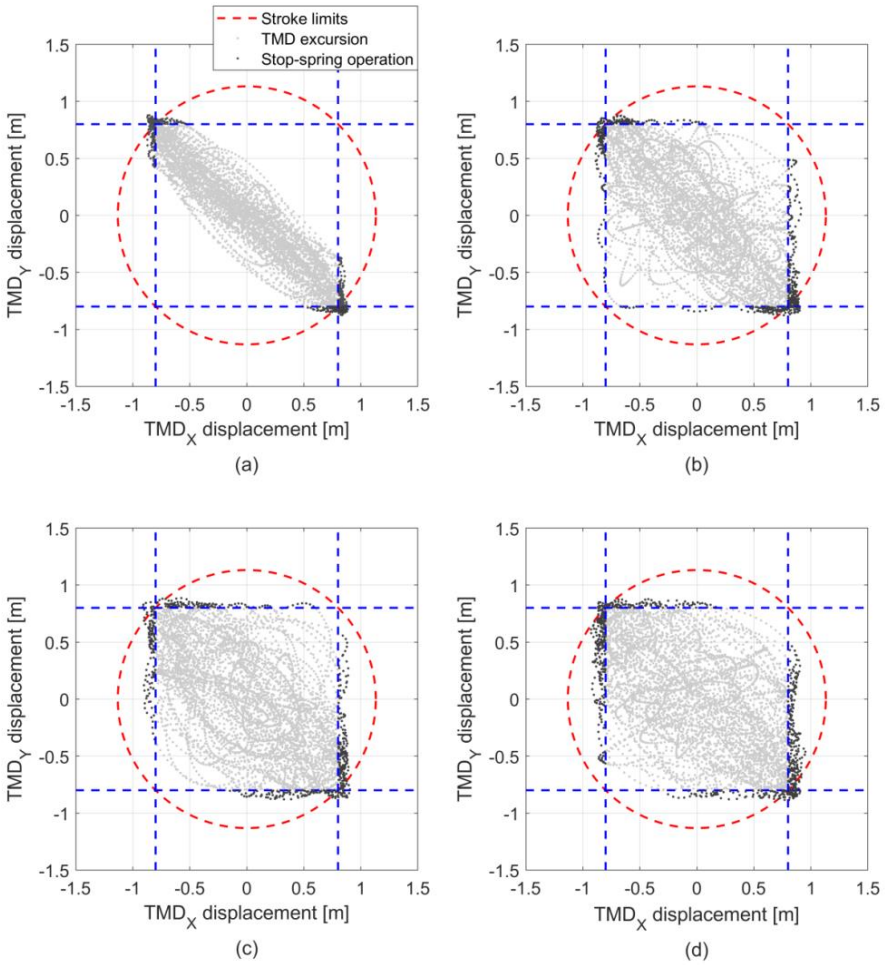

Figure 6.10: TMD excursion in all directions for the floating OWT, (a) mean wind speed of 6 m/s, (b) mean win speed of 10 m/s, (c) mean wind speed of 14 m/s, (d) mean win speed of 18 m/s

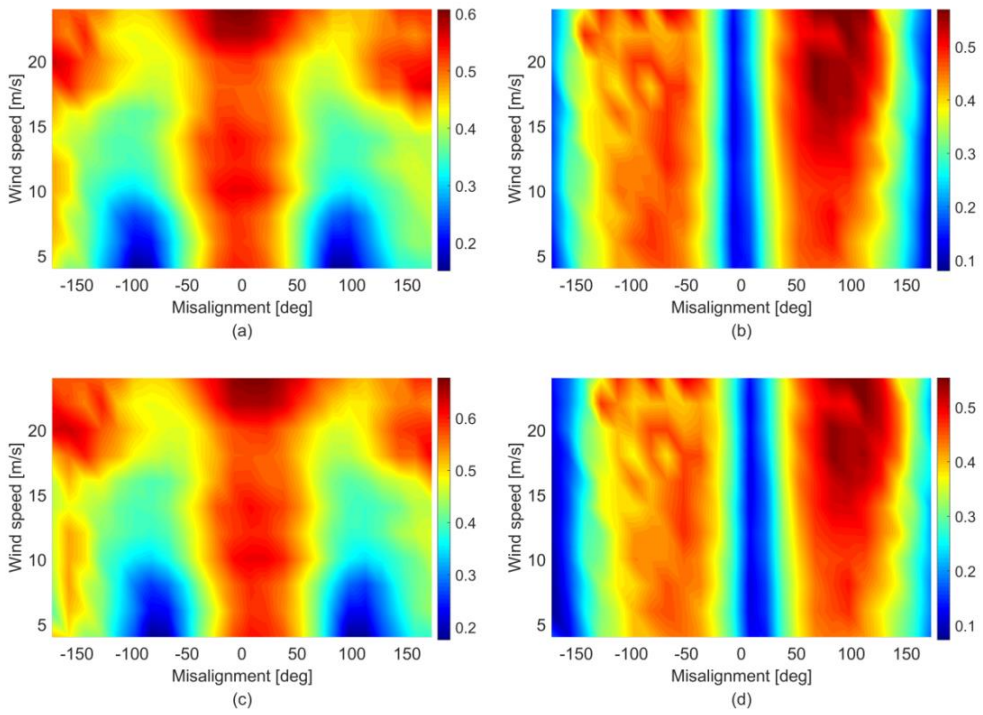

Figure 6.11: Surface plot of the liquid displacement (a): FA-TLCD for case 3, (b): SS-TLCD for case 3, (c): FA-TLCD for case 1, (d): SS-TLCD for case 1

6.1.2 Extreme Load Analysis for NREL 5-MW OWTs

An analysis is performed in order to evaluate the impacts of the tower-TMDs (passive and semi-active ways) and the nacelle-TLCDs (passive only) on reducing the extreme loads of OWTs. The turbine models used in this section are the NREL 5-MW monopile OWT and TLP OWT. The external conditions used to determine the extreme loads are defined by DLC 6.2. Together with the extreme wind and wave conditions (50-year return periods), the IEC standard also recommends analyzing the situation where abnormally large yaw error occurs due to the inability of the nacelle-yaw controller. The wind/wave misalignments are also applied to DLC 6.2 in this analysis. The 50-year

return period wind and wave conditions at SE of Nantucket are defined in Table 4.3. According to Table 4.3, the extreme 50-year return period wind speed at SE of Nantucket is 43 m/s, and the significant wave height and wave spectral period at SE of Nantucket are 12.6 m and 15.1 s. The turbine rotor, including the pitch and torque controller, is shut down to prevent failure of the structure, and the blades are all fully feathered to the maximum pitch angle of 90 degrees to minimize aerodynamic loading. The total number of simulations for all cases is listed in Table 6.4.

OWTs	Case	Number of simulatons
NREL/TLP	Baseline	13 yaw errors × 3 wind/wave misalignments × 3 random seeds =117
	Passive Tower-TMD	117
	S-A Tower-TMD	117
	Nacelle-TLCD case 1	117
	Nacelle-TLCD case 2	117
	Nacelle-TLCD case 3	117
NREL/Monopile	Baseline	13 yaw errors × 3 wind/wave misalignments × 3 random seeds =117
	Passive Tower-TMD	117
	S-A Tower-TMD	117
	Nacelle-TLCD case 1	117
	Nacelle-TLCD case 2	117
	Nacelle-TLCD case 3	117

Table 6.4: The number of simulations for each case

The simulation length for the DLC 6.2 is 1 hour. 13 yaw error bins from -180 to 180 degrees and 3 wind/wave misalignments (-30, 0 and 30 degrees) and 3 random seeds are applied for the simulations. The performance indicators to evaluate the effects of structural control techniques are the maximum moments at the tower base (TwrBsMyt (fore-aft) and TwrBsMxt (side-to-side)), the maximum nacelle acceleration (NacAccFA and NacAccSS) and the maximum tower top displacement (TTDspFA and TTDspSS). The performance indicators are compared to the baseline system with no structural control approaches.

6.1.2.1 Monopile OWTs

Figure 6.12 shows the ultimate loadings in the fore-aft and side-to-side directions for the baseline case according to the yaw errors and wind/wave misalignments. It can be seen that the tower loading and the tower top motion in the fore-aft direction reach maxima at a yaw error of 90 degrees regardless of the wind/wave misalignment. For the side-to-side direction, they reach maxima at a yaw error of 30 degrees. The maxima for each performance indicators are marked as green solid circles. Table 6.5 lists the reduction rates of the ultimate loadings (green solid circles) for each performance index by employing the tower-TMD (passive and semi-active) and the nacelle-TLCDs (case 1, 2 and 3). Like the fatigue analysis result for the fixed-bottom OWT (Table 6.2), one can see that the tower-TMD has a better control performance in all directions than the nacelle-TLCDs, and the semi-active TMD using the IVB-GH algorithm is the best in terms of the loads reduction. The strength of the IVB-GH, which can reduce the height of the first peak in the frequency response, plays a significant role in reducing the extreme loads of the OWTs excited by the extreme waves with low frequency. The tower base moments in the fore-aft and side-to-side direction can be reduced by 17.6% and 30.8%, respectively. Figure 6.13 and 6.14 show the time response and frequency response for the tower base moment in the fore-aft and the side-to-side directions. The time response graphs are zoomed in near the point at which the maximum loading occurs. The ultimate loadings occur at 297 seconds and these can be significantly reduced by the S-A TMD. The superiority of the TMD can also be explained through the investigation of the probability of the stop-spring action as discussed in Section 6.1.1.2. More detailed

discussion regarding the stop-spring action will be made by comparing with the floating OWT case in the next section.

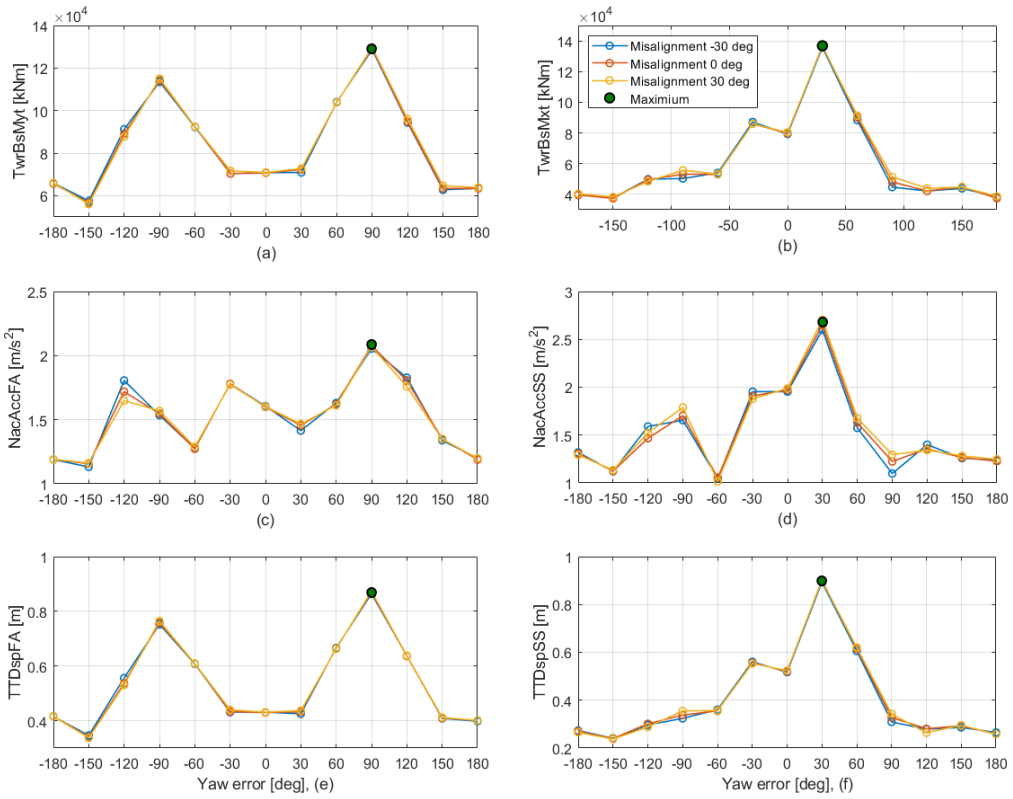

Figure 6.12: Ultimate loadings as functions of the yaw errors and β, (a): tower base moment (fore-aft), (b): tower base moment (StS), (c): nacelle acceleration (fore-aft), (d): nacelle acceleration (StS), (e): tower top displacement (fore-aft), (f): tower top displacement (StS)

Case		TwrBsMyt	TwrBsMxt	NacAccFA	NacAccSS	TTDspFA	TTDspSS
Passive Tower-TMD		15.6 %	28.5 %	36.2 %	18.1 %	16.0 %	26.8 %
S-A Tower-TMD		17.6 %	30.8 %	39.0 %	19.6 %	17.9 %	29.6 %
Nacelle TLCDs	case 1	9.5 %	24.7 %	27.8 %	16.3 %	9.7 %	25.7 %
	case 2	13.3 %	22.6 %	29.6 %	14.7 %	14.3 %	24.3 %
	case 3	15.3 %	20.3 %	32.7 %	12.3 %	16.7 %	21.6 %

Table 6.5: Simulation results for the extreme loads analysis for the fixed-bottom OWT

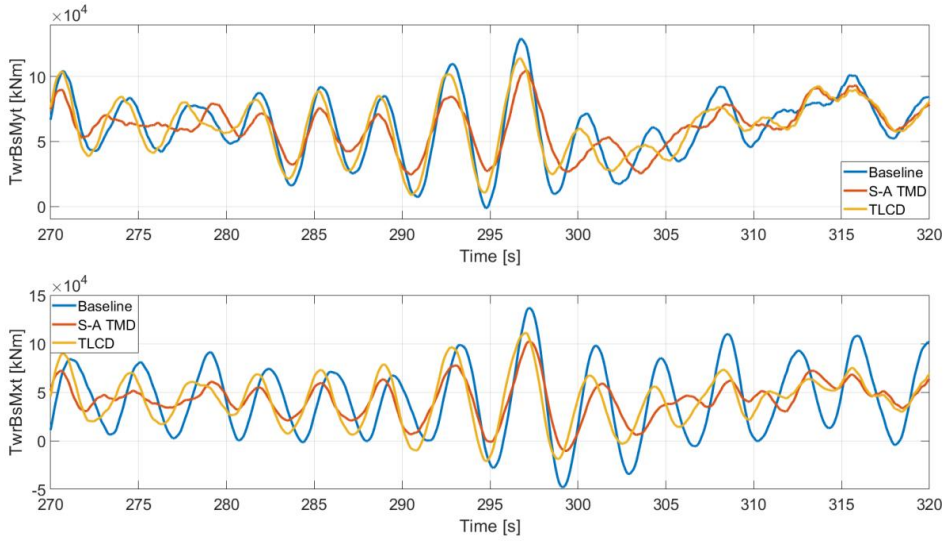

Figure 6.13: Time response of the tower base moment in the fore-aft and side-to-side direction

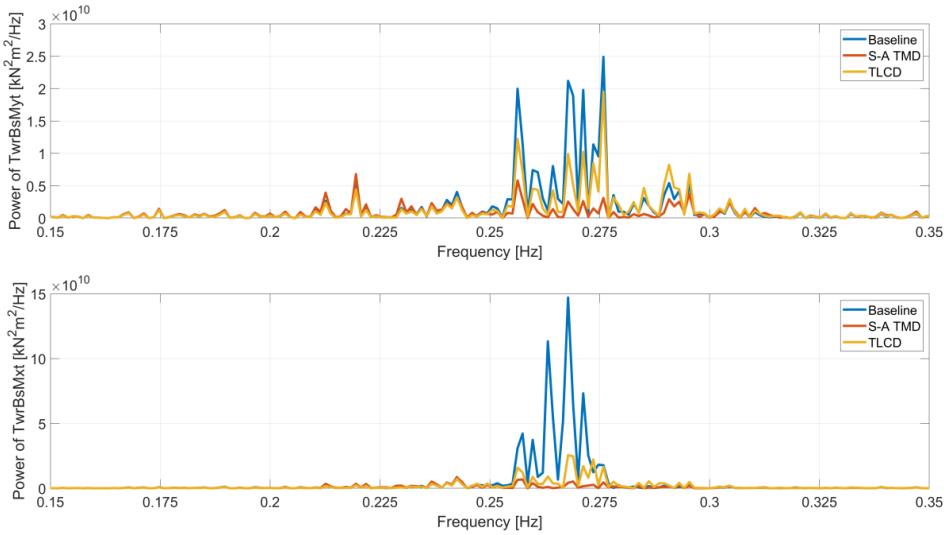

Figure 6.14: Frequency response of the tower base moment in the fore-aft and side-to-side

Investigating the effect of load reduction at a point where the ultimate loading occurs is a priority in extreme load analysis (Table 6.5), but it is somewhat unreasonable to define the overall effect of structural control by one sample. So, the ultimate loadings

from each case are averaged over the 117 simulations in order to demonstrate the overall impacts of the tower-TMDs and nacelle-TLCDs. The averaged values are compared to the baseline case and can be seen in Table 6.6.

Case	Evaluation index	Value	Reduction rate
Passive Tower-TMD	TwrBsMyt	64,572 kNm	22.8 %
	TwrBsMxt	43,112 kNm	29.9 %
	NacAccFA	1.09 m/s^2	34.5 %
	NacAccSS	1.05 m/s^2	31.3 %
	TTDspFA	0.41 m	22.9 %
	TTDspSS	0.28 m	29.7 %
S-A Tower-TMD (IVB-GH)	TwrBsMyt	62,481 kNm	25.3 %
	TwrBsMxt	41,698 kNm	32.2 %
	NacAccFA	1.06 m/s^2	36.6 %
	NacAccSS	1.03 m/s^2	32.7 %
	TTDspFA	0.40 m	25.3 %
	TTDspSS	0.27 m	33.6 %
Nacelle TLCDs Case 3 (μ=0.55)	TwrBsMyt	70,929 kNm	15.2 %
	TwrBsMxt	49,631 kNm	19.3 %
	NacAccFA	1.32 m/s^2	21.0 %
	NacAccSS	1.28 m/s^2	16.9 %
	TTDspFA	0.45 m	16.1 %
	TTDspSS	0.33 m	18.8 %
Nacelle TLCDs Case 2 (μ=0.75)	TwrBsMyt	69,591 kNm	16.8 %
	TwrBsMxt	50,246 kNm	18.3 %
	NacAccFA	1.29 m/s^2	22.3 %
	NacAccSS	1.29 m/s^2	16.1 %
	TTDspFA	0.44 m	17.2 %
	TTDspSS	0.33 m	18.0 %
Nacelle TLCDs Case 3 (μ=0.87)	TwrBsMyt	68,921 kNm	17.6 %
	TwrBsMxt	50,492 kNm	17.9 %
	NacAccFA	1.28 m/s^2	22.9 %
	NacAccSS	1.30 m/s^2	15.5 %
	TTDspFA	0.44 m	17.9 %
	TTDspSS	0.33 m	17.5 %

Table 6.6: The reduction rate of the averaged ultimate loadings

From the Table 6.6, the semi-active TMD still has the best control performance compared to the others. The averaged maximum tower base moments in the fore-aft and side-to-side directions can be decreased by 25.3% and 32.2%, respectively. As found from the fatigue analysis result, the larger the mass, the better the control performance.

6.1.2.2 TLP OWTs

Figure 6.15 shows the ultimate loadings in the fore-aft and the side-to-side directions for the baseline case according to the yaw errors and β.

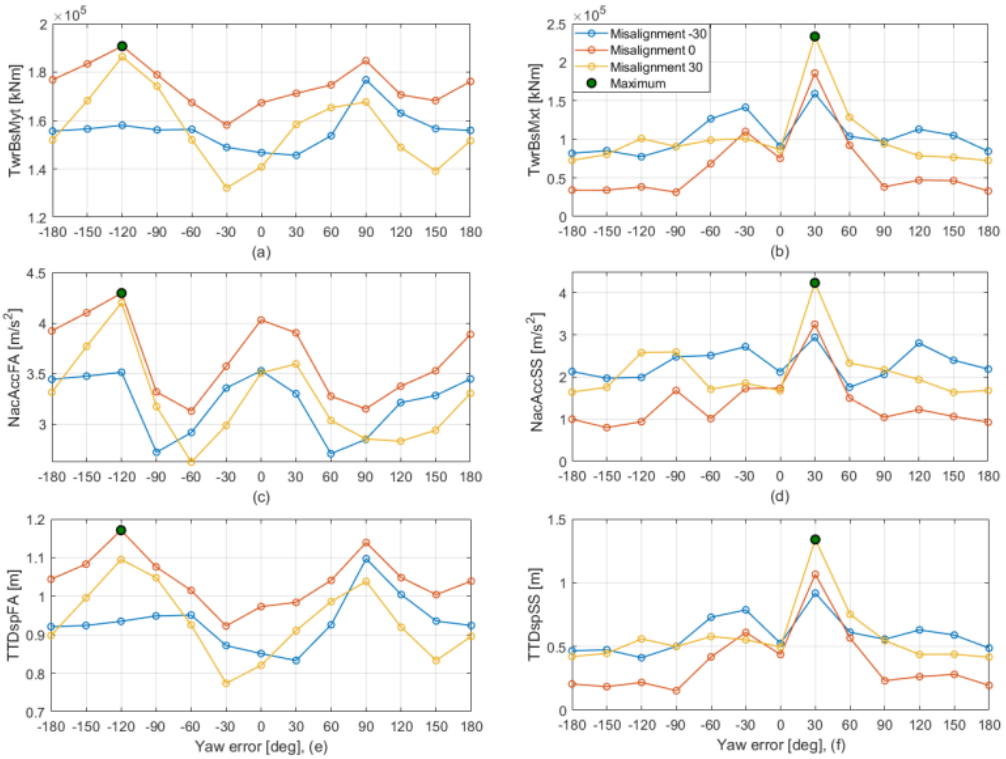

Figure 6.15: Ultimate loadings as functions of the yaw errors and β (a): tower base moment (fore-aft), (b): tower base moment (StS), (c): nacelle acceleration (fore-aft), (d): nacelle acceleration (StS), (e): tower top displacement (fore-aft), (f): tower top displacement (StS)

It can be seen from Figure 6.15 that the tower loading and the tower top motion in the fore-aft direction reach maxima at a yaw error of -120 degrees when the wind and waves are aligned. For the side-to-side direction, they reach maxima at a yaw error of 30 degrees and β of 30 degrees. From these results, one can expect that the maximum aerodynamic forces as the winds pass through the rotor occur at the yaw errors of -120 and 30 degrees for the fore-aft and side-to-side directions, respectively. Table 6.7 lists the reduction rates of the ultimate loadings (green solid circles) for each performance index by employing the tower-TMD (passive and semi-active) and the nacelle-TLCDs (case 1, 2 and 3). Like the fatigue analysis for the floating OWT (Table 6.3), the nacelle-TLCDs have the best control performance compared to the others. This can be clearly explained by investigating the frequency response and the stop-spring action as already discussed in section 6.1.1.2. Similar to Figure 6.5, the tower motion also includes the lower frequency components with strong intensity under extreme wind and wave conditions as shown in Figure 6.16. This results in a significant increase in the TMD stroke, causing an increase in the amount of the stop-spring operation.

Case		TwrBsMyt	TwrBsMxt	NacAccFA	NacAccSS	TTDspFA	TTDspSS
Passive Tower-TMD		14.2 %	15.0 %	20.9 %	18.7 %	13.0 %	14.8 %
S-A Tower-TMD (IVB-GH)		16.2 %	18.8 %	22.6 %	20.9 %	14.6 %	17.0 %
Nacelle TLCDs	case 1	19.9 %	35.5 %	21.6 %	34.1 %	19.3 %	30.8 %
	case 2	19.5 %	33.9 %	22.3 %	35.6 %	19.1 %	33.0 %
	case 3	19.6 %	31.8 %	24.2 %	36.0 %	19.3 %	34.8 %

Table 6.7: Simulation results for the extreme loads analysis for the floating OWT

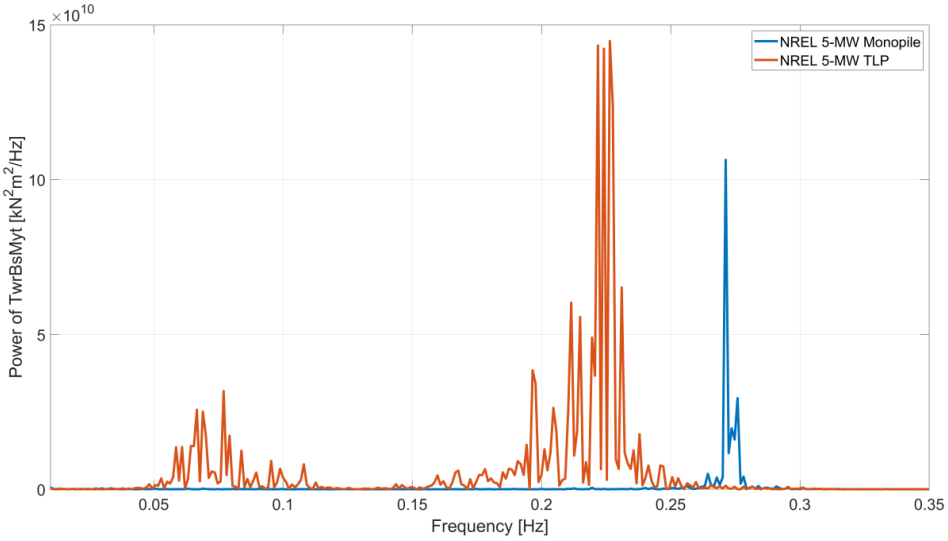

Figure 6.16: Frequency response of the tower motion for the fixed-bottom and the floating OWTs

Figure 6.17 shows the probability that the stop-spring operates during the entire simulations. Like the normal operation (Figure 6.9), more stop-spring action is required to maintain the stroke of the TMD for the floating OWT in comparison with the fixed-bottom OWT.

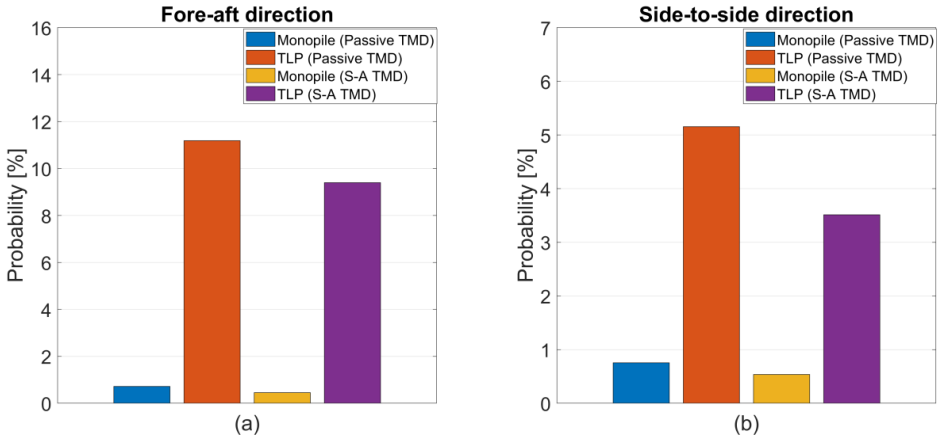

Figure 6.17: Probability of the stop spring operation during the entire simulations

Additionally, the ultimate loadings from each case are averaged over the 117 simulations in order to demonstrate the overall impact of the tower-TMDs and the nacelle-TLCDs. The averaged values are compared to the baseline case and can be seen in Table 6.8.

Case	Evaluation index	Value	Reduction rate
Passive Tower-TMD	TwrBsMyt	154,726 kNm	4.7 %
	TwrBsMxt	79,360 kNm	11.8 %
	NacAccFA	3.02 m/s^2	10.3 %
	NacAccSS	1.66 m/s^2	14.9 %
	TTDspFA	0.93 m	3.8 %
	TTDspSS	0.45 m	10.8 %
S-A Tower-TMD (IVB-GH)	TwrBsMyt	149,206 kNm	8.1 %
	TwrBsMxt	74,771 kNm	16.9 %
	NacAccFA	2.89 m/s^2	14.1 %
	NacAccSS	1.55 m/s^2	20.3 %
	TTDspFA	0.89 m	7.2 %
	TTDspSS	0.42 m	16.6 %
Nacelle TLCDs Case 3 (μ=0.41)	TwrBsMyt	131,185 kNm	19.2 %
	TwrBsMxt	72,342 kNm	19.6 %
	NacAccFA	2.71 m/s^2	19.5 %
	NacAccSS	1.58 m/s^2	19.0 %
	TTDspFA	0.78 m	19.1 %
	TTDspSS	0.41 m	19.2 %
Nacelle TLCDs Case 2 (μ=0.60)	TwrBsMyt	129,415 kNm	20.3 %
	TwrBsMxt	72,900 kNm	18.9 %
	NacAccFA	2.68 m/s^2	20.4 %
	NacAccSS	1.59 m/s^2	21.1 %
	TTDspFA	0.77 m	19.0 %
	TTDspSS	0.42 m	18.3 %
Nacelle TLCDs Case 3 (μ=0.74)	TwrBsMyt	127,943 kNm	21.2 %
	TwrBsMxt	73,906 kNm	17.8 %
	NacAccFA	2.66 m/s^2	21.1 %
	NacAccSS	1.61 m/s^2	17.2 %
	TTDspFA	0.76 m	21.1 %
	TTDspSS	0.42 m	17.3 %

Table 6.8: The reduction rate of the averaged ultimate loadings

From Table 6.8, the nacelle-TLCD still has the best control performance compared to the others. The averaged maximum tower base moments in the fore-aft and the side-to-side directions can be decreased by around 20%. The fact that the control performance in each direction is proportional to the mass ratio is also demonstrated in this analysis. Time response plots to show the control effect of the structural control devices are shown in Figure 6.18. The time response graphs are zoomed in near the point at which the maximum loading occurs.

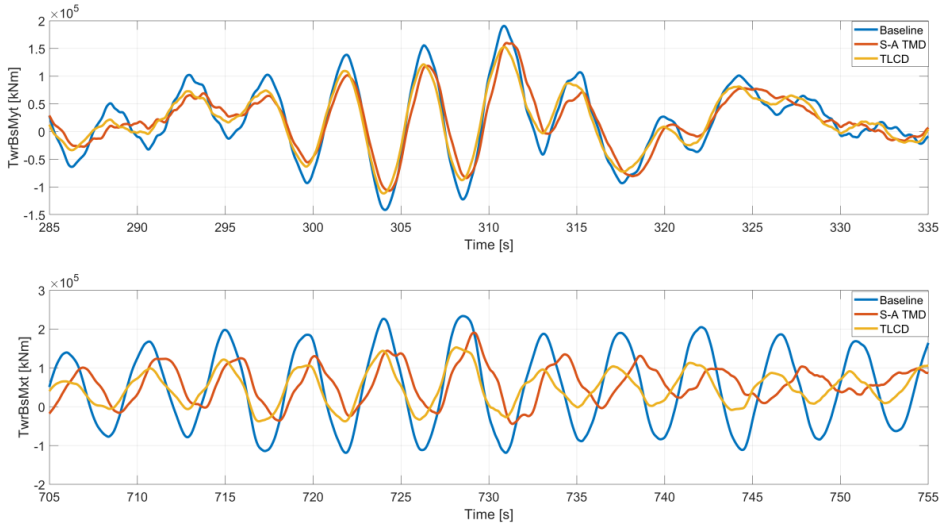

Figure 6.18: Time response of the tower base moment in the fore-aft and side-to-side direction

Tension leg mooring systems have vertical mooring lines under moderate tension to provide large restoring moments in pitch motion of the platform. Sometimes, slack-line incidents occur under extreme wave conditions [103, 104]; when the mooring line is slackened, the platform pitch motion increases significantly due to the lack of restoring moments. In addition, the snap-back loads may follow immediately after the mooring

line is slackened. The snap loads are a kind of shock load which causes a fatal damage and an impulse on the structure. Figure 6.19 presents the minimum mooring line tensions as a function of the yaw errors and β. The minimum tensions are evaluated for each mooring line. Since the two lines are paired, only four lines that are evenly distributed by 90 degrees are evaluated (Line #1: 0°, Line #2: 90°, Line #3: 180°, Line #4: 270°). It can be seen from Figure 6.19 (b) that Line #3 is slackened at the entire range of yaw errors where the direction of wind and waves are aligned. This loosened mooring line can be tightened by employing the TLCDs as seen in Figure 6.19 (d). Figure 6.20 shows one case where the slack line incident occurs. For the baseline case, the larger pitch motion causes slackening in the mooring line at 313 seconds. Otherwise, the mooring line remains tight due to the reduced pitch motion of the platform by the TLCDs.

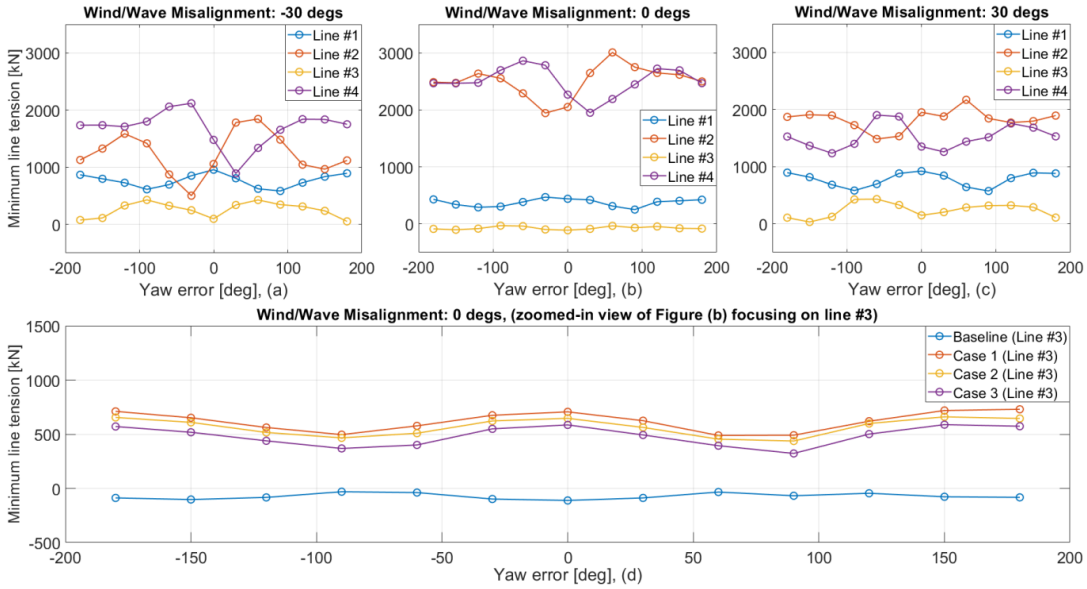

Figure 6.19: Minimum mooring line tension for line #1 to #4, (a) β of -30 deg, (b): β of 0 deg, (c): β of 30 deg, (d): zoomed-in view of (b) focusing on line #3 for the baseline and TLCD cases

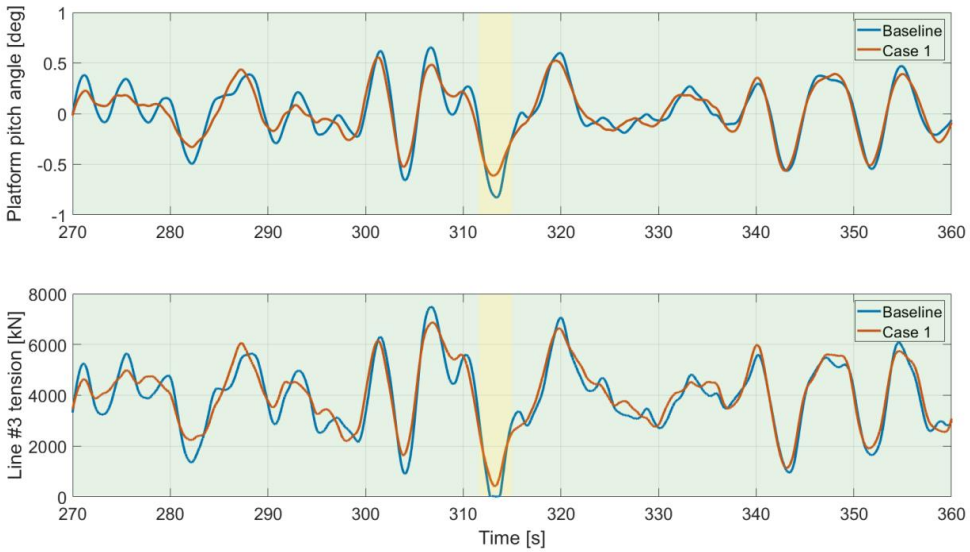

Figure 6.20: Time response plot of the platform pitch motion and the minimum line tension

6.1.3 Fatigue Load Analysis for GE 6-MW OWTs

In this section, fatigue load analysis is performed for the GE 6-MW OWTs. The analysis procedure is nearly identical to the fatigue load analysis for the NREL 5-MW OWTs. The differences are that other external conditions are applied and only the tower-TMDs are considered in this analysis. The conditions for DLC 1.2 recommend by IEC standard are established based on the metocean conditions of the Wave Hub site determined in Section 4.2.2. As discussed in Section 4.2.2, four wind/wave misalignments are considered in DLC 1.2 and their probabilities (Figure 4.6) are applied in the post-processing. Like the fatigue analysis for the NREL 5-MW turbine, the lifetime DELs at the tower base and top in the fore-aft and the side-to-side directions expected over the lifetime (25 years) of the turbine are estimated. The total number of simulations for all cases is listed in Table 6.9. The simulation length is 10 minutes.

OWTs	Case	Number of simulatons
GE/TLP	Baseline	11 wind bins × 4 wind/wave misalignments × 6 random seeds = 264
	Passive Tower-TMD	264
	S-A Tower-TMD (DB-GH)	264
	S-A Tower-TMD (IVB-GH)	264
GE Monopile	Baseline	11 wind bins × 4 wind/wave misalignments × 6 random seeds = 264
	Passive Tower-TMD	264
	S-A Tower-TMD (DB-GH)	264
	S-A Tower-TMD (IVB-GH)	264

Table 6.9: The number of simulations for each case

6.1.3.1 Monopile OWTs

Table 6.10 shows the results for the fixed-bottom OWT.

Case	Evaluation index	m = 3	m = 4	m = 5
Passive Tower-TMD	Lifetime DELs TwrBsMyt	10.1 %	8.9 %	7.9 %
	Lifetime DELs TwrBsMxt	60.4 %	61.6 %	60.4 %
	Lifetime DELs TwrTopFxt	6.6 %	7.0 %	6.8 %
	Lifetime DELs TwrTopFyt	60.5 %	61.0 %	60.1 %
S-A Tower-TMD (DB-GH)	Lifetime DELs TwrBsMyt	13.0 %	11.8 %	10.9 %
	Lifetime DELs TwrBsMxt	64.4 %	64.5 %	63.7 %
	Lifetime DELs TwrTopFxt	9.6 %	9.9 %	9.7 %
	Lifetime DELs TwrTopFyt	64.5 %	65.2 %	64.6 %
S-A Tower-TMD (IVB-GH)	Lifetime DELs TwrBsMyt	8.9 %	7.8 %	7.0 %
	Lifetime DELs TwrBsMxt	60.1 %	61.8 %	63.0 %
	Lifetime DELs TwrTopFxt	5.8 %	6.1 %	5.9 %
	Lifetime DELs TwrTopFyt	59.8 %	61.9 %	61.0 %

Table 6.10: Simulation results for the fatigue loads analysis for the fixed-bottom OWT

The DB-GH control approach has the best performance. In the side-to-side motion, only the motion of the tower critical mode (0.24 Hz) is dominant due to the lack of aerodynamic damping compared to the fore-aft motion as shown in Figure 6.21 (upper right). The impacts of a well-tuned TMD can be maximized when a peak near the critical mode is distinct in the frequency response. In addition, the control performance can also be enhanced with the DB-GH approach by its inherent dynamic nature. In contrast to the side-to-side motion, the frequency components of the tower fore-aft motion are distributed in a wider frequency band due to the influence of the operation of the RNA controller (pitch control) and considerable aerodynamic damping, which may reduce the impact of the TMD tuned to the tower 1st natural frequency. Nevertheless, the peak of the 1st tower mode in the fore-aft direction in the frequency response can also be reduced by employing the passive and S-A TMD.

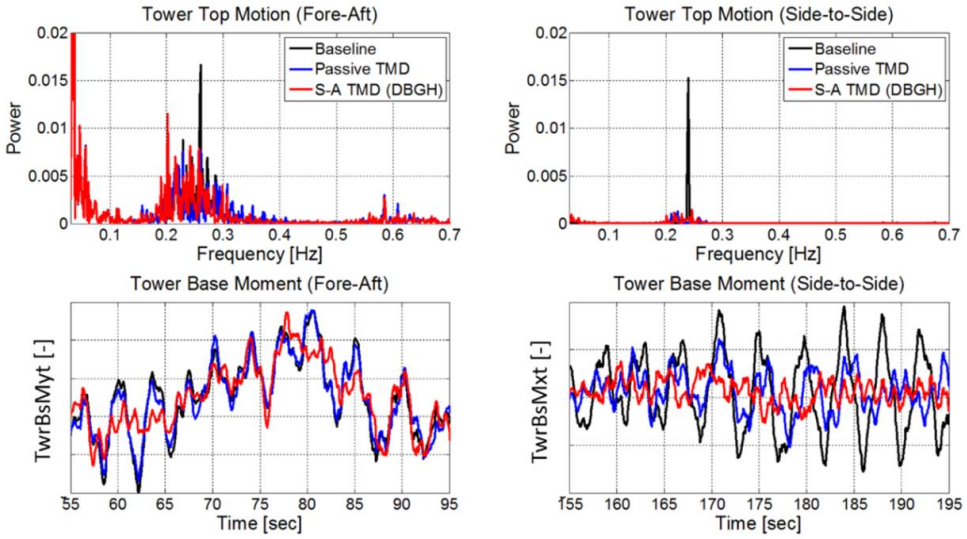

Figure 6.21: Frequency response plots (upper) and time response plots (lower) of the fixed-bottom OWT under DLC 1.2

It can be seen from Figure 6.21 (lower left and right) that the use of the passive and the S-A TMD does improve the structural response of the tower motions, and the impact of the load reduction in the side-to-side motion is much greater than the fore-aft motion.

6.1.3.2 TLP OWTs

Table 6.11 shows the amount of reduction in DELs for the passive TMD and the SA-TMDs (DB-GH and IVB-GH), for water depths of 55 m and 100 m. The numbers in parentheses refers to the load reduction rates when the turbine is installed at a depth of 55 m, and negative values indicate that the load is increased.

Case	Evaluation index	m = 3	m = 4	m = 5
Passive Tower-TMD	Lifetime DELs TwrBsMyt	-4.0 % (1.0 %)	-4.9 % (0.7 %)	-5.5 % (0.4 %)
	Lifetime DELs TwrBsMxt	19.9 % (62.6 %)	15.4 % (61.9 %)	12.6 % (60.8 %)
	Lifetime DELs TwrTopFxt	-1.1 % (0.2 %)	-1.8 % (0.2 %)	-2.0 % (0.2 %)
	Lifetime DELs TwrTopFyt	9.3 % (29.0 %)	8.9 % (28.8 %)	7.4 % (29.1 %)
S-A Tower-TMD (DB-GH)	Lifetime DELs TwrBsMyt	-4.0 % (3.0 %)	-4.0 % (2.3 %)	-4.6 % (1.6 %)
	Lifetime DELs TwrBsMxt	29.3 % (64.5 %)	25.9 % (64.0 %)	23.5 % (62.7 %)
	Lifetime DELs TwrTopFxt	-0.4 % (2.2 %)	-0.9 % (2.0 %)	-1.2 % (1.8 %)
	Lifetime DELs TwrTopFyt	11.8 % (28.7 %)	13.3 % (29.3 %)	13.6 % (30.5 %)
S-A Tower-TMD (IVB-GH)	Lifetime DELs TwrBsMyt	-2.7 % (0.1 %)	-3.6 % (-0.2 %)	-4.0 % (-0.4 %)
	Lifetime DELs TwrBsMxt	24.7 % (61.7 %)	20.8 % (61.2 %)	18.2 % (60.4 %)
	Lifetime DELs TwrTopFxt	-0.6 % (-1.7 %)	-1.1 % (-2.3 %)	-1.3 % (-2.7 %)
	Lifetime DELs TwrTopFyt	10.9 % (25.4 %)	11.4 % (28.7 %)	10.7 % (29.5 %)

Table 6.11: Simulation results for the fatigue loads analysis for the floating OWT

Similar to the fatigue behavior of the fixed-bottom OWT, the DB-GH control approach has the best performance in reducing DELs. Specifically, the tower base moment (side-to-side) can be significantly reduced by 64% (Wöhler exponent of 4 for steel) in shallow water depth (55 m). The DB-GH controller can reduce DELs in the fore-aft direction as well, unlike the IVB-GH approach. In deeper water (100 m), the TMDs are still effective in reducing DELs, especially side-to-side motion, but the performance is relatively low. Figure 6.22 and 6.23 show selected frequency and time responses for the various cases. It can be seen that the critical mode of the tower can be significantly reduced by the passive and the S-A control in the side-to-side direction. The time response also shows a significant reduction of the tower base moment in the side-to-side direction by the passive and the S-A TMD. However, in the fore-aft direction, the TMD has little effect on reducing the tower base moment (fore-aft direction) as the TMD is not able to cope with a much broader frequency distribution near the tower critical mode.

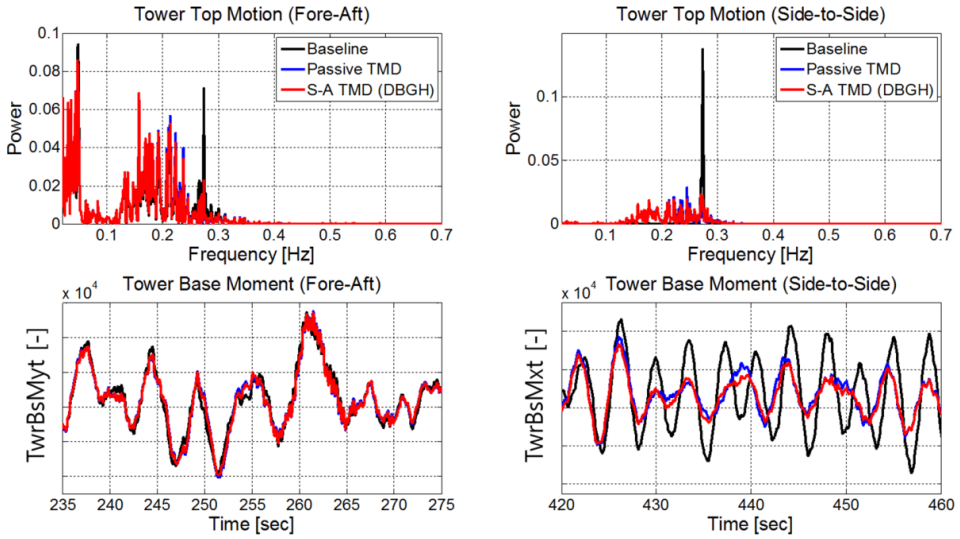

Figure 6.22: Frequency response of the tower-top motion (upper) and time response (lower) of the tower base moments for the floating OWT (depth of 55 m) under DLC 1.2

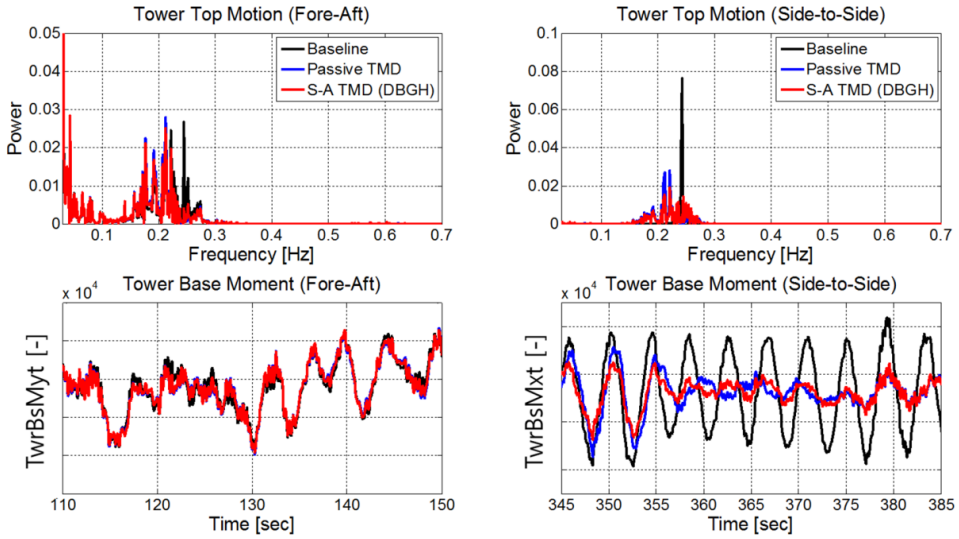

Figure 6.23: Frequency response of the tower-top motion (upper) and time response (lower) of the tower base moments for the floating OWT (depth of 100 m) under DLC 1.2

6.1.4 Extreme Load Analysis for GE 6-MW OWTs

An extreme load analysis is performed for the GE 6-MW OWTs. The analysis procedure is nearly identical to the extreme load analysis for the NREL 5-MW OWTs. Like the fatigue analysis, the metocean conditions at the Wave Hub site are applied and only the tower-TMDs are considered for the analysis. As discussed in Chapter 4, the conditions such as wind, wave and sea-current statistics are derived from site measurements, and estimated through a hind cast approach conducted by HR Wallingford hydraulics laboratory in UK. The extreme wind and wave conditions are defined in Table 4.5 and additional conditions regarding the platform orientations and water depths are added in order to set the conditions for DLC 6.1. Water depths of 55 m and 100 m at mean sea level are considered. The water depth of 55 m is regarded as extremely shallow. The cases at wind/wave headings of 0 and 36 degrees to the platform

are analyzed to ensure the worst conditions. The total number of simulations for all cases is listed in Table 6.12. A 1 hour simulation time is used to include sufficient phase differences between the wind and wave to capture the extreme load combinations.

OWTs	Case	Number of simulatons
GE/TLP	Baseline	2 TLP orientations × 2 water depths × 10 random seeds = 40
	Passive Tower-TMD	40
	S-A Tower-TMD (DB-GH)	40
	S-A Tower-TMD (IVB-GH)	40
GE Monopile	Baseline	3 wind/wave misalignments × 6 random seeds = 18
	Passive Tower-TMD	90
	S-A Tower-TMD (DB-GH)	90
	S-A Tower-TMD (IVB-GH)	90

Table 6.12: The number of simulations for each case

The performance indicators to evaluate the control effects of structural control approaches are the maximum moments at the tower base and the mud-line, and the maximum translational forces at the tower top and the mud-line, as well as the maximum nacelle acceleration. The performance indicators are compared to the baseline system with no structural control approaches.

6.1.4.1 Monopile OWTs

The ultimate loads are defined as the absolute maximum loads of each simulation averaged over the 18 simulations (six different random seeds and the three-different wind/wave misalignments). Table 6.13 lists the reduction rate of maximum forces and moments for the passive and the S-A TMD with respect to the baseline loads. In the fore-aft direction, the passive TMD results in a 30% decrease in the maximum force at the

tower top while the S-A TMD results in an even larger decrease of 44.7%. In addition, the S-A TMD results in noticeable moment reductions of 31.7% at the tower base, compared to 25% for the passive TMD.

Evaluation index	Linear Damper		MR Damper	
	Passive TMD	S-A TMD (IVB-GH)	Passive TMD	S-A TMD (IVB-GH)
Tower Base Moment	25.8 %	32.7 %	25.0 %	31.7 %
Tower Top fore-aft force	30.7 %	44.8 %	30.0 %	44.7 %
Tower Top side-to-side force	7.9 %	10.3 %	7.5 %	9.5 %
Nacelle acceleration	32.4 %	41.1 %	31.7 %	40.5 %
Mud-line Moment	37.3 %	41.0 %	36.8 %	40.1 %
Mud-line fore-aft force	15.0 %	16.3 %	14.7 %	15.2 %
Mud-line side-to-side force	6.0 %	7.8 %	5.7 %	7.2 %
90^{th} Percentile TMD stroke	0.58 m	0.4 m	0.57 m	0.37 m
RMS Damper Force	3380 N	5210 N	3310 N	5960 N
Damper Power Consumption	-	-	-	25.3 W

Table 6.13: Simulation results for the extreme loads analysis for the fixed-bottom OWT (GE 6MW)

Simulations using the ideal linear damper for S-A control were also performed, assuming that the damping coefficient can be changed between the on/off states without any dynamics. While such an ideal device is not realizable in practice, it is useful in evaluating the performance to the MR damper model, which takes into account the non-linear dynamics associated with the device. Despite the hysteretic characteristics of the MR damper, the performance in terms of load reduction for the TMDs using the ideal linear damper and the MR damper shows little difference (less than 1%). It can be also seen from Figure 6.24 that the damper force generated by the MR damper can mimic the

force of the linear damper at all areas in the passive control case. In the on-state of S-A control, the force-velocity behavior between the MR damper and the linear damper is quite different in the low velocity region. The difference can be seen through the time response plot as shown in Figure 6.24, however, it does not have a significant effect on the results. The power consumption to operate the MR damper semi-actively is about 25.3 Watts on average, which could be supplied from commercial batteries. More comparison figures and tables between the linear damper and MR damper are provided in Appendix E: Comparison of Linear and MR Damper.

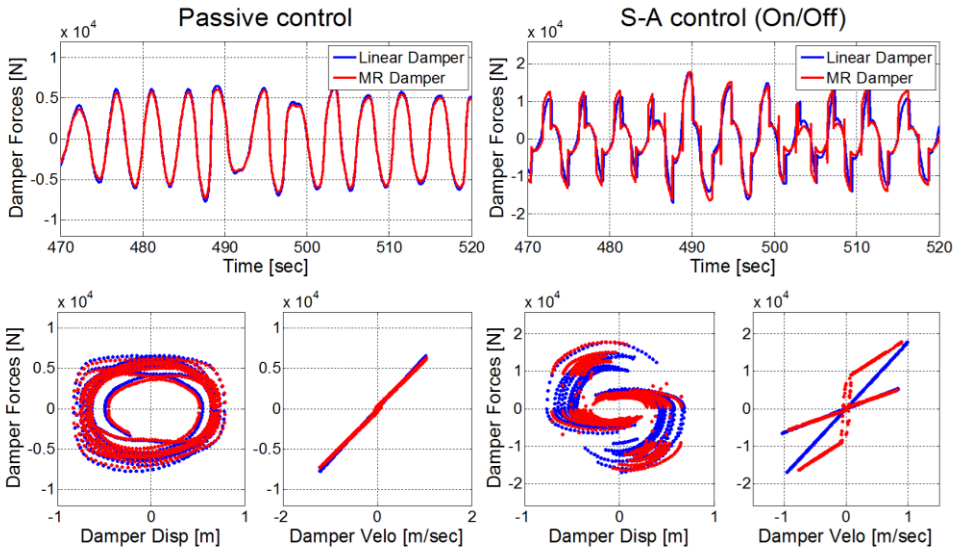

Figure 6.24: Comparison of force capacity between the linear and MR damper under DLC 6.1

It has also been confirmed that the TMD oscillates within the maximum allowable limit of ±0.8 m. In addition, it is interesting to note that the 90th percentile stroke of the S-A TMD can be significantly reduced by 35% compared to the passive

case while maintaining better performance. This may be a major advantage of the S-A TMD if there is limited installation space.

6.1.4.2 TLP OWTs

The responses used to evaluate the performances of the TMDs are the tower loads, nacelle acceleration, and mooring line tension. The relevant tower loads are the maximum tower bending moments at the tower base and the upper part of the transition piece. The upper part of the piece acts as the interface between the tower and the platform substructure, and is, therefore, important for the tower's safety. In addition, the 90^{th} percentile strokes are evaluated. The simulation results summarizing the reduction rates for each control approach in comparison to the baseline case are shown in Table 6.14.

Evaluation index	55 m Depth		100 m Depth	
	Passive TMD	S-A TMD (IVB-GH)	Passive TMD	S-A TMD (IVB-GH)
Tower Base Moment	-4.2	-3.2	4.5	8.9
Tower Interface Moment	-3.5	-2.6	4.9	9.0
Nacelle acceleration	-1.9	-0.2	7.4	11.4
Minimum Tendon Tension	14.8	12.6	-8.3	-19.3
Maximum Tendon Tension	-1.4	-1.1	1.0	2.1
90^{th} percentile TMD stroke	0.98 m	0.88 m	0.87 m	0.76 m
95^{th} percentile TMD stroke	1.01 m	0.91 m	0.89 m	0.78 m
RMS Damper Force	3980 N	11710 N	3565 N	10247 N
Power consumption	-	31.8 W	-	30.3 W

Table 6.14: Simulation results for the extreme loads analysis for the floating OWT (GE 6MW)

Numerous meaningful conclusions can be drawn from the results. In shallow water depth (55 m), almost all results show that structural control has negative impacts on loads. The impact of the TMD is negative due to the dominant loading frequency on the platform that is lower than the TMD tuning frequency as shown in Figure 6.25 (b).

The TMD reduces loads uniformly in deeper water (100 m). These positive impacts of the TMD can be explained using a similar logic to the 55-m case. In 100-m of depth, the power density near the 1st tower modal frequency, in contrast to the 55-m case, is greater than its lower frequency region (0.05~0.15 Hz). This dominant power density near the 1st tower modal frequency makes the TMD much more effective because the TMD is tuned to the 1st tower modal frequency. Figure 6.25 (c) shows the time series of the tower bending moment at the base for the 100-m depth. The passive and S-A TMDs are clearly more effective in mitigating loads on the tower compared to the 55-m case (Figure 6.25 (d)). S-A control using IVB-GH has better performance than the passive approach. Maximum loads at the base can be decreased by approximately 9% with the IVB-GH control. In addition, the minimum mooring line tension can be increased by more than 19% with the IVB-GH configuration. This increased minimum tension of the mooring lines reduces the probability of slack mooring line events. Figure 6.26 (a) and (c) show a time series of mooring line tension loads and tower base moment for the 100-m case. In contrast to the 55-m case, the maximum loads can be decreased with increased minimum tension of the mooring lines as shown in Figure 6.26 (b) and (d). The nacelle acceleration is also reduced by 11% in the 100-m case. The reduction of the nacelle acceleration is a key metric that can reduce the risks of failure of electromechanical components and blades. It is also significant to see that for the IVB-GH control, the 90th

percentile TMD stroke doesn't exceed the TMD stroke limitation of ±0.8 m while maintaining better performance.

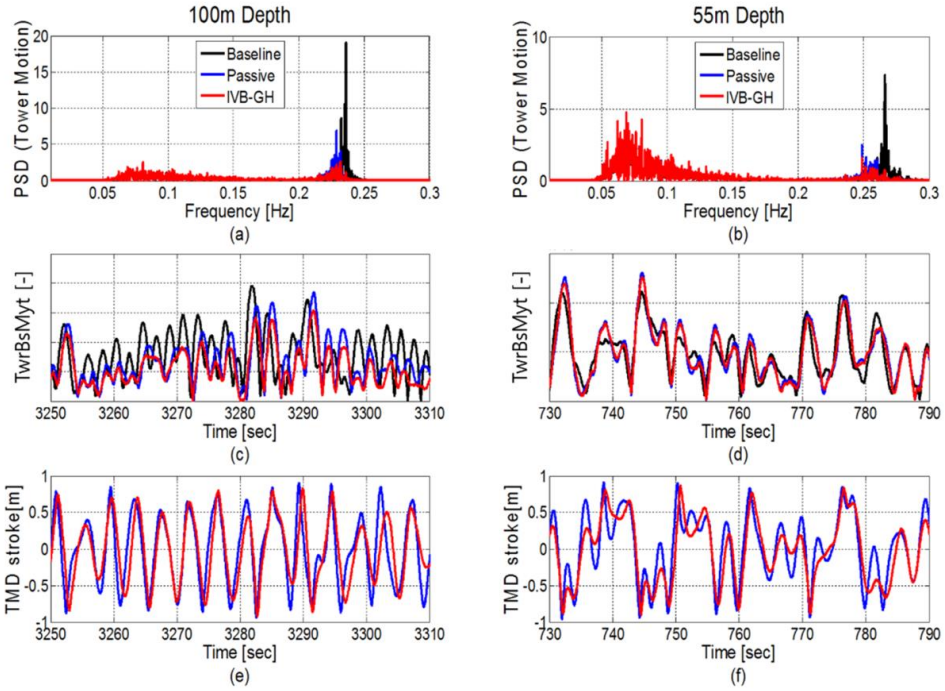

Figure 6.25: Frequency response of the tower top motion (upper) and time response (lower) of the tower base moment for the floating OWT under DLC 6.1

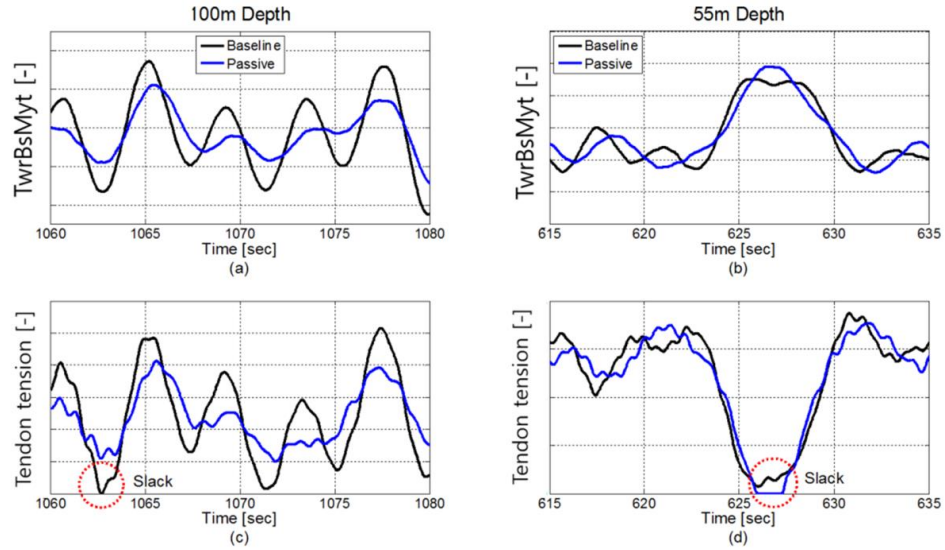

Figure 6.26: Time response for the tower base moment (upper) and the tendon tension (lower)

6.1.4.3 Impacts of Stroke Limitation of a Tower-TMD

In order to examine the impacts of the stroke limitation of the TMDs, a sensitivity analysis is conducted by applying 5 different non-linear spring force curves to the TMDs. In Figure 6.27, the black dotted line, which is used for an unlimited TMD stroke simulation, shows a linear spring force curve. To restrict the TMD stroke, higher non-linear spring forces are applied to stop the TMDs after a certain displacement, as depicted in other colored lines. Although the operation of the stop spring with a higher non-linear spring force can restrict the TMD motions at specific positions, they also act as reaction forces in the opposite direction, which may deteriorate the structural response of a main structure. In addition to causing a reaction force by the highly non-linear spring forces, there can be other negative effects of the TMDs, such as de-tuning issues due to the higher stiffness by the stop-spring.

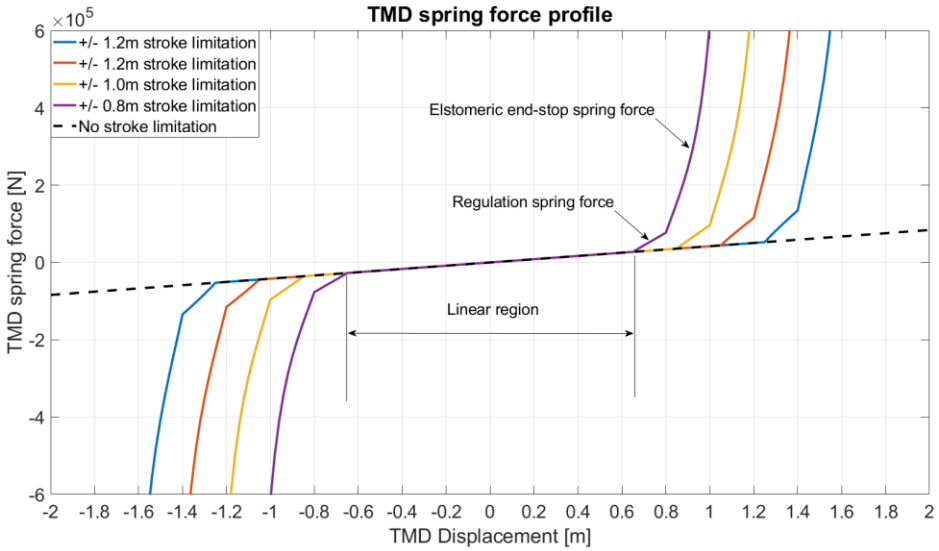

Figure 6.27: Non-linear spring force curves according to the stroke limitations

Figure 6.28 shows an example of a frequency response of a structure under excitation according to various stiffness values of the TMD, where γ is the ratio of the TMD natural frequency to the main structure natural frequency. This demonstrates the negative effect of the de-tuned TMD on the frequency response. The first peak in the frequency response increases as the TMD is tuned to the higher frequency.

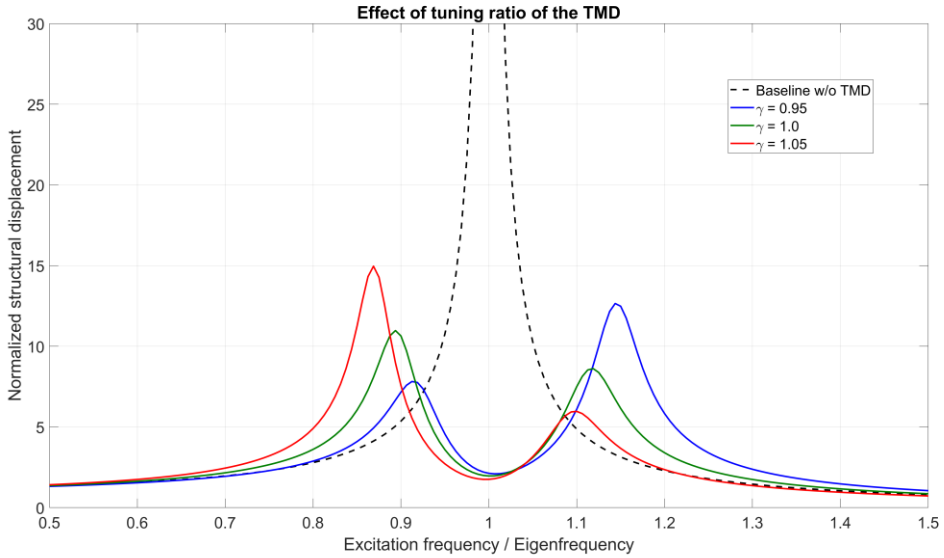

Figure 6.28: Effect of tuning frequency on a structural response

It can be seen that the first peak of the red line increases when the TMD is tuned to the higher frequency. The operation of the stop-spring increases the tuning frequency of the TMD, so the first peak is inevitably increased sharply. Since the influence of the stop-spring on the control performance is significant, investigating the impact of the stroke limitation is an important factor in the design of TMDs. A sensitivity analysis for the TMD strokes is performed under DLC 6.1, which is used for the extreme load analysis in Section 6.1.4.2. The same external conditions are applied for this analysis with the five different TMD stroke limitations.

As speculated in previous research by Lackner and Rotea [27], these results affirm that load reduction can be increased with larger strokes of the TMDs. According to Figure 6.29, the maximum tower base moments and the nacelle acceleration can be reduced by 15% and 20%, respectively. Also, the reduction with a $\pm$1.4m stroke limitation eventually converges to the TMD case without stroke limitations. In Figure 6.30 (time series of tower the base moment), the TMD with $\pm$0.8m stroke limitation has a negative effect on loads at a certain time (3340~3350sec). Otherwise, the negative effect does not occur when the TMD stroke limitation is large enough. Figure 6.31 shows the frequency response of the tower base moment for the baseline and the semi-active TMD cases with the different stroke limitations. It can be seen that the first peak can be reduced significantly with the larger stroke limitation of the TMD. Although the operation of the stop-spring has an adverse effect on the control performance, it is an essential element to limit the TMD stroke. Thus, the trade-off must be considered in the process of designs.

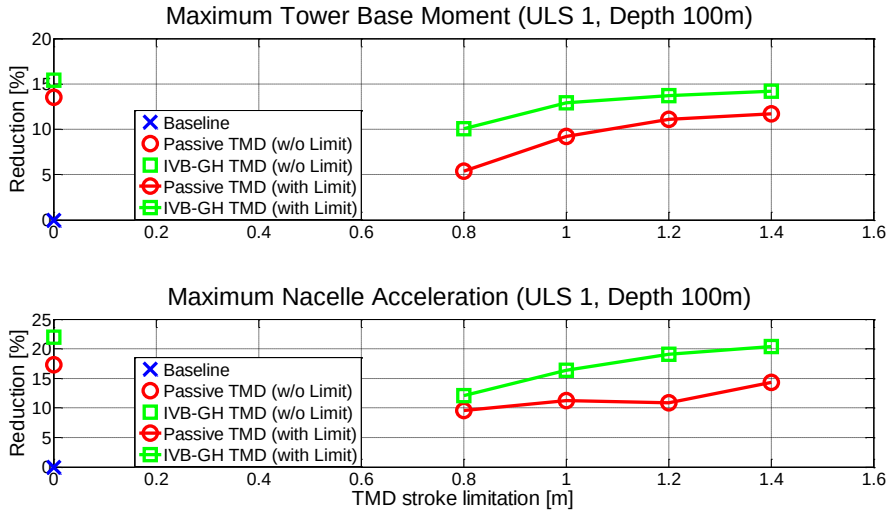

Figure 6.29: Effect of TMD stroke on reducing maximum loads

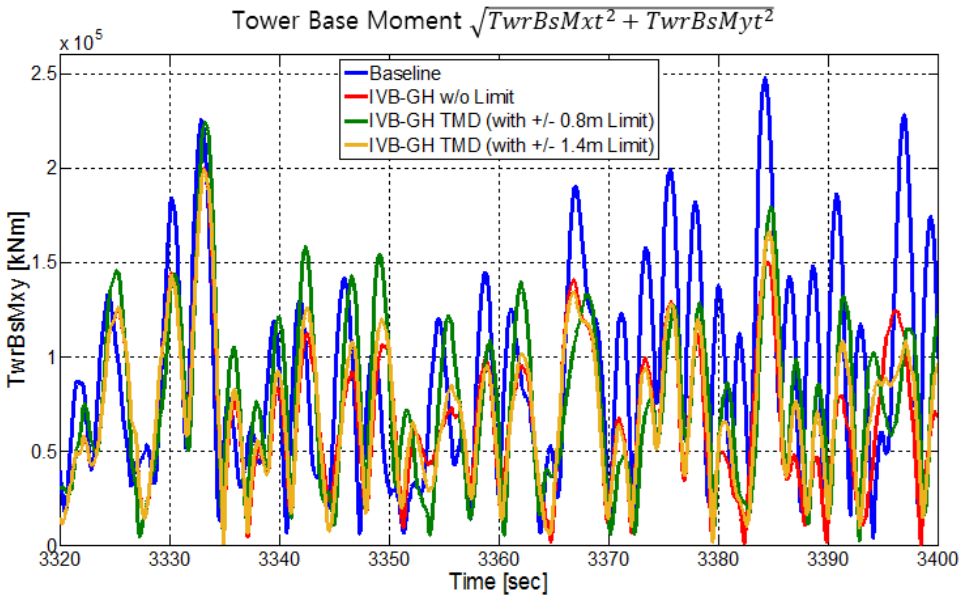

Figure 6.30: Time response of the tower base moment to show the negative effect of the stop-spring

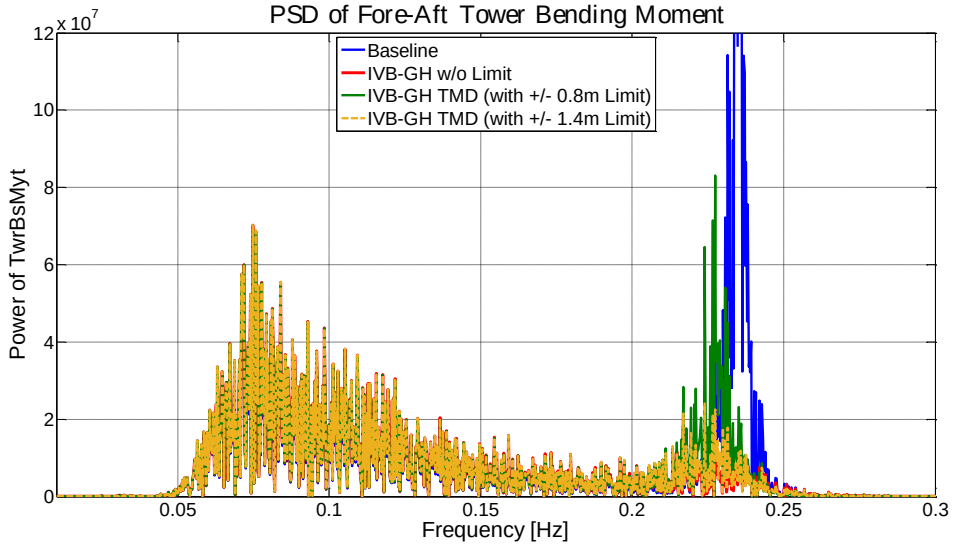

Figure 6.31: Frequency response of the tower base moment to show the negative effect of the stop-spring

6.1.4.4 Mooring Line Sensitivity Analysis

This section explores the impact of the mooring line stiffness on the dynamic responses of the floating OWT. The extreme wind and wave conditions and the GE 6-MW Haliade TLP OWT for a depth of 55m and 100m are used for this analysis. The simulations are repeated for mooring line stiffness values that are 9%, 18%, 27% and 36% larger than the baseline. The critical mode, which is the main target frequency for structural control, increases as the stiffness of the mooring line increases as shown in Table 6.15. Also, the power density of the tower bending moments near the critical mode can be reduced by the high stiffness of the mooring lines as shown in Figure 6.32.

When the critical mode is further away from the low frequency region, the structural response and the TMD for structural control can be enhanced. In 55 m water depth, the power density at the low frequency range is dominant across the whole frequency region. This causes the TMD, when tuned to the critical mode of the tower, to be ineffective. The low power density in the low frequency region and the increased 1^{st} modal frequency are positive features for a structure when applying structural control. This is largely because higher tuning frequencies for the TMD result in lower TMD excursions. This in turn raises the possibility of avoiding some negative effects, such as a significant reaction force to the tower and a de-tuning of the TMD when the non-linear high spring force for the TMD stops are applied.

Figure 6.33 and 6.34 show the load reductions on the tower, nacelle acceleration and TMD stroke with various values of mooring line stiffness. The baseline with the original mooring line stiffness acts as a basis of comparison, and is used to calculate reductions rates in load and nacelle acceleration. Maximum tower base moments and

nacelle acceleration can be reduced, compared to the original stiffness case. In the two baseline cases with original and higher mooring line stiffness, respectively, there are little differences in maximum loads, while the TMD has noticeable effects in terms of the load and acceleration reduction as the mooring line stiffness increases.

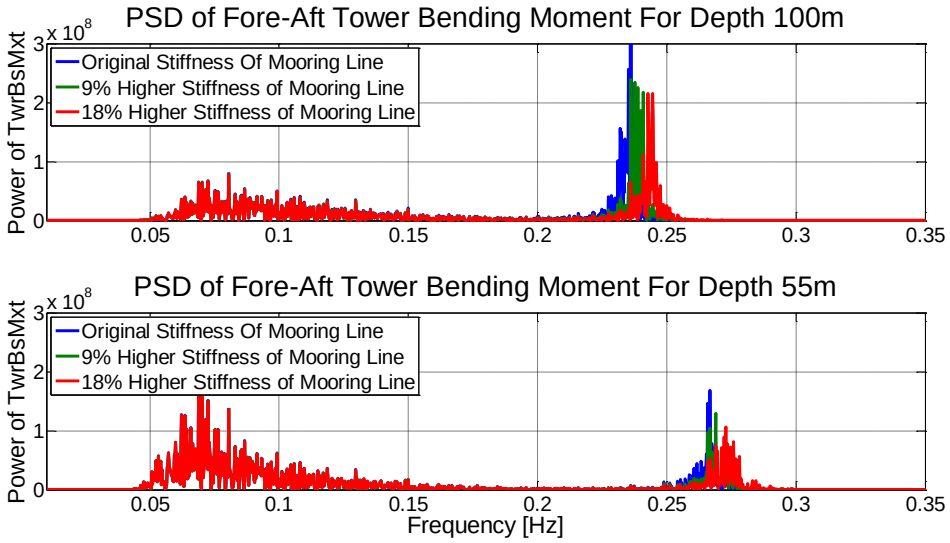

Figure 6.32: Frequency response of the tower base moment according to the mooring line stiffness

		OriginalEA	9% Higher stiffness	18% Higher stiffness	27% Higher stiffness	36% Higher stiffness
Depth 55m	Tendon Stiffness[N]	1.36E09	1.49E09	1.61E09	1.73E09	1.85E09
	Critical mode [Hz]	0.265 (-)	0.267 (1.1%)	0.270 (2.3%)	0.272 (3.0%)	0.273 (3.4%)
Depth 100m	Tendon Stiffness[N]	1.58E09	1.72E09	1.88E09	2.01E09	2.15E09
	Critical mode [Hz]	0.231 (-)	0.238 (3.0%)	0.246 (6.5%)	0.250 (8.2%)	0.253 (9.5%)

Table 6.15: Changes in the frequency of the critical mode versus mooring line stiffness

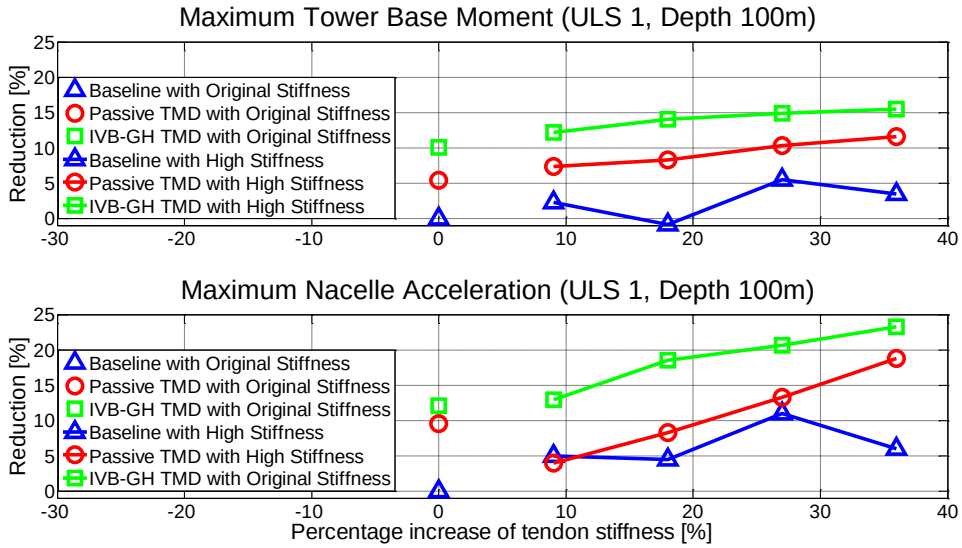

Figure 6.33: Reduction in maximum tower base moment and nacelle acceleration, as a function of mooring line stiffness

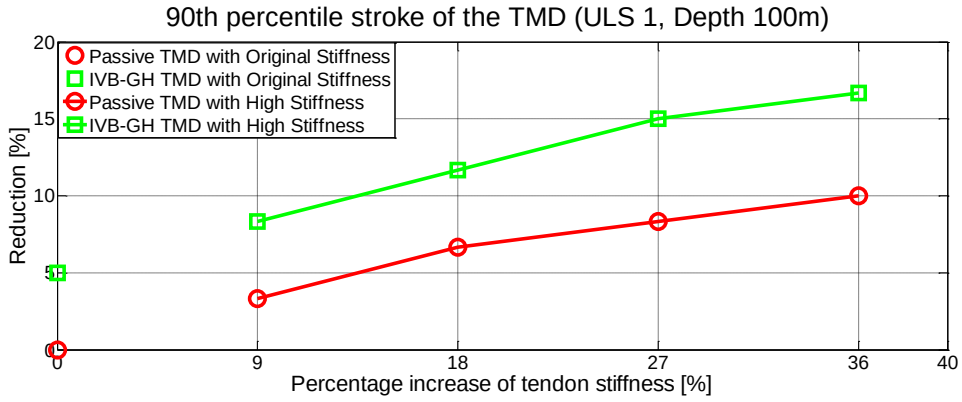

Figure 6.34: Reduction in 90th percentile TMD stroke according to the mooring line stiffness

6.2 Blade Response Control

This section presents the simulation results regarding the impact of the passive blade-TMD in terms of fatigue and extreme load reductions. Promising parameters for the blade-TMD are selected from the optimal design formulas determined in Chapter 5. The control performance of each design case is compared with the baseline system. It should also be noted that in all cases the inclusion of the blade-TMDs has negligible impacts on the behavior of the baseline variable speed and collective pitch control system.

6.2.1 Fatigue Load Analysis

Simulations with DLC 1.2 are performed to assess how much the fatigue behavior of the turbine blades can be improved by applying structural control technique. The main simulation conditions are shown in Figure 4.4 in Section 4.1. The total number of simulations for all cases (Baseline, case 1 to 8) is 1782 (each 109: 11 wind bins, 3 yaw errors (-8, 0 8 degrees) and 6 random seeds) and the simulation length is 10 minutes. The blade models used in this analysis are the NREL 5-MW blade and the DTU 10-MW blade. From the design formulas determined in Section 5.2, eight design cases for the NREL and DTU blades have been selected as shown in Table 6.16 and 6.17. The performance indicators are the lifetime damage equivalent moments and forces at the blade roots. In Table 6.18, $RootF_x$ and $RootF_y$ are the blade root out-of-plane and in-plane shear force at a blade root, respectively. $RootM_y$ and $RootM_x$ are the blade root out-of-plane and in-plane moment at a blade root, respectively. In order to calculate the lifetime damage equivalent loads, the probabilities corresponding to operational wind speeds (4 to 24 m/s) determined in Section 5.2 (at Southeast of Nantucket) are applied.

With the forces and moments at the blade root calculated by FASTv8, the lifetime damage equivalent loads expected over the lifetime (25 years) of the turbine blade are estimated based on a rain flow counting algorithm with S/N curve slopes of 9, 10 and 11 for the typical blade materials.

Case	Mass ratio μ	TMD Location	Frequency ratio	Damping ratio	Chord length
1	0.017	60.4 m	0.989	0.074	1.73 m
2	0.026	55.4 m	0.984	0.091	2.39 m
3	0.032	52.4 m	0.980	0.100	2.62 m
4	0.038	49.8 m	0.977	0.109	2.76 m
5	0.043	47.7 m	0.974	0.117	2.86 m
6	0.069	40.3 m	0.957	0.147	3.22 m
7	0.095	36.0 m	0.941	0.172	3.49 m
8	0.121	33.4 m	0.924	0.192	3.66 m

Table 6.16: The optimal location, frequency ratio and damping ratio as a function of μ (NREL)

Case	Mass ratio μ	TMD Location	Frequency ratio	Damping ratio	Chord length
1	0.017	86.8 m	0.989	0.062	1.31 m
2	0.026	80.1 m	0.984	0.078	1.87 m
3	0.032	76.2 m	0.980	0.087	2.05 m
4	0.038	72.8 m	0.976	0.096	2.35 m
5	0.043	70.2 m	0.973	0.102	2.55 m
6	0.069	60.5 m	0.957	0.131	3.26 m
7	0.095	54.7 m	0.939	0.153	3.73 m
8	0.121	51.2 m	0.923	0.173	4.05 m

Table 6.17: The optimal location, frequency ratio and damping ratio as a function of μ (DTU)

The performance indicators are compared to the baseline in order to present the reduction rates as seen in Table 6.18 and Figure 6.35 and 6.36. Based on Table 6.18, it can be seen that the control performance drops as the location of the TMD is moved towards the root. This is because the vibrational energy is mostly concentrated on the blade tip and the TMD is more active at the blade tip where the centrifugal force is the largest. The in-plane blade root force and moment can be decreased by almost 10%. It can be seen that the heavier TMD is used at the lower position, but complete compensation of the control performance cannot be achieved. Despite this, the TMD located near the blade tip is not regarded as the best design selection as the available space at the blade tip becomes significantly narrow. So, it is necessary to check whether the space inside the blade is sufficient to drive the TMD.

Blade	Case	$RootF_x$ *(Out of plane)*	$RootF_y$ *(In-plane)*	$RootM_y$ *(Out of plane)*	$RootM_x$ *(In-plane)*
NREL 5-MW Blade	1	3.5 %	7.7 %	3.6 %	11.1 %
	2	3.4 %	7.3 %	3.4 %	10.8 %
	3	3.2 %	7.1 %	3.4 %	10.3%
	4	3.1 %	6.9 %	3.3 %	9.9 %
	5	3.1 %	6.7 %	3.3 %	9.5 %
	6	3.0 %	6.4 %	3.1 %	9.1 %
	7	2.7 %	5.9 %	2.8 %	8.3 %
	8	2.5 %	5.4 %	2.3 %	7.6 %
DTU 10-MW Blade	1	2.7 %	8.2 %	2.8 %	12.1 %
	2	2.6 %	7.9 %	2.7 %	11.8 %
	3	2.4 %	7.7 %	2.6 %	11.3%
	4	2.4 %	7.3 %	2.5 %	10.9 %
	5	2.1 %	7.1 %	2.3 %	10.3 %
	6	1.9 %	7.1 %	2.1 %	9.9 %
	7	1.8 %	6.7 %	1.9 %	9.6 %
	8	1.7 %	6.6 %	1.9 %	9.2 %

Table 6.18: Simulation results for the fatigue loads analysis for the NREL 5-MW and DTU 10-MW blades

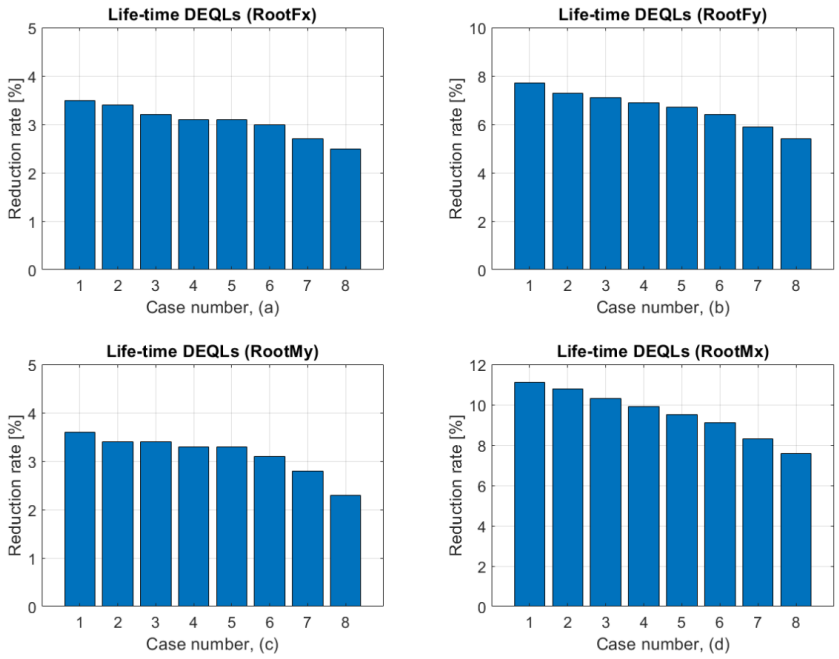

Figure 6.35: Reduction rates of DELs according to different design cases for the NREL blade

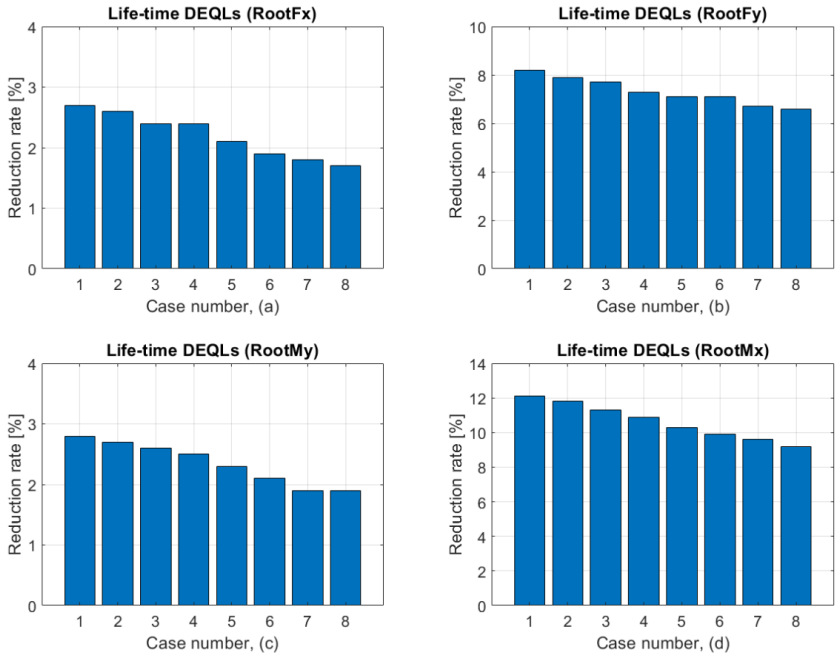

Figure 6.36: Reduction rates of DELs according to different design cases for the DTU blade

Figure 6.37 shows the ratio of the peak to peak TMD stroke to the blade chord length where the blade-TMD is mounted. Design case 1 for the NREL 5-MW blade that has the best control performance is no longer feasible since the stroke ratio is over 1; that is, the peak to peak TMD stroke exceeds the available space for the TMD operation. For the DTU 10-MW blade, case 2 also has the stroke issue. So, the design cases near the blade tip should be excluded from the list of the feasible designs.

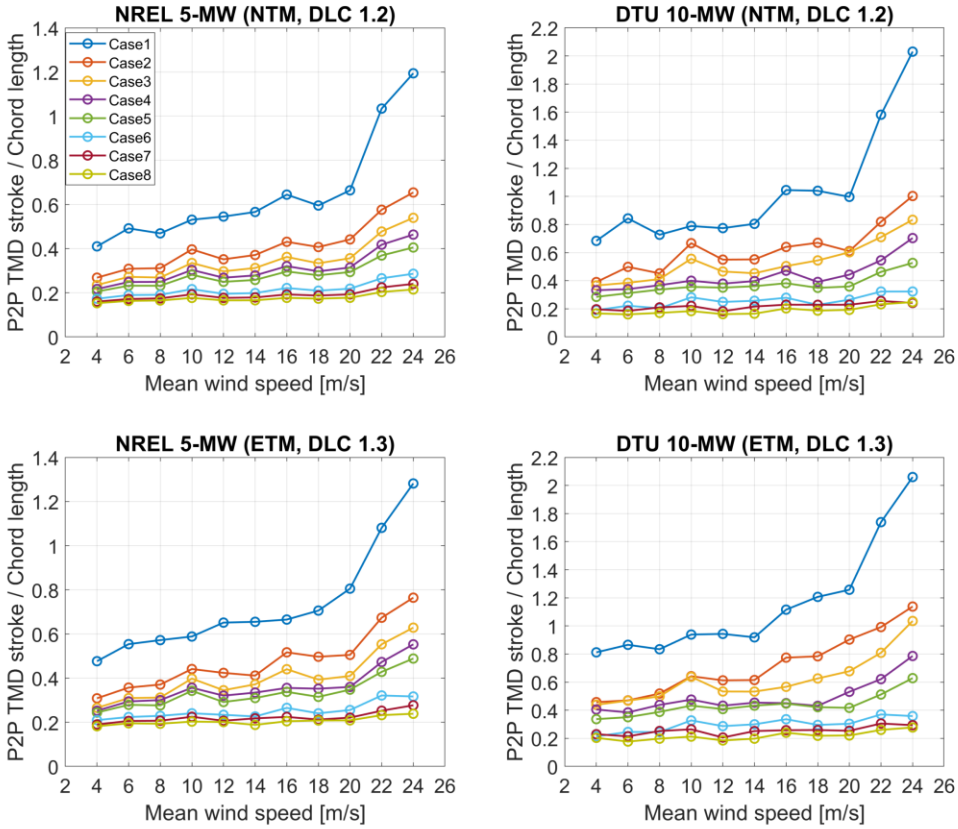

Figure 6.37: Ratio of the peak to peak TMD stroke to the chord length where the TMD is mounted

6.2.2 Extreme Load Analysis

DLC 1.3 is characterized by the extreme turbulence model and plays a significant role in driving the extreme loads on the turbine structures. The radical changes of wind speed due to the extreme turbulence intensity significantly affect the dynamic response of turbine components and create large deflections and loads on the turbine components. So, DLC 1.3 a critical load case in wind turbine design, particularly for the blades. The conditions for DLC 1.3 are defined in Figure 4.4 and the turbulence intensity follows the IEC category B. The total number of simulations for all cases (Baseline, case 1 to 8) is 1782 (each 109: 11 wind bins, 3 yaw errors (-8, 0 8 degrees) and 6 random seeds) and the simulation length is 30 minutes. The wind speeds used for DLC 1.3 are ranged in the entire operational region (4 to 24 m/s) and yaw errors are set to ± 8 degrees. The performance indicators are the maximum edgewise blade tip displacement and the maximum in-plane moments at the blade root. Figure 6.38 and 6.39 shows the blade edgewise tip deflection and the ultimate in-plane moments at the blade root. It can be seen that the extreme tip deflection reaches a maximum at a yaw error of -8 degree at the mean wind speed of 10 m/s. The ultimate in-plane moments occur at a yaw error of -8 degree together with a mean wind speed of 12 m/s. The performance indicators are compared with the baseline case where the extreme values occur in order to present the reduction rates as seen in Table 6.19. The extreme loads can also be improved by the blade-TMD as in the fatigue case. Similar to the fatigue load analysis results, the TMD located closer to the blade tip provides better performance. However, given the TMD stroke, design cases 1 and 2 are infeasible as shown in Figure 6.37. Considering both the TMD performance and the stroke, design case 3 would be the most promising to improve

the edgewise structural response. Figure 6.40 shows time response plot for different wind speeds to show the impact of the blade-TMD.

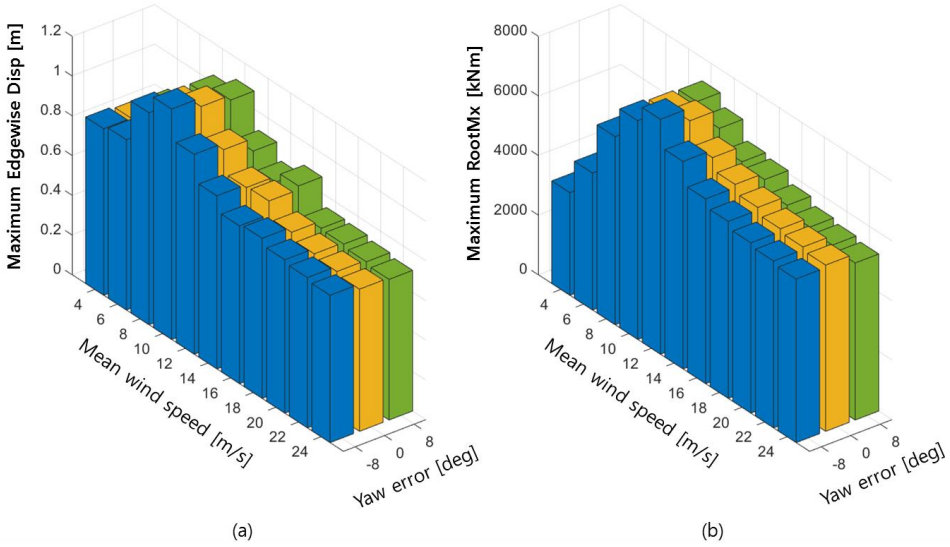

Figure 6.38: Ultimate loadings as functions of the yaw errors and β for the NREL blade, (a): blade root moment (fore-aft), (b): blade root moment (StS)

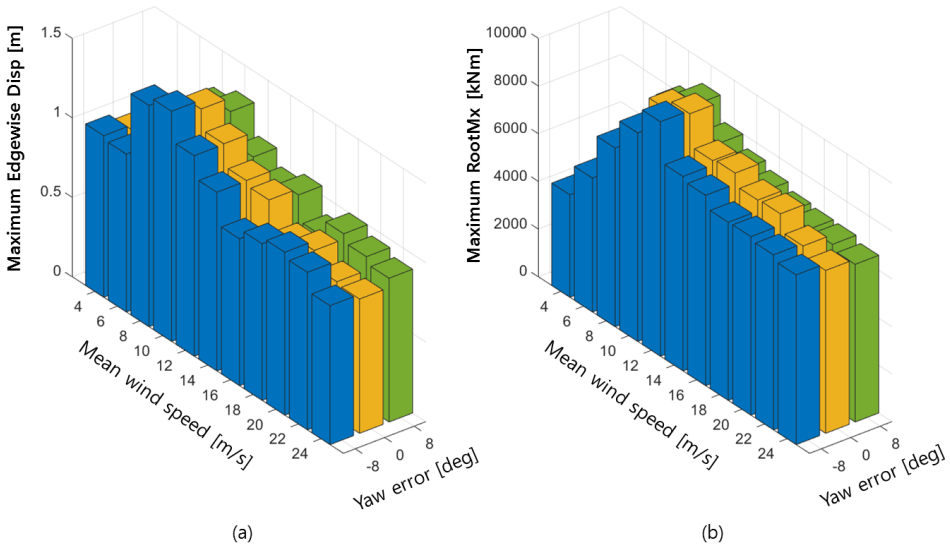

Figure 6.39: Ultimate loadings as functions of the yaw errors and β for the DTU blade, (a): blade root moment (fore-aft), (b): blade root moment (StS)

Blade	Case	*Maximum Edgewise disp* *(Out of plane)*	*Maximum RootM_x* *(In-plane)*
NREL 5-MW Blade	1	7.7 %	8.3 %
	2	7.5 %	8.0 %
	3	7.3 %	7.9 %
	4	7.4 %	7.6 %
	5	7.3 %	7.7 %
	6	7.3 %	7.9 %
	7	6.9 %	7.2 %
	8	6.2 %	6.7 %
DTU 10-MW Blade	1	9.6 %	9.4 %
	2	9.1 %	9.4 %
	3	8.9 %	9.1 %
	4	8.8 %	8.5 %
	5	8.7 %	8.6 %
	6	8.6 %	8.6 %
	7	8.4 %	8.5 %
	8	7.5 %	7.7 %

Table 6.19: Simulation results for the extreme loads analysis for the NREL and DTU blade

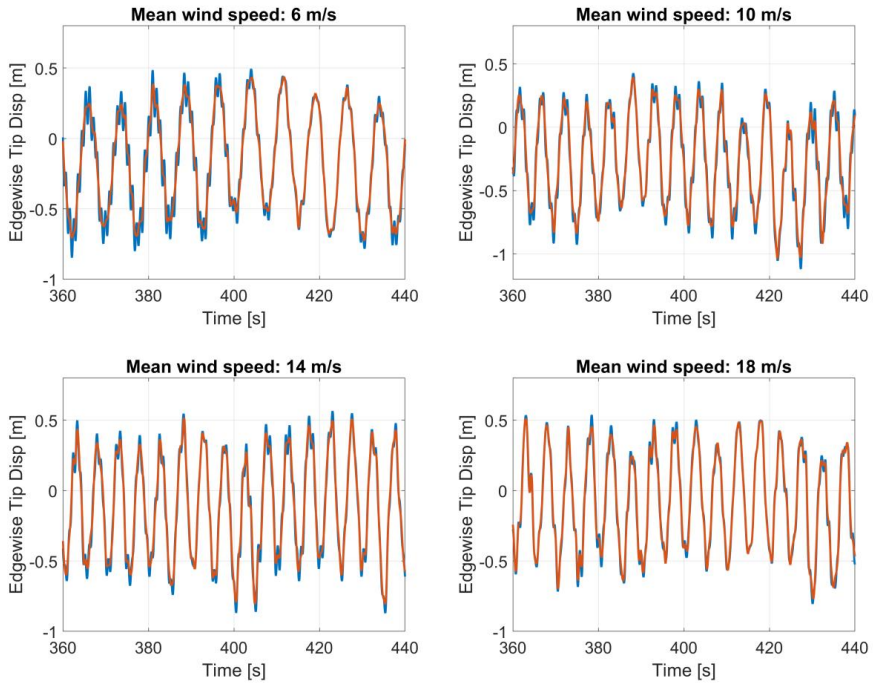

Figure 6.40: Time response of the blade motion in the edge-wise direction (DTU 10-MW)

6.2.3 Sensitivity Analysis

In order to investigate the robustness of the optimal design formulas determined in Section 5.2, a sensitivity analysis is performed to measure the performance variance according to the change in the TMD parameters such as the mass ratio, location, frequency ratio and damping ratio. Among the four parameters, a single parameter for evaluating the sensitivity is changed within a specific range, and the remaining parameters are set to their original values and fixed. Case 1, 2 and 3 are adopted for the sensitivity analysis. Figure 6.41 shows the sensitivity analysis results. The performance indicator (y-axis) is the reduction rate of the standard deviation of the blade edgewise tip displacement compared to the baseline case. The normal turbulence field with a mean wind speed of 10 m/s is applied for the simulation.

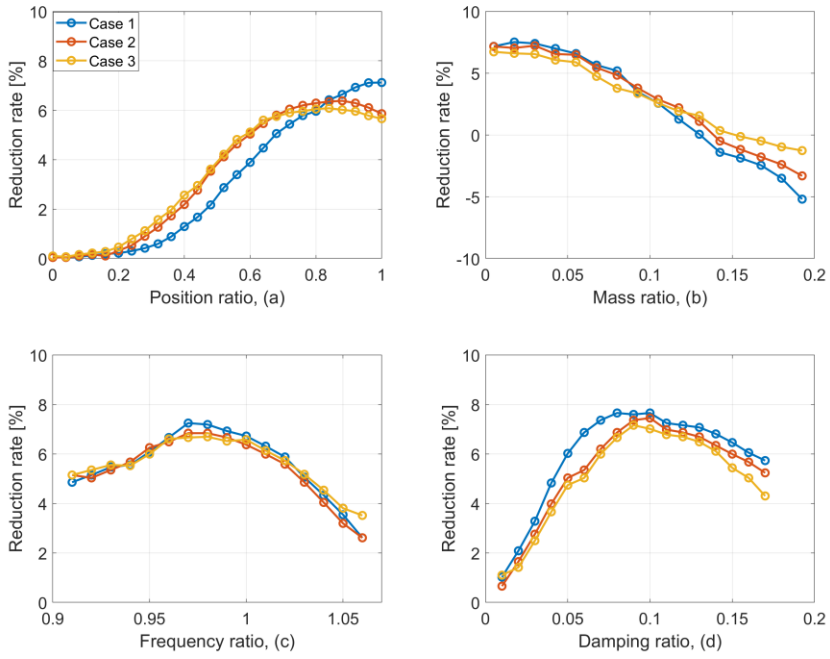

Figure 6.41: Sensitivity analysis result as a function of (a): position ratio, (b): mass ratio, (c): frequency ratio, (d): damping ratio

There are several meaningful observations to be made from the sensitivity analysis:

- As shown in Figure 6.41 (a), the best control performance can be achieved as the blade-TMD is positioned closer to the blade tip. This is because the vibrational energy is mostly concentrated near the blade tip, and the centrifugal force, which plays a critical role in driving the blade TMD, becomes larger toward the blade tip. Also, the control performance is negligible below the position ratio of 0.3, but it increases rapidly in the position ratio range of 0.3 to 0.8, and then the slope is noticeably reduced near the blade tip. Based on the observation, one can expect that case 3 can be considered as a better design in comparison with case 1 as case 3 has comparable control performance with case 1 while the blade-TMD is mounted on the lower position. This is a quite reasonable inference considering that the space in the vicinity of the blade tip is very narrow.
- In general structural control theory, it is widely known that the control performance improves as the mass ratio increases within a certain range. However, in the case of the blade-TMD, quite a different pattern arises compared to the general theory. The control performance decreases with the increased mass ratio, and the TMD even has a negative effect when the mass ratio is beyond a certain level. The blade rotating at a constant speed during normal operation is additionally deflected in the in-plane direction (mostly edgewise direction during normal operation) by the self-weight of the blade. The deflection grows with the additional mass of the blade-TMD. So, control performance is very sensitive to the mass ratio and should be carefully selected for the blade-TMD design.

- The changes in frequency ratio in the region exceeding the optimum frequency ratio have greater influences on the control performance compared to the changes in the region lower than the optimum frequency ratio. In contrast, the control performance drops rapidly as the damping ratio goes to 0. Beyond the optimal damping ratio, increase in the damping ratio does not necessarily improve the control performance. Based on the observations, it can be deduced that the parameters for the frequency ratio and the optimal ratio have less impact on the performance compared to the other two parameters (TMD mass and location).
- Collectively, the sensitivity analysis results show that the optimal parameters derived by the design formulas are close to the true optimum.

CHAPTER 7

CONCLUSIONS

The research presented in this dissertation provides insight into the potential benefits and impacts of passive and semi-active structural control techniques for OWTs. The major contributions and concluding remarks of the dissertation are listed below:

- As discussed in Chapter 1, the majority of previous research regarding the application of structural control techniques to OWTs has been limited to reduced order models considering some of critical modes of the turbine and control system rather than using a high-fidelity wind turbine design code, potentially neglecting the complicated non-linear dynamics of OWTs. This is likely to result in a further decrease in modeling fidelity in the case of a floating substructure that has more complex dynamics. In order to address such issues, Lackner et al. developed a new structural control simulator in 2011, named FAST-SC, which was coupled with FASTv7 and enabled the fully-coupled aero-hydro-servo-elastic simulations while analyzing the impact of TMDs for floating OWTs. La Cava and Lackner updated the structural control tool as a module (named TMD) to be compatible with FASTv8. The module "TMD" coupled with FASTv8 has been limited to considering two independent single degree of freedom TMDs operating only passively for turbine tower control. In this dissertation, the control module has been updated to add a variety of functions and control devices, i.e. omni-directional pendulum-type mass dampers, tuned liquid column dampers, semi-active control algorithms, etc. The newly developed control module coupled with FASTv8, allows for aero-hydro-servo-elastic simulations

considering the rigorous analysis of the impact of structural control. This provides a high-fidelity examination of various structural control techniques by utilizing a number of functions and reliable OWTs models already provided in FASTv8.

- With the developed tool, the structural control devices to improve structural responses of the turbine tower can be optimized. Through the results of the optimization problem, the influences of design variables on the control performance and the dynamic characteristic of the system are thoroughly analyzed, and the design guidelines of each device for the turbine tower control are presented by establishing the optimal design formulas for important parameters.
- The developed module can also employ the TMD for blade response control. In the current trend towards the use of larger rotors for modern multi-megawatt wind turbines, the diameter of turbine blades increases and they become more flexible compared to the shorter blades, making them relatively vulnerable to external loads. So, it is also highly desirable to apply structural control concepts to the blades themselves, rather than confining them to towers. With a comprehensive set of optimization problem for the blade-TMDs, we proposed generalized optimal design formulas encompassing different blade-TMD locations and mass ratios as well as the frequency ratio and the damping ratio. The design formulas are easy to use and can be a guideline to apply to other multi-megawatts OWTs.
- A reduced order ES approach is conducted for the preliminary design of TLCDs. The preliminary design presented the appropriate ranges of the design variables of interest for the full-scale multi-objective optimization problem. Through the multi-objective optimization scheme using NSGA-II with parallel computing, the non-

dominant Pareto optimal front was derived, which provides insight for a decision maker considering a trade-off between the two objective functions in conflict. In addition, the dynamic characteristics of the design variables are investigated based on the optimization results. Meanwhile, it was confirmed that the mass ratio is a critical factor that causes the trade-off between two objectives in conflict. Also, the superiority of using the non-uniform cross-sections was confirmed in terms of the control performance and sizing of the TLCDs.

- With the determined site-specific metocean conditions, fatigue and extreme loads analyses were performed by running a series of design load cases in order to investigate the impacts of the optimized structural control devices. The results showed that the structural control techniques can play a critical role in reducing the fatigue and extreme loads on the tower and blade. Moreover, the control performance of each control device was compared to show their effectiveness according to the external loading conditions.

The summary of the control effects of each control device are as follows:

- **Fatigue load analysis for the tower response control:**

- The TMDs have better control performance than the TLCDs for the NREL 5-MW fixed-bottom OWT (monopile). In particular, the S-A TMD can reduce the lifetime DELs for the tower base moments in the fore-aft and side-to-side direction by 18.5% and 79.3%, respectively. For the NREL 5-MW floating OWT (TLP), the TLCDs are much more effective at reducing the fore-aft motion of the floating OWT. Design case 3 can reduce the lifetime DELs in the fore-aft direction by 13.2%, whereas the

reduction rate of the S-A TMD is only 4.4%. As such, the control effects differ significantly depending on the type of the support structure and the control device. As discussed in Chapter 6, this is due to the stop-spring operation and the detuning issues of the control devices. Therefore, it may be concluded that the TMDs are more promising for fixed-bottom OWTs with lower probability of stop-spring operation, whereas the TLCDs are more advantageous for floating OWTs with higher probability of the stop-spring operation.

- For the GE 6-MW monopile OWT, the S-A TMD using the DB-GH algorithm has the best control performance, and it can reduce the lifetime DELs for the tower base moments in the fore-aft and side-to-side direction by 11.8% and 64.5%, respectively. The DB-GH algorithm is expected to be more effective during normal operation due to its intrinsic frequency response characteristic as discussed in Chapter 5. Similar to the fixed-bottom OWT, the DB-GH control approach also has the best performance in reducing lifetime DELs for the floating TLP, especially for the side-to-side direction. It can reduce the lifetime DELs (StS) by 64% (water depth of 55 m) and 25.9% (water depth of 100 m).

- **Extreme load analysis for the tower response control:**

- Unlike the fatigue load analysis, the control effects are not significantly different between the fore-aft and side-to-side direction. This is because the blades are feathered to 90 degrees, so there is minimal difference in aerodynamic damping between the two directions.

- The S-A TMD using the IVB-GH algorithm can reduce the average maximum tower base moments of the NREL monopile OWT by 25.3% (fore-aft) and 32.2% (side-to-side). For the NREL TLP OWT, TLCDs have better control performance than the TMDs. Design case 1 can reduce the average maximum tower base moments of the NREL TLP OWT by 19.2% (fore-aft) and 19.6% (Side-to-side). Similar to the fatigue load analysis, this is due to the stop-spring operation that causes negative effects on the tower responses for the TMD. Consequently, the TMDs are more effective to reduce extreme loads on the fixed-bottom OWT, whereas the TLCDs are more promising for the floating OWT.
- For the GE 6-MW monopile OWT, the S-A TMD has better control performance compared to the passive TMD, and it can reduce the magnitude of the maximum tower base moment by 31.7%. For the GE 6-MW TLP OWT, the IVB-GH control approach is still effective for the water depth of 100 m. It can reduce the magnitude of the maximum tower base moment by 9%. In contrast, almost all results show that structural control has negative impacts on the extreme loads of the floating OWT installed in the shallow water depth. The negative effects are because the dominant loading is mostly distributed in the lower frequency region, which causes detuning of the TMD.

- **Blade response control:**

- Eight different design cases were selected from the optimal design formulas determined in Chapter 3. The control performance drops as the position of the TMD is moved towards the root. The lifetime edgewise blade root damage equivalent

moment can be reduced from 7.6% to 11.1% for the NREL blades and 9.2% to 12.1% for the DTU blades, depending on the TMD location. Similar to the fatigue load reductions, the extreme edgewise root moment can be reduced from 6.7% to 8.3% for the NREL blades and 7.7% to 9.4% for the DTU blades. Despite the use of the heavier TMD at the lower positions, complete compensation of the control performance cannot be achieved. Nevertheless, some of design cases cannot be regarded as feasible because the peak to peak TMD stroke exceeds the available space (on the scale of chord length) for the TMD operation. Thus, the trade-off between the control performance and the TMD stroke should be considered when selecting the designs.

APPENDIX A

NOMENCLATURE

Common nomenclature	
O	Origin point of global inertial reference frame
P	Origin point of non-inertial reference frame fixed to tower or blade
TMD	Origin point of a TMD
G	Axis orientation of global reference frame
$\vec{r}_{TMD/O_G}$	Position vector of TMD with respect to O with orientation G
$\vec{r}_{P/O_G}$	Position vector of tower with respect to O_G
$\vec{r}_{TMD/P_G}$	Position vector of TMD with respect to P_G
$\dot{\theta}$	Element of angular velocity in the direction of *x*
$\dot{\phi}$	Element of angular velocity in the direction of *y*
$\dot{\psi}$	Element of angular velocity in the direction of *z*
m	TMD mass
c_x	TMD damping coefficient in the direction of *x*
c_y	TMD damping coefficient in the direction of *y*
k_x	TMD spring stiffness in the direction of *x*
k_y	TMD spring stiffness in the direction of *y*
Tower-TMD	
T	Axis orientation of tower reference frame with unit vectors
$R_{T/G}$	3×3 rotation matrix transforming orientation G to T
$R_{G/T}$	3×3 rotation matrix transforming orientation T to G
$\vec{r}_{TMD/O_T}$	$=R_{T/G}\vec{r}_{TMD/O_G}$ Position of tower-TMD with respect to O_T
$\vec{r}_{P/O_T}$	$=R_{T/G}\vec{r}_{P/O_G}$ Position of tower with respect to O_T
$\vec{r}_{TMD/P_T}$	$=R_{T/G}\vec{r}_{TMD/P_G}$ Position of tower-TMD with respect to P_T
$\vec{\omega}_{T/O_T}$	Angular velocity vector of tower in orientation T
$\vec{\alpha}_{T/O_T}$	Translational acceleration vector of tower in orientation T
$\vec{\alpha}_{G/O_T}$	Gravity vector with respect to O_T
$F_{z,TMD/O_T}$	Reaction force by tower-TMD acting on tower in the direction of *z*
Blade-TMD	
B	Axis orientation of blade reference frame with unit vectors
$R_{B/G}$	3×3 rotation matrix transforming orientation G to B
$R_{G/B}$	3×3 rotation matrix transforming orientation B to G
$\vec{r}_{TMD/O_B}$	$=R_{B/G}\vec{r}_{TMD/O_G}$ Position of blade-TMD with respect to O_B
$\vec{r}_{P/O_B}$	$=R_{B/G}\vec{r}_{P/O_G}$ Position of blade with respect to O_B
$\vec{r}_{TMD/P_B}$	$=R_{B/G}\vec{r}_{TMD/P_G}$ Position of blade-TMD with respect to P_B
$\vec{\omega}_{B/O_B}$	Angular velocity vector of tower in orientation B
$\vec{\alpha}_{B/O_B}$	Translational acceleration vector of tower in orientation B
$\vec{\alpha}_{G/O_B}$	Gravity vector with respect to O_B
$F_{x,TMD/O_B}$	Reaction force by blade-TMD acting on blade in the direction of *x*
$F_{z,TMD/O_B}$	Reaction force by blade-TMD acting on blade in the direction of *z*

Table A.1: Nomenclature for the tower-TMD and blade-TMD

Nacelle-TLCDs	
N	Axis orientation of nacelle reference frame with unit vectors
$R_{N/G}$	3×3 rotation matrix transforming orientation G to N
$R_{G/N}$	3×3 rotation matrix transforming orientation N to G
${}^{G}\vec{r}^{OW}$	Position vector of center of liquid mass with respect to O with orientation G
${}^{G}\vec{r}^{OP}$	Position vector from point O to point P in global coordinate
${}^{N}\vec{r}^{PW}$	Position vector from point P to point W in nacelle coordinate
${}^{OW}_{G}[x\ y\ z]^{T}$	Components of position vector ${}^{G}\vec{r}^{OW}$
${}^{PW}_{N}[x\ y\ z]^{T}$	Components of position vector ${}^{N}\vec{r}^{PW}$
W	Origin point of center of liquid mass
${}^{G}\vec{\omega}^{N}$	Angular velocity vector of nacelle in orientation G
${}^{G}\vec{\alpha}^{N}$	Translational acceleration vector of nacelle in orientation G
$F_x^{W_{F_V}}$	Reaction force by water in front vertical column acting on nacelle in the direction of x
$F_x^{W_{B_V}}$	Reaction force by water in back vertical column acting on nacelle in the direction of x
$F_y^{W_{F_V}}$	Reaction force by water in front vertical column acting on nacelle in the direction of y
$F_y^{W_{B_V}}$	Reaction force by water in back vertical column acting on nacelle in the direction of y
$F_x^{W_{L_V}}$	Reaction force by water in left vertical column acting on nacelle in the direction of x
$F_x^{W_{R_V}}$	Reaction force by water in right vertical column acting on nacelle in the direction of x
$F_y^{W_{L_V}}$	Reaction force by water in left vertical column acting on nacelle in the direction of y
$F_y^{W_{R_V}}$	Reaction force by water in right vertical column acting on nacelle in the direction of y
$F_x^{W_{H_{SS}}}$	Reaction force by water in horizontal column acting on nacelle in the direction of x
$F_y^{W_{H_{FA}}}$	Reaction force by water in horizontal column acting on nacelle in the direction of y
$F_z^{W_{H_{SS}}}$	Reaction force by water in horizontal column acting on nacelle in the direction of z
$F_z^{W_{H_{FA}}}$	Reaction force by water in horizontal column acting on nacelle in the direction of z
A_V	Vertical cross-sectional area (m^2)
A_H	Horizontal cross-sectional area (m^2)
α	Area ratio of A_V to A_H
B	Horizontal length (m)
L	Total length (m)
L_{ee}	Equivalent length with the same energy (m)
L_{em}	Equivalent length with the same mass (m)
f_{TLCD}	Tuning frequency of a TLCD (Hz)
μ	Mass ratio between SS and FA-TLCD
ρ	Liquid density (kg/m^3)
ξ	Head loss coefficient

Table A.2: Nomenclature for the nacelle-TLCD

APPENDIX B

EXPECTED VALUES AND CORRESPONDING PROBABILITIES

Wind Speed Bin (m/s)(→) / Misalignment Bin (deg)(↓)	3 ~ 5			5 ~ 7			7 ~ 9			9 ~ 11			11 ~ 13			13 ~ 15			15 ~ 17			17 ~ 19			19 ~ 21			21 ~ 23			23 ~ 25		
	Hs [m]	Tp [s]	γ [-]	Hs [m]	Tp [s]	γ [-]	Hs [m]	Tp [s]	γ [-]	Hs [m]	Tp [s]	γ [-]	Hs [m]	Tp [s]	γ [-]	Hs [m]	Tp [s]	γ [-]	Hs [m]	Tp [s]	γ [-]	Hs [m]	Tp [s]	γ [-]	Hs [m]	Tp [s]	γ [-]	Hs [m]	Tp [s]	γ [-]	Hs [m]	Tp [s]	γ [-]
-180 ~ -165	1.9	7.8	1.0	2.1	7.9	1.0	2.3	7.8	1.0	2.6	7.8	1.0	2.9	8.1	1.0	2.7	8.4	1.0	2.3	7.9	1.0	1.6	7.4	1.0	2.8	7.9	1.0	2.8	8.7	1.0	1.7	7.3	1.0
-165 ~ -150	1.6	7.8	1.0	2.0	7.7	1.0	2.1	8.2	1.0	2.6	8.1	1.0	3.1	9.1	1.0	2.3	7.9	1.0	1.9	7.9	1.0	2.8	8.2	1.0	2.7	8.1	1.0	1.8	7.0	1.0	2.3	8.2	1.0
-150 ~ -135	2.1	8.3	1.0	1.9	7.9	1.0	2.1	8.1	1.0	2.0	8.2	1.0	1.9	8.0	1.0	2.4	7.9	1.0	2.9	8.9	1.0	2.4	8.5	1.0	2.1	7.7	1.0	5.2	8.5	1.0	2.5	8.2	1.0
-135 ~ -120	1.8	8.2	1.0	1.9	8.3	1.0	2.0	8.0	1.0	2.1	8.2	1.0	1.9	7.7	1.0	2.4	8.8	1.0	3.0	9.8	1.0	2.6	8.9	1.0	2.7	9.0	1.0	2.4	7.9	1.0	4.1	9.2	1.0
-120 ~ -105	2.0	8.3	1.0	2.2	8.7	1.0	2.0	8.4	1.0	2.3	8.2	1.0	2.4	8.6	1.0	2.5	9.5	1.0	2.5	8.6	1.0	2.0	8.9	1.0	2.8	9.7	1.0	2.2	8.9	1.0	3.1	9.9	1.0
-105 ~ -90	2.0	8.7	1.0	2.2	8.4	1.0	2.2	8.7	1.0	2.3	8.6	1.0	2.5	9.0	1.0	2.0	8.3	1.0	2.2	8.9	1.0	2.4	8.6	1.0	3.1	9.5	1.0	2.1	8.7	1.0	3.9	9.9	1.0
-90 ~ -75	2.1	8.4	1.0	2.5	8.7	1.0	2.5	8.5	1.0	2.4	8.7	1.0	2.6	9.1	1.0	2.8	9.1	1.0	2.7	9.2	1.0	2.0	8.8	1.0	3.1	9.4	1.0	2.5	9.1	1.0	2.5	9.5	1.0
-75 ~ -60	2.4	8.4	1.0	2.4	8.4	1.0	2.5	8.6	1.0	2.7	8.5	1.0	3.4	9.1	1.0	3.5	9.3	1.0	3.4	9.3	1.0	2.9	8.7	1.0	2.9	9.4	1.0	2.9	9.7	1.2	4.7	9.2	1.2
-60 ~ -45	2.4	8.1	1.0	2.6	8.5	1.0	2.6	8.0	1.0	2.8	8.1	1.0	3.3	8.5	1.0	3.3	8.8	1.0	3.4	8.8	1.0	4.2	9.0	1.1	3.4	8.9	1.4	3.6	9.4	1.5	4.5	8.4	1.7
-45 ~ -30	2.3	7.6	1.0	2.3	7.9	1.0	2.7	7.7	1.0	2.8	7.9	1.0	3.4	7.8	1.0	3.5	7.9	1.0	3.2	8.0	1.1	3.9	8.7	1.4	4.7	9.1	1.5	4.4	8.9	1.6	4.0	8.3	2.0
-30 ~ -15	2.5	7.4	1.0	2.4	7.4	1.0	2.6	7.4	1.0	3.0	7.1	1.0	3.2	7.4	1.0	3.0	7.5	1.1	3.8	7.8	1.4	4.2	8.1	1.7	3.9	7.6	2.0	4.7	8.4	2.1	4.1	7.4	2.4
-15 ~ 0	2.4	7.1	1.0	2.5	7.2	1.0	2.7	7.2	1.0	2.8	7.1	1.0	3.1	7.2	1.0	3.2	7.2	1.2	3.3	7.3	1.6	3.5	7.5	2.0	3.8	7.4	2.4	3.7	7.5	2.4	4.0	7.7	2.6
0 ~ 15	2.4	7.2	1.0	2.6	7.5	1.0	2.6	7.3	1.0	3.0	7.3	1.0	3.2	7.3	1.0	3.1	7.3	1.2	3.0	7.2	1.5	3.4	7.2	1.9	3.9	7.2	2.3	3.7	7.3	2.4	3.4	6.8	2.8
15 ~ 30	2.5	7.6	1.0	2.4	7.5	1.0	2.6	7.5	1.0	3.1	7.7	1.0	3.3	7.6	1.0	3.4	7.7	1.1	3.7	7.7	1.3	3.6	7.4	1.6	3.8	7.7	2.1	4.1	8.1	2.1	3.5	7.3	2.3
30 ~45	2.4	7.8	1.0	2.6	7.9	1.0	2.6	7.9	1.0	3.0	8.0	1.0	3.2	7.9	1.0	3.8	8.2	1.0	4.0	8.2	1.0	3.6	8.1	1.2	3.8	7.8	1.3	3.4	8.2	1.8	4.6	8.6	2.3
45 ~ 60	2.6	8.2	1.0	2.5	8.0	1.0	2.6	8.1	1.0	3.1	8.3	1.0	3.4	8.4	1.0	3.8	8.6	1.0	3.5	8.4	1.0	3.6	8.3	1.0	4.1	8.8	1.3	3.5	8.3	1.4	4.1	8.4	1.6
60 ~ 75	2.3	8.3	1.0	2.4	8.2	1.0	2.7	8.5	1.0	2.7	8.4	1.0	3.0	8.6	1.0	3.8	9.0	1.0	3.6	8.7	1.0	4.5	8.9	1.0	4.6	9.0	1.0	3.7	9.3	1.0	4.7	8.8	1.7
75 ~ 90	2.2	8.4	1.0	2.6	8.5	1.0	2.8	8.6	1.0	2.7	8.5	1.0	3.0	8.9	1.0	3.4	9.0	1.0	3.9	9.1	1.0	3.9	9.1	1.0	4.0	9.3	1.0	3.0	8.8	1.0	4.6	9.1	1.0
90 ~ 105	2.2	8.8	1.0	2.2	8.8	1.0	2.4	8.6	1.0	2.8	8.8	1.0	3.2	9.1	1.0	3.3	9.4	1.0	3.6	9.0	1.0	4.4	9.5	1.0	3.9	9.1	1.0	4.3	8.7	1.0	5.8	10.0	1.0
105 ~ 120	2.2	9.1	1.0	2.0	8.7	1.0	2.5	9.0	1.0	2.8	9.2	1.0	3.0	9.3	1.0	3.0	9.3	1.0	3.6	9.2	1.0	4.2	9.7	1.0	4.6	9.3	1.0	4.7	9.1	1.0	5.1	10.0	1.0
120 ~ 135	1.9	8.9	1.0	2.1	9.0	1.0	2.5	8.9	1.0	2.6	9.5	1.0	3.0	9.2	1.0	2.6	9.2	1.0	2.9	9.3	1.0	4.1	9.6	1.0	4.1	9.3	1.0	4.4	9.9	1.0	3.3	10.0	1.0
135 ~ 150	2.0	9.0	1.0	2.2	9.2	1.0	2.4	9.2	1.0	2.4	9.3	1.0	3.0	9.6	1.0	3.2	9.6	1.0	2.5	9.1	1.0	2.9	9.3	1.0	3.6	10.0	1.0	4.0	10.5	1.0	3.7	9.4	1.0
150 ~ 165	1.8	9.1	1.0	2.1	9.1	1.0	2.3	9.4	1.0	2.6	9.3	1.0	2.7	9.4	1.0	2.8	9.6	1.0	3.2	9.3	1.0	3.6	9.2	1.0	2.8	9.1	1.0	2.5	9.2	1.0	3.4	9.8	1.0
165 ~ 180	1.8	9.3	1.0	2.2	9.5	1.0	2.5	9.5	1.0	2.6	9.4	1.0	2.5	9.8	1.0	2.7	9.5	1.0	3.1	9.6	1.0	4.3	10.2	1.0	3.2	9.8	1.0	3.3	10.0	1.0	2.6	8.7	1.0

Table B.1: Expected values of H_s and T_p corresponding the intersection between U and β

Wind Speed Bin (m/s)(→) / Misalignment Bin (deg)(↓)	3 ~ 5	5 ~ 7	7 ~ 9	9 ~ 11	11 ~ 13	13 ~ 15	15 ~ 17	17 ~ 19	19 ~ 21	21 ~ 23	23 ~ 25
	Probability (%)										
-180 ~ -165	0.35	0.35	0.36	0.30	0.20	0.11	0.06	0.03	0.02	0.01	0.00
-165 ~ -150	0.40	0.40	0.39	0.30	0.23	0.11	0.06	0.03	0.02	0.00	0.00
-150 ~ -135	0.46	0.50	0.41	0.29	0.17	0.13	0.08	0.03	0.01	0.01	0.00
-135 ~ -120	0.52	0.52	0.59	0.31	0.26	0.17	0.08	0.03	0.04	0.01	0.02
-120 ~ -105	0.59	0.67	0.61	0.41	0.27	0.20	0.12	0.08	0.06	0.04	0.02
-105 ~ -90	0.76	0.78	0.64	0.45	0.31	0.26	0.16	0.17	0.09	0.03	0.03
-90 ~ -75	0.80	0.86	0.75	0.60	0.47	0.38	0.23	0.14	0.10	0.07	0.04
-75 ~ -60	0.88	0.96	0.87	0.67	0.61	0.35	0.27	0.18	0.12	0.08	0.07
-60 ~ -45	1.00	1.18	1.11	0.81	0.71	0.50	0.36	0.29	0.22	0.15	0.12
-45 ~ -30	0.90	1.25	1.08	0.93	0.78	0.60	0.39	0.32	0.26	0.17	0.14
-30 ~ -15	1.00	1.18	1.23	1.13	0.99	0.79	0.58	0.35	0.34	0.23	0.16
-15 ~ 0	0.90	1.21	1.33	1.37	1.16	1.18	0.90	0.54	0.43	0.30	0.14
0 ~ 15	0.90	1.05	1.24	1.29	1.11	1.09	0.98	0.63	0.44	0.27	0.16
15 ~ 30	0.71	1.00	1.12	1.05	0.97	0.81	0.80	0.48	0.30	0.22	0.21
30 ~45	0.66	0.81	0.92	0.84	0.74	0.54	0.43	0.32	0.29	0.16	0.11
45 ~ 60	0.60	0.65	0.69	0.65	0.54	0.41	0.28	0.20	0.14	0.14	0.11
60 ~ 75	0.46	0.52	0.57	0.54	0.39	0.35	0.23	0.10	0.10	0.06	0.06
75 ~ 90	0.50	0.49	0.50	0.43	0.36	0.21	0.14	0.08	0.05	0.02	0.03
90 ~ 105	0.38	0.44	0.51	0.42	0.30	0.19	0.10	0.08	0.03	0.02	0.02
105 ~ 120	0.37	0.38	0.43	0.37	0.21	0.15	0.09	0.06	0.02	0.01	0.01
120 ~ 135	0.33	0.40	0.43	0.30	0.20	0.14	0.08	0.04	0.01	0.00	0.00
135 ~ 150	0.34	0.36	0.40	0.26	0.16	0.09	0.09	0.05	0.01	0.01	0.00
150 ~ 165	0.33	0.28	0.30	0.24	0.16	0.10	0.06	0.04	0.01	0.00	0.00
165 ~ 180	0.34	0.32	0.36	0.27	0.17	0.10	0.06	0.02	0.03	0.01	0.00

Table B.2: Probabilities corresponding the intersection between U and β

APPENDIX C

FREQUENCY RESPONSE OF TOWER TOP MOTION FOR NREL 5-MW AND GE 6-MW OWTs

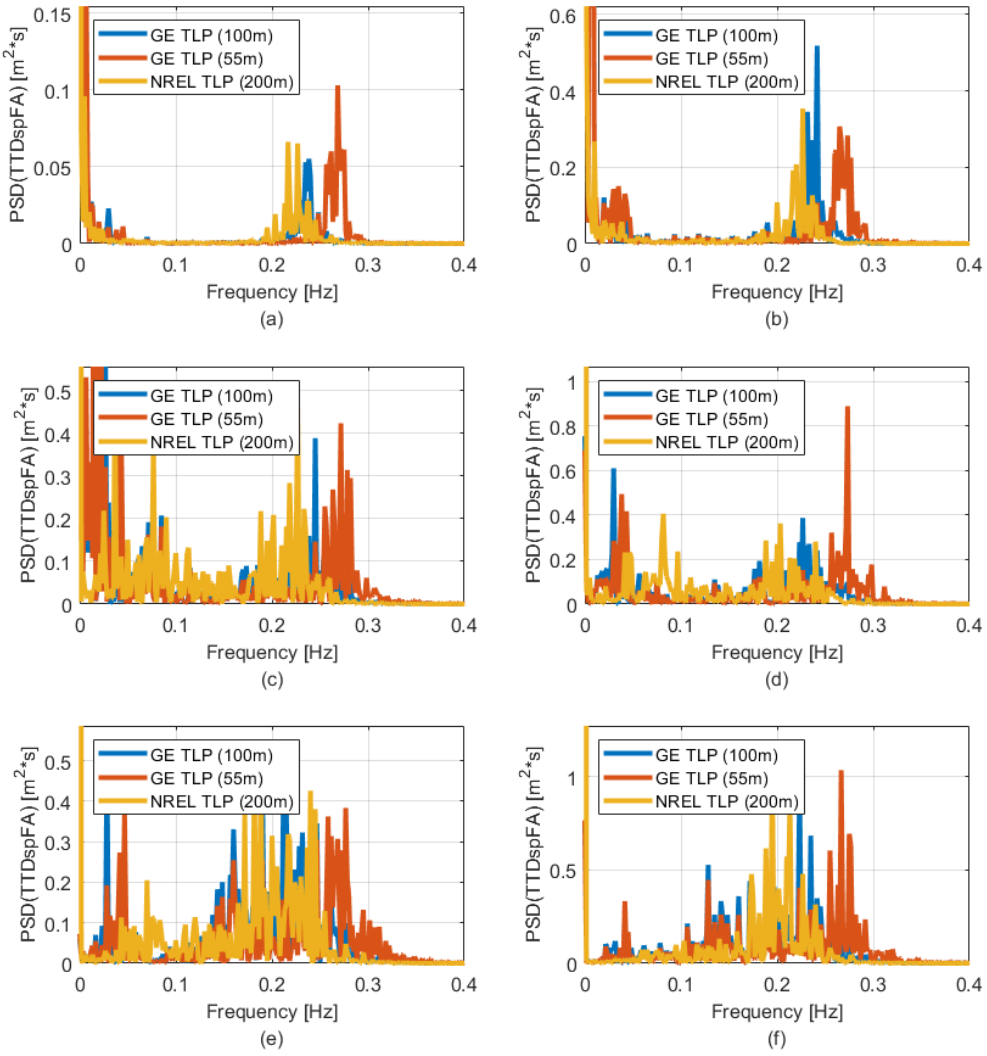

Figure C.1: Frequency response of TTDspFA for floating OWTs (NREL TLP and GE TLP), Mean wind speed of (a): 4 m/s, (b): 8 m/s, (c): 12 m/s, (d): 16 m/s, (e): 20 m/s, (f): 24 m/s

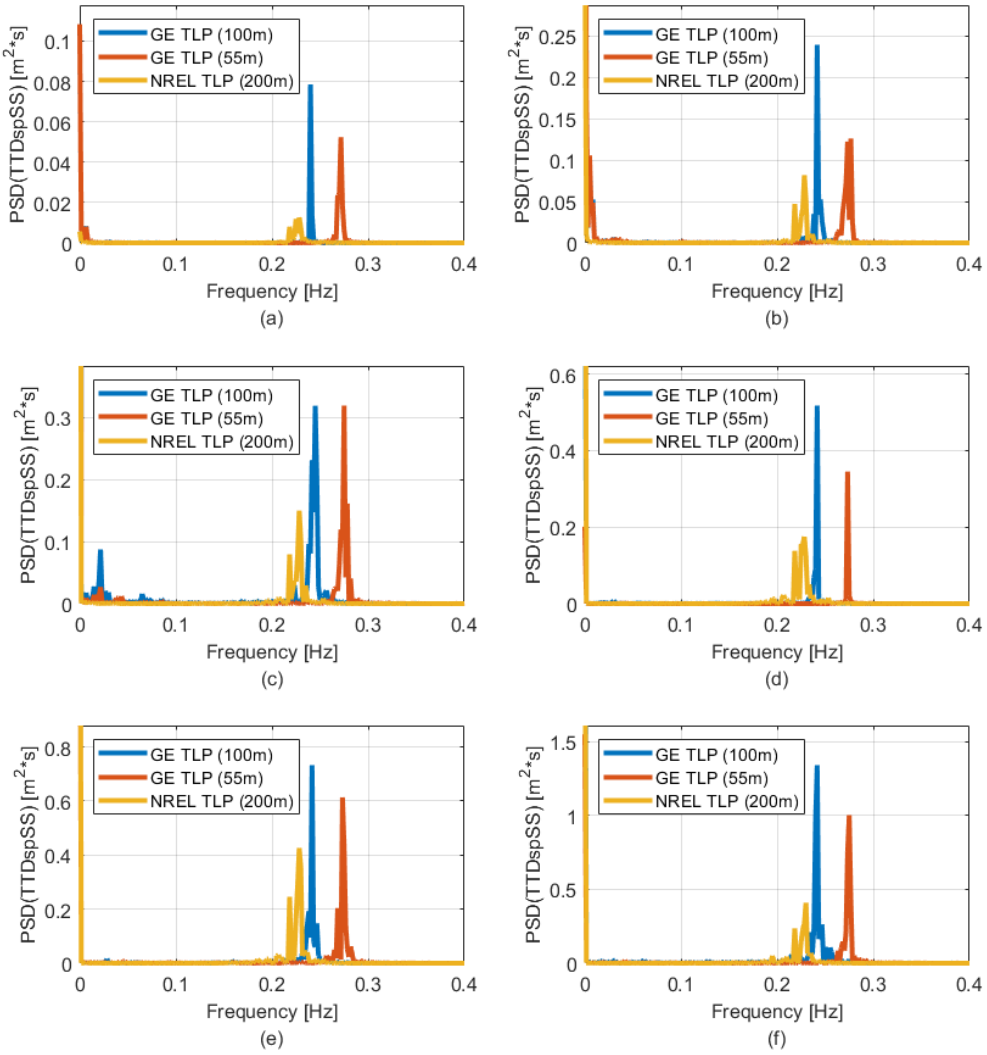

Figure C.2: Frequency response of TTDspSS for floating OWTs (NREL TLP and GE TLP), Mean wind speed of (a): 4 m/s, (b): 8 m/s, (c): 12 m/s, (d): 16 m/s, (e): 20 m/s, (f): 24 m/s

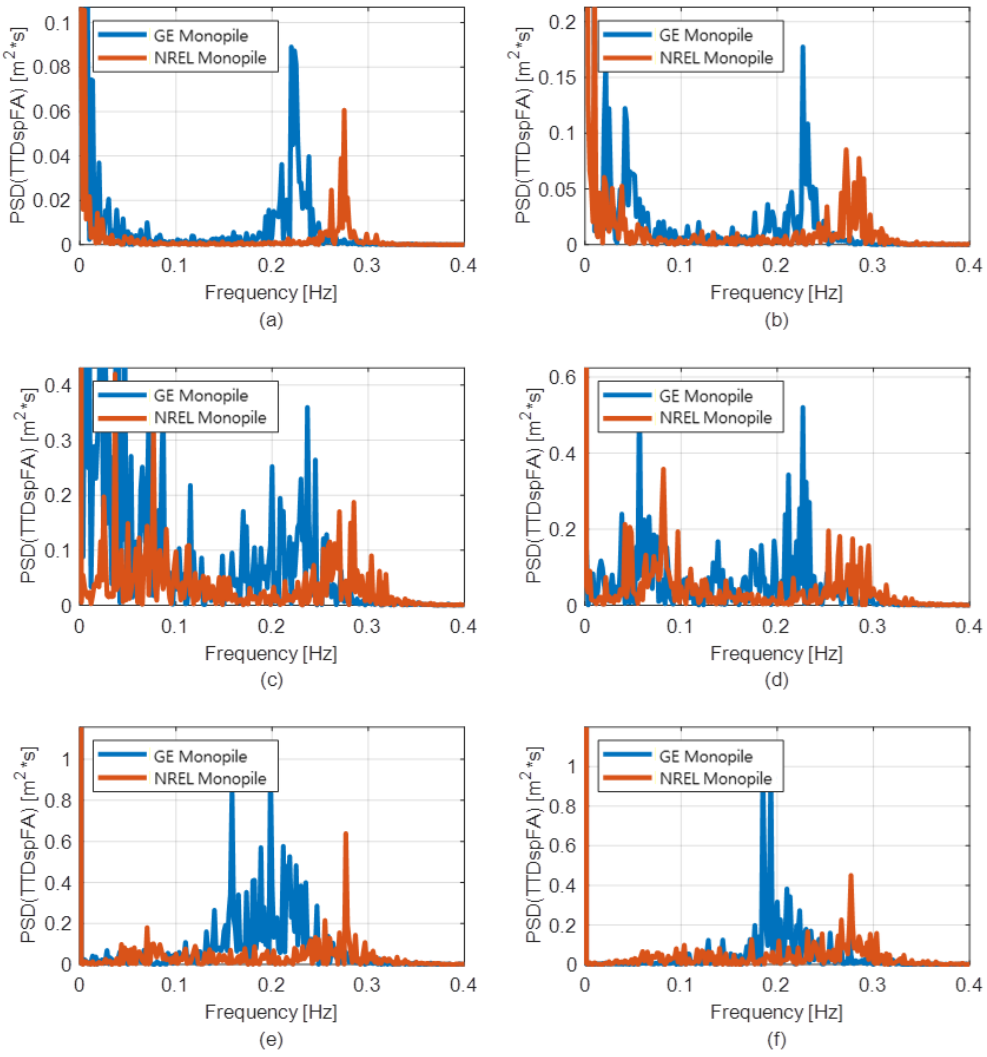

Figure C.3: Frequency response of TTDspFA for fixed-bottom OWTs (NREL monopile and GE monopile), Mean wind speed of (a): 4 m/s, (b): 8 m/s, (c): 12 m/s, (d): 16 m/s, (e): 20 m/s, (f): 24 m/s

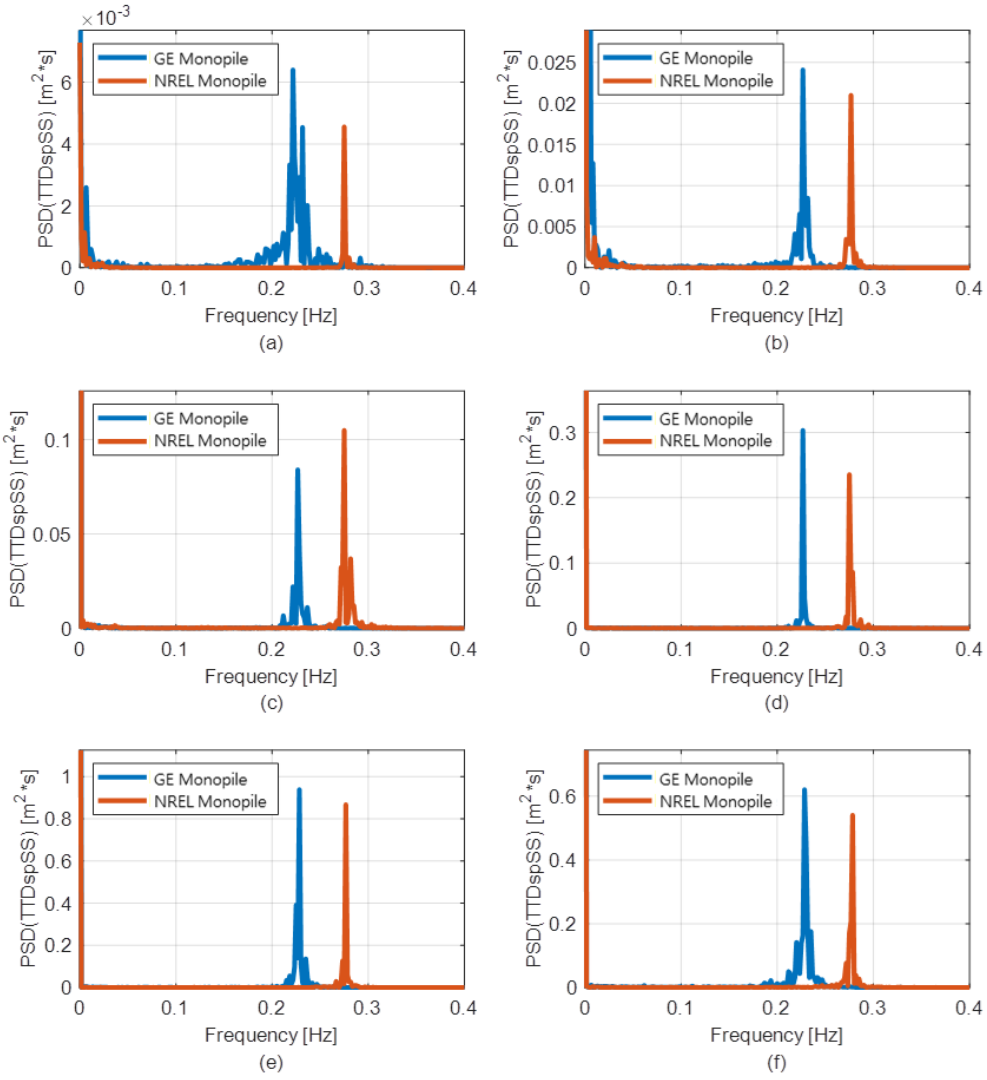

Figure C.4: Frequency response of TTDspSS for fixed-bottom OWTs (NREL monopile and GE monopile), Mean wind speed of (a): 4 m/s, (b): 8 m/s, (c): 12 m/s, (d): 16 m/s, (e): 20 m/s, (f): 24 m/s

APPENDIX D

EXAMPLE TMD MODULE INPUT FILE

```
------- TOWER-TMD, BLADE_TMD AND NACELLE-TLCD INPUT FILE ------------------------------------------------------------------------------------------------------
Module by William La Cava & Matt Lackner (UMass), module has been updated by Semyung Park, Meghan Glade & Matt Lackner
---------------- TMD DEGREES OF FREEDOM ---------------------------------------------------------------------------------------------------------------------
         3   TMD_DOF_MODE     - DOF mode (switch) {0: No TMD DOF; 1: TMD_X_DOF and TMD_Y_DOF 2: TMD_XY_DOF (Omni-Directional TMD)} 3: TLCD
      True   TMD_X_DOF        - DOF on or off (flag) {Used only when TMD_DOF_MODE is 1}
      True   TMD_Y_DOF        - DOF on or off (flag) {Used only when TMD_DOF_MODE is 1}
      True   TLCD_X_DOF       - DOF on or off (flag) {Used only when TMD_DOF_MODE is 3}
      True   TLCD_Y_DOF       - DOF on or off (flag) {Used only when TMD_DOF_MODE is 3}
--------------------- TMD INITIAL CONDITIONS ----------------------------------------------------------------------------------------------------------------
         0   TMD_X_DSP        - TMD_X initial displacement (m)
         0   TMD_Y_DSP        - TMD_Y initial displacement (m)
---------------- TMD CONFIGURATION --------------------------------------------------------------------------------------------------------------------------
         0   TMD_P_X          - At rest position of TMDs (X) (m) [relative to the nacelle (NTMD) or tower base (TTMD)]
         0   TMD_P_Y          - At rest position of TMDs (Y) (m) [relative to the nacelle (NTMD) or tower base (TTMD)]
         0   TMD_P_Z          - At rest position of TMDs (Z) (m) [relative to the nacelle (NTMD) or tower base (TTMD)]
         0   TMD_X_DWSP       - DW stop position (maximum X mass displacement) (m)
         0   TMD_X_UWSP       - UW stop position (minimum X mass displacement) (m)
         0   TMD_Y_PLSP       - Positive lateral stop position (maximum Y mass displacement) (m)
         0   TMD_Y_NLSP       - Negative lateral stop position (minimum Y mass displacement) (m)
---------------- TMD MASS, STIFFNESS, & DAMPING -------------------------------------------------------------------------------------------------------------
         0   DAMPER_MODE      - MR DAMPER MODE on or off (flag) {0: Linear Damper Mode; 1: MR Damper Mode;} (-)
         0   TMD_X_M          - TMD mass (kg)
         0   TMD_Y_M          - TMD mass (kg)
         0   TMD_XY_M         - TMDXY mass (kg)
         0   TMD_X_K          - TMD stiffness (N/m)
         0   TMD_Y_K          - TMD stiffness (N/m)
         0   TMD_X_C          - TMD damping (N/(m/s))
         0   TMD_Y_C          - TMD damping (N/(m/s))
         0   TMD_X_KS         - Stop spring stiffness of TMD_X (N/m)
         0   TMD_Y_KS         - Stop spring stiffness of TMD_Y (N/m)
         0   TMD_X_CS         - Stop spring damping (N/(m/s))
         0   TMD_Y_CS         - Stop spring damping (N/(m/s))
---------------- FORE-AFT TLCD TOTAL LENGTH, HORIZONTAL LENGTH, VERTICAL AREA, AREA RATIO, DAMPING COEFF, & DENSITY ------------------------
         0   L_FA             - Fore-Aft TLCD total length (m)
         0   B_FA             - Fore-Aft TLCD horizontal length (m)
         0   area_FA          - Fore-Aft TLCD cross-sectional area of vertical column (m^2)
         0   area_ratio_FA    - Fore-Aft TLCD cross-sectional area ratio (vertical column area divided by horizontal column area) (-)
         0   headLossCoeff_FA - Fore-Aft TLCD head loss coeff (-)
         0   rho_FA           - Fore-Aft TLCD liquid density (kg/m^3))
---------------- SIDE-TO-SIDE TLCD TOTAL LENGTH, HORIZONTAL LENGTH, VERTICAL AREA, AREA RATIO, DAMPING COEFF, & DENSITY --------------------
         0   L_SS             - Side-Side TLCD total length (m)
         0   B_SS             - Side-Side TLCD horizontal length (m)
         0   area_SS          - Side-Side TLCD cross-sectional area of vertical column (m^2)
         0   area_ratio_SS    - Side-SideTLCD cross-sectional area ratio (vertical column area divided by horizontal column area) (-)
         0   headLossCoeff_SS - Side-Side TLCD head loss coeff (-)
         0   rho_SS           - Side-Side TLCD liquid density (kg/m^3))
--------------------- TMD USER-DEFINED SPRING FORCES --------------------------------------------------------------------------------------------------------
False        Use_F_TBL        - Use spring force from user-defined table (flag)
         3   NKInpSt          - Number of spring force input stations
---------------- TMD SPRING FORCES TABLE --------------------------------------------------------------------------------------------------------------------
   X               F_X              Y              F_Y
  (m)              (N)             (m)             (N)
-6.0000000E+00  -4.8000000E+06  -6.0000000E+00  -4.8000000E+06
 0.0000000E+00   0.0000000E+00   0.0000000E+00   0.0000000E+00
 6.0000000E+00   4.8000000E+06   6.0000000E+00   4.8000000E+06
---------------- TMD CONTROL --------------------------------------------------------------------------------------------------------------------------
         0   TMD_CMODE        - Control mode (switch) {0:none; 1: Semi-Active Control Mode; 2: Active Control Mode}
         1   TMD_SA_MODE      - Semi-Active control mode {1: VB-GH; 2: IVB-GH; 3: DB-GH 4: PDA-FF 5: PDA-DF} (-)
         0   TMD_X_C_HIGH     - TMD X high damping for ground hook control
         0   TMD_X_C_LOW      - TMD X low damping for ground hook control
         0   TMD_Y_C_HIGH     - TMD Y high damping for ground hook control
         0   TMD_Y_C_LOW      - TMD Y low damping for ground hook control
         0   TMD_X_C_BRAKE    - TMD X high damping for braking the TMDX (Don't use it now. should be zero)
         0   TMD_Y_C_BRAKE    - TMD Y high damping for braking the TMDX (Don't use it now. should be zero)
         0   MRD_X_AMP_H      - MRD X high ampere for ground hook control  (Used only when DAMPER_MODE = 1 and TMD_CMODE = 2)
         0   MRD_X_AMP_L      - MRD X low ampere for ground hook control   (Used only when DAMPER_MODE = 1 and TMD_CMODE = 2)
         0   MRD_Y_AMP_H      - MRD Y high ampere for ground hook control  (Used only when DAMPER_MODE = 1 and TMD_CMODE = 2)
         0   MRD_Y_AMP_L      - MRD Y low ampere for ground hook control   (Used only when DAMPER_MODE = 1 and TMD_CMODE = 2)
```

Figure D.1: TMD module input file

APPENDIX E

COMPARISON OF LINEAR AND MR DAMPER

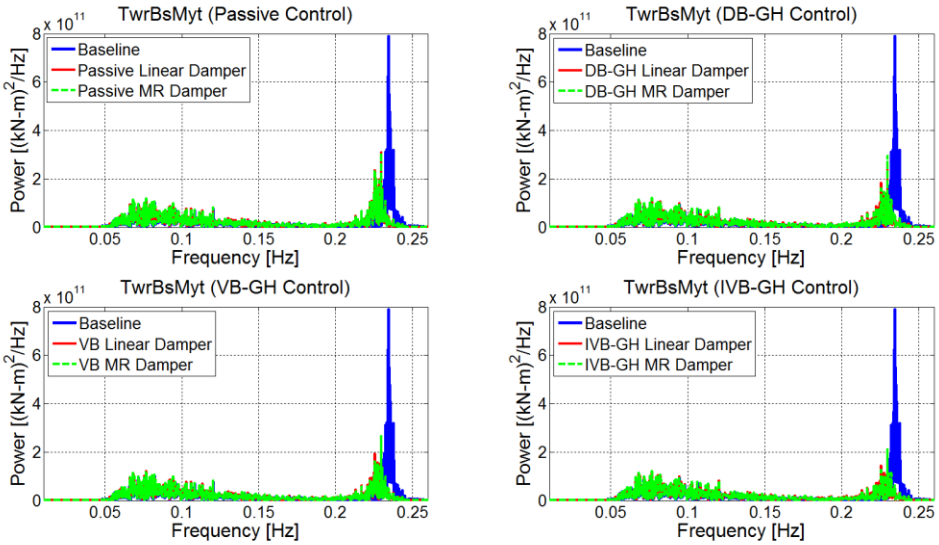

Figure E.1: Power spectral density of the fore-aft tower base moments for the baseline and IVB-GH approach using the linear and MR damper

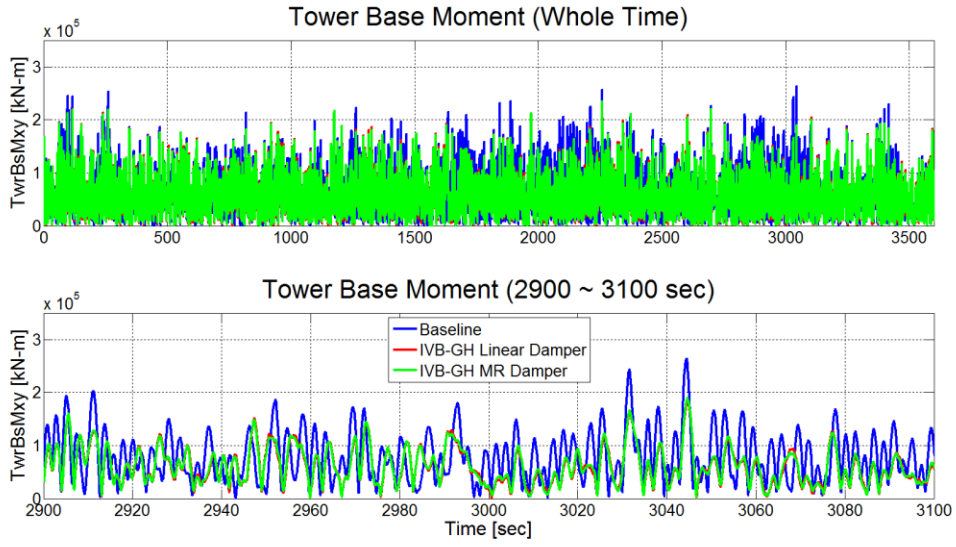

Figure E.2: Time response plot of the tower base moment for the baseline and IVB-GH approach using the linear and MR damper

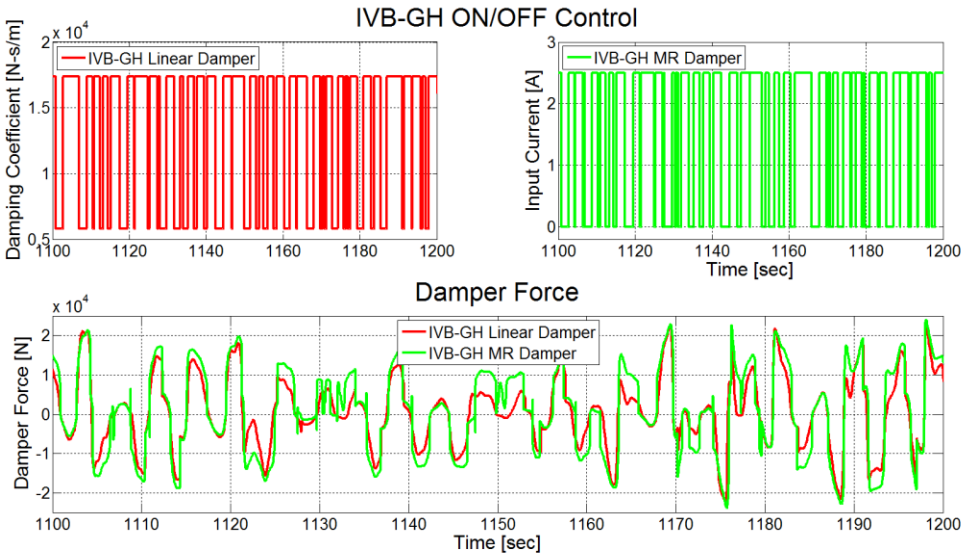

Figure E.3: Input damping coefficient and current following the IVB-GH algorithms, and damping forces

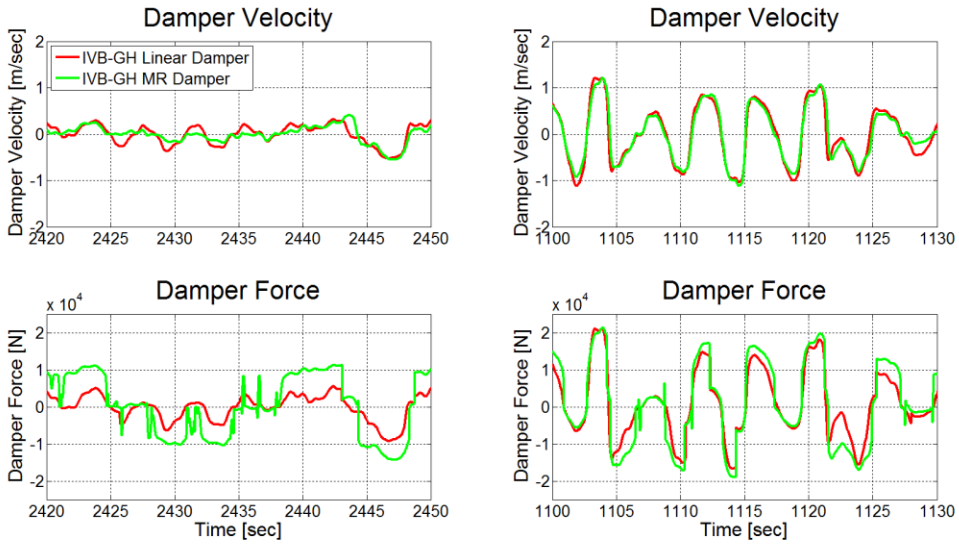

Figure E.4: Comparison of the damper forces between the linear and MR damper in the low and high velocity region

Damper Type	Control Type	Rotation [Deg]	ULS Case	TB Moment [%]	TI Moment [%]	Nacelle Acc [%]	Tendon Tension	
							Maximum [%]	Minimum [%]
Idealized Linear Damper	Passive	0	1	5.1	4.3	7.2	0.2	-12.7
			2	4.6	4.3	9.0	0.4	14.0
		36	1	4.2	4.0	8.7	2.9	10.1
			2	3.5	3.3	9.8	1.4	-1.0
	DB-GH	0	1	7.3	6.6	8.8	1.2	-19.7
			2	6.3	6.6	10.6	1.1	-20.8
		36	1	6.2	6.3	9.9	3.6	2.4
			2	5.3	6.0	11.0	1.9	-9.0
	VB-GH	0	1	7.1	6.5	9.3	0.9	-20.1
			2	6.1	6.4	10.4	0.9	-21.1
		36	1	5.8	6.1	10.2	3.5	3.4
			2	5.0	5.6	10.3	1.8	-8.4
	IVB-GH	0	1	8.7	8.2	11.5	1.5	-25.7
			2	7.4	7.7	11.8	1.4	-25.6
		36	1	7.3	7.5	11.9	4.0	1.6
			2	6.5	7.0	12.1	2.3	13.4
MR Damper	Passive	0	1	5.3	4.6	7.5	0.2	-13.7
			2	4.7	4.5	9.1	0.4	-14.8
		36	1	4.4	4.3	8.8	3.0	9.5
			2	3.7	3.6	9.8	1.5	-1.5
	DB-GH	0	1	6.4	6.2	8.5	1.2	-18.9
			2	5.5	6.0	10.3	1.1	-20.0
		36	1	5.7	6.0	9.4	3.5	2.7
			2	4.9	5.6	10.4	1.8	-9.0
	VB-GH	0	1	7.4	6.9	9.8	1.1	-21.3
			2	6.3	6.5	10.6	1.1	-21.4
		36	1	5.9	6.1	9.6	3.5	1.8
			2	5.2	5.5	9.6	1.9	-9.5
	IVB-GH	0	1	8.7	8.6	11.3	1.6	-25.3
			2	7.3	7.7	11.8	1.4	-24.8
		36	1	7.6	7.9	12.2	4.0	-2.3
			2	6.6	7.0	11.9	2.3	-14.0

Table E.1: Performance comparison of the linear and MR damper

Damper Type	Control Type	Rotation [Deg]	ULS Case	RMS Damper Force [N]	RMS Power consumption [W]	95th TMD stroke (x-direction) [m]	95th TMD stroke (y-direction) [m]
Idealized Linear Damper	Passive	0	1	3,510	-	0.657	0.590
			2	3,423	-	0.650	0.590
		36	1	3,507	-	0.656	0.590
			2	3,423	-	0.650	0.589
	DB-GH	0	1	6,117	-	0.649	0.553
			2	5,955	-	0.642	0.551
		36	1	6,113	-	0.648	0.548
			2	5,946	-	0.642	0.547
	VB-GH	0	1	5,491	-	0.640	0.547
			2	5,362	-	0.634	0.545
		36	1	5,475	-	0.639	0.549
			2	5,347	-	0.633	0.547
	IVB-GH	0	1	7,284	-	0.633	0.532
			2	7,036	-	0.626	0.530
		36	1	7,277	-	0.631	0.533
			2	7,028	-	0.625	0.531
MR Damper	Passive	0	1	3,651	-	0.655	0.586
			2	3,565	-	0.648	0.586
		36	1	3,649	-	0.655	0.586
			2	3,563	-	0.648	0.586
	DB-GH	0	1	8,494	25.8	0.642	0.485
			2	8,382	25.9	0.637	0.481
		36	1	8,477	25.8	0.641	0.484
			2	8,364	25.9	0.635	0.481
	VB-GH	0	1	7,267	21.7	0.630	0.528
			2	7,191	21.9	0.632	0.525
		36	1	7,252	21.8	0.638	0.530
			2	7,183	22.0	0.631	0.527
	IVB-GH	0	1	10,247	30.4	0.627	0.449
			2	10,050	30.3	0.620	0.448
		36	1	10,244	30.4	0.626	0.449
			2	10,046	30.3	0.620	0.449

Table E.2: Dynamic characteristic comparison of the linear and MR damper

BIBLIOGRAPHY

1. Musial, W., Butterfield, S., & Ram, B. (2006, January). Energy from offshore wind. *In Offshore technology conference*. Offshore Technology Conference.
2. Henderson, A. R., Morgan, C., Smith, B., Sørensen, H. C., Barthelmie, R. J., & Boesmans, B. (2003). Offshore wind energy in Europe-A review of the state-of-the-art. *Wind energy*, 6(1), 35-52.
3. Jonkman, J., Butterfield, S., Musial, W., & Scott, G. (2009). *Definition of a 5-MW reference wind turbine for offshore system development* (No. NREL/TP-500-38060). National Renewable Energy Lab.(NREL), Golden, CO (United States).
4. Jonkman, J. M. (2007). *Dynamics modeling and loads analysis of an offshore floating wind turbine* (No. NREL/TP-500-41958). National Renewable Energy Lab.(NREL), Golden, CO (United States).
5. Lackner, M. (2009). Controlling platform motions and reducing blade loads for floating wind turbines. *Wind Engineering*, 33(6), 541-554.
6. Bossanyi, E. A. (2003). Wind turbine control for load reduction. *Wind energy*, 6(3), 229-244.
7. Thomsen, S. C., Niemann, H., & Poulsen, N. K. (2008, July). Individual pitch control of wind turbines using local inflow measurements. *In Proceedings of the 17th World Congress on the International Federation of Automatic Control* (pp. 5587-5592).
8. Van Engelen, T. G. (2006, March). Design model and load reduction assessment for multi-rotational mode individual pitch control (higher harmonics control). *In European Wind Energy Conference* (pp. 27-2).
9. Bossanyi, E. A. (2003). Individual blade pitch control for load reduction. *Wind energy*, 6(2), 119-128.
10. Namik, H., & Stol, K. (2010). Individual blade pitch control of floating offshore wind turbines. *Wind energy*, 13(1), 74-85.
11. Selvam, K. (2007). Individual pitch control for large scale wind turbines. *ECN*, The Netherlands.

12. Bossanyi, E. A. (2005). Further load reductions with individual pitch control. *Wind energy*, 8(4), 481-485.
13. Wortmann, S., Geisler, J., & Konigorski, U. (2016, September). Lidar-Assisted Feedforward Individual Pitch Control to Compensate Wind Shear and Yawed Inflow. In *Journal of Physics: Conference Series* (Vol. 753, No. 5, p. 052014). IOP Publishing.
14. Schlipf, D., Schuler, S., Grau, P., Allgöwer, F., & Kühn, M. (2010). Look-ahead cyclic pitch control using lidar.
15. Mirzaei, M., Henriksen, L. C., Poulsen, N. K., Niemann, H. H., & Hansen, M. H. (2012, October). Individual pitch control using lidar measurements. *In Control Applications (CCA), 2012 IEEE International Conference on* (pp. 1646-1651). IEEE.
16. Chopra, I. (2002). Review of state of art of smart structures and integrated systems. *AIAA journal*, 40(11), 2145-2187.
17. Ge, M. W., Wang, S., & Xiao, H. W. (2015, February). Passive control of floating wind turbine for vibration and load reduction based on TMD. *In Energy and Environmental Engineering: Proceedings of the 2014 International Conference on Energy and Environmental Engineering* (ICEEE 2014), September 21-22, 2014, Hong Kong (Vol. 1, p. 39). CRC Press.
18. Yang, Z. (2013). Wind Turbine Controls for Farm and Offshore Operation.
19. Soong, T. T. (1988). State-of-the-art review: active structural control in civil engineering. *Engineering Structures*, 10(2), 74-84.
20. Soong, T. T., & Costantinou, M. C. (Eds.). (2014). Passive and active structural vibration control in civil engineering (Vol. 345). Springer.
21. Hrovat, D., Barak, P., & Rabins, M. (1983). Semi-active versus passive or active tuned mass dampers for structural control. *Journal of Engineering Mechanics*, 109(3), 691-705.
22. Lackner, M. A., & Rotea, M. A. (2011). Passive structural control of offshore wind turbines. *Wind energy*, 14(3), 373-388.
23. Stewart, G., & Lackner, M. (2013). Offshore wind turbine load reduction employing optimal passive tuned mass damping systems. *Control Systems Technology, IEEE Transactions on*, 21(4), 1090-1104.

24. Dinh, V. N., & Basu, B. (2015). Passive control of floating offshore wind turbine nacelle and spar vibrations by multiple tuned mass dampers. *Structural Control and Health Monitoring*, 22(1), 152-176.
25. Stewart, G. M., & Lackner, M. A. (2011). The effect of actuator dynamics on active structural control of offshore wind turbines. *Engineering Structures*, 33(5), 1807-1816.
26. Si, Y., & Karimi, H. R. (2014, August). Gain Scheduling $ H_2 $/$ H_infty $ Structural Control of a Floating Wind Turbine. *In World Congress* (Vol. 19, No. 1, pp. 6788-6793).
27. Lackner, M. A., & Rotea, M. A. (2011). Structural control of floating wind turbines. *Mechatronics*, 21(4), 704-719.
28. Colwell, S., & Basu, B. (2009). Tuned liquid column dampers in offshore wind turbines for structural control. *Engineering Structures*, *31*(2), 358-368.
29. Jonkman, B., & Jonkman, J. (2016). FAST v8.16.00 a-bjj. National Renewable Energy Laboratory.
30. IEC 61400 3 Ed.1: wind turbines part 3: design requirements for offshore wind turbines. Technical Report, *International Electrotechnical Commission*, The Netherlands, 2008.
31. Musial W, Beiter P, Schwabe P, et al. *2016 Offshore Wind Technologies Market Report (No. NREL/TP-5000-68587; DOE/GO-102017-5031).* Golden, CO National Renewable Energy Laboratory (NREL); 2017.
32. Arany L, Bhattacharya S, Macdonald JH, Hogan SJ. Closed from solution of Eigen frequency of monopile supported offshore wind turbines in deeper waters incorporating stiffness of substructure and SSI. *Soil Dynamics and Earthquake Engineering.* 2016;83:18-32.
33. Musial W, Butterfield S, Boone A. Feasibility of floating platform systems for wind turbines. In: *23rd ASME Wind Energy Symposium*. Reno, NV: NREL; 2004:1-11.
34. Jonkman, J. M., & Matha, D. (2011). Dynamics of offshore floating wind turbines—analysis of three concepts. *Wind Energy*, 14(4), 557-569.

35. Muliawan, M. J., Karimirad, M., & Moan, T. (2013). Dynamic response and power performance of a combined spar-type floating wind turbine and coaxial floating wave energy converter. *Renewable Energy*, 50, 47-57.
36. Van Phuc, P., & Ishihara, T. (2007). A study on the dynamic response of a semi-submersible floating offshore wind turbine system Part 2: numerical simulation. *ICWE12. Cairns*, Australia, 959-966.
37. Charles R Briggs (Project Manager SgurrEnergy Ltd). (2010). Floating Wind Turbine *Technologies* and their Associated Risks. Retrieved from http://wiki-leantech.com/wind-energy
38. Sclavounos, P. D., Lee, S., DiPietro, J., Potenza, G., Caramuscio, P., & De Michele, G. (2010, April). Floating offshore wind turbines: tension leg platform and taught leg buoy concepts supporting 3-5 MW wind turbines. *In European wind energy conference EWEC* (pp. 20-23).
39. Stewart, G. M. (2012). Load reduction of floating wind turbines using tuned mass dampers. (Doctoral dissertation, Department of Mechanical and Industrial Engineering, University of Massachusetts Amherst).
40. Bachynski, E. E., & Moan, T. (2012). Design considerations for tension leg platform wind turbines. *Marine Structures*, *29*(1), 89-114.
41. Kareem, A., Kijewski, T., & Tamura, Y. (1999). Mitigation of motions of tall buildings with specific examples of recent applications. *Wind and structures*, 2(3), 201-251.
42. Sun, J. Q., Jolly, M. R., & Norris, M. A. (1995). Passive, adaptive and active tuned vibration absorbers—a survey. *Journal of mechanical design*, 117(B), 234-242.
43. Luo, N., Bottasso, C. L., Karimi, H. R., & Zapateiro, M. (2011, April). Semiactive control for floating offshore wind turbines subject to aero-hydro dynamic loads. *In International Conference on Renewable Energies and Power Quality* (ICREPQ'11) Las Palmas de Gran Canaria (Spain), 13th to 15th April.
44. Arrigan, J., Pakrashi, V., Basu, B., & Nagarajaiah, S. (2011). Control of flapwise vibrations in wind turbine blades using semi-active tuned mass dampers. *Structural Control and Health Monitoring*, 18(8), 840-851.

45. Chen, J., Liu, Y., & Bai, X. (2015). Shaking table test and numerical analysis of offshore wind turbine tower systems controlled by TLCD. *Earthquake Engineering and Engineering Vibration*, 14(1), 55-75.
46. Sun, C., & Jahangiri, V. (2018). Bi-directional vibration control of offshore wind turbines using a 3D pendulum tuned mass damper. *Mechanical Systems and Signal Processing*, *105*, 338-360.
47. Li, J., Zhang, Z., & Chen, J. (2012). Experimental study on vibration control of offshore wind turbines using a ball vibration absorber. *Energy and Power Engineering*, 4(03), 153.
48. Guimarães PVB, de Morais MVG, Avila SM. Tuned mass damper inverted pendulum to reduce offshore wind turbine vibrations. In: Sinha JK, ed. *Vibration Engineering and Technology of Machinery*. Cham: Springer International Publishing; 2015:379-388.
49. Si Y, Karimi HR, Gao H. Modeling and parameter analysis of the OC3-hywind floating wind turbine with a tuned mass damper in nacelle. *J Applied Math.* 2013;2013:1-10.
50. Coudurier, C., Lepreux, O., & Petit, N. (2015). Passive and semi-active control of an offshore floating wind turbine using a tuned liquid column damper. *IFAC-PapersOnLine*, 48(16), 241-247.
51. O'Donnell, D., Murphy, J., Desmond, C., Jaksic, V., & Pakrashi, V. (2017, May). Tuned Liquid Column Damper based Reduction of Dynamic Responses of Scaled Offshore Platforms in Different Ocean Wave Basins. *In Journal of Physics*: Conference Series (Vol. 842, No. 1, p. 012043). IOP Publishing.
52. Kirkegaard, P. H., Nielsen, S. R., Poulsen, B. L., Andersen, J., Pedersen, L. H., & Pedersen, B. J. (2002). Semiactive vibration control of a wind turbine tower using an MR damper. *In Proceedings of The Fifth European Conference on Structural Dynamics* (pp. 1575-1580). CRC Press/Balkema.
53. Karimi, H. R., Zapateiro, M., & Luo, N. (2010, September). Semiactive vibration control of offshore wind turbine towers with tuned liquid column dampers using H∞ output feedback control. *In 2010 IEEE International Conference on Control Applications* (pp. 2245-2249). IEEE.

54. Dinh, V. N., Basu, B., & Nagarajaiah, S. (2016). Semi-active control of vibrations of spar type floating offshore wind turbines. *Smart Struct Syst*, 18(4), 683-705.
55. Zhang, Z., Li, J., Nielsen, S. R., & Basu, B. (2014). Mitigation of edgewise vibrations in wind turbine blades by means of roller dampers. *Journal of Sound and Vibration*, 333(21), 5283-5298.
56. Zhang, Z., Basu, B., & Nielsen, S. R. (2015). Tuned liquid column dampers for mitigation of edgewise vibrations in rotating wind turbine blades. *Structural Control and Health Monitoring*, 22(3), 500-517.
57. Park, S., Lackner, M. A., Cross-Whiter, J., Tsouroukdissian, A. R., & La Cava, W. (2016, June). An Investigation of Passive and Semi-Active Tuned Mass Dampers for a Tension Leg Platform Floating Offshore Wind Turbine in ULS Conditions. *In ASME 2016 35th International Conference on Ocean, Offshore and Arctic Engineering* (pp. V003T02A061-V003T02A061). American Society of Mechanical Engineers.
58. Jonkman, J., Butterfield, S., Passon, P., Larsen, T., Camp, T., Nichols, J., ... & Martinez, A. (2008). Offshore code comparison collaboration within IEA wind annex XXIII: phase II results regarding monopile foundation modeling (No. NREL/CP-500-42471). National Renewable Energy Lab.(NREL), Golden, CO (United States).
59. Matha, D., Fischer, T., Kuhn, M., & Jonkman, J. (2010). Model development and loads analysis of a wind turbine on a floating offshore tension leg platform (No. NREL/CP-500-46725). National Renewable Energy Lab.(NREL), Golden, CO (United States).
60. DNV. DNV-OS-J101 - Design of Offshore Wind Turbines Structures. Oslo, Norway: DNV; 2014.
61. Bak, C., Zahle, F., Bitsche, R., Kim, T., Yde, A., Henriksen, L. C., ... & Natarajan, A. (2013). The DTU 10-MW reference wind turbine. In Danish Wind Power Research 2013.
62. Jonkman, B. J. (2009). TurbSim user's guide: Version 1.50(No. NREL/TP-500-46198). National Renewable Energy Lab.(NREL), Golden, CO (United States).

63. Bir, G. (2005). User's Guide to BModes (Software for Computing Rotating Beam-Coupled Modes) (No. NREL/TP-500-39133). National Renewable Energy Lab.(NREL), Golden, CO (United States).
64. Hayman, G. J., & Buhl Jr, M. (2012). Mlife users guide for version 1.00. National Renewable Energy Laboratory, Golden, CO, 74(75), 112.
65. La Cava, W., & Lackner, M. A. (2015). Theory manual for the tuned mass damper module in fast v8. University of Massachusetts Amherst: Amherst, MA, USA.
66. Park, S., Lackner, M. A., Pourazarm, P., Rodriguez, A., Cross-Whiter, J., (2019). An investigation on the impacts of passive and semi-active structural control on a fixed-bottom and a floating offshore wind turbine. *Wind energy*, In press.
67. Park, S., Glade, M., Lackner, M. A., (2019). Multi-objective optimization of orthogonal TLCDs for reducing fatigue and extreme loads of a floating offshore wind turbine. *Renewable and sustainable energy reviews*, In preparation
68. *NWTC Information Portal (TMD).* https://nwtc.nrel.gov/TMD. Last modified 08-April-2016 ; Accessed 06-August-2019
69. National data buoy center. (2016). Historical NDBC Data. http://www.ndbc.noaa.gov/.
70. Castillo, E. (2012). Extreme value theory in engineering. Elsevier.
71. Tester, P. A., Feldman, R. L., Nau, A. W., Kibler, S. R., & Litaker, R. W. (2010). Ciguatera fish poisoning and sea surface temperatures in the Caribbean Sea and the West Indies. *Toxicon*, *56*(5), 698-710.
72. Tsouroukdissian AR, Park S, Pourazarm P, et al. Smart novel semi-active tuned mass damper for fixed-bottom and floating offshore wind. In: *Offshore Technology Conference*. Houston, Texas, USA: Offshore Technology Conference; 2016:19.
73. Adam C, Furtmüller T. Seismic performance of tuned mass dampers. In: Irschik H, Krommer M, Watanabe K, Furukawa T, eds. *Mechanics and Model-Based Control of Smart Materials and Structures*. Vienna: Springer Vienna; 2010:11-18.
74. He E-M, Hu Y-Q, Zhang Y. Optimization design of tuned mass damper for vibration suppression of a barge-type offshore floating wind turbine. *Proceedings of the Institution of Mechanical Engineers, Part M: Journal of Engineering for the Maritime Environment.* 2017;231(1):302-315.

75. Warburton, G.B. (1982). Optimum absorber parameters for various combinations of response and excitation parameters. *Earthquake Engineering & Structural Dynamics*, 10(3), 381-401.
76. Aksencer, T., & Aydogdu, M. (2018). Vibration of a rotating composite beam with an attached point mass. *Composite Structures*, 190, 1-9.
77. Kooijman, H. J. T., Lindenburg, C., Winkelaar, D., & Van der Hooft, E. L. (2003). DOWEC 6 MW pre-design. *Energy Research Center of the Netherlands (ECN)*.
78. Yalla, S. K., & Kareem, A. (2000). Optimum absorber parameters for tuned liquid column dampers. *Journal of Structural Engineering*, *126*(8), 906-915.
79. Schaffer, J. D. (1985). Multiple objective optimization with vector evaluated genetic algorithms. In *Proceedings of the First International Conference on Genetic Algorithms and Their Applications, 1985*. Lawrence Erlbaum Associates. Inc., Publishers.
80. rey Horn, J., Nafpliotis, N., & Goldberg, D. E. (1994, June). A niched Pareto genetic algorithm for multiobjective optimization. In *Proceedings of the first IEEE conference on evolutionary computation, IEEE world congress on computational intelligence* (Vol. 1, pp. 82-87).
81. Fonseca, C. M., & Fleming, P. J. (1993, June). Genetic Algorithms for Multiobjective Optimization: Formulation Discussion and Generalization. In *Icga* (Vol. 93, No. July, pp. 416-423).
82. Fogel, D. B. (1997, January). The Advantages of Evolutionary Computation. In *BCEC* (pp. 1-11).
83. Hedar, A. R., & Fukushima, M. (2003). Minimizing multimodal functions by simplex coding genetic algorithm. *Optimization Methods and Software*, *18*(3), 265-282.
84. Srinivas, N., & Deb, K. (1994). Muiltiobjective optimization using nondominated sorting in genetic algorithms. *Evolutionary computation*, *2*(3), 221-248.
85. Deb, K., Pratap, A., Agarwal, S., & Meyarivan, T. A. M. T. (2002). A fast and elitist multiobjective genetic algorithm: NSGA-II. *IEEE transactions on evolutionary computation*, *6*(2), 182-197.

86. Lin, S. (2011). NGPM -- A NSGA-II Program in Matlab v1.6.0.0, MATLAB Central File Exchange. Retrived July 26, 2011.
87. He E-M, Hu Y-Q, Zhang Y. Optimization design of tuned mass damper for vibration suppression of a barge-type offshore floating wind turbine. Proceedings of the Institution of Mechanical Engineers, Part M: *Journal of Engineering for the Maritime Environment*. 2017;231(1):302-315.
88. Si Y, Karimi HR, Gao H. Modeling and parameter analysis of the OC3-hywind floating wind turbine with a tuned mass damper in nacelle. *J Applied Math*. 2013;2013:1-10.
89. Laura MJ, Shirley JD. Semiactive control strategies for MR dampers: comparative study. *J Eng Mech.* 2000;126(8):795-803.
90. Spencer BF, Dyke SJ, Sain MK, Carlson JD. Phenomenological model for magnetorheological dampers. *J Eng Mech.* 1997;123(3):230-238.
91. Kwok NM, Ha QP, Nguyen TH, Li J, Samali B. A novel hysteretic model for magnetorheological fluid dampers and parameter identification using particle swarm optimization. *Sens Actuators A Phys.* 2006;132(2):441-451.
92. Jiang Z, Christenson R. A comparison of 200 kN magneto-rheological damper models for use in real-time hybrid simulation pretesting. *Smart Mater Struct.* 2011;20(6):065011.
93. Kang J, Kim H-S, Lee D-G. Mitigation of wind response of a tall building using semi-active tuned mass dampers. *The Structural Design of Tall and Special Buildings.* 2011;20(5):552-565.
94. Koo JH. *Using Magneto-Rheological Dampers in Semiactive Tuned Vibration Absorbers to Control Structural Vibrations* Virginia, Virginia Tech; 2003.
95. Brodersen ML, Bjørke A-S, Høgsberg J. Active tuned mass damper for damping of offshore wind turbine vibrations. *Wind Energy.* 2017;20(5):783-796.
96. Casciati F, Magonette G, Marazzi F. *Technology of Semiactive Devices and Applications in Vibration Mitigation.* Hoboken, US: John Wiley & Sons; 2006.
97. Lin PY, Chung LL, Loh CH. Semiactive control of building structures with semiactive tuned mass damper. *Computer-Aided Civil and Infrastructure Engineering.* 2005;20(1):35-51.

98. Ji HR, Moon YJ, Kim CH, Lee IW. Structural vibration control using semiactive tuned mass damper. In: *The Eighteenth KKCNN Symposium on Civil Engineering-KAIST6*. Taiwan: KKCNN; 2005:18-20.
99. Kim H-S, Kang J-W. Semi-active fuzzy control of a wind-excited tall building using multi-objective genetic algorithm. *Eng Struct.* 2012;41:242-257.
100. Hyo Seon Park, Hong Gyoo Sohn, Ill Soo Kim, and Jae Hwan Park. Application of gps to monitoring of wind-induced responses of high-rise buildings. *Structural Design of Tall and Special Buildings*, 17(1):117, 2008.
101. Viet LD, Nghi NB, Hieu NN, Hung DT, Linh NN, Hung LX. On a combination of ground-hook controllers for semi-active tuned mass dampers. *J Mech Sci Technol.* 2014;28(6):2059-2064.
102. Sutherland, H. J. (1999). *On the fatigue analysis of wind turbines* (No. SAND99-0089). Sandia National Labs., Albuquerque, NM (US); Sandia National Labs., Livermore, CA (US).
103. Prowell, I., Robertson, A., Jonkman, J., Stewart, G. M., & Goupee, A. J. (2013). *Numerical prediction of experimentally observed behavior of a scale model of an offshore wind turbine supported by a tension-leg platform* (No. NREL/CP-5000-57615). National Renewable Energy Lab.(NREL), Golden, CO (United States).
104. Wehmeyer, C. (2014). *A Floating Offshore Wind Turbine in Extreme Wave Conditions* (Doctoral dissertation, Department of Civil Engineering, Aalborg University).